

# Night Vision and Electronic Sensors Directorate

AMSRD-CER-NV-TR-C240

## Physics-Based Radiometric Signature Modeling And Detection Algorithms of Landmines Using Electro-Optical Sensors

July 2005

*Approved for Public Release: Distribution Unlimited*



Fort Belvoir, Virginia 22060-5806

# REPORT DOCUMENTATION PAGE

*Form Approved*  
OMB No. 0704-0188

Public reporting burden for this collection of information is estimated to average 1 hour per response, including the time for reviewing instructions, searching existing data sources, gathering and maintaining the data needed, and completing and reviewing the collection of information. Send comments regarding this burden estimate or any other aspect of this collection of information, including suggestions for reducing this burden, to Washington Headquarters Services, Directorate for Information Operations and Reports, 1215 Jefferson Davis Highway, Suite 1204, Arlington, VA 22202-4302, and to the Office of Management and Budget, Paperwork Reduction Project (0704-0188), Washington, DC 20503.

1. AGENCY USE ONLY <i>(Leave blank)</i>	2. REPORT DATE June 15, 2003	3. REPORT TYPE AND DATES COVERED Final	
4. TITLE AND SUBTITLE Physics-Based Radiometric Signature Modeling and Detection Algorithms of Landmines Using Electro-Optical Sensors		5. FUNDING NUMBERS	
6. AUTHOR(S) Wen-Jiao Liao		8. PERFORMING ORGANIZATION REPORT NUMBER	
7. PERFORMING ORGANIZATION NAME(S) AND ADDRESS(ES) The Ohio State University Columbus, Ohio		10. SPONSORING / MONITORING AGENCY REPORT NUMBER AMSRD-CER-NV-TR-C240	
9. SPONSORING / MONITORING AGENCY NAME(S) AND ADDRESS(ES) Night Vision and Electronic Sensors Directorate 10221 Burbeck Road Attn: AMSRD-CER-NV-CMD Fort Belvoir, Virginia 22060		11. SUPPLEMENTARY NOTES	
12a. DISTRIBUTION / AVAILABILITY STATEMENT Approved for Public Release: Distribution Unlimited		12b. DISTRIBUTION CODE A	
13. ABSTRACT <i>(Maximum 200 words)</i> This work, supported by the USA RDECOM CERDEC Night Vision and Electronic Sensors Directorate, focuses on signature modeling and detection algorithms. Signature modeling helps to provide insight for sensor deployment. The model addresses relevant issues in sources, targets, and sensors. Natural sources such as thermal emission, solar radiation, and solar scattering were considered and incorporated using empirical models. A BRDF model that defines scattering and emission from rough surfaces was developed that integrates geometric relations with intrinsic surfaces properties. Stokes' vectors are used throughout this work to describe incident and scattered radiances, which permits a polarimetric study of the signatures. The simulated signatures are compared with several measured data sets from different scenarios and exhibit strong quantitative agreement. The advancements described throughout the document will serve to improve real-time mine detection.			
14. SUBJECT TERMS Landmine Detection, Stokes' Vector, Thermal Radiation, Solar Radiation, Bidirectional Reflectance Distribution Function (BRDF), Radiometry, Radiometric Model Construction, Phong Model, Scattering Models		15. NUMBER OF PAGES 277	
17. SECURITY CLASSIFICATION OF REPORT UNCLASSIFIED		16. PRICE CODE	
18. SECURITY CLASSIFICATION OF THIS PAGE UNCLASSIFIED	19. SECURITY CLASSIFICATION OF ABSTRACT UNCLASSIFIED	20. LIMITATION OF ABSTRACT None	

# Night Vision and Electronic Sensors Directorate

AMSRD-CER-NV-TR-C240

## Physics-Based Radiometric Signature Modeling And Detection Algorithms of Landmines Using Electro-Optical Sensors

by

Wen-Jiao Liao  
The Ohio State University

July 2005



Countermining Division  
FORT BELVOIR, VIRGINIA 22060-5806

Physics-Based Radiometric Signature Modeling and Detection  
Algorithms of Land Mines Using Electro-Optical Sensors

DISSERTATION

Presented in Partial Fulfillment of the Requirements for  
the Degree Doctor of Philosophy in the  
Graduate School of The Ohio State University

By

Wen-Jiao Liao, M.S.E.E.

\* \* \* \* \*

The Ohio State University

2003

Dissertation Committee:

Joel T. Johnson, Co-Adviser

Brian A. Baertlein, Co-Adviser

Edward H. Newman

Approved by

---

Co-Adviser

---

Co-Adviser

Department of Electrical  
Engineering

# Physics-Based Radiometric Signature Modeling and Detection Algorithms of Land Mines Using Electro-Optical Sensors

By

Wen-Jiao Liao, Ph.D.

The Ohio State University, 2003

Joel T. Johnson, Co-Adviser

Brian A. Baertlein, Co-Adviser

Airborne EO sensors possess several desirable properties for finding surface-laid anti-vehicle mines. They are capable of stand-off operation and can quickly survey a large area. This work focuses on signature modeling and detection algorithms, two topics that are useful in realizing a real-time minefield detector using EO imagery.

Signature modeling helps to provide insight for sensor deployment. The model addresses relevant issues in sources, targets, and sensors. Natural sources such as thermal emission, solar radiation, and solar scattering were considered and incorporated using empirical models. A BRDF model that defines scattering and emission from rough surfaces was developed that integrates geometric relations with intrinsic surface properties. Stokes' vectors are used throughout this work to describe incident and scattered radiances, which permits a polarimetric study of the signatures. The

simulated signatures are compared with several measured data sets from different scenarios and exhibit strong quantitative agreement.

Mine detection algorithms are a critical system component. The existing baseline “RX” algorithm makes little use of signature information. An alternative to the RX algorithm is constructed using an estimator-correlator formulation and uses spatial target information to enhance the clutter rejection rate. A filter-bank configuration was proposed to fuse results from multiple references to boost the mine detection rate. A locally adaptive implementation was developed to obtain a reliable detection in inhomogeneous backgrounds. The proposed detectors were used to process a large measured data set. Substantial gains were observed for the techniques proposed here. The advancements described throughout this work will serve to improve real-time mine detection.

© Copyright by

Wen-Jiao Liao

2003

## ABSTRACT

Airborne EO sensors possess several desirable properties for finding surface-laid anti-vehicle mines. They are capable of stand-off operation and can quickly survey a large area. This work focuses on signature modeling and detection algorithms, two topics that are useful in realizing a real-time minefield detector using EO imagery.

Signature modeling helps to provide insight for sensor deployment. The model addresses relevant issues in sources, targets, and sensors. Natural sources such as thermal emission, solar radiation, and solar scattering were considered and incorporated using empirical models. A BRDF model that defines scattering and emission from rough surfaces was developed that integrates geometric relations with intrinsic surface properties. Stokes' vectors are used throughout this work to describe incident and scattered radiances, which permits a polarimetric study of the signatures. The simulated signatures are compared with several measured data sets from different scenarios and exhibit strong quantitative agreement.

Mine detection algorithms are a critical system component. The existing baseline "RX" algorithm makes little use of signature information. An alternative to the RX algorithm is constructed using an estimator-correlator formulation and uses spatial target information to enhance the clutter rejection rate. A filter-bank configuration was proposed to fuse results from multiple references to boost the mine detection rate. A locally adaptive implementation was developed to obtain a reliable detection

in inhomogeneous backgrounds. The proposed detectors were used to process a large measured data set. Substantial gains were observed for the techniques proposed here. The advancements described throughout this work will serve to improve real-time mine detection.

To my family

## ACKNOWLEDGMENTS

I would like to express my sincere thanks to Dr. Brian A. Baertlein for his patience and continual guidance during the course of this and other research activities, to Prof. Joel T. Johnson and Prof. Edward H. Newman for taking the time to review this thesis and provide invaluable advice, and to my family and friends for their encouragement and support over the years.

This project was supported by the US Army Night Vision Electronic Sensors Directorate (NVESD). The findings, opinions and recommendations expressed therein are those of the authors and are not necessarily those of NVESD.

## VITA

September 14, 1972 .....Born - Taipei, TAIWAN

1995 .....B.S. Electrical Engineering,  
The National Taiwan University,  
Taipei, TAIWAN

1999 .....M.S. Electrical Engineering.  
The Ohio State University,  
Columbus, OH

1997-present .....Graduate Research Associate,  
The Ohio State University,  
Columbus, OH

## PUBLICATIONS

### Research Publications

W.-J. Liao, I. K. Sendur, and B. A. Baertlein, “Radiometric signatures of surface-laid land mines”, *submitted to IEEE Trans. Geo. Rem. Sens.*

F. Cremer, W. de Jong, K. Schutte, W.-J. Liao and B. A. Baertlein, “Detectibility of surface-laid landmines with a polarimetric infrared sensor”, *submitted to Proc. SPIE Vol. 5089*, 2002.

W.-J. Liao and B. A. Baertlein, “Fused performance of passive thermal and active polarimetric EO demining sensor”, *Proc. SPIE Vol. 4742*, pp. 880-891, 2002.

W.-J. Liao, D.-H. Chen, and B. A. Baertlein, “Algorithms for detection of surface mines in multispectral IR and visible imagery”, *Proc. SPIE Vol. 4394*, pp. 310-321, 2001.

B. A. Baertlein, W.-J. Liao, and D.-H. Chen, "Fusion of acoustic LDV and GPR data", *Proc. SPIE Vol. 4394*, pp. 970-978, 2001.

B. A. Baertlein, W.-J. Liao, and D.-H. Chen, "Predicting sensor fusion performance using theoretical models", *Proc. SPIE Vol. 4394*, pp. 1035-1046, 2001.

D.-H. Chen, I. K. Sendur, W.-J. Liao, and B. A. Baertlein, "Using physical models to improve thermal IR detection of buried mines", *Proc. SPIE Vol. 4394*, pp. 207-218, 2001.

B. A. Baertlein, and W.-J. Liao, "Wavelet-based higher-order neural networks for mine detection in thermal IR imagery", *Proc. SPIE Vol. 4038*, pp. 168-178, 2000.

W.-J. Liao and B. A. Baertlein, "The role of grounding in automotive EMC", *IEEE International Symposium on Electromagnetic Comp.*, pp. 745-750, 1999.

## FIELDS OF STUDY

Major Field: Electrical Engineering

Studies in:

Electromagnetics  
Signal Processing

# TABLE OF CONTENTS

	Page
Abstract . . . . .	ii
Dedication . . . . .	iv
Acknowledgments . . . . .	v
Vita . . . . .	vi
List of Tables . . . . .	xii
List of Figures . . . . .	xiii
Chapters:	
1. Introduction . . . . .	1
1.1 Motivation . . . . .	2
1.2 EO Mine Detection Sensors . . . . .	3
1.3 Objectives . . . . .	4
1.4 Organization . . . . .	5
2. Issues Affecting EO Mine Signature Modeling . . . . .	7
2.1 Definitions . . . . .	7
2.2 Radiation Sources and Paths . . . . .	9
2.2.1 Thermal Radiation . . . . .	10
2.2.2 Solar Radiation . . . . .	12
2.2.3 Skylight (Atmosphere-Scattered Solar Radiation) . . . . .	13
2.2.4 Radiometric Sources Considered in This Work . . . . .	17
2.3 Physical Properties and Geometric Structure . . . . .	19
2.3.1 Thermal Properties . . . . .	19

2.3.2	Small-Scale Surface Structure . . . . .	20
2.4	Bidirectional Reflectance Distribution Function (BRDF) . . . . .	21
2.4.1	BRDF for Non-Polarimetric Sensors . . . . .	22
2.4.2	BRDF for Polarimetric Sensors . . . . .	24
2.5	An Overview of Scattering Models . . . . .	26
2.5.1	Specular Models for Smooth Surfaces . . . . .	27
2.5.2	Diffuse (Lambertian) Models . . . . .	28
2.5.3	The Phong Model . . . . .	30
2.5.4	The Beckmann Model (Physical Optics) . . . . .	30
2.5.5	The Torrance-Sparrow (Geometrical Optics) Model . . . . .	32
2.5.6	The Beard-Maxwell Model . . . . .	34
2.5.7	Perturbation Methods . . . . .	35
2.6	Relation of Emissivity and Scattering Properties . . . . .	35
2.7	EO Imagery Data Sets . . . . .	39
2.7.1	Northern Temperate Site 1 . . . . .	39
2.7.2	Northern Temperate Site 2 . . . . .	40
2.7.3	TNO Polarimetric Imagery . . . . .	42
2.8	Summary . . . . .	44
3.	Radiometric Mine Signature Model Implementation . . . . .	46
3.1	Problem Geometry . . . . .	47
3.2	Radiative Source Computation . . . . .	48
3.2.1	3-D FEM Thermal Model . . . . .	48
3.2.2	Example Surface Temperature Calculations . . . . .	58
3.2.3	Solar Spectral Irradiance . . . . .	64
3.2.4	Spectral Radiance of Skylight . . . . .	69
3.3	A Mueller Matrix for Mine and Soil . . . . .	74
3.3.1	Physical Optics Model . . . . .	74
3.3.2	Geometrical Optics Model . . . . .	82
3.3.3	Comparison of PO and GO Models . . . . .	84
3.3.4	A Proposed Polarimetric Mueller Matrix . . . . .	86
3.3.5	Sample Rough-Surface BRDFs . . . . .	87
3.3.6	Comparison to Experimental BRDF Data . . . . .	91
3.3.7	Implementation of Emissivity Model . . . . .	96
3.4	Radiometric Model Construction . . . . .	101
3.4.1	Simulation Procedure . . . . .	101
3.4.2	Derivation of Individual Components . . . . .	107
3.5	Simulated Signatures For Ideal Sensors . . . . .	112
3.5.1	Comparative Study of Radiometric Components . . . . .	113
3.5.2	Radiometric Signatures of an Oblique Sensor . . . . .	120
3.5.3	Radiometric Signature and Sensor Orientation . . . . .	124

3.5.4	Comparative Study of Sensor Bands . . . . .	127
3.6	Sensor Point Spread Function . . . . .	133
3.7	Summary . . . . .	137
4.	Model Validation and Signature Analysis . . . . .	140
4.1	Case 1: Temporal Response of Non-Polarimetric Sensor . . . . .	140
4.1.1	Radiometric Model Validation . . . . .	141
4.1.2	Signatures for Sunlit Conditions . . . . .	148
4.1.3	Signatures During Darkness . . . . .	154
4.1.4	Signatures at Dawn and Dusk . . . . .	155
4.2	Case 2: Polarimetric MWIR Signatures . . . . .	157
4.2.1	Parameter Selection for TNO Data . . . . .	157
4.2.2	Comparison to Measured Polarimetric Images . . . . .	159
4.2.3	Evaluation of Signature Components . . . . .	161
4.3	Case 3: Non-polarimetric Visible Band Imagery . . . . .	167
4.3.1	The NT-S2 May 2000 Data . . . . .	167
4.3.2	Illumination and Scattering Properties in the Visible Band . . . . .	169
4.3.3	Comparison of Radiometric Components . . . . .	175
4.3.4	Model Validation for the Visible Band . . . . .	178
4.4	Summary . . . . .	182
5.	Mine Detection Algorithms for EO Imagery . . . . .	186
5.1	Prior Works . . . . .	187
5.2	RX Algorithm (GLRT Approach) . . . . .	189
5.3	Implementations of the RX Algorithm . . . . .	190
5.3.1	Standard RX Algorithm . . . . .	191
5.3.2	Modified RX Algorithm . . . . .	192
5.3.3	Frequency-Domain RX Implementation . . . . .	195
5.4	Performance Enhancements . . . . .	196
5.4.1	Multiple Target Components . . . . .	196
5.4.2	Clutter Whitening . . . . .	198
5.5	Random Signal Approach (Estimator Correlator) . . . . .	200
5.6	Implementation of EC Algorithm . . . . .	205
5.6.1	Construction of EC Detector Elements . . . . .	206
5.6.2	Sample Wiener Filter . . . . .	210
5.6.3	Filter-Bank Configuration . . . . .	212
5.7	Locally Adaptive EC Detector . . . . .	214
5.8	Performance Evaluation . . . . .	217
5.9	Summary . . . . .	221

6.	Conclusion . . . . .	223
6.1	Summary of and Findings for the Radiometric Model . . . . .	224
6.2	Summary of and Findings for Mine Detection Algorithms . . . . .	227
6.3	Future Work . . . . .	228
6.4	Concluding Remarks on EO Mine Detection . . . . .	230
Appendices:		
A.	Radiometry . . . . .	231
A.1	Radiometry Terms . . . . .	231
A.1.1	Solid Angle and Projected Solid Angle . . . . .	231
A.1.2	Flux, Radiance, and Irradiance . . . . .	232
A.1.3	Spectral Dependency . . . . .	233
A.2	Radiative Transfer . . . . .	233
A.3	Radiometric Framework of EO Sensors . . . . .	234
A.4	Blackbody Radiation . . . . .	235
B.	Electro-Optic Sensors . . . . .	237
B.1	Physics of EO sensors . . . . .	237
B.2	Types of EO sensors . . . . .	238
B.2.1	Passive and Active Sensors . . . . .	240
B.2.2	Single- and Multi-Spectral Sensors . . . . .	241
B.2.3	Polarimetric Sensors . . . . .	241
C.	Derivation of the RX algorithm . . . . .	243
	Bibliography . . . . .	247

## LIST OF TABLES

Table	Page
2.1 Mine characteristics in the NT-S2 data set. . . . .	41
2.2 Mine distribution in the NT-S2 data set. . . . .	42
3.1 Critical meteorological parameters used in the baseline simulation. . .	58
3.2 Critical thermal properties of materials used in the baseline simulation.	59
3.3 Critical meteorological parameters used in the simulation for seasonal changes in surface temperatures. . . . .	62
3.4 Surface scattering parameters for the mine and soil used in SWIR, MWIR, and LWIR sensor simulations. . . . .	127
4.1 Surface parameters used in simulations of TNO's surrogate LP mines.	159
4.2 Radiometric calibration parameters for visible band images at 11 AM, May 24th, NT-S2. . . . .	169
4.3 Surface parameters for LM_B mine simulations at NT-S2 using a visible band camera. . . . .	176
4.4 Sensor zenith and hour angles for simulation sites "A", "B", and "C".	179

## LIST OF FIGURES

Figure	Page
2.1 Scattered solar irradiance from a unit volume. . . . .	14
2.2 Transmission paths of sensor received flux from various sources. . . . .	18
2.3 The small- and large-scale roughness of a surface. . . . .	21
2.4 Geometric definitions. . . . .	23
2.5 Sample surveillance image containing LP_B mines. Red diamonds are added indicating positions of mines (top row) and fiducial markers (middle row). . . . .	40
2.6 Surface temperatures of soil and mine and meteorological data measured at TNO on November 27th, 2001. . . . .	43
2.7 Layout of TNO test site. . . . .	43
3.1 Geometry of mine detection application. . . . .	47
3.2 Cross-sectional nodal profile ( $\hat{r} - \hat{z}$ plane)for soil and a LP_B mine. . . . .	55
3.3 Cut-away 3-D view of the mesh of soil and a LP_B mine. . . . .	55
3.4 Zoomed-in cut-away 3-D view of the LP_B mine mesh. . . . .	56
3.5 3-D view of original LP_B mine and soil surface mesh. . . . .	57
3.6 3-D view of refined LP_B mine and soil surface mesh. . . . .	57
3.7 Diurnal cycle convergence of surface temperatures. . . . .	60

3.8	Boundaries (solid lines) of mine and soil regions in simulated thermal images. Averages over gray regions are used for comparison. . . . .	60
3.9	Examples of surface temperature profiles during the day. . . . .	61
3.10	Surface temperatures and contrast for different time of the year. Baseline conditions: latitude=40.3°N, wind speed=3 m/s. Solid lines: mine. Dash lines: soil. . . . .	63
3.11	Surface temperatures and contrast for different wind speeds during summer. Baseline conditions: latitude=40.3°N, air temperature: mean=25°C maximal deviation=5°C. . . . .	64
3.12	Surface temperatures and contrast for different wind speeds during summer. Baseline conditions: latitude=40.3°N, air temperature: mean=0°C maximal deviation=5°C. . . . .	65
3.13	Solar elevation angle of different months at latitude 43.5°N. . . . .	67
3.14	Solar elevation angle of different months at latitude 23.5°N. . . . .	67
3.15	Solar irradiance at MWIR band (3~5 $\mu\text{m}$ ) v.s. solar elevation angle in mid-latitude winter and summer. . . . .	68
3.16	Diurnal variations in solar irradiance at MWIR band (3~5 $\mu\text{m}$ ) in December and June at latitude 43.5°N. . . . .	69
3.17	Mesh used in skylight calculation. . . . .	70
3.18	Sample skylight profile at 8:30AM in May at latitude 52°N. . . . .	71
3.19	Sample skylight profile at 12:30PM in May at latitude 52°N. . . . .	72
3.20	Sample skylight degree of linear polarization based on Rayleigh scattering. . . . .	73
3.21	Geometrical definitions of a locally tilted surface. . . . .	77
3.22	A sample surface spectral density function. . . . .	80

3.23 Moderately rough surface BRDF ( $\theta_i = 22^\circ$ , $s^2 = 0.01$ , $m = 1.5$ , $\rho_{dc}=0.01$ , $\rho_{dx} = 0.005$ ). . . . .	88
3.24 BRDFs of a slightly rough surface ( $s^2 = 0.0025$ , $m = 1.5$ , $\rho_{dc}=0.01$ , $\rho_{dx} = 0.005$ ) and a very rough surface ( $s^2 = 0.05$ , $m = 1.5$ , $\rho_{dc}=0.0075$ , $\rho_{dx} = 0.0037$ ) at $\theta_i = 22^\circ$ . . . . .	89
3.25 BRDFs of a slightly rough surface ( $s^2 = 0.0025$ , $m = 1.5$ , $\rho_{dc}=0.01$ , $\rho_{dx} = 0.005$ ) and a very rough surface ( $s^2 = 0.05$ , $m = 1.5$ , $\rho_{dc}=0.0075$ , $\rho_{dx} = 0.0037$ ) at $\theta_i = 42^\circ$ . . . . .	90
3.26 Very rough surface BRDF without the self-shadowing correction $G$ ( $\theta_i = 42^\circ$ , $s^2 = 0.05$ , $m = 1.5$ , $\rho_{dc}=0.0075$ , $\rho_{dx} = 0.0037$ ). . . . .	91
3.27 Slightly rough surface BRDF without the diffuse term ( $\theta_i = 42^\circ$ , $s^2 = 0.0025$ , $m = 1.5$ , $\rho_{dc}=10^{-6}$ , $\rho_{dx}=0.5 \times 10^{-6}$ ). . . . .	92
3.28 Comparison of measured and modeled BRDF results in the incident plane. The measured surface is aluminum with green paint and zinc chromate coatings. The illumination is $0.63 \mu\text{m}$ wavelength. The simulated surface has the parameters $s^2 = 0.01$ , $m = 1.5$ . Co- and cross-polarized diffuse albedos are 0.015 and 0.0075. . . . .	94
3.29 Comparison of measured and modeled BRDF results in the incident plane. The measured surface is metal with green paint at $0.63 \mu\text{m}$ and $10.6 \mu\text{m}$ . The simulated surface has the parameters $m = 1.5$ . $s^2=0.015$ and 0.0009. Co- and cross-polarized diffuse albedos are 0.03 and 0.015 for $0.63 \mu\text{m}$ and 0.01 and 0.005 for $10.6 \mu\text{m}$ . . . . .	95
3.30 Measured BRDF results in the incident plane. The measured surface is concrete. The illumination is $0.63 \mu\text{m}$ wavelength. The corresponding simulations (not shown) are simply constants. . . . .	96
3.31 Horizontal and vertical emissivity for various refractive indices ( $s^2 = 0.01$ , no diffuse component). . . . .	98
3.32 Horizontal and vertical emissivity for various surface roughnesses ( $m=1.5$ , no diffuse component). . . . .	99

3.33	Horizontal and vertical emissivity of simulated mine and soil surfaces with and without the diffuse component (mine: $s^2 = 0.0025$ and $m=1.4$ ; soil: $s^2 = 0.05$ and $m=1.6$ ). . . . .	100
3.34	Block diagram of the activities and data sources used in generating radiometric mine signatures. The principle functions of the simulator appear in the left column. The radiometric components are given in the center column. The right column shows external data sources. . .	102
3.35	Block diagram of the procedures used in generating surface temperature profiles from the thermal model. . . . .	104
3.36	Block diagram of the procedures used in generating solar irradiance and skylight radiance from the MODTRAN code. . . . .	105
3.37	Simulated signatures in the $I$ , $Q$ , and $U$ components for direct thermal emission and nadir viewing. . . . .	113
3.38	Emissivity difference ( $\mathcal{E}_v - \mathcal{E}_h$ ) for mine and soil surfaces. . . . .	114
3.39	Simulated signatures in the $I$ , $Q$ , and $U$ components for single-bounce solar radiation and nadir viewing. . . . .	115
3.40	Simulated signatures in the $I$ , $Q$ , and $U$ components for single-bounce skylight radiation and nadir viewing. . . . .	116
3.41	Degree of linear polarization (DoLP) for skylight, reflected sunlight, and thermal emission for nadir viewing. . . . .	117
3.42	Simulated signature in the $I$ , $Q$ , and $U$ components for single-bounce thermal emission and nadir viewing. . . . .	117
3.43	Simulated signature in the $I$ , $Q$ , and $U$ components for total thermal emission and nadir viewing. . . . .	118
3.44	Simulated signature in the $I$ , $Q$ , and $U$ components for double-bounce solar radiation and nadir viewing. . . . .	119
3.45	Simulated signature in the $I$ , $Q$ , and $U$ components for total solar radiation and nadir viewing. . . . .	119

3.46	Simulated signature in the $I$ , $Q$ , and $U$ components for total radiation and nadir viewing. . . . .	119
3.47	Simulated signature in the $I$ , $Q$ , and $U$ components for the sum of direct thermal and single-bounce solar radiation and nadir viewing. . . . .	120
3.48	Simulated signatures in the $I$ , $Q$ , and $U$ components for direct thermal emission and oblique viewing ( $\theta_s = 45^\circ$ ). . . . .	121
3.49	Simulated signatures in the $I$ , $Q$ , and $U$ components for single-bounce solar radiation and oblique viewing ( $\theta_s = 45^\circ$ ). . . . .	122
3.50	Simulated signatures in the $I$ , $Q$ , and $U$ components for single-bounce skylight radiation and oblique viewing ( $\theta_s = 45^\circ$ ). . . . .	122
3.51	Degree of linear polarization (DoLP) for skylight, reflected sunlight, and thermal emission for oblique viewing ( $\theta_s = 45^\circ$ ). . . . .	122
3.52	Simulated signature in the $I$ , $Q$ , and $U$ components for single-bounce thermal emission and oblique viewing ( $\theta_s = 45^\circ$ ). . . . .	123
3.53	Simulated signature in the $I$ , $Q$ , and $U$ components for double-bounce solar radiation and oblique viewing ( $\theta_s = 45^\circ$ ). . . . .	123
3.54	Simulated signature in the $I$ , $Q$ , and $U$ components for total radiation and oblique viewing ( $\theta_s = 45^\circ$ ). . . . .	124
3.55	Simulated $I$ images of an oblique sensor ( $\theta_s = 45$ ) oriented toward east, south, west and north. . . . .	125
3.56	Simulated $Q$ images of an oblique sensor ( $\theta_s = 45$ ) oriented toward east, south, west and north. . . . .	126
3.57	Simulated $U$ images of an oblique sensor ( $\theta_s = 45$ ) oriented toward east, south, west and north. . . . .	126
3.58	Solar irradiance versus solar zenith angle in various IR bands for a mid-latitude winter atmosphere. . . . .	128
3.59	Skylight radiance at the solar meridian in various IR bands for a mid-latitude winter atmosphere. . . . .	129

3.60	Simulated intensity images ( $I$ ) of individual components and the total signature in the SWIR band (1-3 $\mu\text{m}$ ) for nadir viewing. . . . .	130
3.61	Simulated intensity images ( $I$ ) of individual components and the total signature in the LWIR band (8-12 $\mu\text{m}$ ) for nadir viewing. . . . .	131
3.62	(a) Received radiance in the MWIR band (3-5 $\mu\text{m}$ ) on soil (average), mine (maximum), and soil next to mine (minimum) where the shadow may be present. (b) Maximum deviation (from average soil radiance) for the mine or its shadow. The green dashed line indicates the incident solar irradiance. . . . .	133
3.63	(a) Received radiance in the SWIR band (1-3 $\mu\text{m}$ ) on soil (average), mine (maximum), and soil next to mine (minimum) where the shadow may be present. (b) Maximum deviation (from average soil radiance) for the mine or its shadow. The green dashed line indicates the incident solar irradiance. . . . .	134
3.64	(a) Received radiance in the LWIR band (8-12 $\mu\text{m}$ ) on soil (average), mine (maximum), and soil next to mine (minimum) where the shadow may be present. (b) Maximum deviation (from average soil radiance) for the mine or its shadow. The green dashed line indicates the incident solar irradiance. . . . .	134
3.65	Gaussian impulse response of sensor. . . . .	135
3.66	Radiometric mine signature before and after applying Gaussian filter that mimics the impulse response of the sensor . . . . .	136
3.67	Down-sampled and rotated simulated radiometric mine signature . . .	137
4.1	$I$ component of individual and total signatures for “NT-S1” data set at 11:00, Oct. 21st. . . . .	142
4.2	Simulated mine signature with cross-section line for radial profile analysis. . . . .	142
4.3	Sample mine chips collected at NT-S1, 11:30AM, October 21st, 2002.	143

4.4	Intensity profiles of simulated and measured signatures along a cross-section. . . . .	145
4.5	$I$ component of individual and total signatures for “NT-S1” data set at 15:00, Oct. 21st. . . . .	146
4.6	Simulated signature for the 3:30 PM run and the cross-section line used for radial profile analysis. . . . .	146
4.7	Sample mine chips collected at “NT-S1”, 15:29, Oct. 21, 2002. . . . .	147
4.8	Intensity profiles of simulated and measured signatures along a cross-section. . . . .	148
4.9	Mosaic of “direct thermal emission” during morning (24:00-7:00), noon (8:00-15:00) and evening (16:00-23:00). . . . .	149
4.10	Mosaic of total radiometric signatures during morning (24:00-7:00), noon (8:00-15:00) and evening (16:00-23:00). . . . .	150
4.11	Solar elevation angle and irradiance on Oct. 21, at “NT-S1”. . . . .	152
4.12	Mosaic of “single-bounce solar reflection” signatures during day time (8:00-15:00). . . . .	152
4.13	Reflected radiance on the solar meridian from mine and soil surfaces at 8 AM and 12 PM, Oct. 21st. . . . .	153
4.14	Simulated signatures of direct thermal, single-bounce thermal, and reflected skylight for “NT-S1” conditions at 23:00. . . . .	154
4.15	The total radiometric signature and surface temperature for “NT-S1” conditions at 23:00. . . . .	155
4.16	Simulated (first row) and measured (second row) $I$ , $Q$ , and $U$ parameters for the “TNO” data set with reduced sensor resolution. . . . .	160
4.17	Simulated $I$ , $Q$ , and $U$ parameters for direct thermal emission for the “TNO” data set. . . . .	162

4.18	Simulated $I$ , $Q$ , and $U$ parameters for single-bounce solar radiation for the “TNO” data set. . . . .	163
4.19	DoLP of single-bounce solar radiation for the “TNO” data set. . . . .	163
4.20	Simulated $I$ , $Q$ , and $U$ parameters for single-bounce skylight radiation for the “TNO” data set. . . . .	164
4.21	Simulated $I$ , $Q$ , and $U$ parameters for single-bounce thermal emission for the “TNO” data set. . . . .	165
4.22	Simulated $I$ , $Q$ , and $U$ parameters for double-bounce solar radiation for the “TNO” data set. . . . .	165
4.23	Simulated $I$ , $Q$ , and $U$ parameters for total radiation for the “TNO” data set. . . . .	166
4.24	Frequency response of R, G, and B channels of the visible camera. . . . .	168
4.25	Measured response in R-, G-, and B-channels and fused image collected by the visible camera from the “NT-S2” data set at 11:00 AM, May 24th, 2000. . . . .	170
4.26	Fused measured images collected by the visible camera from the “NT-S2” data set at 12:00 PM, 3:30 PM, and 5:00 PM on May 24th, 2000. . . . .	171
4.27	Sample visible band extraterrestrial and ground solar irradiance spectrum and atmosphere transmittance for a zenith sun. . . . .	173
4.28	Sample visible band total solar irradiance versus solar elevation angle of rural and urban extinction at mid-latitude summer. . . . .	174
4.29	Sample visible band skylight radiance profile at 12 PM, May 24th, for NT-S2. . . . .	175
4.30	$I$ component of individual and total signatures for “NT-S2” data set at 12 PM, May 24th. . . . .	177
4.31	Geometric relations of the sensor, the sun and mine positions in the measured image. . . . .	179

4.32	Simulated signatures for LM_B mines at location “A”, “B”, and “C” at four times (11 AM, 12 PM, 3 PM, and 5 PM) on May 24th, at NT-S2.	181
4.33	Measured signatures for LM_B mines at location “A”, “B”, and “C” at four times (11 AM, 12 PM, 3 PM, and 5 PM) on May 24th, at NT-S2.	183
5.1	Block diagram of standard RX algorithm implementation.	191
5.2	Sample RX processing results.	193
5.3	Target and background covariance estimation masks.	194
5.4	Performance comparison of standard and modified RX algorithms.	196
5.5	Sample mine and clutter chips and their power spectra.	199
5.6	Block diagram of EC algorithm.	206
5.7	EC algorithm templates.	208
5.8	Histograms of the ratios of mine amplitudes to clutter standard deviations.	209
5.9	Essential components of the Wiener filter.	211
5.10	The Wiener filter for LM_B mine.	212
5.11	Sample raw and filtered images.	213
5.12	Normalized images around the mine position before and after Wiener filtering.	213
5.13	Block diagram of the filter-bank configuration.	214
5.14	Sample EC processing results with global and local clutter estimation.	216
5.15	Performance of RX and EC algorithms.	218
5.16	Performance of RX and EC algorithms with global clutter estimation in homogeneous background.	219

5.17 Performance of EC algorithm with fused and single references. . . . .	220
A.1 Radiometric framework of EO Sensors. . . . .	235

# CHAPTER 1

## INTRODUCTION

Land mines are among the most dangerous forms of unexploded ordnance. With tens of millions of landmines deployed in more than 70 countries, mine detection is of critical importance in both humanitarian and military operations. In spite of more than 40 years of research [1], reliable mine detection remains an elusive goal.

In standard military operations, mines are deployed in minefields with the intent of reducing the mobility of ground forces. During wartime, finding minefields in a timely fashion is critical to the safety and success of ground forces. EO sensors are attractive for demining, because those sensors are capable of stand-off operation and airborne sensors can rapidly survey a wide area. On the other hand, mine signature are easily lost in clutter (especially for buried mines), and the sensor resolution varies with changes in aircraft altitude. The above advantages and limitations have largely restricted the use of airborne EO demining sensors to detection of surface-laid anti-vehicle (large) mines. Specialized EO sensors, including polarimetric sensors and multi-spectral sensors, are available and have been investigated, but are still immature.

In this dissertation, basic studies are presented that address the performance of minefield detectors. Two topics were explored: radiometric signature models and

mine detection algorithms. A physics-based radiometric model was developed, and comparison of its simulations with measured EO imagery shows reasonable agreement. A minefield detection system requires a reliable mine detection algorithm. A novel algorithm was devised for this purpose and compared to a baseline algorithm.

## 1.1 Motivation

Work on EO signature modeling was motivated by the fact that, in general, the performance of a detection algorithm can be improved by exploiting knowledge about the signature of the intended target. For land mine detection, this requires a priori knowledge of the mine signatures at the time of data collection.

Mine signatures are challenging to predict. It has long been observed that such signatures are highly variable, depending strongly on sensor characteristics and current and past environmental condition. Time-of-day, day-of-year, sensor bandwidth, image resolution and viewing geometry are a few of the many parameters that affect EO mine signatures. Predicting signatures as a function of these parameters requires a sophisticated model that addresses both the thermal and radiometric aspects of the processes involved.

Given knowledge of a mine's signature, a detection algorithm capable of exploiting the signature information is required. Because of the aforementioned signature variability, the algorithms currently used to detect land mines exploit only the most basic signature information (e.g., size and shape) by assuming, for example, a round target of uniform contrast. More detailed signatures provided by the above-described model could be integrated into a detection algorithm to improve its performance.

## 1.2 EO Mine Detection Sensors

A number of systems have been developed to process EO imagery for mine detection. Early work on multi-spectral detectors was reported by Witherspoon and Holloway [2] who fused six channels of imagery collected by a 400-900 nm camera with a spinning filter wheel. That sensor was later used on an airborne platform under the Coastal Battlefield Reconnaissance and Analysis (COBRA) program [3, 4]. The REMIDS sensor [5] combined a passive thermal IR channel with two co-registered linearly polarized near-IR sensor of laser reflectance. That combined passive/active sensor concept later becomes part of the ASTAMIDS system [6].

There has also been extensive work in hyper-spectral imaging for demining. McFee et al. developed a compact airborne spectrographic imager (*casi*) [7, 8, 9, 10], which employs up to 288 spectral bands over the 400-1000 nm range. An extensive experimental study of hyper-spectral phenomenology has recently been presented by Smith et al. [11].

EO mine signature modeling has been attempted from a physics-based prospect. A thermal model using FEM approach was developed by Sendur [12] for prediction of temperature contrast among buried mines and surrounding soil. Cremer et al. [13] adapted this model to estimate polarimetric signatures in the MWIR band for surface-laid mines. Primary features of the temperature distribution due to insolation were found in fair agreement with measurements.

### 1.3 Objectives

This work has two major objectives. First, a physically based mine signature model will be developed with the capability of treating diverse sensors and environmental conditions. To ensure that the model is useful in practice, it is validated using measured signatures. As noted above, mine signatures are influenced by a large number of factors, and the model must address many issues including the physics of natural radiation sources (e.g., direct and scattered sunlight), sensor parameters (bandwidth, resolution, and noise level), the imaging geometry, and scattering and emission by rough random surfaces. Accurate modeling of scattering and emission as functions of source and observer directions is particularly important to the success of the model. A model for a bi-directional reflectance distribution function (BRDF) of rough surfaces is described that is based on physical optics (PO) and geometrical optics (GO) approximations to classical random rough surface scattering formulations.

The second major objective of this dissertation is to develop a mine detection algorithm that can exploit predicted signature information. The so-called “RX” algorithm of Reed and Yu [14, 15], which is based on a generalized likelihood ratio test (GLRT), is currently employed by the US Army and will be used as a baseline algorithm. RX makes relatively little use of mine signature information. It assumes a deterministic circular signature of known size and unknown amplitude, and it assumes spatially uncorrelated clutter. As an alternative, an estimator-correlator (EC) approach is described. For the case of additive Gaussian noise, the EC algorithm degenerates to a Wiener filter, which is capable of exploiting more detailed signature and clutter information.

## 1.4 Organization

The organization and content of the dissertation are as follows:

Chapter 2 reviews physical issues that affect EO mine signature modeling. We first review critical radiation sources and transmission paths used in mine detection. Physical properties and modeling methods for random rough surfaces are described along with a literature review of existing rough surface scattering models. The relation of emissivity and BRDF is discussed. Three data sets used to validate and illustrate the models are also described.

Chapter 3 presents the mine signature model. The problem geometry is defined. The thermal model used to predict surface temperature profiles is described. The MODTRAN code, developed by US Air Force, to compute spectral source radiance from direct and scattered solar radiation, is discussed. The BRDF model used for scattering and emission from rough surfaces is developed from classical BRDF models based on physical and geometrical optics. The derivation and validation of the BRDF model are provided in Section 3.3. Integration of the BRDF model, the FEM thermal model and MODTRAN are documented in Section 3.4. Section 3.5 contains studies of an ideal sensor's signatures. The significance of radiometric components and effects of the sensor's angle, orientation and passband are discussed. The effect of finite sensor resolution, which is necessary for a comparison with measured data, is discussed in Section 3.6.

In Chapter 4 simulated results are compared with measured signatures from three different data sets. Temporal MWIR signature variations over a diurnal cycle are studied, and polarimetric MWIR responses are investigated. In both cases, the model exhibits qualitative agreement with major features observed in the measured images.

Mine signatures were also simulated in the visible band to identify major radiometric contributions, and qualitative agreement was also noted.

Chapter 5 reviews prior work on mine detection algorithms and describes the development of an estimator-correlator mine detection algorithm. The baseline RX algorithm is discussed along with some beneficial modifications. The estimator-correlator (EC) approach is described in Sections 5.5 and 5.6. A locally adaptive EC detector was developed to cope with spatially varying clutter environments. Processing results from experimental data are used to demonstrate the effectiveness of the proposed algorithms.

Conclusions, presented in Chapter 6, summarize the work and highlight its main contributions. Suggestions for future work are also presented.

## CHAPTER 2

### ISSUES AFFECTING EO MINE SIGNATURE MODELING

In this chapter we review some physical issues relevant to EO mine signature modeling. We begin by defining the scattering geometry in Section 2.1. Radiation sources and transmission paths involved in EO mine sensing are described in Section 2.2. Critical surface properties and models for random rough surfaces, which are commonly assumed for landmines and natural clutter, are discussed in Section 2.3. A critical target property, the bidirectional reflectance distribution function (BRDF) is discussed in Sections 2.4. A review of previous attempts to derive analytical and numerical BRDF models for random rough surfaces appear in Section 2.5. Another key property, the emissivity, is discussed in Section 2.6. The data sets used in this dissertation are presented in Section 2.7. A review of basic radiometric concepts and their application to mine detection can be found in Appendix A.

#### 2.1 Definitions

In electromagnetic scattering problems it is conventional to refer polarization directions to the so-called “plane of incidence” defined by the surface normal and the wave vector of the incident wave. Polarimetric components in this plane are referred

to as “vertically” polarized, and orthogonally polarized components are referred to as “horizontally” polarized. For a unit wave vector  $\hat{\mathbf{k}}_j$ , where  $j = i, s$  denoted to incident and scattered directions, its associated horizontal and vertical vectors are

$$\hat{\mathbf{h}}_j = \frac{\hat{\mathbf{k}}_j \times \hat{\mathbf{n}}}{|\hat{\mathbf{k}}_j \times \hat{\mathbf{n}}|} \quad (2.1)$$

$$\hat{\mathbf{v}}_j = \hat{\mathbf{h}}_j \times \hat{\mathbf{k}}_j \quad (2.2)$$

in which  $\hat{\mathbf{n}}$  is the surface normal.

The Stokes vector [16] uses four real quantities to accomplish the same purpose. The vector components are the intensity  $I$ , the degree of polarization  $Q$ , the plane of polarization  $U$ , and the ellipticity  $V$  [17]. The complex electric field components,  $e_h$  and  $e_v$ , in the horizontal and vertical directions respectively, are related to the Stokes vector components as follows:

$$\mathbf{I} = \begin{bmatrix} I \\ Q \\ U \\ V \end{bmatrix} = \frac{1}{2\eta_0} \begin{bmatrix} \langle e_h e_h^* + e_v e_v^* \rangle \\ \langle e_h e_h^* - e_v e_v^* \rangle \\ 2\text{Re} \langle e_h e_v^* \rangle \\ 2\text{Im} \langle e_h e_v^* \rangle \end{bmatrix} \quad (2.3)$$

All of the Stokes vector components have the units of radiance (i.e.,  $\text{W}/\text{m}^2\text{sr}$ ), and the quantity  $I$  is the total scattered radiance (also sometimes referred to as “specific intensity” [18]). An EO sensor records irradiance ( $\text{W}/\text{m}^2$ ) received on its image plane, but in this work we will evaluate radiometric signatures in terms of radiance because for a small patch at the image plane (a pixel), the measured irradiance is proportional to the incident radiance on the lens and is subject to changes in optical parameters of the sensor [19] (f-number  $f_p$  and lens diameter  $d$ ). Comparisons of signatures in radiance are invariant to sensor parameters and focus on physical properties of radiative transfer.

While the parameters  $I$  and  $Q$  are evident, the meanings of the quantities  $U$  and  $V$  are less apparent. Egan [20] explains that  $U$  expresses the excess of radiation polarized in the  $+45^\circ$  direction over that in the  $-45^\circ$  direction relative to the plane of incidence, and  $V$  indicates the amount of circularly polarized radiation.

In many of the calculations that follow it will also be convenient to use a modified Stokes vector [21]

$$\mathbf{I} = \begin{bmatrix} I_h \\ I_v \\ U \\ V \end{bmatrix} = \frac{1}{2\eta_0} \begin{bmatrix} \langle e_h e_h^* \rangle \\ \langle e_v e_v^* \rangle \\ 2\text{Re} \langle e_h e_v^* \rangle \\ 2\text{Im} \langle e_h e_v^* \rangle \end{bmatrix} \quad (2.4)$$

in which the classical  $I$  and  $Q$  components have been replaced by the radiance in the  $\hat{\mathbf{h}}$  and  $\hat{\mathbf{v}}$  polarizations respectively.<sup>1</sup> The classical Stokes vector is readily reconstructed from

$$\begin{bmatrix} I \\ Q \end{bmatrix} = \begin{bmatrix} I_h + I_v \\ I_h - I_v \end{bmatrix} \quad (2.5)$$

## 2.2 Radiation Sources and Paths

Passive EO images of landmines and clutter include radiometric contributions that propagate to the sensor via different paths. This section provides information on several common sources and their transmission paths.

The radiance received by an EO sensor includes both thermal emission and reflected illumination. In the first half of this section, we study the properties of thermal emitters and the sun. Their polarization properties are also addressed.

The received radiance may propagate directly from the source to the detector or it may propagate along a complicated path with scattering at multiple locations. One can categorize the radiation paths as direct emission, single scattered or multiply

<sup>1</sup>Note the ordering of the horizontal and vertical components. Some authors (e.g., [18]) use the opposite convention.

scattered. In this analysis we will neglect the paths with more than two reflections, since many objects in the environment tend to partially absorb the incident radiance. Later in this section we describe viewing geometries in which direct emission, single scattering, and multiple scattering are important.

### 2.2.1 Thermal Radiation

For passive infrared sensors, thermal emission from the target is the radiometric component of primary interest. The amount and spectral dependence of thermal emission are defined by the temperature of the target. Because solar radiation has little energy at wavelengths longer than  $3 \mu\text{m}$ , MWIR and LWIR sensors respond to the solar illumination only to the extent that the target absorbs energy and converts it to thermal radiation.

Thermal emission derives from blackbody radiation. As mentioned in Section A.4, a blackbody absorbs all incident radiation regardless of wavelength and incident direction. During emission, a blackbody behaves like a perfect diffuse emitter with a spectrum specified by its temperature and the Planck distribution. For any real surface, the incident radiation is partially absorbed and partially reflected. In addition the amount of emitted energy is always less than the incoming energy. Such a surface is often referred as a graybody. The directional dependence of thermal emission for a graybody is not necessarily diffuse, but is a function of several surface properties.

Thermal emission from graybodies is related to blackbody radiation via the emissivity  $\mathcal{E}$ . The emissivity is defined as the ratio of the actual emitted radiance  $L_G$  to the radiance  $L_{BB}$  emitted by a blackbody at the same temperature. In general, emissivity  $\mathcal{E}$  depends on the wavelength  $\lambda$ , temperature  $T$  and viewing geometry  $(\theta, \phi)$ .

We write

$$\mathcal{E}(\lambda, \theta, \phi, T) \equiv \frac{L_G(\lambda, \theta, \phi, T)}{L_{BB}(\lambda, T)} \quad (2.6)$$

The value of emissivity lies between zero and one. Other representations for emissivity that involve spectral or spatial averages are commonly used. In this work the sensors integrate over a relatively broad passband, and we will use the total directional emissivity, in which the spectral variation has been averaged out. In addition, it will be assumed that the emissivity is independent of the temperature and the surface is isotropic (no dependence on  $\phi$  in emission), leading to

$$\mathcal{E}(\theta) = \frac{\int L_G(\lambda, \theta, T) d\lambda}{\int L_{BB}(\lambda, T) d\lambda} \quad (2.7)$$

in which the integral extends over the sensor passband.

Some materials and viewing geometries [20] produce polarized thermal emissions. For smooth surfaces the polarization can be explained by Fresnel's equations. Referring to the parallel and perpendicular scattering planes, which are defined by the surface normal and the incident wave direction, the parallel and perpendicular emissivity components are given by

$$\mathcal{E}_{\parallel} = \left[ \frac{2 \sin \theta \cos \phi}{\sin(\theta + \phi) \cos(\phi - \theta)} \right]^2 \quad (2.8)$$

$$\mathcal{E}_{\perp} = \left[ \frac{2 \sin \theta \cos \phi}{\sin(\theta + \phi)} \right]^2 \quad (2.9)$$

where  $\theta$  is the emission angle and  $\phi$  is the angle of refraction in the medium given by Snell's law

$$\sin \theta = m \sin \phi \quad (2.10)$$

in which  $m$  is the complex refractive index. The difference in the two polarization planes increases as the emission angle diverges from the surface normal. For unpolarized sensors, the effective emissivity is the mean of the two polarizations.

$$\mathcal{E} = \frac{1}{2}(\mathcal{E}_{\parallel} + \mathcal{E}_{\perp}) \quad (2.11)$$

For rough surfaces, the analysis is significantly more complex, and it appears in Chapter 3.

## 2.2.2 Solar Radiation

Solar radiation is the dominant source for visible sensors, and it strongly influences IR sensors via surface heating. In this section we discuss the properties of direct solar radiation (sunlight). Solar radiation that is scattered by the atmosphere (skylight) is described in the next section.

Outside the earth's atmosphere, the spectrum of solar radiation can be approximated by a blackbody radiator at 5785K. The incident flux is approximately 1390 W/m<sup>2</sup> [22]. The insolation at the earth's surface is affected by the celestial relation of the sun and the earth, which determines the slant path and the atmospheric composition, which regulate absorption and scattering. The actual insolation may change significantly due to various meteorological conditions. On a cloudless day for a near vertical sun, about 80 percent of the incident flux reaches the ground. Only 50 percent of incident flux may pass during a cloudy day [23].

Atmospheric scattering losses are quantified by the "optical thickness" parameter  $\tau$ , which is the integral of the volume scattering coefficient  $\beta$  [24]. For a vertical slant path at altitude  $z$ ,  $\tau$  is

$$\tau(\lambda, z) = \int_z^{\infty} \beta(\lambda, z') dz' \quad (2.12)$$

For a Rayleigh atmosphere, the volume scattering coefficient is a function of the molecular number density  $N$ , the refraction index of air  $m$ , and the wavelength  $\lambda$ .

$$\beta = \frac{24\pi^3}{N\lambda^4} \left( \frac{m^2 - 1}{m^2 + 2} \right)^2 \quad (2.13)$$

The optical thickness is highly sensitive to wavelength ( $\propto 1/\lambda^4$ ). A large optical thickness, which arises for a shorter wavelength, implies more flux is lost to scattering. For the U.S. standard atmosphere, the optical thickness for red light (700 nm) is only a tenth that for blue light (400 nm) at sea level [25].

Solar radiation is unpolarized. It can become polarized when scattered by the atmosphere, as discussed below.

### 2.2.3 Skylight (Atmosphere-Scattered Solar Radiation)

Solar radiation can reach the target via atmospheric scattering. This scattered radiation is often referred to as skylight. In this section, we discuss the scattering processes, polarization properties, and meteorological dependence of skylight.

Skylight includes both scattered solar radiation and thermal emission from the atmosphere. At shorter wavelengths (visible and near IR), the effect of the latter is small compared to the former except during night time.

The scattering process is illustrated in Figure 2.1. A concise representation of the scattered spectral volume irradiance is [26]

$$dE(\lambda) = \frac{E_s(\lambda)\tau_{r1}(\lambda)\beta_{sca}(\lambda, \theta)\tau_{r2}(\lambda) \cos \sigma dV}{r_2^2} \quad (2.14)$$

where  $E_s(\lambda)$  is the exoatmospheric spectral solar irradiance,  $\beta_{sca}$  is the scattering coefficient of a unit volume of the composite atmosphere, and  $\tau(\lambda)$  is the transmission coefficient of the path. The angles,  $\theta$  and  $\sigma$ , which define the relation between

the sun, the scatterer and the target surface, affect the scattering coefficient and the scattered irradiance as well. If the above parameters are known, the total irradiance from scattered solar radiation can be derived via a volume integral over the upper hemisphere, but exact solutions are not available, because of the complicated, time-varying atmosphere composition. Analytical models such as Rayleigh and Mie scattering permit one to predict the scattering behavior under certain conditions. The MODTRAN/LOWTRAN codes, which are simulation packages for light propagation in the atmosphere, use numerical integrations to estimate the radiance received by sensors under specified conditions. These programs take gas and aerosol composition into account and are widely used in remote sensing.

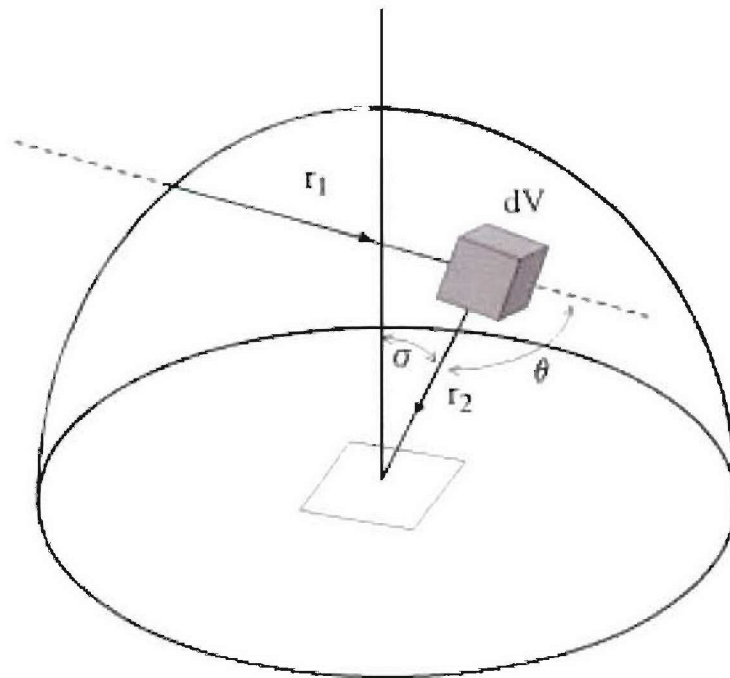


Figure 2.1: Scattered solar irradiance from a unit volume.

An important property of skylight is its polarization. Solar radiation becomes partially linearly polarized upon scattering. The degree of linear polarization is a function of wavelength and the geometric relation of the sun, the scatterer and the observer.

An explanation for the polarization and intensity of skylight was presented by Lord Rayleigh based on the so-called Rayleigh atmosphere assumption, which specifies that particles in the atmosphere are spherical, isotropic, nonionized, much smaller than the wavelength of the incident light, and exhibit a significant density contrast with respect to the surrounding medium. A simple expression for the degree of linear polarization  $\text{DoLP}(\theta)$  of skylight, which is the ratio of the difference and sum of intensities in the perpendicular and parallel polarization planes, is derived from Rayleigh's theory as

$$\text{DoLP}(\theta) = \frac{I_h - I_v}{I_h + I_v} = \frac{\sin^2 \theta}{1 + \cos^2 \theta} \quad (2.15)$$

where  $\theta$  is the angle between source and observer, measured from a scattering particle. This formula predicts a zero polarization in the sun's direction and a total linear polarization at 90 degrees away from the sun. Observation of skylight confirms that it has a smaller polarization near  $\theta = 0$  and reaches its maximum when  $\theta=90^\circ$  as predicted, but the degree of polarization is smaller than Equation (2.15) predicts. The discrepancy becomes more significant as the observation wavelength decreases. Rayleigh's theory also fails to explain the neutral points mentioned earlier. These failures arise because the Rayleigh theory does not consider multiple scattering, and the Rayleigh atmosphere ignores larger aerosols.

More comprehensive models have been developed to describe scattering and absorption in planetary atmosphere. Coulson [24] lists analytical, approximate, and computational methods. Among them, the radiative transfer approach [17] presented

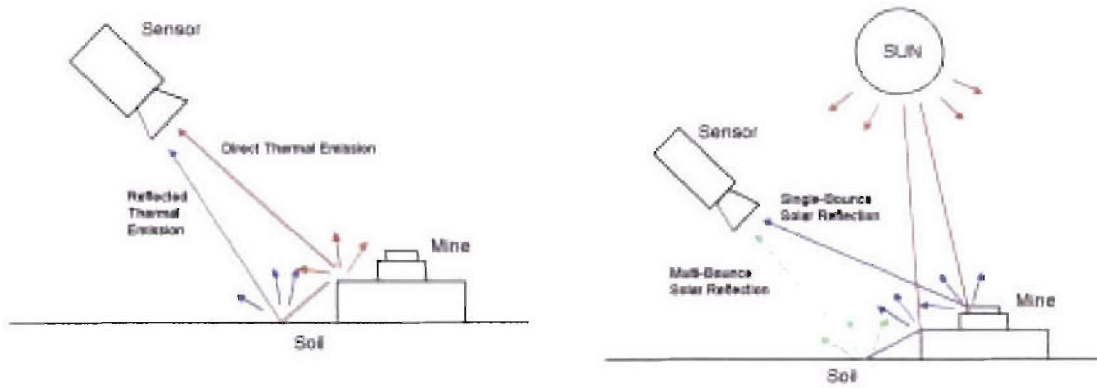
by Chandrasekhar provides a realistic estimate of scattering in stellar atmospheres. Chandrasekhar introduces three non-linear integral equations involving  $H$ -,  $X$ -, and  $Y$ -functions for scattered radiation in a plane-parallel Rayleigh atmosphere. That approach is applicable to an atmosphere with anisotropically distributed gases. The difference in polarizability is accounted for by the optical thickness  $\tau$ , which is a function of wavelength. Evaluation of those nonlinear integral equations shows that the degree of linear polarization for visible light reaches a maximum that is less than unity, as seen in field measurements. At MWIR and longer wavelengths, the optical thickness is small. Therefore, little depolarization occurs, and the simple Rayleigh scattering equation shown in Equation (2.15) is sufficient to estimate the degree of polarization of skylight.

Although analytical methods provide physical insight into the nature of skylight, they are seldom applicable in practice, because of the complex composition of real atmospheres. Attempts have been made to predict atmospheric transmission and absorption using computational methods. The LOWTRAN code and its descendant, MODTRAN, were developed for this purpose. An extensive parameters set is input to characterize the composition of atmospheric gases and aerosols. Corrections for multiple scattering are used to generate estimates of the direct and scattered radiance. This dissertation employs the LOWTRAN/MODTRAN codes to calculate unpolarized ( $I_h + I_v$ ) skylight radiance and solar irradiance. The polarization of skylight is derived from Rayleigh scattering, as shown in Equation (2.15).

## 2.2.4 Radiometric Sources Considered in This Work

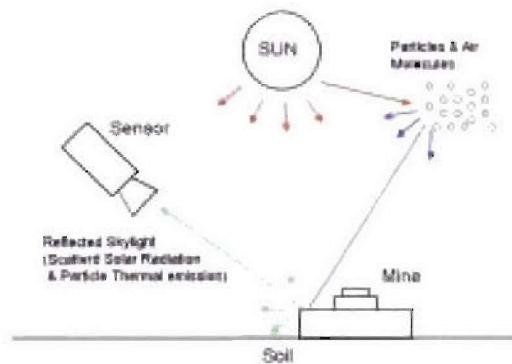
As noted previously emitted and reflected radiance can reach the sensor via direct and scattered routes. Both the direct and scattered paths are needed for a realistic simulation. In general, the direct path and lower-order scattering dominate the radiance, because these components have less attenuation. Their relative importance depends on the sensor band, the source type, and the viewing geometry. Higher-order radiation paths are often ignorable, because of their greater path length and absorption and scattering losses that occur during reflection.

In this work, three sources are considered, which are thermal emission, solar reflection and skylight reflection. Figure 2.2 illustrates these primary radiation sources and the ray paths that contribute to the radiometric signature. Because of the elevated surface-laid mine structure, higher-order paths are possible to form among mine and nearby soil surfaces. Direct and single-scattered components are examined first. A few higher-order paths are then considered as possible corrections. The direct path provides the largest contribution from thermal emission. Single-bounce solar reflection dominates the solar response in the visible and near IR bands. Single-bounce skylight is also included. Even though its source radiance is small compared to the sun, the hemispherical extent of skylight can result in a substantial contribution, particularly when polarization is important. When the scene includes special geometric shapes (e.g., dihedrals and trihedrals) the importance of some higher-order paths can be enhanced.



(a) Thermal emission.

(b) Solar reflection.



(c) Skylight reflection.

Figure 2.2: Transmission paths of sensor received flux from various sources.

## 2.3 Physical Properties and Geometric Structure

The most important target properties for a radiometric sensor are the surface temperature and reflectance. In this section parameters that affect those properties are reviewed. Terminology and common models used to describe the structure of a surface are also introduced.

### 2.3.1 Thermal Properties

The thermal emission from a surface is specified by the surface temperature and emissivity. The surface temperature is determined by solving the heat transfer equation, which takes into account conduction, and, via boundary conditions, convection, absorption and emission. Temperature gradients within a medium cause conduction, which transfers energy by diffusion. Convection transfers energy between solid surfaces and fluids. In the mine detection application, convection takes place at the ground/air interface. Solar energy is absorbed while the thermal emission is radiated from the surface.

The heat transfer equation describes thermal conduction in solid matter and is given by [12]

$$C(\mathbf{r}) \frac{\partial T(\mathbf{r}, \mathbf{t})}{\partial t} = \nabla \cdot (K(\mathbf{r}) \nabla T(\mathbf{r}, \mathbf{t})) \quad (2.16)$$

where  $K$  is the thermal conductivity of the material in units of  $[\text{Wm}^{-1}\text{K}^{-1}]$  and  $C$  is the volumetric heat capacity in  $[\text{Jm}^{-3}\text{K}^{-1}]$ . The ratio of the thermal conductivity to the volumetric heat capacity defines the thermal diffusivity  $k$   $[\text{m}^2\text{s}^{-1}]$ .

In the numerical approach used here, the semi-infinite soil region is truncated at a finite distance, thereby introducing artificial boundaries where boundary conditions must be applied. In addition, the heat transfer equation does not hold in the air above

the mine and soil, so another boundary condition is required at the air interface. At that interface, an energy balance is imposed as the boundary condition. Specifically, the net heat flux into the ground is related to the spatial temperature gradient at the surface as

$$F_{net}(t) = -K \frac{\partial T(\mathbf{r}, t)}{\partial t} \Big|_{z=0} \quad (2.17)$$

where the net heat flux comprises incident radiation from the sun and sky, thermal emission to or from the ground, and convection that exchanges heat energy with the air. We write

$$F_{net}(t) = F_{sun}(t) + F_{sky}(t) - F_{eml}(t) - F_{cnv}(t) \quad (2.18)$$

Modeling approaches for radiation and convection are presented in Section 3.2

### 2.3.2 Small-Scale Surface Structure

The roughness of a surface at microscopic scales has a strong effect on surface scattering and emission properties. In this section we present a mathematical description of rough surfaces that can be used for the construction of a radiometric signature model. Natural and man-made objects will be modeled as large-scale facets with a material-specific roughness as shown in Figure 2.3.

Gaussian random processes are commonly used in random rough surface modeling. For the convenience of model development, Gaussian correlation function is often used to simplify the rough surface representation, although it is not necessarily a realistic description for many natural surfaces. If the surface is assumed to have a Gaussian correlation function, two parameters are critical in describing the surface: the surface height standard deviation  $\sigma$ , and the surface height correlation distance  $l$ . We will employ a zero-mean normal distribution for the surface height as a function of spatial

coordinates ( $z = f_z(x, y)$ ).

$$p(f_z(x, y)) = \frac{1}{\sqrt{2\pi\sigma^2}} \exp\left(-\frac{f_z^2}{2\sigma^2}\right) \quad (2.19)$$

The joint probability density is

$$p(f_z(x, y), f'_z(x', y')) = \frac{1}{2\pi\sigma^2\sqrt{1-C^2}} \exp\left(-\frac{f_z^2 - 2Cf_zf'_z + f'^2_z}{2\sigma^2(1-C^2)}\right) \quad (2.20)$$

For a stationary isotropic surface, a Gaussian correlation function  $C$  can be expressed in terms of the distance between two points in the local plane ( $\tau = \sqrt{(x-x')^2 + (y-y')^2}$ )

$$C(\tau) = \exp\left(-\frac{\tau^2}{l^2}\right) \quad (2.21)$$

For a given  $\sigma$ , a smaller  $l$  implies a rougher surface.

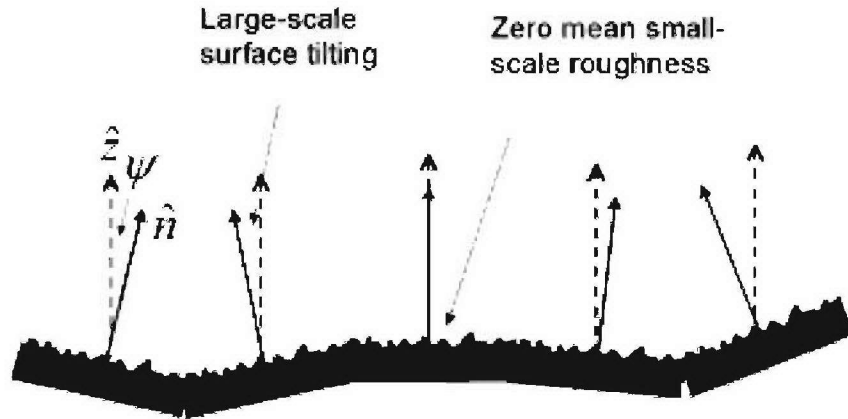


Figure 2.3: The small- and large-scale roughness of a surface.

## 2.4 Bidirectional Reflectance Distribution Function (BRDF)

The bidirectional reflectance distribution function (BRDF), which was introduced by Nicodemus [27], defines the directional reflectance of a surface. This reflectance

is a function of several variables including the properties of the surface material, the viewing geometry, and the incident and sensed polarization. For mine detection applications, the difference in reflectance between mines and clutter may produce contrast in EO imagery. The polarization dependence of mine signatures is of particular interest here, since it has been observed that polarimetric contrast may exist even when the unpolarized contrast vanishes. Natural surfaces tend to produce unpolarized returns, while (typically smooth) man-made surfaces tend to produce linear polarization.

In this section, we begin with a review of the definition of BRDF for unpolarized sensors. The case of polarimetric sensors is treated in Section 2.4.2, where we introduce the Stokes vector and Mueller matrix. Finally, we review a number of BRDF models in Section 2.5, including those that treat rough surface scattering phenomena.

### 2.4.1 BRDF for Non-Polarimetric Sensors

The BRDF of an unpolarized wideband sensor is defined [28] as the ratio of the differential radiance  $dL_r(\theta_r, \phi_r)$  reflected in a given direction to the differential incidence (irradiance)  $dE_i(\theta_i, \phi_i)$  coming from a second direction:

$$\mathcal{F}(\theta_i, \phi_i, \theta_r, \phi_r) = \frac{dL_r(\theta_r, \phi_r)}{dE_i(\theta_i, \phi_i)} \quad (2.22)$$

Using the relation between the differential radiance  $dL_i$  and the differential incidence  $dE_i$  on a surface

$$dE_i(\theta_i, \phi_i) = \int_{d\Omega_i} d\Omega L_i(\theta, \phi) \cos \theta \approx d\Omega_i L_i(\theta_i, \phi_i) \cos \theta_i \quad (2.23)$$

we can derive a relation between the incident and scattered radiance

$$\mathcal{F}(\theta_i, \phi_i, \theta_r, \phi_r) = \frac{dL_r(\theta_r, \phi_r)}{L_i(\theta_i, \phi_i) \cos \theta_i d\Omega_i} \quad (2.24)$$

Figure 2.4 shows the incident and scattered wave vectors as well as their relations to the three axes of a Cartesian coordinate system  $(\hat{x}, \hat{y}, \hat{z})$  and a spherical coordinate system  $(\hat{R}, \hat{\theta}, \hat{\phi})$ . The subscript  $i$  indicates a relation to the incident wave, while the subscript  $s$  refers to the scattered field. The differential surface is assumed to be planar, to lie at the origin, and to be oriented with  $\hat{n} = \hat{z}$ .

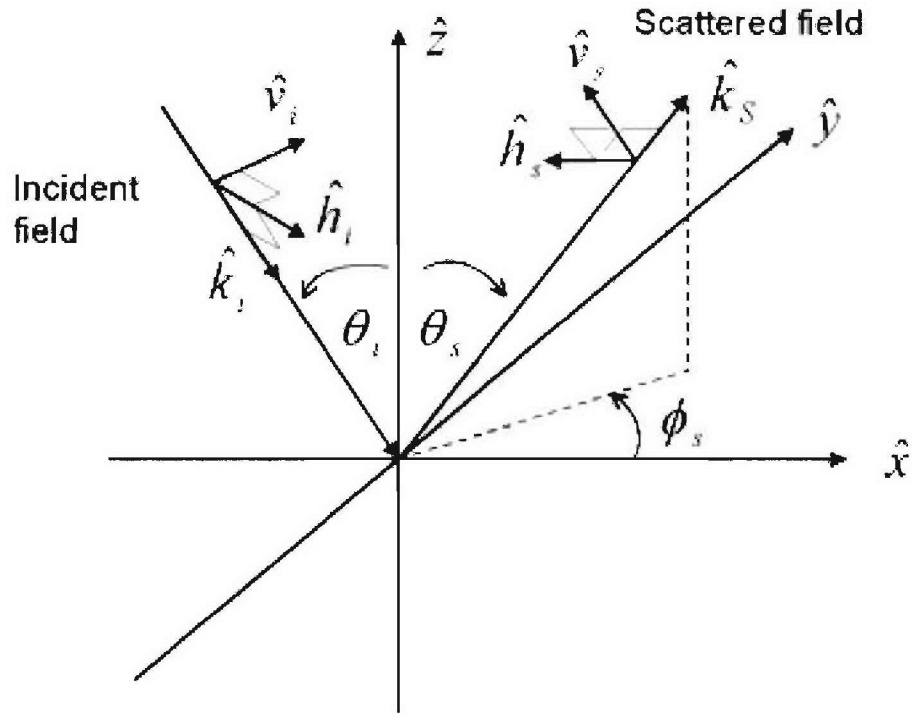


Figure 2.4: Geometric definitions.

By convention, the incident wave is defined in the  $x-z$  plane with  $\theta_i \in [0, 90^\circ]$  and  $\phi = 0$ . The scattering direction can lie anywhere in the upper hemisphere ( $\theta_r \in [0, 90^\circ]$  and  $\phi_r \in [-180^\circ, 180^\circ]$ ). The quantities that appear in these expressions are functions of wavelength  $\lambda$ . When narrow-band sensors are being used, it is appropriate to state

this dependence explicitly

$$\mathcal{F}(\theta_i, \phi_i, \theta_r, \phi_r, \lambda) = \frac{dL_r(\theta_r, \phi_r, \lambda)}{dE_i(\theta_i, \phi_i, \lambda)} \quad (2.25)$$

## 2.4.2 BRDF for Polarimetric Sensors

A concept similar to that underlying Equation (2.22) can be used to define a polarimetric BRDF. We have [29]

$$\mathcal{F}_{\alpha_s, \alpha_i}(\theta_s, \phi_s | \theta_i, \phi_i, \lambda) = \frac{dL_{\alpha_s}^r(\theta_s, \phi_s, \lambda)}{dE_{\alpha_i}^i(\theta_i, \phi_i, \lambda)} \quad (2.26)$$

where the polarization angles of the incident and scattered waves are denoted  $\alpha_i$  and  $\alpha_s$ , respectively. These angles, which satisfy  $-\pi/2 \leq \alpha \leq \pi/2$ , are defined as positive for an electric field polarization that makes an angle  $\alpha$  measured counter-clockwise from the plane of incidence for an observer seen looking toward the oncoming ray. The BRDF components defined in Equation (2.26) completely describe the scattering process and are the basis for most results presented in the literature.

The principle of reciprocity demands that the same response be obtained if we interchange source and observer. Thus, the BRDF must satisfy [29, p. 5]<sup>2</sup>

$$\cos \theta_s \mathcal{F}_{\alpha_i, \alpha_s}(\theta_i, \phi_i | \theta_s, \phi_s, \lambda) = \cos \theta_i \mathcal{F}_{\alpha_s, \alpha_i}(\theta_s, \phi_s | \theta_i, \phi_i, \lambda) \quad (2.27)$$

The Mueller matrix [30] is an alternative and widely accepted method to address scattering. The Mueller matrix defines a linear transformation of Stokes vectors that occurs during scattering (or transmission), such that the scattered Stokes vector is the product of a differential incident Stokes vector  $d\mathbf{I}_i$  and the Mueller matrix  $\mathbf{M}$ . We write

$$d\mathbf{I}_s(\theta_s, \phi_s) = \mathbf{M}(\theta_s, \phi_s | \theta_i, \phi_i) d\mathbf{I}_i(\theta_i, \phi_i) \quad (2.28)$$

<sup>2</sup>Also see [18, p. 14].

The Mueller matrix has also been referred to [17, 31, 32] as a “Stokes matrix”, a ”transformation matrix” and a “phase matrix.” When extended sources are involved, the above expression must be written in integral form as

$$\begin{aligned}\mathbf{I}_s(\theta_s, \phi_s) &= \int \int d\theta_i d\phi_i \sin \theta_i \cos \theta_i \mathbf{M}(\theta_s, \phi_s | \theta_i, \phi_i) \mathbf{I}_i(\theta_i, \phi_i) \\ &= \int d\Omega_i \cos \theta_i \mathbf{M}(\theta_s, \phi_s | \theta_i, \phi_i) \mathbf{I}_i(\theta_i, \phi_i)\end{aligned}\quad (2.29)$$

Since they relate the incident and scattered radiance, the elements of the Mueller matrix are analogous to BRDF functions for the components of the Stokes vector. Both quantities have units of reciprocal steradians. The four frequently used polarimetric BRDFs:  $\mathcal{F}_{vv}$ ,  $\mathcal{F}_{vh}$ ,  $\mathcal{F}_{hv}$ , are  $\mathcal{F}_{hh}$ , are the elements in the upper-left quadrant of the Mueller matrix.

The elements of  $\mathbf{M}$  can be derived from first-principles electromagnetic analysis. A wave scattered from an elemental surface  $dA$  with normal oriented at angle  $\theta_i$  to the illuminating wave can be expressed as

$$\mathbf{e}^s(\theta_s, \phi_s) = \frac{e^{-ikR}}{R} \begin{bmatrix} S_{vv} & S_{vh} \\ S_{hv} & S_{hh} \end{bmatrix} \mathbf{e}^i \quad (2.30)$$

If one solves the electromagnetic scattering problem, then the quantities  $S_{\beta\alpha}$  are known, and the Mueller matrix is given by [21, §2.12], [33, p. 13]

$$\mathbf{M} = \frac{1}{\cos \theta_i} \times \quad (2.31)$$

$$\begin{bmatrix} \langle S_{hh} S_{hh}^* \rangle & \langle S_{vh} S_{vh}^* \rangle & \text{Re} \langle S_{hh} S_{vh}^* \rangle & -\text{Im} \langle S_{hh} S_{vh}^* \rangle \\ \langle S_{hv} S_{hv}^* \rangle & \langle S_{vv} S_{vv}^* \rangle & \text{Re} \langle S_{hv} S_{vv}^* \rangle & -\text{Im} \langle S_{hv} S_{vv}^* \rangle \\ 2\text{Re} \langle S_{hh} S_{hv}^* \rangle & 2\text{Re} \langle S_{vh} S_{vv}^* \rangle & \text{Re} \langle S_{hh} S_{vv}^* + S_{vh} S_{hv}^* \rangle & -\text{Im} \langle S_{hh} S_{vv}^* + S_{vh} S_{hv}^* \rangle \\ 2\text{Im} \langle S_{hh} S_{hv}^* \rangle & 2\text{Im} \langle S_{vh} S_{vv}^* \rangle & \text{Im} \langle S_{hh} S_{vv}^* + S_{vh} S_{hv}^* \rangle & \text{Re} \langle S_{hh} S_{vv}^* + S_{vh} S_{hv}^* \rangle \end{bmatrix}$$

This equation is the basis for calculations of the Mueller matrix that appear below.

Equation (2.31) suggests that 16 unique quantities are needed to completely specify  $\mathbf{M}$  for each source-viewer geometry. In the case of mine detection, the incident

polarization states of interest are (1) unpolarized (for solar radiation and surface thermal emission), (2) partially linearly polarized (for skylight), or (3) fully linearly polarized (for an active (laser) illuminator ). Those sources have no circularly polarized component, and their corresponding  $V$  parameters are zero. This in turn reduces the number of necessary elements from 16 to 12. Furthermore, mines typically have no exposed bare metal surfaces, which implies that no circular polarization is excited from those non-conductive surfaces without circularly-polarized sources. Therefore, we can further reduce the number of required matrix elements from 12 to 9. In a large data collection reported by Willow Run Laboratories [34], only four matrix elements were recorded (those that relate parallel and orthogonal polarizations). Those four components are sufficient to estimate scattered fields if only unpolarized or horizontal or vertical polarized sources are used.

## 2.5 An Overview of Scattering Models

Although it is possible to determine a Mueller matrix through measurement, the cost of the required data collection is enormous, since the matrix is a function of wavelength and both the incident and reflected angles. As a result, many attempts have been made to construct scattering models that are both physically correct and computationally tractable. Due to the tremendous variations in the properties of natural and man-made surfaces, it is challenging to develop a universal scattering model. Nonetheless, several acceptable models have been developed for specific surface properties. In this section we describe a number of those models. Although rigorous numerical simulations of scattering from random surfaces have been presented, the

most useful approaches to the problem employ some form of analytical approximation. Unpolarized BRDF models are also of considerable interest to the computer graphics (CG) community in their quest for photo-realistic imagery, although CG BRDF models tend to be somewhat simplistic because of computational efficiency requirements.

### 2.5.1 Specular Models for Smooth Surfaces

When the surfaces of interest are smooth (i.e., planar over regions very large compared to a wavelength), the scattered fields can be approximated by reflected rays, which are determined from the classical Fresnel reflection coefficients. This approach, which assumes that all reflections are specular, is easy to implement numerically, and it is the basis for many ray-based image simulators. As long as the electromagnetic properties of the surface (i.e., the permittivity and permeability) are specified, the reflected radiances are the product of the incident radiance and the reflection coefficient. The direction of the reflected radiation is given by Snell's law. We have [18, p. 202-203]

$$\mathbf{M} = \begin{bmatrix} |R_v(\theta_i)|^2 & 0 & 0 & 0 \\ 0 & |R_h(\theta_i)|^2 & 0 & 0 \\ 0 & 0 & \text{Re}(R_v(\theta_i)R_h^*(\theta_i)) & -\text{Im}(R_v(\theta_i)R_h^*(\theta_i)) \\ 0 & 0 & \text{Im}(R_v(\theta_i)R_h^*(\theta_i)) & \text{Re}(R_v(\theta_i)R_h^*(\theta_i)) \end{bmatrix} \times \frac{\delta(\cos \theta_s - \cos \theta_i)\delta(\phi_s - \phi_i + \pi)}{\cos \theta_i} \quad (2.32)$$

in which the Fresnel reflection coefficients (for nonmagnetic media) are given by

$$R_h(\theta_i) = \frac{\cos \theta_i - \sqrt{m^2 - \sin^2 \theta_i}}{\cos \theta_i + \sqrt{m^2 - \sin^2 \theta_i}} \quad (2.33)$$

$$R_v(\theta_i) = \frac{m^2 \cos \theta_i - \sqrt{m^2 - \sin^2 \theta_i}}{m^2 \cos \theta_i + \sqrt{m^2 - \sin^2 \theta_i}} \quad (2.34)$$

In these expressions  $m$  is the complex refractive index of the surface, and  $\theta$ , is the incident angle measured with respect to the local surface normal.

### 2.5.2 Diffuse (Lambertian) Models

The specular model described above, in which all scattered energy leaves along the specular direction, is the limiting case of a perfectly smooth surface. A perfectly diffuse (Lambertian) scatterer represents the opposite extreme, in which the scattered energy is equally distributed in all directions.

Diffuse scattering is not produced by scattering from an infinitely rough surface. Instead, it is thought to be the result of multiple scattering that occurs below the surface and, as a result, its modeling is somewhat more complex. The diffuse component is, nonetheless, very important. Diffuse reflectance is commonly assumed in radiative heat transfer, and it is also used in the well-known radiosity method [35].

The polarimetric properties of a scatterer are independent of its specular or diffuse nature and, as a result, the Mueller matrix is not completely specified by a specification that the material is simply a diffuse scatterer. We can, however, specify the matrix for a scatterer which is completely depolarizing, non-absorbing, and diffuse:

$$\mathbf{M} = \frac{1}{\pi} \begin{bmatrix} 1/2 & 1/2 & 0 & 0 \\ 1/2 & 1/2 & 0 & 0 \\ 0 & 0 & 0 & 0 \\ 0 & 0 & 0 & 0 \end{bmatrix} \quad (2.35)$$

This material converts all incident polarizations into equal components of the  $v$  and  $h$  linear polarizations, and it reflects all incident radiance, absorbing nothing. An analog of the above material is an optical depolarizer, which has the same Mueller matrix [36].

Studies of the physical basis for diffuse scattering are relatively uncommon, but a work by Hanrahan and Krueger [37] treated the problem of subsurface scattering in layered media. In that work it was asserted that many natural materials, including leaves, skin, snow, and sand, were well described by thin layers of random media, and a model for such materials was developed. The formulation involves a Monte Carlo solution of a one-dimensional integral equation for the radiance. The results compare favorably to experimental data.

Diffuse subsurface reflection from inhomogeneous media was examined by Wolff [38]. By using the classical Fresnel transmission coefficients to describe the radiation entering and exiting the medium and combining that result with Chandrasekhars's classical radiative transfer analysis of multiple scattering in planetary atmospheres [17], Wolff was able to derive a more robust predictor of scattering from non-specular surfaces.

A related topic was investigated by Oren and Nayar [39]. It has been noted that when an observer views an otherwise diffusely reflecting object along the incident direction (a backscattering geometry), then the scattered field is decidedly non-Lambertian. Specifically, the surface reflectance increases strongly at grazing angles, instead of the  $\cos\theta$  attenuation predicted for a Lambertian surface. Using an analysis similar to that of Torrance and Sparrow but giving each surface facet a Lambertian (rather than specular) response, Oren and Nayar were able to show that this effect could be explained by surface roughness. They present approximate expressions for the BRDF which agree well with experiment. The models of Wolff [38] and Oren and Nayar [39] have been compared in [40].

### 2.5.3 The Phong Model

The Phong reflection model [41], widely known in computer graphics, is a purely empirical construction for non-polarimetric returns. The scattered light is assumed to be a combination of ambient light, diffuse reflection, and imperfect specular reflection. The three terms are combined using weighting factors  $w_a$ ,  $w_d$  and  $w_s$  as follows:

$$I_s(\hat{\mathbf{k}}_s) = w_a I_a + I_i \left[ w_d (-\hat{\mathbf{k}}_i \cdot \hat{\mathbf{n}}) + w_s (\hat{\mathbf{k}}_r \cdot \hat{\mathbf{k}}_s)^n \right] \quad (2.36)$$

in which the scalar  $n$  is a user-defined parameter, the vector  $\hat{\mathbf{n}}$  is the local surface normal, and  $\hat{\mathbf{k}}_i$ ,  $\hat{\mathbf{k}}_r$ , and  $\hat{\mathbf{k}}_s$  are unit vectors in the direction of the incident ray, the specular reflected ray, and observer, respectively. The weighting factors are constrained to sum to unity

$$w_a + w_d + w_s = 1 \quad (2.37)$$

The power law  $n$  is chosen to simulate imperfect specular reflection. Typical values range from 10 to over 100 depending on the surface roughness. Note that the addition of the ambient light makes this model a nonlinear function of the incident radiance.

### 2.5.4 The Beckmann Model (Physical Optics)

Real surfaces are neither perfectly specular nor perfectly diffuse, and predicting their behavior requires a more careful treatment. Beckmann [42] was among the first to present a rough-surface scattering analysis based on rigorous electromagnetic concepts. He assumed that the surface of interest was a perfect conductor with a random surface height. The scattered field was derived using a physical optics (PO) approach, which is also known as a “Kirchoff approximation.”

The formulation begins by expressing the scattered field as an integral over a dyadic Green's function and the unknown current density. The integral is evaluated by assuming that the local surface radius of curvature is large compared to the wavelength, which in turn imposes an upper limit on the wavelength. A random (Gaussian) surface height distribution with a finite correlation length is used to represent the rough surface. The PO model is applicable to surfaces ranging from very smooth to moderately rough. The resulting expression for the scattered field contains two terms which correspond to coherent and incoherent scattering. The coherent term corresponds to the specular return from a smooth surface, and it vanishes in the small wavelength limit. The incoherent term accounts for diffraction due to roughness. For a perfectly smooth surface, an incident ray is reflected along the specular direction. As the degree of surface roughness increases, the single reflected ray is reduced to a broad scattered lobe (the incoherent return) that is roughly centered about the specular direction. If the surface is relatively smooth, the incoherent term tends to a broad beam and is referred to as a specular lobe. That lobe becomes broader and more diffuse as the surface roughness increases, and it may also shift away from the specular direction.

Tsang et al. [18] presented an analysis that makes explicit the polarimetric dependence of the PO model. The PO model can be reduced to an analytic form if the PO integral is evaluated asymptotically using the method of stationary phase, which is equivalent to the geometrical optics limit. The PO model is described in more detail in Section 3.3.

### 2.5.5 The Torrance-Sparrow (Geometrical Optics) Model

Another early approach to the rough surface scattering problem was described by Torrance and Sparrow [43]. In that formulation specular and diffuse contributions are combined in an ad hoc manner. The rough surface is modeled as a composition of planar facets having random orientation. The facets are assumed to be much larger than a wavelength, and a geometrical optics (specular) approximation to their scattering is employed. The approach can be used to explain the off-specular maxima observed in rough surface scattering. The work in [43] was developed for unpolarized light. The results are somewhat involved, but its essential components are given by the following BRDF

$$f(\hat{\mathbf{k}}_s|\hat{\mathbf{k}}_i) = w_d \frac{\rho_d}{\pi} + w_s \frac{F(\hat{\mathbf{k}}'_i, \hat{\mathbf{k}}'_s) G e^{-\alpha^2/m^2}}{4(\hat{\mathbf{k}}_s \cdot \hat{\mathbf{n}})(-\hat{\mathbf{k}}_i \cdot \hat{\mathbf{n}})} \quad (2.38)$$

in which  $w_d$  and  $w_s$  are weights for the diffuse and specular components,  $\rho_d$  is the albedo for the diffuse component,  $F$  is the (unpolarized) Fresnel reflection coefficient,  $G$  is the self-shadowing correction,  $\hat{\mathbf{k}}_i$  and  $\hat{\mathbf{k}}_s$  are unit vectors in the direction of the source and observer respectively,  $\hat{\mathbf{n}}$  is the unit normal of the surface,  $\alpha$  is angle between the surface normal  $\hat{\mathbf{n}}$  and the normal of a surface facet that would produce specular reflection in the direction of the observer. The latter normal vector is simply the normalized mean of the incident and observer vectors, namely:

$$\hat{\mathbf{n}}' = \frac{-\hat{\mathbf{k}}_i + \hat{\mathbf{k}}_s}{|-\hat{\mathbf{k}}_i + \hat{\mathbf{k}}_s|} \quad (2.39)$$

and we have

$$\cos \alpha = \hat{\mathbf{n}}' \cdot \hat{\mathbf{z}} \quad (2.40)$$

The primed unit vectors have the same meaning as the unprimed vectors, but they are expressed in the coordinate system centered about  $\hat{\mathbf{n}}'$ .

Both the Beckmann (B) model and the Torrance-Sparrow (TS) model are based (largely) on physical insight [44]. Both use Fresnel reflection coefficients to account for reflections from locally smooth facets of arbitrary materials, and both use a normal density to describe some random features of the surface. (For B, the surface height is normally distributed. For TS, it is the number of facets at the angle  $\alpha$  that is normally distributed.) The TS model, however, includes two significant corrections not present in the B model: (1) the empirical combination of diffuse and specular components, and (2) the self-shadowing function  $G$ . It is apparent that the TS model involves several free parameters that can be adjusted to replicate the appearance of various surface materials. Cook and Torrance [45] adopted the TS BRDF as the basis for their work in computer graphics. Those authors also included the scatterer's spectral dependence so that the spectral composition of the reflected light would be correctly modeled.

The shadowing function  $G$  is an important component of the TS BRDF, since it eliminates nonphysical behavior for grazing angles of observation. In developing  $G$ , Torrance and Sparrow assumed that all facets formed “v”-shaped troughs, which could both shadow the incident field and obscure the observer. This concept is also used in other scattering models [46] involving observation near grazing.

A concise representation of the geometric attenuation function is given by Wolff in [47] as

$$G(\hat{\mathbf{k}}_s|\hat{\mathbf{k}}_i) = \min \left\{ 1, \frac{2 \cos \delta \cos \theta_i}{\cos \psi}, \frac{2 \cos \delta \cos \theta_r}{\cos \psi} \right\} \quad (2.41)$$

where  $\delta$  is the angle between the local surface normal  $\hat{\mathbf{n}}$  and the highlight vector  $\hat{\mathbf{h}}$  ( $= \hat{\mathbf{k}}_s - \hat{\mathbf{k}}_i$ ), and  $\psi$  is the angle between the highlight vector and the incident vector  $\hat{\mathbf{k}}_i$ .

As originally described, the TS formulation deals with unpolarized light. It can, however, be extended to polarized light by using the appropriate Fresnel reflection coefficients in the expression for the specular term. This approach was used by Wolff [47] to infer surface orientation from measured depolarization.

### 2.5.6 The Beard-Maxwell Model

The Beard-Maxwell (BM) model, first described by Maxwell et al. [46], is closely related to the TS model, but it uses a number of additional empirically derived constants to provide a more general modeling capability. In its non-polarimetric form it employs both specular and diffuse components as follows:

$$\mathcal{F} = \mathcal{F}_s + \mathcal{F}_d \quad (2.42)$$

in which  $\mathcal{F}_s$  is the specular term in the form

$$\mathcal{F}_s = \frac{F(\hat{\mathbf{k}}'_i \cdot \hat{\mathbf{n}}')GH(\hat{\mathbf{n}}' \cdot \hat{\mathbf{n}})}{4(\hat{\mathbf{k}}_s \cdot \hat{\mathbf{n}})(\hat{\mathbf{k}}_i \cdot \hat{\mathbf{n}})} \quad (2.43)$$

and  $\mathcal{F}_d$  is the diffuse contribution, for which one of two expressions is used

$$\mathcal{F}_d = \begin{cases} \rho_d \\ \frac{2\rho_v}{(\hat{\mathbf{k}}_s \cdot \hat{\mathbf{n}}) + (\hat{\mathbf{k}}_i \cdot \hat{\mathbf{n}})} \end{cases} \quad (2.44)$$

The decision of whether to use the constant or ratio forms is determined by whether the specular component adequately expresses the angle dependence observed in measurements. As in the TS model,  $F$  is the Fresnel reflection coefficient and  $G$  is a self-obscuration factor. The expression for  $G$  used by BM is somewhat different than that used by TS, and it involves a small number of empirical parameters. The factor  $H$  expresses the density of random facets and is inferred indirectly from measurements.

Some modifications to the BM model are presented by Westlund and Meyer [48], who use their results in a public-domain BRDF database known as the Nonconventional Exploitation Factors Data System (NEFDS).<sup>3</sup> That database, which is maintained by NIST, contains BM model parameters for some 400 materials.

### 2.5.7 Perturbation Methods

A number of perturbation techniques have also been used to derive rough-surface scattering matrices. The Small Perturbation Method (SPM) [49] is a popular analytic approach for rough surface scattering, and it is widely used in satellite-based remote sensing applications. Unlike the PO model, which assumes a large curvature radius and a short wavelength, the SPM approach requires small (with respect to wavelength) surface height and slope variations. Although it seems that the PO and SPM approaches are valid in different limiting ranges, Holliday [50] shows that by including higher-order terms in PO it converges to the SPM solution in the small height limit.

Other perturbation approaches have also been developed for analyzing rough surface scattering. Voronovich [51] devised the Small Slope Approximation (SSA), in which the surface slope is assumed to be a small parameter. Jackson et al. developed the phase perturbation technique for a complex surface source density excited by an incident field [52].

## 2.6 Relation of Emissivity and Scattering Properties

We can also relate the emissivity of a surface to its BRDF or its Mueller matrix. For a surface element  $dA$  in thermal equilibrium with its surroundings, the absorbed

<sup>3</sup><http://math.nist.gov/~FHunt/appearance/nefds.html>

and emitted power must be equal. In addition, energy conservation requires that the scattered and absorbed power must equal the incident power  $P_i$ . Thus,

$$P_e = P_i - P_s \quad (2.45)$$

where  $P_s$  and  $P_e$  are the scattered and emitted power. The emissivity  $\mathcal{E}_\beta(\theta_i, \phi_i)$  is equal to the ratio  $P_e/P_i$ . The power incident on a surface of area  $dA$  is  $dA \cos \theta_i [|e^i|^2/2\eta_0]$ , where  $\eta_0$  is the intrinsic impedance for the free space, and the scattered power is given by the integral of  $\cos \theta_s |e_\beta^s|^2/2\eta_0$  over the hemisphere. We have

$$\begin{aligned} \mathcal{E}_\beta(\theta_i, \phi_i) &= 1 - \frac{\sum_{\alpha=v,h} \int d\Omega_s \cos \theta_s r^2 |e_\alpha^s|^2/2\eta_0}{dA \cos \theta_i [|e_\beta^i|^2/2\eta_0]} \quad (2.46) \\ &= 1 - \frac{\sum_{\alpha=v,h} \int d\Omega_s \cos \theta_s f_{\alpha\beta}(\theta_i, \phi_i | \theta_s, \phi_s)}{4\pi \cos \theta_i} \\ &= 1 - \sum_{\alpha=v,h} \int d\Omega_s f_{\beta\alpha}(\theta_s, \phi_s | \theta_i, \phi_i) \end{aligned}$$

where we have used Equation (2.27) and the relation between the bistatic scattering coefficient and the BRDF. The above expression is consistent with the well known emissivity-reflectivity relation:

$$\mathcal{E} = 1 - \mathcal{R} \quad (2.47)$$

In remote sensing, the emissivity is often associated with the brightness temperature  $T_B$  [53, 18]. Assuming the body of interest has a uniform physical temperature  $T$ , we can write  $T_B$  as

$$T_B(\theta, \phi) = T \cdot \mathcal{E}(\theta, \phi) \quad (2.48)$$

Macelloni et al. [54] conducted emissivity measurements to compare the performance of several classical BRDF models. It was shown that analytical models can produce reasonable agreement with measured data if used in valid surface roughness regimes and frequency bands.

Although we have shown that emissivity can be derived by integration of the bistatic reflection coefficients, it may be difficult or expensive to carry out the integration directly. Yueh et al. [55] proposed an alternative scheme to compute brightness temperatures for ocean surfaces. The scattering coefficients derived from SPM models were integrated over all spectral length scales instead. This approach avoids errors that result from large scattering cross sections in the original integration domain, and it enhances emissivity calculation accuracy.

The emissivity received by a polarimetric sensor can also be expressed using the modified Stokes parameters presented in Section 2.4.2.

$$\mathcal{E} = \begin{bmatrix} \mathcal{E}_h \\ \mathcal{E}_v \\ U_{\mathcal{E}} \\ V_{\mathcal{E}} \end{bmatrix} = \mathcal{C} \begin{bmatrix} \langle e_h e_h^* \rangle \\ \langle e_v e_v^* \rangle \\ 2\text{Re} \langle e_h e_v^* \rangle \\ 2\text{Im} \langle e_h e_v^* \rangle \end{bmatrix} \quad (2.49)$$

where  $\mathcal{C}$  is a constant and the expressions for  $\mathcal{E}_h$  and  $\mathcal{E}_v$  are shown in Equation (2.46). The  $U_{\mathcal{E}}$  and  $V_{\mathcal{E}}$  Stokes parameters are proportional to the real and imaginary parts of the correlation of horizontal and vertical polarized fields [55]. Tsang et al. [18] showed that for a reciprocal, isotropic surface,  $U_{\mathcal{E}}$  and  $V_{\mathcal{E}}$  reduce to the absorption, and we can relate polarimetric emissivities with reflectivities [56, 12] as

$$\begin{bmatrix} \mathcal{E}_h \\ \mathcal{E}_v \\ U_{\mathcal{E}} \\ V_{\mathcal{E}} \end{bmatrix} = \begin{bmatrix} 1 - \mathcal{R}_h \\ 1 - \mathcal{R}_v \\ -U_{\mathcal{R}} \\ -V_{\mathcal{R}} \end{bmatrix} \quad (2.50)$$

As suggested previously, emissivity can be computed via spatial integration. By assuming an unpolarized source, Sendur expressed  $U_{\mathcal{E}}$  and  $V_{\mathcal{E}}$  in terms of elements in the Muller matrix [12].

$$U_{\mathcal{E}}(\theta_i, \phi_i) = - \int d\Omega_s [M_{31}(\theta_s, \phi_s | \theta_i, \phi_i) + M_{32}(\theta_s, \phi_s | \theta_i, \phi_i)] \quad (2.51)$$

$$V_{\mathcal{E}}(\theta_i, \phi_i) = - \int d\Omega_s [M_{41}(\theta_s, \phi_s | \theta_i, \phi_i) + M_{42}(\theta_s, \phi_s | \theta_i, \phi_i)] \quad (2.52)$$

where  $M_{31}$ ,  $M_{32}$ ,  $M_{41}$ , and  $M_{42}$  are expressed in Equation (3.38) and are proportional to

$$\begin{bmatrix} M_{31} & M_{32} \\ M_{41} & M_{42} \end{bmatrix} \propto \begin{bmatrix} 2\text{Re} \langle f_{vh} f_{hh}^* \rangle & 2\text{Re} \langle f_{vv} f_{hv}^* \rangle \\ 2\text{Im} \langle f_{vh} f_{hh}^* \rangle & 2\text{Im} \langle f_{vv} f_{hv}^* \rangle \end{bmatrix} \quad (2.53)$$

where the horizontal and vertical polarization coupling terms ( $f_{hh}$ ,  $f_{vv}$ ,  $f_{hv}$ , and  $f_{vh}$ ) are found in Equation (3.41) through (3.44). The above expression is similar to the first-order scattering coefficients derived using SPM approach for  $T_U$  and  $T_V$  in [56, 57].

For perfectly flat surfaces, the integration can be done in closed form, since the Mueller matrix for a flat surface contains a Dirac delta function in the specular direction. Hence, the emissivity can be expressed in terms of Fresnel reflection coefficients. For rough surfaces, the integral cannot be done in closed form, but several rules of thumb have been formulated. Millikan [58], who conducted an extensive study of the polarization of thermal emission in the late nineteenth century, found that the largest partial polarization occurs at the most oblique angle to the surface normal. He also found that in general, metals have a significantly higher partial polarization than dielectrics. A forward-looking infrared (FLIR) band model, which is based on a geometrical optics approach, was developed by Wolff [59]. His study showed that for an isotropic rough surface, the degree of polarization decreased as the surface roughness increased. This is the result of randomization of linear polarization components and is consistent with Millikan's observation.

## 2.7 EO Imagery Data Sets

Measured IR and visible images from three different sites will be used for model validation in this work. The Northern Temperate Site 1 (NT-S1) and Northern Temperate Site 2 (NT-S2) are located in north America. The TNO site is at the TNO FEL facility in The Netherlands. Environmental parameters from NT-S1 will be used as baseline conditions for studies of the radiometric model. Polarimetric models of mine signatures will be evaluated using the polarimetric TNO imagery. The NT-S2 data set contains visible band images useful for validating the surface scattering model, and an extensive MWIR collection that can be used to compare the performance of mine detection algorithms.

### 2.7.1 Northern Temperate Site 1

Images at NT-S1 were acquired by the US Army Night Vision Electronic Sensors Directorate (NVESD) during October, 2002. The latitude of NT-S1 is approximately 40.3°N. The test site contains several types of surface-laid mines. Nadir-looking images were acquired by an MWIR sensor (3-5  $\mu\text{m}$ ) mounted on a surveillance helicopter. During each run over the test site 143 images were collected. Several runs were conducted during mid day and afternoon. Images were acquired with and without spectral filters to investigate the merits of certain bands.

Figure 2.5 shows a sample image collected by the sensor. In this scene, three large plastic anti-vehicle (LP\_B) mines were present (in the top row) along with three fiducial markers (in the middle row) indicated by red diamonds. The image resolution is about 1.1 inches per pixel and each image contains 640 $\times$ 512 pixels. Because the

sensor's response is not uniform across the scene, the measured images were calibrated by subtracting the ensemble average of all images.

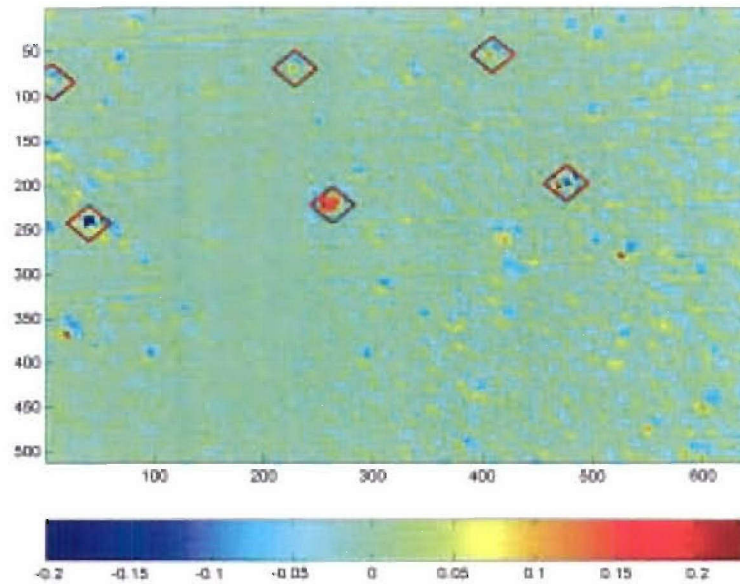


Figure 2.5: Sample surveillance image containing LP\_B mines. Red diamonds are added indicating positions of mines (top row) and fiducial markers (middle row).

## 2.7.2 Northern Temperate Site 2

A multi-spectral data set was collected at NT-S2 by the NVESD. Two cameras were employed to acquire registered multi-channel imagery. Five channels were collected by a visible band CCD camera, while a MWIR camera produced three channels of IR imagery. The visible imagery contains  $512 \times 768$  pixels with a resolution of 1.6 cm and covers an area of about  $100 \text{ m}^2$ . The MWIR imager has  $256 \times 256$  pixels with 3 cm resolution, which is equivalent to a  $60 \text{ m}^2$  field of view. Both cameras were

Name	Color	Case	Size
MP_A	Tan	Plastic	8.5" D, 3" H
SM_A	Green	Metal	5" D, 2.25" H
LM_B	Green	Metal	12" D, 2.5" H
LP_B2	Pink	Plastic	12" D, 3" H
LP_B3	Bright Green	Metal	12" D, 2.75" H
LM_A	Dark green	Metal	12.25" D, 3.5" H

Table 2.1: Mine characteristics in the NT-S2 data set.

mounted on a scissors lift, and the platform was elevated about 60 feet above the ground.

Six types of anti-tank mines were placed in 5 meters wide test lanes with four ground cover types: short grass, tall grass, bare soil and sand. AT mines were laid on the surface or buried within the lanes. Surface mines were placed in a zigzag pattern and the nearest distance between mines was around 2.5 meters. AT mine dimensions, colors, and casings are listed in Table 2.1 [60]. The LM\_B, LP\_B2 and LP\_B3 mines are of similar size and shape, although their casings are made of metal or plastic. The size of LM\_A mines is around 12.25" in diameter, which is about the same as LM\_B mines. The MP\_A mine has a 7" diameter, while the SM\_A mine is the smallest mine with a 5" diameter. Some man-made clutter objects were also emplaced, including soda cans, pizza boxes, and wooden sticks.

A total of 247 scenes from the image collection were used in this work. Image collection time ranged from 8:30 AM to 7:00 PM. Because target signatures in the MWIR channels have a more consistent signal-to-clutter ratio than those in the visible channels, only the MWIR imagery is used for the comparison of mine detection

Ground Cover	MP_A	SM_A	LM_B	LP_B2	LP_B3	LM_A
Bare soil	11	11	12			
Sand	13	15	12	1	1	
Short grass	22	20	24			70
Tall grass	23	22	24	14	19	

Table 2.2: Mine distribution in the NT-S2 data set.

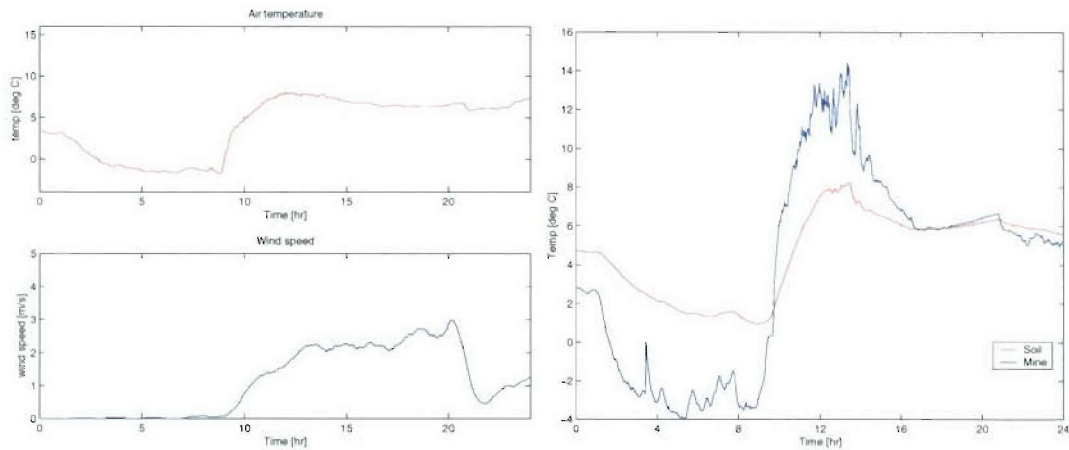
algorithms presented in Section 5.8. Among the 247 scenes, we have 103 scenes with a tall grass background, 99 with short grass, 22 with sand and 23 with bare soil. There are 315 surface mines<sup>4</sup> in these scenes. Table 2.2 documents the number of each mine type in the four ground cover types.

### 2.7.3 TNO Polarimetric Imagery

The TNO data was acquired at The Hague, The Netherlands (52°N latitude) [13]. One set of imagery was collected at 1:31 PM, November 27th, 2001 and was processed to yield  $I$ ,  $Q$ , and  $U$  channel images. The test site comprises a sand box containing several surface-laid dummy mines as shown in Figure 2.7. Thermocouples were placed at several points on and under mine and soil surfaces. Meteorological parameters including air temperature, wind speed, and air pressure were collected. Cloud conditions were measured via radiometers. Figure 2.6 displays data from the thermocouples, wind speed sensor, and air temperature sensor. Simulation parameters were selected based on the meteorological data.

The camera, a 3-5  $\mu\text{m}$  MWIR sensor, viewed the sandbox from a height of 2.88 m with a 70° zenith angle and a FOV of 18° by 18°. A spinning polarization filter was

<sup>4</sup>The test site contains 32 buried mines, which are not labeled as targets in our ground truth data due to their low signal-to-noise ratio and significant signature difference with surface mines



(a) Meteorological Data.

(b) Thermocouple Data.

Figure 2.6: Surface temperatures of soil and mine and meteorological data measured at TNO on November 27th, 2001.

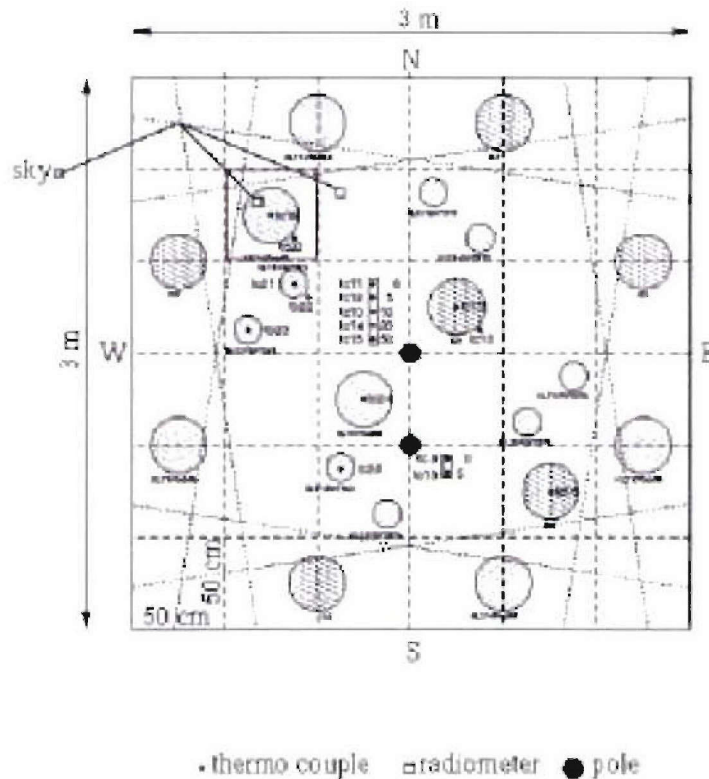


Figure 2.7: Layout of TNO test site.

placed in front of the objective lens, and the camera acquired 30 images at 6° rotation intervals. Stokes parameters were calculated as averages of measured radiance  $L(\phi_j)$  using the following expressions:

$$\hat{I} = \frac{2}{N} \sum_{j=1}^N L(\phi_j) \quad (2.54)$$

$$\hat{Q} = \frac{4}{N} \sum_{j=1}^N L(\phi_j) \cos(2\phi_j) \quad (2.55)$$

$$\hat{U} = \frac{4}{N} \sum_{j=1}^N L(\phi_j) \sin(2\phi_j) \quad (2.56)$$

where  $N=30$  is the number of measurements. Since the camera measures only linear polarization components, the  $V$  component cannot be determined. Calibration was performed via measurements of blackbodies in the field of view.

## 2.8 Summary

In this chapter, we reviewed issues that affect the modeling of EO mine signatures. The development of the radiometric model presented in Chapter 3 requires an understanding of the subjects discussed here, which are summarized below. Also, the model validation and performance comparison can be performed using the measured data described at the end of this chapter.

Among radiation sources, thermal emission is critical to IR signatures and is modeled as the product of blackbody radiation and surface emissivity. Solar radiation, including sunlight and skylight, has a spectrum centered in the visible band and affects the EO signature via surface reflections and heating. The MODTRAN code, which (partially) accounts for the complex atmospheric effects, is useful for the computation of solar radiance.

Surface properties concerning the EO signature characteristics were discussed. The random surface model used in this work has a Gaussian-distributed surface height and correlation distance. Surface temperatures can be determined with the heat transfer equation using boundary conditions for the heat flux at the air-soil interface. Surface scattering can be characterized by its BRDF. To describe polarimetric EO signature, we will use a Mueller matrix formulation. Surface emissivity can be derived from angular integration of the BRDF.

A review of scattering models showed that a moderately rough surface tends to form a broad lobe in the specular direction, while internal scattering may result in a diffuse return. The effects of multiple-scattering and self-shadowing become apparent when either the incident or scattered direction is near grazing.

Three sets of EO imagery of different sensor types (MWIR and visible) and sensor orientations (nadir and oblique viewing) were presented and will be used for signature model validation and performance evaluation of detection algorithms.

## CHAPTER 3

### RADIOMETRIC MINE SIGNATURE MODEL IMPLEMENTATION

The practical issues that arise in implementing a surface-mine radiometric-signature model are described in this chapter. Section 3.1 presents the problem geometry. Section 3.2 reviews the components of the sources, which include thermal emissions and reflections of sunlight and skylight. The finite element method (FEM) is used to determine the thermal emission by solving the heat transfer equation in a computational volume that includes the mine and adjacent soil. Incident sunlight and skylight are computed via the LOWTRAN/MODTRAN program. Reflections and emissions require the BRDF or emissivity of the surface. A rough surface BRDF model derived from physical optics (PO) and geometrical optics (GO) is described in Section 3.3. The effects of atmospheric transmission are reviewed. Issues relating the source-target-sensor geometry to the Stokes vectors are addressed in Section 3.4. Examples of the radiometric components are presented in Section 3.5 for different viewing geometries and sensor passbands. In Section 3.6 the effect of the sensor point spread function is examined.

### 3.1 Problem Geometry

Figure 3.1 illustrates the problem under investigation. The sensor is depicted with a small off-nadir viewing angle  $\theta_i$ . Some existing airborne IR mine sensors use a small nadir angle to minimize obscuration of the mine by foliage. Conversely, vehicle mounted sensors necessarily use a small grazing angle (large  $\theta_i$ ), which can cause the mine to be obscured by a rough surface.

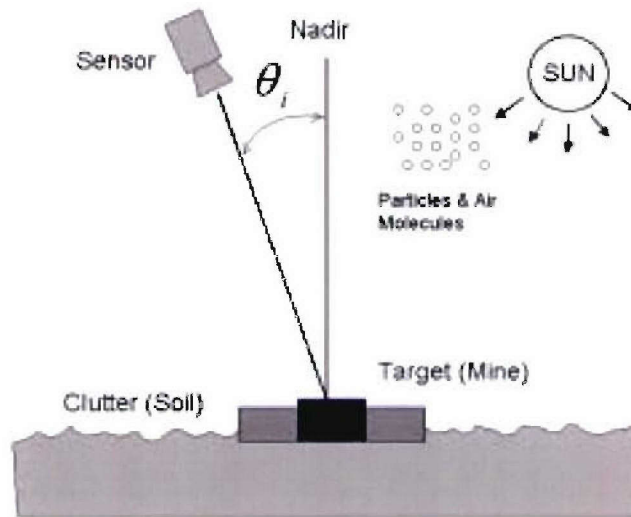


Figure 3.1: Geometry of mine detection application.

The scene viewed by the sensor includes both the mine and clutter such as man-made objects, soil, vegetation, rocks, and other natural materials. Both targets and clutter are modeled as rough surfaces. As noted in Chapter 2, a Gaussian random process height variation is assumed for surface roughness.

## 3.2 Radiative Source Computation

Correct modeling and estimation of the source irradiance is the first step in constructing a physics-based radiometric signature model. In this section the components of the radiometric sources are described in detail. We begin with a review of the FEM method used in calculating surface temperature, the precursor to thermal emission. We also outline the use of MODTRAN in computing the solar position and irradiance as well as the skylight distribution and polarization.

### 3.2.1 3-D FEM Thermal Model

As noted in Chapter 2, thermal emission is calculated as the product of the surface emissivity and the blackbody radiation. The latter is determined by the surface temperature. Temperatures within and on the mine satisfy the heat transfer equation (HTE), which can be solved numerically. Several numerical methods have been used to solve this problem in the past. In this work we employ a code written by I. K. Sendur [12]. In the remainder of this section we briefly review issues that arise in temperature prediction.

#### Heat Transfer Equation

As noted in Chapter 2, the HTE (Equation (2.16)) can be used to predict the temperature distribution in a thermally conductive region. Source conditions that define the forcing functions are needed to solve that equation. The sources that drive the problem enter via the boundary condition at the air interface. An energy balance at that interface requires

$$-\mathcal{K}(\mathbf{r}) \left. \frac{\partial T(\mathbf{r}, t)}{\partial t} \right|_{z=0} = \mathcal{F}_{sun} + \mathcal{F}_{sky} - \mathcal{F}_{emi} + \mathcal{F}_{conv} \quad (3.1)$$

where the left-hand side expresses heat transfer due to the temperature gradient at the surface, and  $\mathcal{F}_{sun}$ ,  $\mathcal{F}_{sky}$ ,  $\mathcal{F}_{emi}$ , and  $\mathcal{F}_{conv}$  denote transfer due to solar irradiance, skylight irradiance, thermal emission, and convection. Below we list the models employed in this work for these terms.

- **Solar Irradiance**

The heat flux deposited by solar irradiance is the product of the surface emissivity  $\mathcal{E}$  and the total irradiance reaching the ground  $E_{sun}(t)$ . An empirical equation that matches the total irradiance computed by the LOWTRAN code is [61]

$$E_{sun}(t) = \frac{1089.5}{m_a(t)} \exp(-0.2819m_a(t)) \text{ [W} \cdot \text{m}^{-2}] \quad (3.2)$$

$$m_a(t) = \frac{1}{\cos \psi(t)} \quad (3.3)$$

The air masses number  $m_a(t)$  is the secant of the solar elevation angle  $\psi(t)$ . Calculation of the solar elevation angle is described in Section 3.2.3.

- **Skylight Irradiance**

The total hemispherical emission from a planar blackbody surface satisfies Stefan-Boltzmann law

$$E_b = \sigma T^4 \quad (3.4)$$

where the Stefan-Boltzmann constant  $\sigma$  is

$$\sigma = 5.67 \times 10^{-8} \text{ [W} \cdot \text{m}^{-2} \cdot \text{K}^{-4}] \quad (3.5)$$

Similarly, the total flux from atmosphere emission can be expressed as

$$\mathcal{F}_{sky} = \mathcal{E} \cdot E_{sky} = \mathcal{E} \sigma T_{sky}^4(t) \quad (3.6)$$

- **Thermal Emission**

Thermal emission from the surface is also described by the Stefan-Boltzmann law. We have

$$\mathcal{F}_{emi} = \mathcal{E}\sigma T^4(t, z = 0) \quad (3.7)$$

- **Interface Convection**

Convective heat exchange between the surface and the atmosphere is the product of the temperature difference and the convection coefficient  $h(t)$

$$\mathcal{F}_{conv} = h(t)(T_{air}(t) - T(t, z = 0)) \quad (3.8)$$

An empirical expression for  $h(t)$  is given by Kahle [62]

$$h(t) = \sigma_{air} c_{sph} C_d (W(t) + 2) \text{ [W} \cdot \text{m}^{-2} \cdot \text{K}^{-1}] \quad (3.9)$$

In simulations performed in this work, the air density  $\sigma_{air}$  is set to be 1.16 [kg/m<sup>3</sup>], the specific heat of air  $c_{sph}$  is 1007 [J kg<sup>-1</sup> K<sup>-1</sup>], the wind drag coefficient  $C_d$  is 0.002, and  $W(t)$  [m/s] is the wind speed (a variable).

- **Sky and Air Temperatures**

In this work the above cited air and sky temperatures are modeled as periodic functions over a diurnal cycle. An empirical model [62, 63] for the air temperature derived from measurements by Kondratyev [64] is

$$T_{air}(t) = \bar{T}_{air} - \Delta T_{air} \cos(2\pi(t - 2)/24) \quad (3.10)$$

where  $\bar{T}_{air}$  and  $\Delta T_{air}$  are the mean and maximum deviation of the air temperatures during a diurnal cycle.

The sky temperature is assumed correlated to the air temperature [62, 63].

Using Brundt's formula, we express the sky temperature as

$$T_{sky}(t) = T_{air}(t)(0.61 + 0.05\sqrt{p})^{1/4} \quad (3.11)$$

where  $p$  is the water vapor pressure in mmHg. Values for  $p$  are available from meteorological data. Some examples include 4.58 [mmHg] for a saturated water vapor at the freezing point and 26.7 [mmHg] at  $300^\circ K$ .

Substituting the expressions presented above into Equation (3.1), the boundary condition at the air interface becomes

$$\begin{aligned} -\mathcal{K}(\mathbf{r}) \left. \frac{\partial T(\mathbf{r}, t)}{\partial t} \right|_{z=0} &= \mathcal{E} E_{sun}(t) + \mathcal{E} \sigma T_{sky}^4(t) - \mathcal{E} \sigma T^4(t, z=0) \\ &+ h(t)(T_{air}(t) - T(t, z=0)) \end{aligned} \quad (3.12)$$

Watson [65] noted that the difference  $|T - T_{sky}|$  was typically small. As a result,  $T^4$  can be well approximated by a first-order Taylor series about  $T_{sky}$ , leading to the linear relation.

$$\begin{aligned} \mathcal{K}(\mathbf{r}) \left. \frac{\partial T(\mathbf{r}, t)}{\partial t} \right|_{z=0} &\approx T(t, z=0)(h(t) + 4\mathcal{E} \sigma T_{sky}^3(t)) \\ &- (\mathcal{E} E_{sun}(t) + 4\mathcal{E} \sigma T_{sky}^4(t) + h(t)T_{air}(t)) \end{aligned} \quad (3.13)$$

Above equation provides a detailed description about source conditions on our interested computational space. Some local variations in source conditions such as the blockage of sunlight due to the elevated mine structure are considered. However, there are other localized source properties not modeled in the current thermal model implementation. For example, there are differences in the amounts of thermal emission and convection for a surface facet placed near the edge of a mine's sidewall and

a flat region without elevated structures nearby. The lack in consideration of above issues imposes limitations to the accuracy of thermal model results.

## FEM Equations

The FEM solution of the HTE begins by dividing the computational volume into tetrahedral volume elements. The unknown temperature is computed at the vertices of the tetrahedra, referred to here as nodes. Tetrahedral volume elements can be assigned different properties to approximate real objects.

The temperature of a point  $\mathbf{r}$  within an element can be expressed via linear spatial interpolation of the nodal temperatures  $T_i^e(t)$  that surround the point

$$T_{\Omega_c}(\mathbf{r}, t) = \sum_{i=1}^{N_e} T_i^e(t) \phi_i^e(\mathbf{r}) \quad (3.14)$$

where  $\phi_i^e(\mathbf{r})$  are basis functions used to expand the spatial dependence of  $T(\mathbf{r}, t)$

Using the standard FEM approach, we can write the HTE in a matrix form as

$$\overline{\mathbf{M}}\dot{\mathbf{T}}(t) + \overline{\mathbf{K}}(t)\mathbf{T}(t) = \mathbf{F}(t) \quad (3.15)$$

where  $\dot{\mathbf{T}}$  is the first derivative of nodal temperatures, and the elements of  $\overline{\mathbf{M}}$ ,  $\overline{\mathbf{K}}$ , and  $\mathbf{F}$  can be found in [12, p. 65].

The matrix expression of the HTE involves time derivatives that are approximated using discrete differences. Assuming a small time step  $\Delta t$  and slow variations in the temperature and boundary condition, we can use the Crank-Nicholson scheme to express the HTE as a linear combination of the temperature at  $t$  and  $t + \Delta t$ . Equation (3.15) can be rewritten as

$$\overline{\mathbf{M}} \frac{\mathbf{T}_2 - \mathbf{T}_1}{\Delta t} + \frac{\overline{\mathbf{K}}_2 \mathbf{T}_2 + \overline{\mathbf{K}}_1 \mathbf{T}_1}{2} = \frac{\mathbf{F}_2 + \mathbf{F}_1}{2} \quad (3.16)$$

where subscripts 2 and 1 represent conditions at  $t + \Delta t$  and  $t$ , respectively. By collecting and rearranging terms, the above expression can be written as the time-stepping equations

$$(2\bar{\mathbf{M}} + \Delta t\bar{\mathbf{K}}_2)\mathbf{T}_2 = \Delta t(\mathbf{F}_2 + \mathbf{F}_1) + (2\bar{\mathbf{M}} - \Delta t\bar{\mathbf{K}}_1)\mathbf{T}_1 \quad (3.17)$$

Extremely large number of unknowns are typically required and, hence, LU decomposition is not a practical approach to solving Equation (3.17). In this work a sparse matrix solver, which makes efficient use of memory, is employed for the solution.

### Boundary and Initial Conditions

As noted in Chapter 2, boundary conditions should be specified at the exterior of the computation volume ( $\Gamma$ ). Boundary conditions at the surface-air interface can be assigned using the source conditions described in Equation (3.13).

The zero normal gradient condition is imposed at the side walls which implies that the temperatures of the soil surrounding  $\Gamma$  are invariant in the radial dimension<sup>5</sup>. A zero gradient is also assumed at the bottom of the computation volume. This assumption is valid if the volume extends deep enough to reach the “diurnal depth”, at which the temperature is roughly invariant over the diurnal cycle.

Initial conditions are specified to begin the time-stepping scheme identified in Equation (3.17), and the calculation continues until the solution reaches a steady-state (periodic) function. Proper choices of initial conditions can accelerate the rate of convergence. Using the time average of source flux over a 24 hour period, a rough

<sup>5</sup>Equivalently, we assume that the boundary of  $\Gamma$  lies beyond the mine’s thermal region of influence.

estimation for initial temperatures is derived via Equation (3.13) as

$$T(\mathbf{r}, t = 0) = \frac{\mathcal{E}\overline{E}_{sun} + 4\mathcal{E}\sigma\overline{T}_{sky}^4 + \overline{h}\overline{T}_{air}}{\overline{h} + 4\mathcal{E}\sigma\overline{T}_{sky}^3} \quad (3.18)$$

### Spatial Discretization for Surface Mines

As noted above, the finite element method requires that we discretize space into an ensemble of finite volume elements (tetrahedra in this work). The spatial discretization, referred to herein as a mesh, has a critical effect on the accuracy of the solution. The mesh should have a high element density in regions with high field gradients, and it should be as sparse as possible in other regions. The automatic definition of optimal meshes is currently a research problem, and a heuristic approach is used here.

Three steps are used to construct the mesh. Throughout this work, the mine and soil are assumed to be bodies of revolution, although the final 3-D mesh deviates from that property slightly. First, a cross-sectional nodal profile of the mine's components (i.e., the generating curves) is defined in the  $\hat{r} - \hat{z}$  plane. An example appears in Figure 3.2. The generating curves bound homogeneous regions. Each color represents a distinctive structure in the mine or a layer of the soil. Nodes are defined at the corners in the generating curves and at user-selected intervals on straight line segments.

Next, the generating curves (nodal profile) are rotated in the  $\hat{\phi}$  direction through 16 positions to create a 3-D nodal space. An automated mesh generator [66] is employed to form tetrahedra by connecting nodes. Figures 3.3 shows a cross-section of the mesh. The mine is centered over a large cylinder of soil. Figure 3.4 provides a closer look at the mine's internal structure.

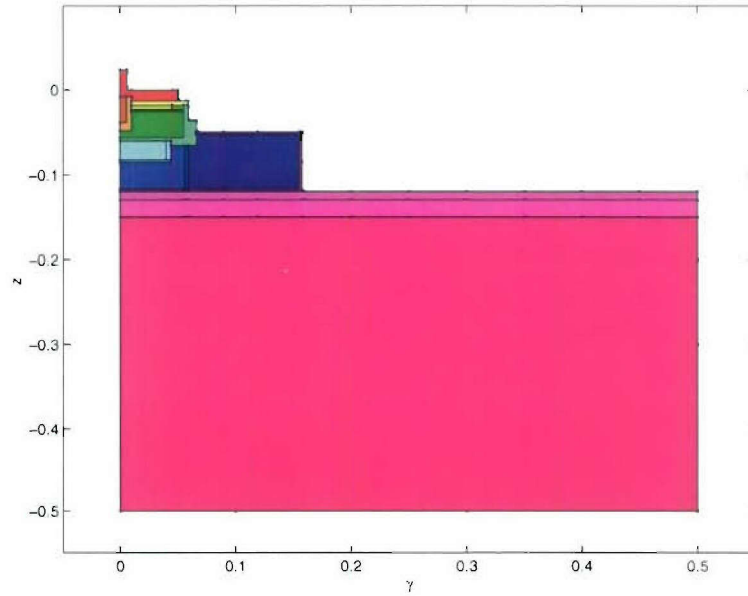


Figure 3.2: Cross-sectional nodal profile ( $\hat{r} - \hat{z}$  plane) for soil and a LP\_B mine.

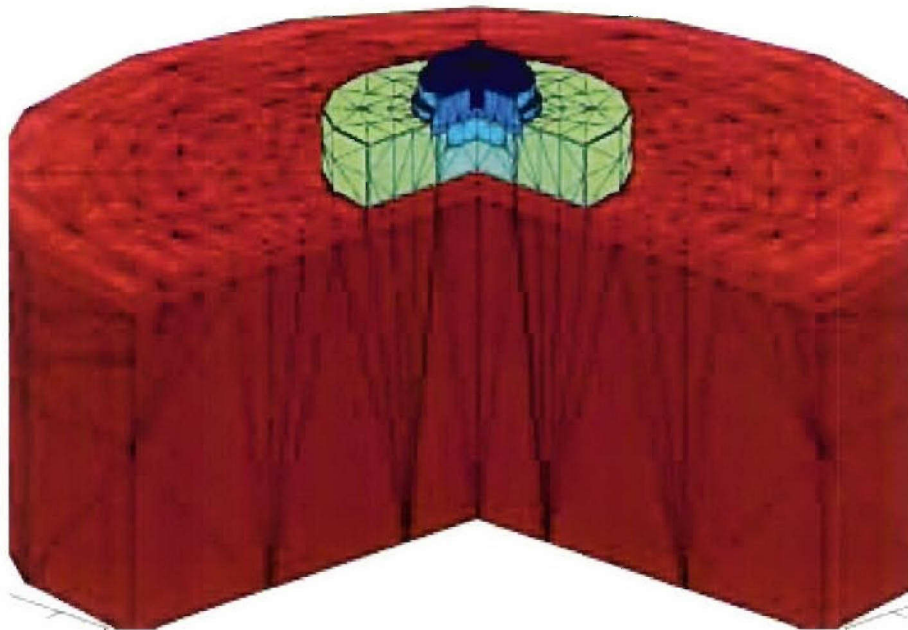


Figure 3.3: Cut-away 3-D view of the mesh of soil and a LP\_B mine.

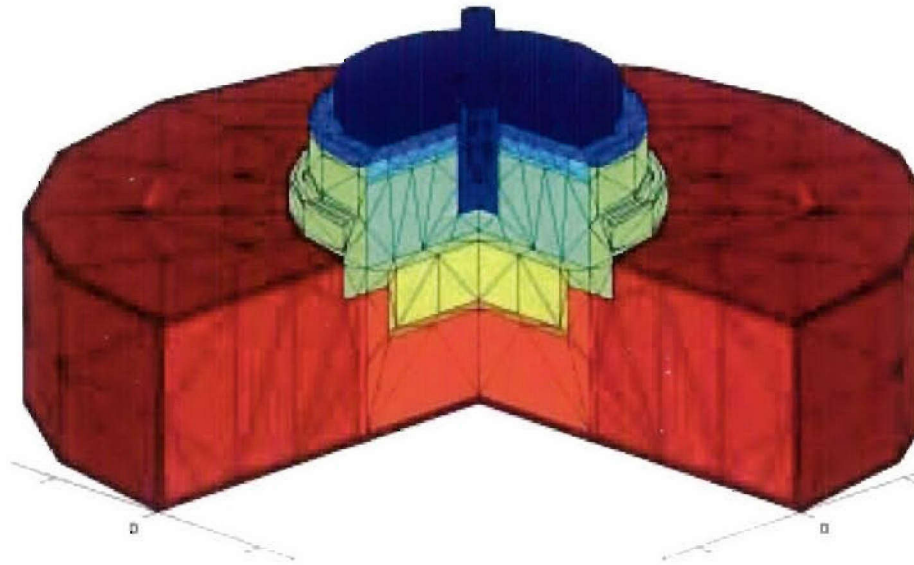


Figure 3.4: Zoomed-in cut-away 3-D view of the LP\_B mine mesh.

The last step is to refine the mesh so that regions with strong gradients contain higher tetrahedral densities. Strong gradients appear at interfaces involving thermally dissimilar media and, hence, finer vertical discretization is required at the air interface on the model's top surface. Horizontal gradients appear at shadow boundaries, which also requires finer meshing on the surface. The mesh generator used here has the ability to divide specified tetrahedra into smaller ones, and that capability is used here. Figure 3.5 shows the top view of the original mesh. Tetrahedra that require sub-division are indicated in yellow. Figure 3.6 illustrates the refined mesh.

The mesh refining measure should also be applied to regions near boundaries. Since we imposed the zero normal-gradient boundary condition and the temperature of a point in the computational volume is found via linear interpolation of nodal

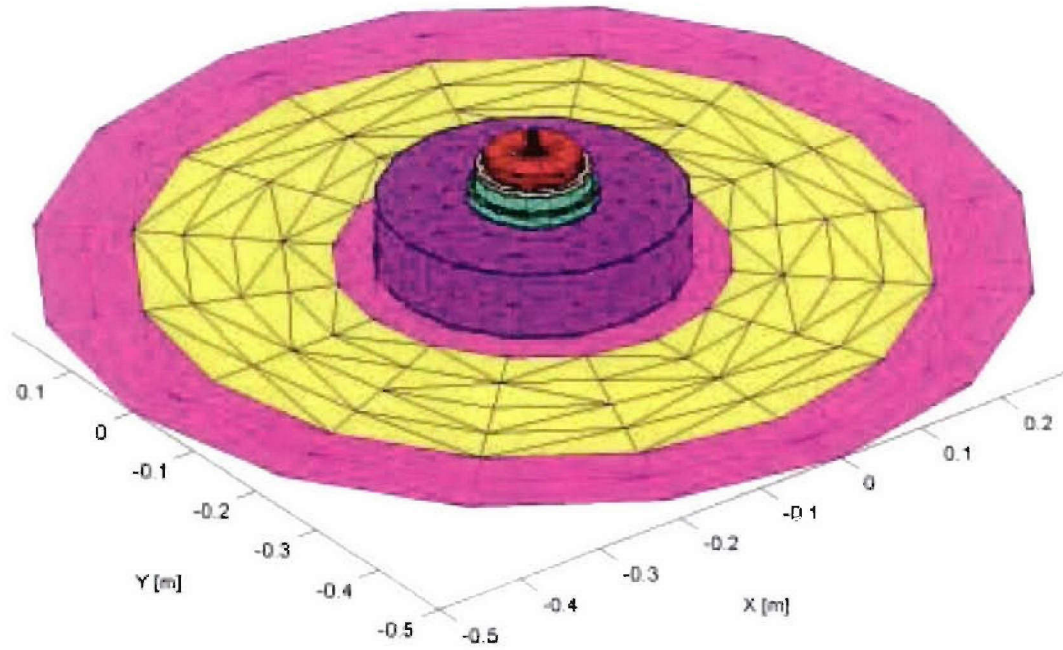


Figure 3.5: 3-D view of original LP\_B mine and soil surface mesh.

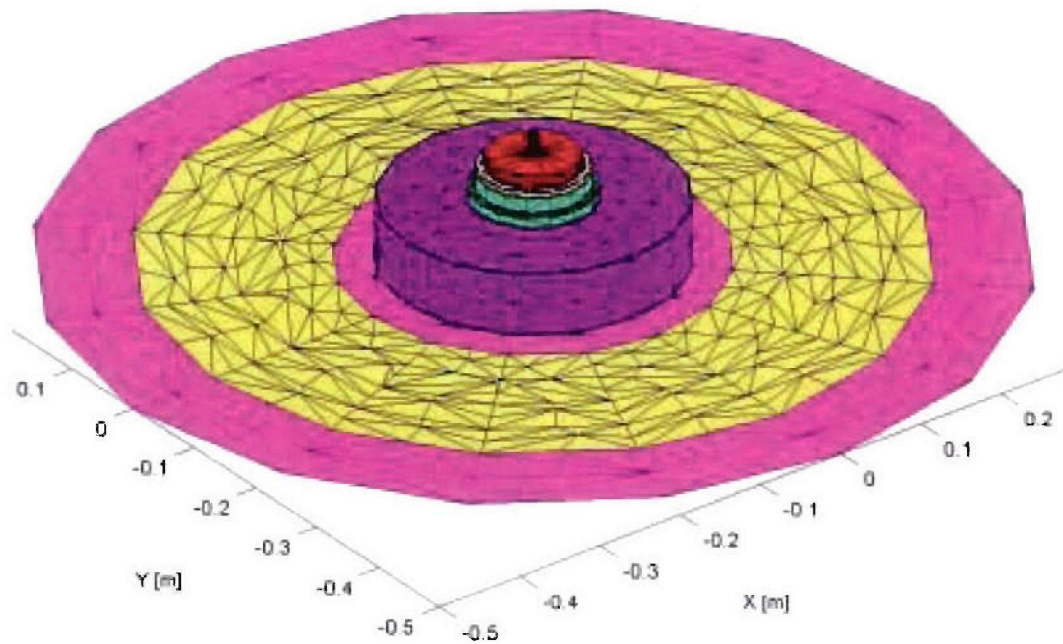


Figure 3.6: 3-D view of refined LP B mine and soil surface mesh.

Parameter name	Value	Unit
Mean air temperature	7	°C
Maximum air temp. deviation	5	°C
Averaged wind speed	3	m/s
Water vapor pressure	0.76	mmHg

Table 3.1: Critical meteorological parameters used in the baseline simulation.

temperatures, the nodal density around the sides and the bottom of the mesh have to be dense enough to yield smooth transitions across the boundary.

### 3.2.2 Example Surface Temperature Calculations

The thermal model developed above was used to simulate the surface temperatures of a LP\_B mine laid on soil. The simulations use as a baseline conditions from the NT-S1 data set. In this section we study the sensitivity of the model to various environmental conditions and model parameters. (A quantitative comparison of simulated and measured images appears in Section 3.4.)

#### Convergence of FEM Solutions

As noted in Section 2.7.1, the NT-S1 data set contains surface-laid landmines of various types. To simulate the measured image thermal and electromagnetic properties of soil and mine constituents were found in the literature [61, 67]. Important meteorological parameters and critical surface properties used in this simulation are tabulated in Tables 3.1 and 3.2, respectively.

The simulated temperature distribution is computed at 6 minute intervals. The temperature history of specific nodes on the mine and in the soil away from the mine,

Material	Thermal conductivity (W m <sup>-1</sup> K <sup>-1</sup> )	Volumetric heat capacity (10 <sup>6</sup> J m <sup>-3</sup> K <sup>-1</sup> )
Sand (moist)	2.223	1.894
Nylon (mine case)	0.24	1.714
TNT	0.2341	2.53
Steel	14.25	1.1778
Air	26.3	0.0012

Table 3.2: Critical thermal properties of materials used in the baseline simulation.

indicated as red and blue Xs on Figure 3.8 respectively, are plotted in Figure 3.7. A total simulation of 5 days was performed and convergence of the FEM solution to steady-state is evident. It is also clear that the mine’s temperature swings are significantly larger than those of the background soil. Twice daily (shortly after dusk and dawn) the curves intersect. At those times, there is no thermal contrast between the selected nodes, and mine detection is hampered. Following current practice, we refer to those times as “crossovers”. Finally, note that the soil temperature takes more than three days to reach convergence, while mine surfaces achieve convergence in less than two days. In what follows we show only the “steady state” solutions, which correspond to the fifth simulated day.

Temperature “images” are formed by linearly interpolating surface nodal temperatures. Figure 3.9 shows the steady-state surface temperature of a LP\_B mine on soil. Images are displayed at two hour intervals from 7 AM through 5 PM. In general, the hottest regions appear near the edges, but there are cooler regions adjacent to elevated structures due to solar shadows. Differences in the temperature of the mine and soil are evident in these images. The mine housing, which is made of plastic, responds

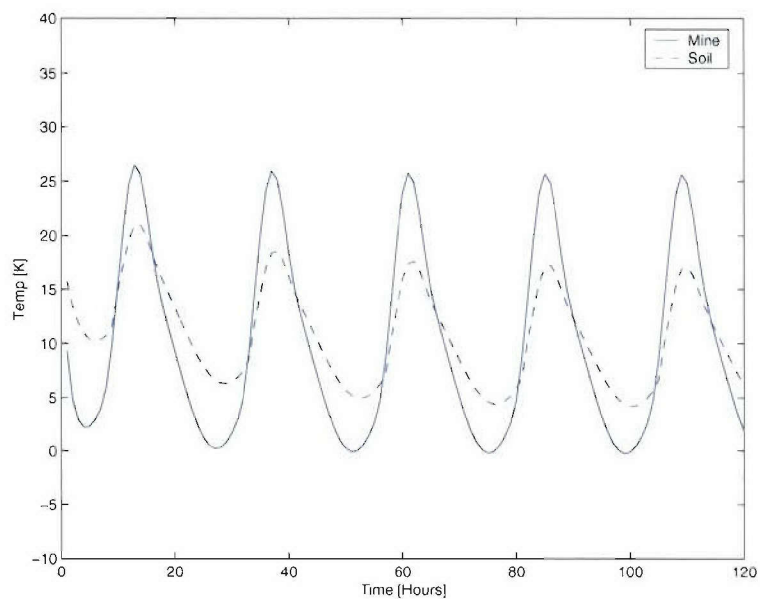


Figure 3.7: Diurnal cycle convergence of surface temperatures.

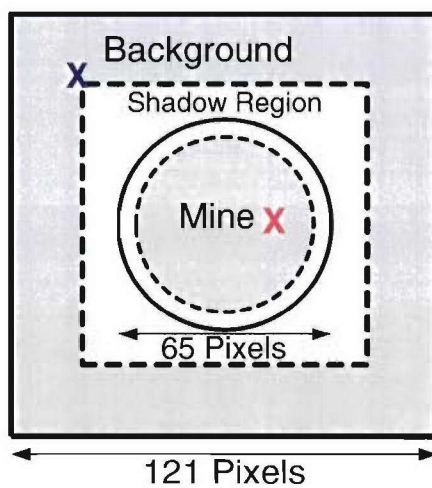


Figure 3.8: Boundaries (solid lines) of mine and soil regions in simulated thermal images. Averages over gray regions are used for comparison.

more rapidly to solar insolation than soil and dissipates its thermal energy faster after sunset. Because the mine does not heat uniformly, it is clear that the “crossover” concept cannot be used to make unambiguous statements about detection.

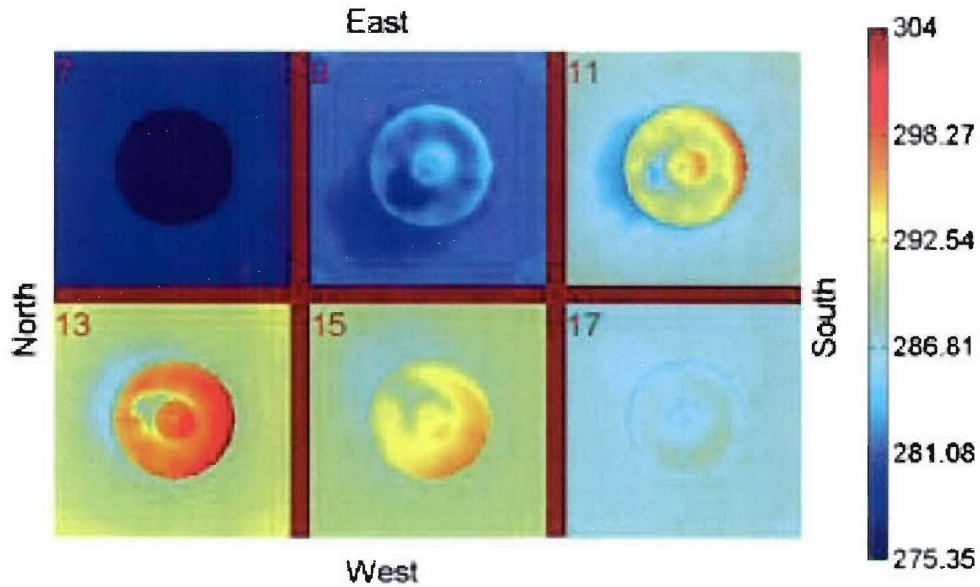


Figure 3.9: Examples of surface temperature profiles during the day.

### Sensitivity to Environmental Parameters

The simulation’s dependence on some important environmental parameters was studied via computed surface temperature histories. We first examined the seasonal dependence of the temperature variation. The effect of the wind speed was then studied. Temperature histories were plotted showing the average temperatures on the mine housing and soil (at least 5 cm away from the mine). The gray regions in Figure 3.8 indicate mine and background pixels used to calculate temperature

Date	Jun. 21st	Aug. 21st	Oct. 21st	Dec. 21st
Mean air temperature [°C]	25	21	7	0
Maximum air temp. deviation [°C]	5	5	5	5
Averaged wind speed [m/s]	3	3	3	3

Table 3.3: Critical meteorological parameters used in the simulation for seasonal changes in surface temperatures.

averages. The difference of mine and soil average temperatures was also plotted to reveal the time of maximum contrast.

The air temperature, and duration and direction of solar insolation undergo seasonal changes. Using the solar positions<sup>6</sup> and weather conditions at the test site<sup>7</sup>, simulations were performed every two months from late June through late December. Table 3.3 lists critical parameters used in the simulations. Results are shown in Figure 3.10. Those curves indicate that during the summer both the mine (solid lines) and soil (dashed lines) have higher surface temperatures due to longer daylight hours and higher air temperature. The contrast shown in Figures 3.10 (b) reveals that larger differences in surface temperatures occur around noon and midnight. The greater summer insolation results in a maximum summer contrast that is twice large as the one observed in winter.

Next, we study the effect of wind speed. Simulations were performed for both the warm and cool winds implied by summer and winter conditions respectively. Figure 3.11 (a) shows the mine and soil temperatures during summer (late June) for

<sup>6</sup>The method used to find solar angles and solar irradiance is presented in Section 3.2.3

<sup>7</sup>Mean and maximum deviation in air temperature were estimated from historical data at <http://www.noaa.gov/climate.html>.

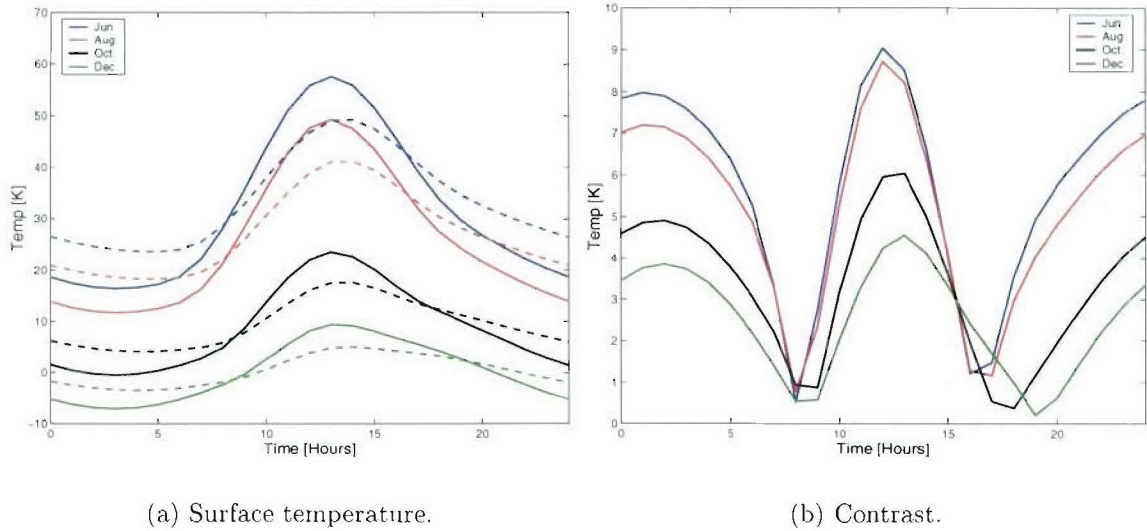
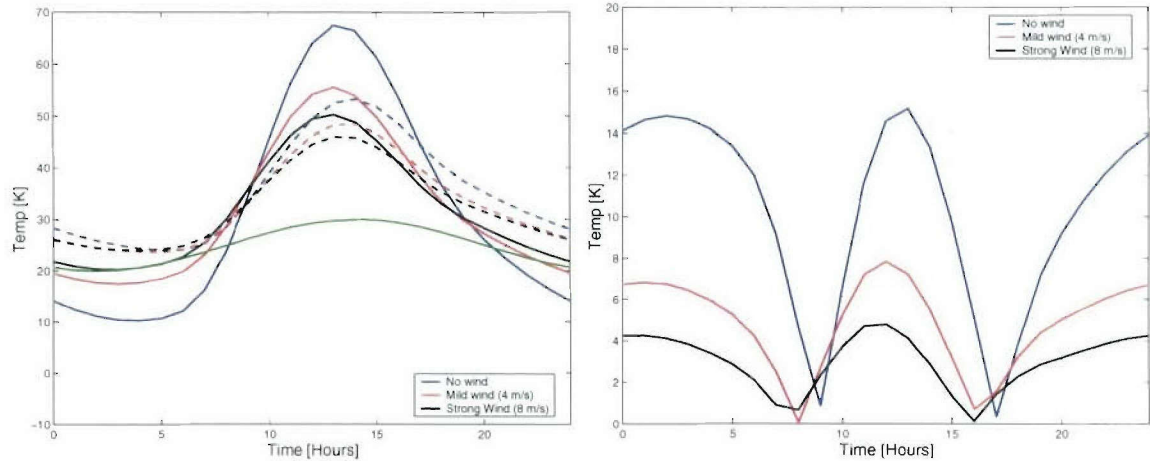


Figure 3.10: Surface temperatures and contrast for different time of the year. Baseline conditions: latitude= $40.3^{\circ}\text{N}$ , wind speed= $3\text{ m/s}$ . Solid lines: mine. Dash lines: soil.

three wind speeds: no wind, mild wind ( $4\text{ m/s}$ ), and strong wind ( $8\text{ m/s}$ ). The green curve is the air temperature. A comparison with the no-wind results shown in blue indicates that the air is cooler than the soil (dashed line) at all times. The cool wind removes heat from the soil through convection and reduces the maximum temperature. The mine surface is both cooler than the air in the evenings and warmer than the air during the day. Hence, convection alternately heats and cools the mine. The overall effect of the wind is to reduce the dynamic range of the mine's temperature. Wind has an adverse effect on the temperature contrast as shown in Figure 3.11 (b).

During winter (late December), the air is warmer than the mine and soil surfaces under calm conditions and, hence, both mine and soil surface temperatures increase considerably if wind is present (see Figure 3.12). Again, wind causes the contrast to



(a) Surface temperature. The green curve is the air temperature. Solid lines: mine. Dashed lines: soil.

(b) Mine-soil contrast.

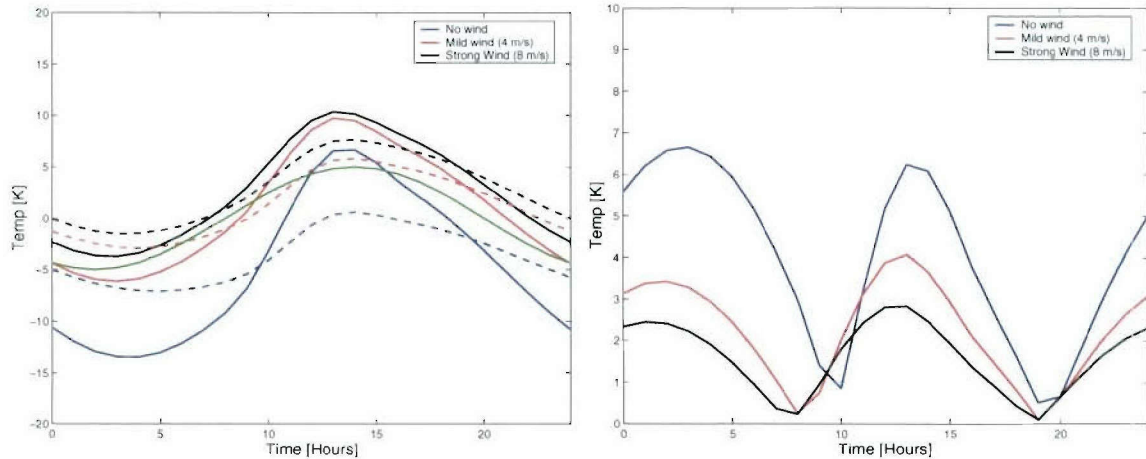
Figure 3.11: Surface temperatures and contrast for different wind speeds during summer. Baseline conditions: latitude=40.3°N, air temperature: mean=25°C maximal deviation=5°C.

decrease. It is significant that wind accelerates the heating and cooling processes. We see in Figure 3.12 (b) that the crossover time for the no-wind case lags more than an hour behind the strong-wind case.

The above experiments illustrate that, as expected, the surface temperature is dependent on the insolation and air temperature. The wind speed alters this dependence significantly. A higher wind tends to reduce thermal contrast.

### 3.2.3 Solar Spectral Irradiance

As stated in Section 2.2.2, solar radiation is an important source for passive remote sensing, especially for visible sensors. Although the extraterrestrial solar irradiance



(a) Surface temperature. The green curve is the air temperature. Solid lines: mine. Dashed lines: soil.

(b) Mine-soil contrast.

Figure 3.12: Surface temperatures and contrast for different wind speeds during summer. Baseline conditions: latitude=40.3°N, air temperature: mean=0°C maximal deviation=5°C.

varies slightly from day-to-day as a result of solar activity, we can assume it is a constant for this analysis.

Insolation is strongly affected by the solar position and the resulting slant path length. The slant path length and atmospheric composition determine the atmospheric attenuation, while the solar position determines the geometric relation between the incident flux and target surfaces. The actual irradiance received by a target is reduced by the ratio of the projected area to the physical area.

The solar irradiance is computed by first determining the angular position of the sun given the time, date, and observer's geolocation. The MODTRAN code is then used to calculate the spectral solar irradiance for the given solar angles. Unlike the thermal model, which must take into account the entire solar spectrum (for its effect

in warming the soil), only spectral irradiance sensible by the detector is considered in the radiometric model.

The celestial position of the sun is described by its declination angle and hour angle. Due to the tilted and elliptical orbit of the earth, the declination  $\theta_{dec}(\pm 23.5^\circ)$  and the time of meridian<sup>8</sup> passage of the sun (12 : 00 $\pm$ 15 min.) are periodic functions with a one year period. The *Nautical Almanac* tabulates the Greenwich hour angle ( $\phi_{GHA}$ ) and declination angle of the sun and is updated annually to document small drifts in the above angles. For example [68], the sun passes the meridian on Jan. 1st, 2003 at 11:56:50 with a  $-23^\circ 03'$  declination angle. On Jan. 1st, 2004, the time is 11:56:56 and the angle is  $-23^\circ 03'$ . Since the observed drift in solar position is negligible for the purposes of this modeling, a look-up table was constructed from a prior year's data to find the solar position for a given time and date.

The solar elevation and azimuth angles denoted  $(\theta_{elev}, \phi_{azim})$ , are defined by the declination and hour angles  $(\theta_{dec}, \phi_{GHA})$  noted above with knowledge about the latitude and longitude of the observer. We have

$$\theta_{elev} = 90 - \theta_{lat} + \theta_{dec} \quad (3.19)$$

$$\phi_{azim} = \phi_{GHA} + \phi_{long} \quad (3.20)$$

where  $\phi_{long}$  is positive for longitude east of Greenwich. As examples, Figures 3.13 and 3.14 depict the seasonal and diurnal variations in the solar elevation angle  $\theta_{elev}$  at a mid-latitude location ( $43.5^\circ\text{N}$ ) and the Tropic of Cancer ( $23.5^\circ\text{N}$ ). The former exhibits a significant change in the length of a day, while the latter is the highest latitude where it is possible to observe a vertical sun (on June 21st or 22nd).

<sup>8</sup>The meridian is the highest point in the daily path of a celestial body.

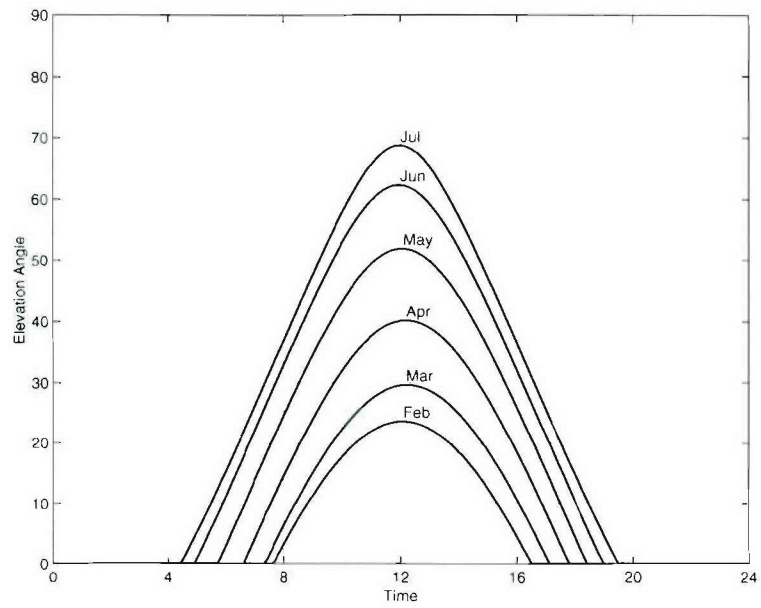


Figure 3.13: Solar elevation angle of different months at latitude  $43.5^{\circ}\text{N}$ .

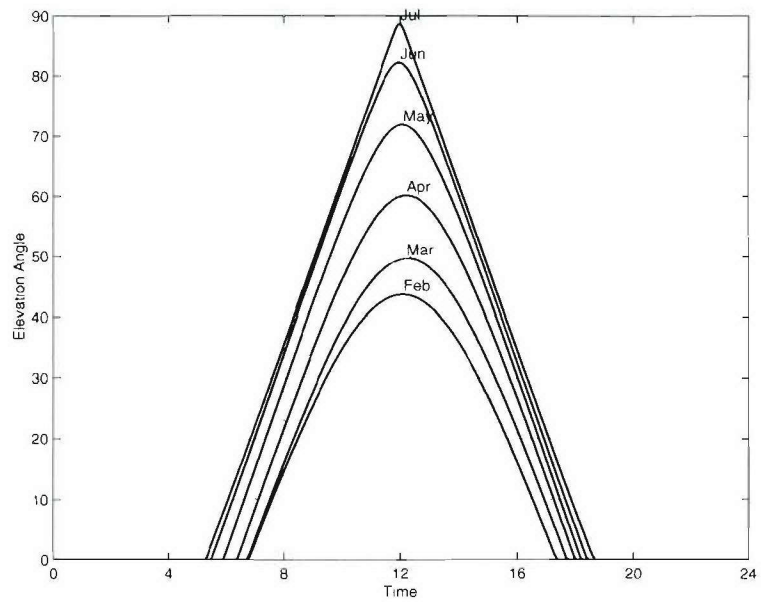


Figure 3.14: Solar elevation angle of different months at latitude  $23.5^{\circ}\text{N}$ .

The radiometric model uses LOWTRAN<sup>9</sup> to calculate the solar irradiance for the default atmosphere model. The spectral irradiance generated by LOWTRAN is then numerically integrated over the sensor's passband. Figure 3.15 shows the total irradiance in the MWIR band, which extends from 3 to 5  $\mu\text{m}$ . Mid-latitude ( $45^\circ\text{N}$ ) winter and mid-latitude summer atmospheric models are used in this calculation. Note that more solar irradiance reaches the ground in the winter because the atmospheric mass is smaller and provides less scattering and absorption, but the projected irradiance is lower due to the lower declination angle.

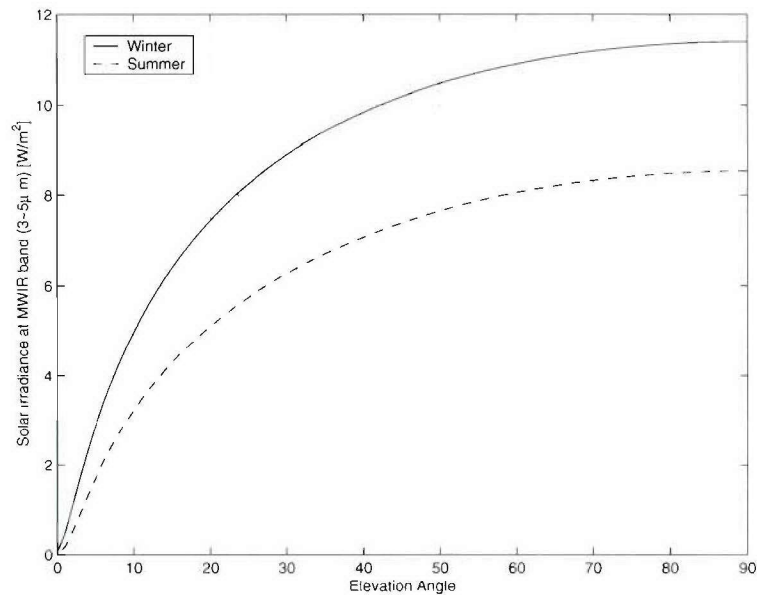


Figure 3.15: Solar irradiance at MWIR band ( $3\sim 5 \mu\text{m}$ ) v.s. solar elevation angle in mid-latitude winter and summer.

The daily solar elevation profiles shown in Figure 3.13 can be used to find the total MWIR irradiance via interpolation of the data in Figure 3.15. Figure 3.16 shows the

<sup>9</sup>The LOWTRAN code, which is the predecessor of MODTRAN, has a lower spectral resolution but requires less computation time.

diurnal variations during December and June at latitude  $43.5^{\circ}\text{N}$ . Note that the two curves predict comparable maximum solar irradiances for summer and winter, but 50% more total solar energy is received during the summer due to the longer daylight hours.

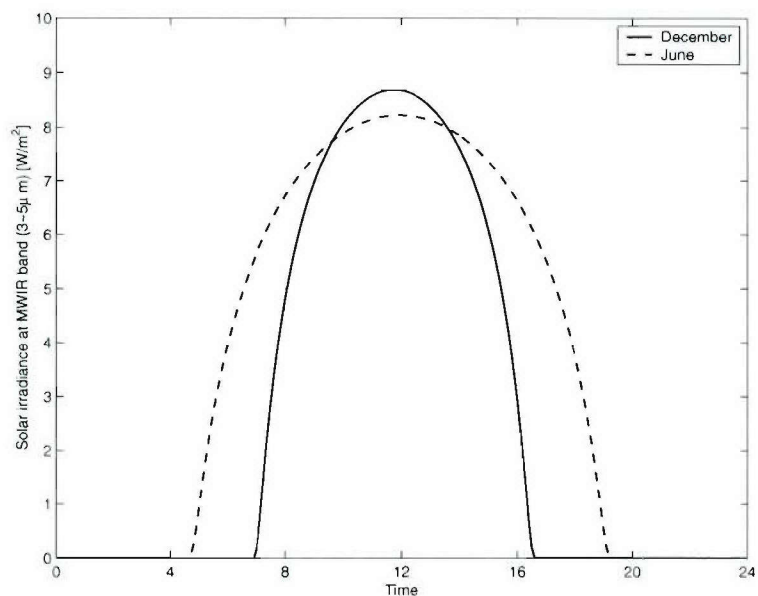


Figure 3.16: Diurnal variations in solar irradiance at MWIR band ( $3\sim 5\ \mu\text{m}$ ) in December and June at latitude  $43.5^{\circ}\text{N}$ .

### 3.2.4 Spectral Radiance of Skylight

Although skylight is much less intense than direct solar radiation, its overall effect is still substantial, because it exists over an entire hemisphere. The spectrum of skylight radiance depends strongly on the content of the atmosphere, but atmospheric scattering is difficult to predict, because of large variations in aerosol populations.

Instead of using analytical models, we employ the LOWTRAN code to compute the spectral radiance of skylight coming from different parts of the sky.

The calculation begins by finding the position of the sun, which is the ultimate source for skylight. A mesh is defined for the upper hemisphere that represents the sky, as shown in Figure 3.17. The mesh contains 668 nodes and 605 facets, and the largest facet is no larger than 0.0165 sr. The skylight arriving through each mesh facet is computed individually using the LOWTRAN code. The spectral radiance is numerically integrated to yield the total skylight radiance. Skylight is partially polarized. Its polarimetric dependence is generated from the Rayleigh scattering assumption described in Section 2.2.3.

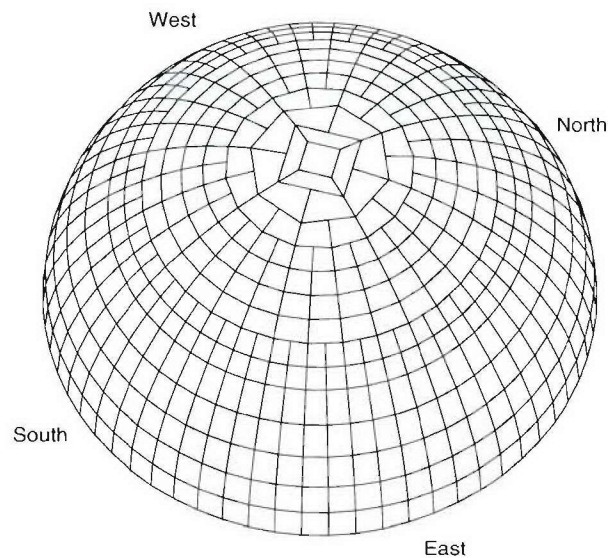


Figure 3.17: Mesh used in skylight calculation.

Example calculations of skylight are shown in Figures 3.18 and 3.19 for latitude  $52^{\circ}\text{N}$  during May. The atmosphere is assumed to have rural extinction properties and good visibility (23 km). Figure 3.18 shows the skylight radiance at 8:30AM. In general, skylight is stronger near the horizon than near zenith. Also, a peak appears around the solar position, as shown in Figure 3.19 for a high solar elevation angle (at noon during summer). The intensity and width of the skylight peak at the solar position are affected by the composition of the atmosphere. Atmospheres with higher particle densities, which often appear above urban areas, not only produce shorter extinction distance, but also introduce a broader skylight peak with a higher intensity, because more sunlight is scattered by particles in the atmosphere.

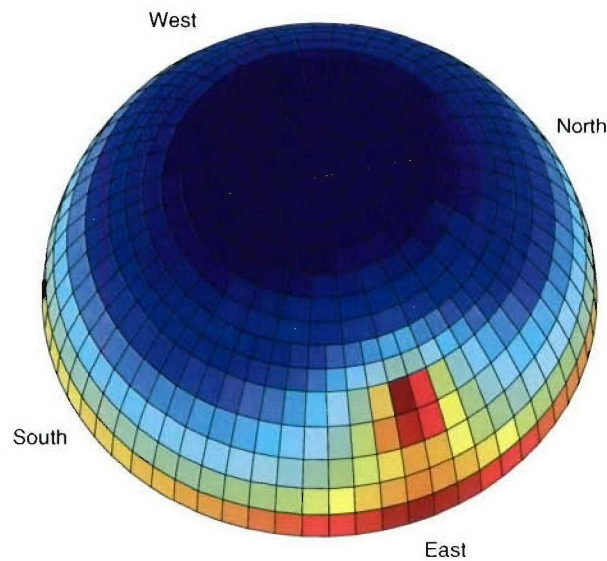


Figure 3.18: Sample skylight profile at 8:30AM in May at latitude  $52^{\circ}\text{N}$ .

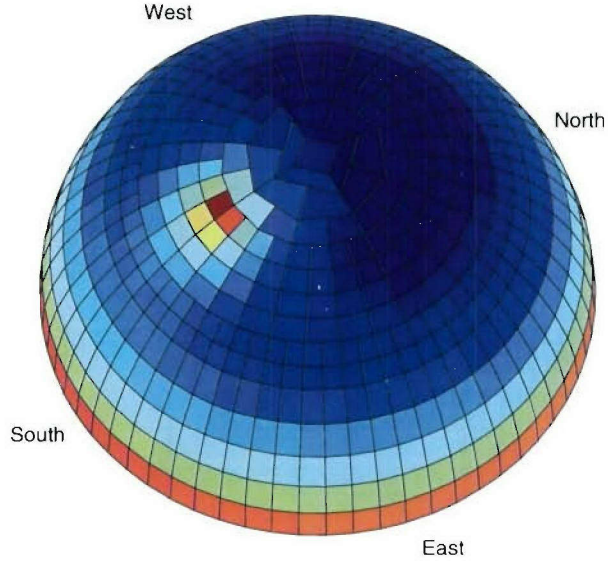


Figure 3.19: Sample skylight profile at 12:30PM in May at latitude 52°N.

### Adding Polarization Dependency

As mentioned in Section 2.2.3, skylight is partially polarized due to scattering by air molecules and aerosols. To use Equation (2.15) for computing the degree of linear polarization (DoLP), the scattering particles must be smaller than the sensor wavelengths, so that Rayleigh scattering is dominant. This condition is satisfied for IR wavelengths, since the optical thickness of the atmosphere is insignificant for wavelengths longer than the visible band. Figure 3.20 shows the degree of linear polarization for skylight in the MWIR band under a clear sky. Skylight is unpolarized around the sun, and the degree of linear polarization increases as the observer moves away from the sun. Skylight coming from directions orthogonal to the solar direction is

fully linearly polarized. In general, the DoLP would be smaller for turbid atmospheres and shorter wavelengths due to multiple scattering.

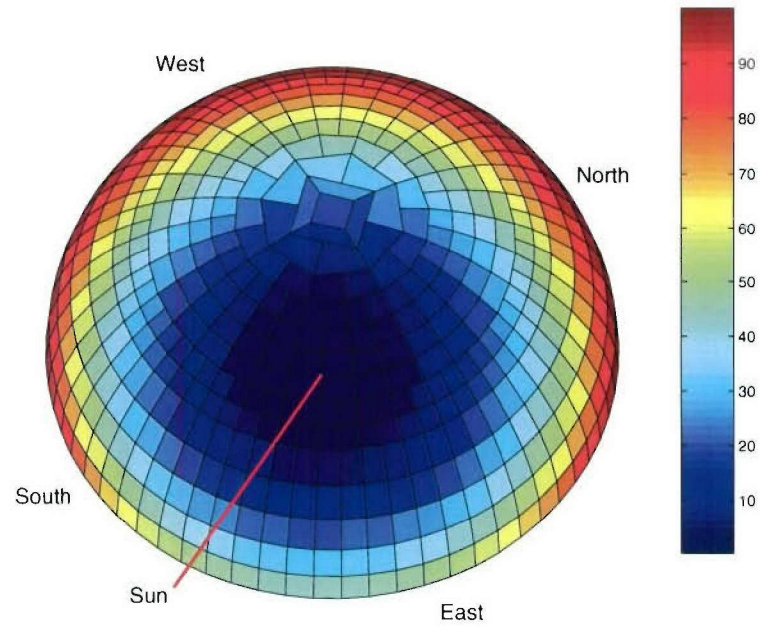


Figure 3.20: Sample skylight degree of linear polarization based on Rayleigh scattering.

### 3.3 A Mueller Matrix for Mine and Soil

Surface reflectivity and emissivity directly affect EO radiometric signatures. In this dissertation a rough-surface bidirectional reflectance distribution function (BRDF) has been developed using a combination of classical physical optics and geometric optics approaches. Energy conservation permits the emissivity of a surface to be computed from the BRDF via spatial integration. This section documents the derivation of the BRDF and its associated emissivity.

Sections 3.3.1 and 3.3.2 review the derivations of physical optics (PO) and geometrical optics (GO) rough-surface scattering models. A comparison of the two models in Section 3.3.3 shows they have similar features for the roughness scales of interest here. A polarimetric BRDF is proposed in Section 3.3.4. Simulations of the proposed BRDF are performed for different amounts of surface roughness and surface EM parameters. A discussion of those results appears in Section 3.3.5. Section 3.3.6 presents selected measurements of the in-plane BRDF for various materials. A comparison of those measurements with the proposed BRDF shows good agreement. Finally, emissivity functions are computed via spatial integration of simulated BRDFs.

#### 3.3.1 Physical Optics Model

As discussed in Section 2.5, the PO method (also sometimes referred to as the Kirchhoff approximation), is often used to explore scattering from random rough surfaces. The PO approach to rough surface scattering was first used by Beckmann [42] for perfectly conducting surfaces. Here, we present key equations and assumptions made in the derivation of the PO model. Measures required to use this model for radiometric mine signature prediction are also addressed.

The derivation begins by representing the scattered field in an integral form. In order to evaluate the integral, a tangent plane approximation is made, which assumes that the radius of surface curvature is large compared to the wavelength. Tsang et al. [18] take the asymptotic limit of the integral resulting in a closed form expression applicable to dielectric surfaces also. In that result, only the incoherent term survives, which appears as a lobe in the specular direction. Tsang et al. also introduce the Mueller matrix notation to express the polarimetric dependence.

### Kirchhoff Approximation

Consider an incident plane wave impinging on a random rough surface. The electric field of the incident wave is

$$\mathbf{E}_i = \hat{\mathbf{e}}_i E_0 e^{i\mathbf{k}_i \cdot \mathbf{r}} \quad (3.21)$$

in which the time dependence  $e^{-i\omega t}$  is implied and suppressed. The polarization vector  $\hat{\mathbf{e}}_i$  can be decomposed into perpendicular  $\hat{\mathbf{v}}_i$  and parallel  $\hat{\mathbf{h}}_i$  terms with respect to the local surface normal as stated in Equations (2.1) and (2.2). The surface normal vector can be expressed as

$$\hat{\mathbf{n}} = \frac{-f'_x(x, y)\hat{x} - f'_y(x, y)\hat{y} + \hat{z}}{\sqrt{1 + (f'_x(x, y))^2 + (f'_y(x, y))^2}} \quad (3.22)$$

where  $f'_x(x, y)$  and  $f'_y(x, y)$  represent the surface slopes at position  $(x, y)$  with respect to the  $\hat{x}$  and  $\hat{y}$  axes.

Using the dyadic Green's function  $\overline{\overline{\mathbf{G}}}$  and evaluating the electric and magnetic fields on the surface, we can express the scattered electric field as

$$\mathbf{E}_s(\mathbf{r}) = \int_{S'} dS' \{ i\omega\mu_0 \overline{\overline{\mathbf{G}}}(\mathbf{r}, \mathbf{r}') \cdot [\hat{\mathbf{n}} \times \mathbf{H}(\mathbf{r}')] + \nabla \times \overline{\overline{\mathbf{G}}}(\mathbf{r}, \mathbf{r}') \cdot [\hat{\mathbf{n}} \times \mathbf{E}(\mathbf{r}')] \} \quad (3.23)$$

in which  $\mathbf{E}$  and  $\mathbf{H}$  are the total fields on  $\mathbf{S}$ . In the far field, the dyadic Green's function becomes

$$\overline{\mathbf{G}}(\mathbf{r}, \mathbf{r}') \simeq (\overline{\mathbf{I}} - \hat{\mathbf{k}}_s \hat{\mathbf{k}}_s) \frac{e^{ikr}}{4\pi r} e^{-i\mathbf{k}_s \cdot \mathbf{r}'} \quad (3.24)$$

where  $\overline{\mathbf{I}}$  is the dyadic identity. With the substitution of Equation (3.24) in (3.23) we obtain

$$\mathbf{E}_s(\mathbf{r}) = \frac{e^{ikr}}{4\pi r} (\overline{\mathbf{I}} - \hat{\mathbf{k}}_s \hat{\mathbf{k}}_s) \cdot \int_{S'} dS' \{ \hat{\mathbf{k}}_s \times [\hat{\mathbf{n}} \times \mathbf{E}(\mathbf{r}')] + \eta [\hat{\mathbf{n}} \times \mathbf{H}(\mathbf{r}')] \} e^{-i\mathbf{k}_s \cdot \mathbf{r}'} \quad (3.25)$$

### Tangent Plane Approximation

Evaluation of the integral in Equation (3.25) requires a description of the surface. Beckmann [42] introduced the tangent plane approximation, which assumes the surface is locally planar. This approximation requires that the incident wavelength is small compared to the surface's radius of curvature. With this approximation and some algebraic manipulations, the scattered field can be expressed as

$$\mathbf{E}_s(\mathbf{r}) = \frac{e^{ikr}}{4\pi r} E_0 (\overline{\mathbf{I}} - \hat{\mathbf{k}}_s \hat{\mathbf{k}}_s) \cdot \int_{S'} dS' \mathbf{F}(\alpha, \beta) e^{-i(\mathbf{k}_i - \mathbf{k}_s) \cdot \mathbf{r}'} \quad (3.26)$$

where  $\mathbf{F}$  is the integrand in Equation (3.26) above and  $\alpha$  and  $\beta$  are in-plane and out-of-plane tilting angles defined in Figure 3.21. Angles  $\alpha$  and  $\beta$  define the local surface normal and are used to describe the surface roughness.

The function  $\mathbf{F}$  can be expressed in terms of the tilting angles and the local Fresnel reflection coefficients as follows: [18]

$$\begin{aligned} \mathbf{F}(\alpha, \beta) = & \sqrt{1 + \tan^2 \alpha + \tan^2 \beta} \cdot \{ -(\hat{\mathbf{e}}_i \cdot \hat{\mathbf{h}}_r)(\hat{\mathbf{n}} \cdot \hat{\mathbf{k}}_i) \hat{\mathbf{h}}_i (1 - R_h) \\ & + (\hat{\mathbf{e}}_i \cdot \hat{\mathbf{v}}_i)(\hat{\mathbf{n}} \times \hat{\mathbf{h}}_i)(1 + R_v) + (\hat{\mathbf{e}}_i \cdot \hat{\mathbf{h}}_i)(\hat{\mathbf{k}}_s \times (\hat{\mathbf{n}} \times \hat{\mathbf{h}}_i))(1 + R_h) \\ & + (\hat{\mathbf{e}}_i \cdot \hat{\mathbf{v}}_i)(\hat{\mathbf{n}} \cdot \hat{\mathbf{k}}_i)(\hat{\mathbf{k}}_s \times \hat{\mathbf{h}}_i)(1 - R_v) \} \end{aligned} \quad (3.27)$$

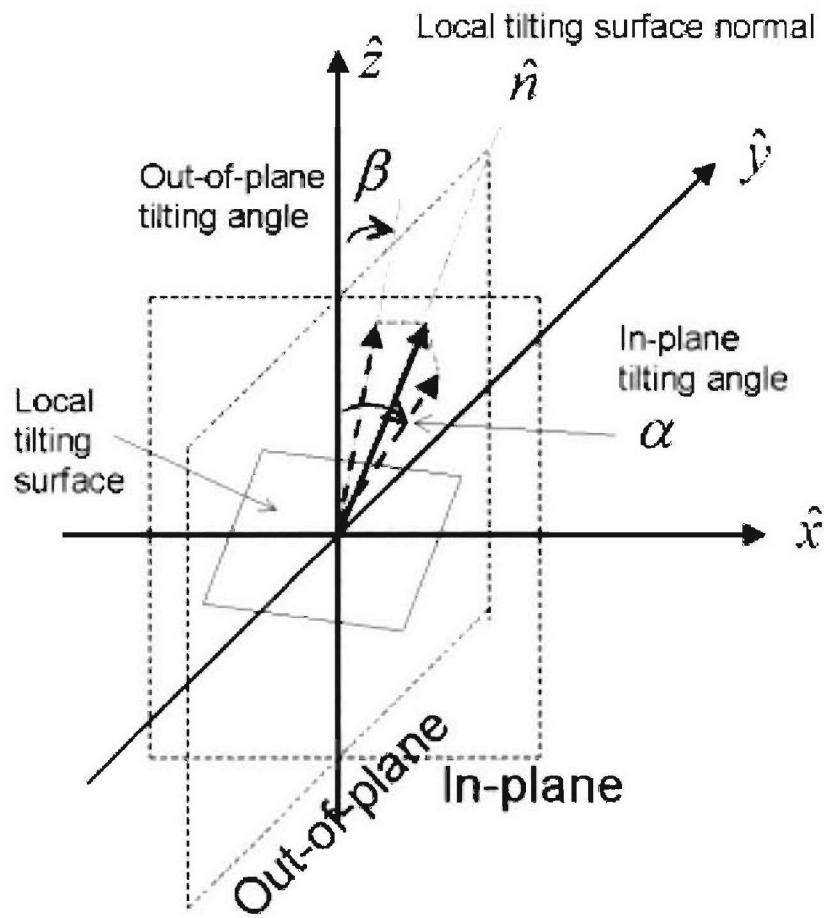


Figure 3.21: Geometrical definitions of a locally tilted surface.

where  $\hat{\mathbf{h}}_i$  and  $\hat{\mathbf{v}}_i$  are local unit horizontal and vertical polarization vectors, given by

$$\hat{\mathbf{h}}_i = \frac{\hat{\mathbf{k}}_i \times \hat{\mathbf{n}}}{|\hat{\mathbf{k}}_i \times \hat{\mathbf{n}}|} \quad (3.28)$$

$$\hat{\mathbf{v}}_i = \hat{\mathbf{h}}_i \times \hat{\mathbf{k}}_i \quad (3.29)$$

The local Fresnel reflection coefficients,  $R_h$  and  $R_v$  were defined in Equations (2.33) and (2.34).

The classical approach to evaluation of Equation (3.26) is to expand  $\mathbf{F}(\alpha, \beta)$  in a Taylor series about the mean slope  $(\alpha_0, \beta_0)$ . We have

$$\mathbf{F}(\alpha, \beta) = \mathbf{F}(\alpha_0, \beta_0) + \alpha \frac{\partial \mathbf{F}}{\partial \alpha} \Big|_{\alpha, \beta = \alpha_0, \beta_0} + \beta \frac{\partial \mathbf{F}}{\partial \beta} \Big|_{\alpha, \beta = \alpha_0, \beta_0} + \dots \quad (3.30)$$

This small slope approximation leads to considerable simplification for the special case when slope angles  $\alpha$  and  $\beta$  are symmetrically distributed about the mean slope. In that case, the linear terms vanish by symmetry, and we are left with

$$\mathbf{E}_s(\mathbf{r}) = \frac{e^{ikr}}{4\pi r} E_0 (\bar{\mathbf{I}} - \hat{\mathbf{k}}_s \hat{\mathbf{k}}_s) \mathbf{F}(\alpha_0, \beta_0) I \quad (3.31)$$

where

$$I = \int_{S'} e^{-i(\hat{\mathbf{k}}_i - \hat{\mathbf{k}}_s) \cdot \mathbf{r}'} dS' \quad (3.32)$$

## Coherent and Incoherent Scattering

The scattered field intensity, which defines the radiant power, is the time average of  $\mathbf{E}_s \cdot \mathbf{E}_s^*$ . It is conventional to invoke the ergodic hypothesis, replacing time averages by ensemble averages. The quantity  $\langle \mathbf{E}_s \cdot \mathbf{E}_s^* \rangle$  has both deterministic (mean) and random components. We write

$$\begin{aligned} \langle \mathbf{E}_s \cdot \mathbf{E}_s^* \rangle &= |\langle \mathbf{E}_s \rangle|^2 + [\langle |\mathbf{E}_s|^2 \rangle - |\langle \mathbf{E}_s \rangle|^2] \\ &= \left(\frac{E_0}{4\pi r}\right)^2 |\bar{\mathbf{I}} - \hat{\mathbf{k}}_s \hat{\mathbf{k}}_s|^2 \{ |\langle I \rangle|^2 - [\langle |I|^2 \rangle - |\langle I \rangle|^2] \} \quad (3.33) \end{aligned}$$

The first term on the right-hand side is referred to as the coherent component. For surfaces with zero-mean slopes,  $\langle \mathbf{E}_s \rangle$  is simply the response of a flat surface and, hence, the coherent component dominates in the limit of a smooth surface. It comprises a ray in the specular direction. The variance  $\langle |I|^2 \rangle - |\langle I \rangle|^2$  is referred to as the incoherent component, which appears as a broad lobe in the specular direction. For a smooth surface, the coherent component is dominant, but that component disappears as the degree of surface roughness increases, leaving only the incoherent component.

$\langle |I|^2 \rangle$  is a delta function in the specular direction and its quantity is difficult to evaluate in general, but progress can be made for Gaussian surfaces. Beckmann [42] derived the result for a PEC surface. Tsang et al. [18] used the geometric optics limit, which assumes an infinitesimally small wavelength, to derive the response of a dielectric surface. Since the coherent term  $|\langle I \rangle|^2$  becomes negligible in the small wavelength limit, only the incoherent term  $\langle |I|^2 \rangle - |\langle I \rangle|^2 \simeq \langle |I|^2 \rangle$  is considered here.

The widely-used Gaussian surface model assumes surface heights that are Gaussian distributed with zero mean and variance  $\sigma^2$ . The correlation  $C(\tau)$  between surface heights measured between any two points separated by a distance  $\tau$  is also assumed to have a Gaussian form, namely:

$$C(\tau) = \exp\left(-\frac{\tau^2}{\ell^2}\right) \quad (3.34)$$

where  $\ell$  is the surface's correlation length. The values of  $\sigma$  and  $\ell$  must be consistent with the assumptions invoked above. Specifically, the surface height standard deviation  $\sigma$  must be large compared to the wavelength  $\lambda$ , and the correlation distance  $\ell$

should be large enough that no sharp edges are present on the surface. The ratio

$$s^2 = 2\sigma^2/\ell^2 \quad (3.35)$$

is the mean-squared surface slope and is an important parameter for describing surface roughness.

Although  $s^2$  is a dimensionless parameter and is a constant for a given surface, in the simulation, we vary the mean-squared surface slope value in proportion to the change in sensor's wavelength as an indicator for the degree of surface roughness. The reason that allows this change can be explained using the surface spectra [21]. Figure 3.22 illustrates a sample surface spectral density function  $W$ , which is the Fourier transform of a given surface correlation function. For a shorter wavelength, the effective surface slope variance, which is the integral from DC to the sensor's passband, includes more energy so that the surface looks rougher.

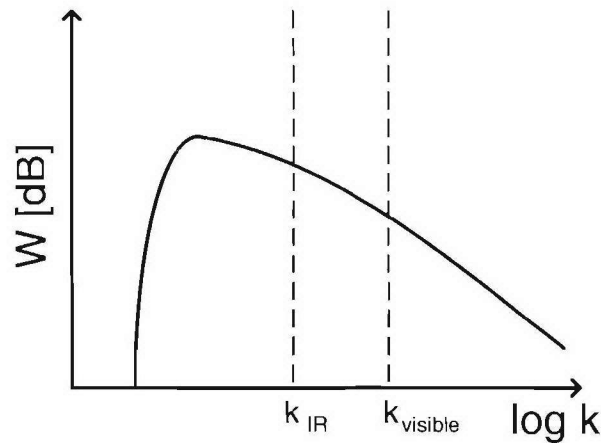


Figure 3.22: A sample surface spectral density function.

Using the above model, Tsang et al. showed the incoherent term becomes

$$\langle |I|^2 \rangle = \frac{\pi A}{s^2 v_z^2} \exp \left[ -\frac{v_{xy}^2}{2s^2 v_z^2} \right] \quad (3.36)$$

where  $v_{xy}$  and  $v_z$  are respectively, projections of the vector  $(\hat{\mathbf{k}}_s - \hat{\mathbf{k}}_i)$  onto the  $\hat{x} - \hat{y}$  plane and the  $\hat{z}$  axis.

### Mueller Matrix Formulation of Reflection Coefficient

Using the result in Equation (3.36), Tsang et al. derived a reflection coefficient matrix to relate the scattered and incident Stokes vectors. We have

$$\mathbf{I}(\hat{\mathbf{k}}_s) = \mathbf{R}(\hat{\mathbf{k}}_s|\hat{\mathbf{k}}_i)\mathbf{I}(\hat{\mathbf{k}}_i) \quad (3.37)$$

where the Mueller matrix  $\mathbf{R}$  is

$$\mathbf{R}(\hat{\mathbf{k}}_s|\hat{\mathbf{k}}_i) = \frac{1}{\cos \theta_s} \frac{|\bar{\mathbf{k}}_{1d}|^4}{8\pi s^2 |\hat{\mathbf{k}}_i \times \hat{\mathbf{k}}_s|^4 (\bar{\mathbf{k}}_{1d} \cdot \hat{\mathbf{n}})^4} \exp \left[ -\frac{|\bar{\mathbf{k}}_{1d}|^2}{2s^2 (\bar{\mathbf{k}}_{1d} \cdot \hat{\mathbf{n}})^2} \right] \mathbf{C} \quad (3.38)$$

in which

$$\bar{\mathbf{k}}_{1d} = \hat{\mathbf{k}}_i - \hat{\mathbf{k}}_s = 2\hat{\mathbf{n}}(\hat{\mathbf{n}} \cdot \hat{\mathbf{k}}_i) \quad (3.39)$$

$$\bar{\mathbf{k}}_{1d} = \bar{\mathbf{k}}_{1d} - \hat{\mathbf{n}}(\bar{\mathbf{k}}_{1d} \cdot \hat{\mathbf{n}}) \quad (3.40)$$

and

$$\mathbf{C} = \begin{bmatrix} \langle f_{hh} f_{hh}^* \rangle & \langle f_{hv} f_{hv}^* \rangle & \text{Re} \langle f_{hv} f_{hh}^* \rangle & -\text{Im} \langle f_{hv} f_{hh}^* \rangle \\ \langle f_{vh} f_{vh}^* \rangle & \langle f_{vv} f_{vv}^* \rangle & \text{Re} \langle f_{vv} f_{vh}^* \rangle & -\text{Im} \langle f_{vv} f_{vh}^* \rangle \\ 2\text{Re} \langle f_{vh} f_{hh}^* \rangle & 2\text{Re} \langle f_{vv} f_{hv}^* \rangle & \text{Re} \langle f_{vv} f_{hh}^* + f_{vh} f_{hv}^* \rangle & -\text{Im} \langle f_{vv} f_{hh}^* - f_{vh} f_{hv}^* \rangle \\ 2\text{Im} \langle f_{vh} f_{hh}^* \rangle & 2\text{Im} \langle f_{vv} f_{hv}^* \rangle & \text{Im} \langle f_{vv} f_{hh}^* + f_{vh} f_{hv}^* \rangle & \text{Re} \langle f_{vv} f_{hh}^* - f_{vh} f_{hv}^* \rangle \end{bmatrix}$$

In this result  $f_{hh}$ ,  $f_{vv}$ ,  $f_{hv}$ , and  $f_{vh}$  describe couplings among horizontal and vertical polarizations

$$f_{hh} = (\hat{\mathbf{v}}_s \cdot \hat{\mathbf{k}}_i)(\hat{\mathbf{v}}_i \cdot \hat{\mathbf{k}}_s)R_h + (\hat{\mathbf{h}}_s \cdot \hat{\mathbf{k}}_i)(\hat{\mathbf{h}}_i \cdot \hat{\mathbf{k}}_s)R_v \quad (3.41)$$

$$f_{vv} = (\hat{\mathbf{h}}_s \cdot \hat{\mathbf{k}}_i)(\hat{\mathbf{h}}_i \cdot \hat{\mathbf{k}}_s)R_h + (\hat{\mathbf{v}}_s \cdot \hat{\mathbf{k}}_i)(\hat{\mathbf{v}}_i \cdot \hat{\mathbf{k}}_s)R_v \quad (3.42)$$

$$f_{hv} = (\hat{\mathbf{v}}_s \cdot \hat{\mathbf{k}}_i)(\hat{\mathbf{h}}_i \cdot \hat{\mathbf{k}}_s)R_h - (\hat{\mathbf{h}}_s \cdot \hat{\mathbf{k}}_i)(\hat{\mathbf{v}}_i \cdot \hat{\mathbf{k}}_s)R_v \quad (3.43)$$

$$f_{vh} = (\hat{\mathbf{h}}_s \cdot \hat{\mathbf{k}}_i)(\hat{\mathbf{v}}_i \cdot \hat{\mathbf{k}}_s)R_h - (\hat{\mathbf{v}}_s \cdot \hat{\mathbf{k}}_i)(\hat{\mathbf{h}}_i \cdot \hat{\mathbf{k}}_s)R_v \quad (3.44)$$

In these expressions  $\hat{\mathbf{v}}$  and  $\hat{\mathbf{h}}$  are unit vectors in the vertical and horizontal directions with respect to the plane of incidence (see Equations (2.1) and (2.2)).

### 3.3.2 Geometrical Optics Model

A semi-empirical approach to geometrical optics rough surface scattering was developed by Torrance and Sparrow [43]. The rough surface is modeled as a composition of planar facets with random orientations. The facets are assumed much larger than the wavelength, and the geometrical optics (specular) approximation is employed to model scattering. The GO formulation contains two principal terms: a “specular lobe” term and a diffuse term. The “specular lobe” comprises multiple specular reflections from small facets that happen to be oriented as required by the incident and observation directions. Clearly, the specular lobe is a function of the surface slope distribution. The diffuse term, which is caused by internal scattering beneath the reflecting surface, is invariant to incident and scattering angles.

This section describes the derivation of specular and diffuse terms. For Gaussian surface statistics the specular lobe in the GO model shows characteristics similar to the incoherent scattering component arising in the PO model.

#### Specular Lobe of GO Model

The GO specular term is derived by assuming that the surface facet’s tilt angle  $\psi$  (measured with respect to  $\hat{\mathbf{z}}$ ) has a probability density function  $p(\psi)$  and by defining the reflectivity with a Fresnel reflectance  $F(\theta'_i, m^2)$ , which is determined by the dielectric constant  $m^2$  and the projection of  $\psi$  on the incident plane  $\theta'_i$  [43]. Using the BRDF definition given in Equation (2.24), we have the BRDF representation for the

GO specular lobe

$$\mathcal{F}_s(\hat{\mathbf{k}}_s|\hat{\mathbf{k}}_i) = \frac{F(\theta'_i, m^2)}{4\pi \cos \theta_s} p(\psi) \quad (3.45)$$

The distribution of the surface normal vector is found [42] by assuming the random surface slope is Gaussian distributed.

$$p(\psi) \propto \frac{1}{4(\sigma/\ell)^2 \cos^4 \psi} \exp \left\{ -\frac{\tan^2 \psi}{4(\sigma/\ell)^2} \right\} \quad (3.46)$$

where angle  $\psi$  is the local incident angle  $\theta'_i$ . The following relations are evident from simple geometry

$$\tan^2 \psi = \frac{|\bar{\mathbf{k}}_{1dt}|^2}{(\mathbf{k}_{1d} \cdot \hat{\mathbf{n}})^2} \quad (3.47)$$

$$\cos^4 \psi = \frac{|\bar{\mathbf{k}}_{1d}|^4}{(\bar{\mathbf{k}}_{1d} \cdot \hat{\mathbf{n}})^4} \quad (3.48)$$

and facilitate comparison with Equation (3.38).

The expressions for Fresnel reflectance  $F$  are given in [69] as a linear combination of perpendicular and parallel Fresnel reflectances, which are actually the squared magnitudes of the horizontal and vertical Fresnel reflection coefficients.

$$F_{\perp} = |R_h|^2 \quad (3.49)$$

$$F_{\parallel} = |R_v|^2 \quad (3.50)$$

A quick check can be performed by assuming a locally-flat surface ( $\theta'_i=0$ ). Substituting Equations (3.46), (3.47), and (3.48) into Equation (3.45) yields a BRDF expression similar to Equation (3.38) in the PO model, which only includes the incoherent return. This finding is not surprising, since we have assumed similar wavelength restrictions and used Gaussian distributions to describe the rough surface (the surface height in PO and the slope in GO). Although the specular lobe expression presented

above does not include a polarization dependence, a polarization sensitive expression for the reflection coefficients was developed by Wolff [47] using the GO model. Note that the self-scattering term  $G$ , which corrects for shadowing and multiple-scattering near grazing angles and was described in Section 2.5.5, should be coupled with results of the above derivation.

### Diffuse Scattering of GO Model

To model multiple scattering occurring below the surface, Torrance and Sparrow introduced a diffuse term with a Lambertian behavior. The term is invariant to the direction of incident flux, and the scattered energy is equally distributed in all directions. The diffuse component is especially important when the scattering angle is far from the specular direction. Because no analytical models are available to characterize non-Lambertian diffuse scattering, most diffuse models, including the one presented here, use a Lambertian model as described in Section 2.5.2.

Using a Mueller matrix representation similar to the one presented in Equation (2.35), we can define a matrix for a diffuse scatterer with a certain degree of depolarization as

$$\mathbf{D} = \frac{1}{2\pi} \begin{bmatrix} \rho_{dc} & \rho_{dx} & 0 & 0 \\ \rho_{dx} & \rho_{dc} & 0 & 0 \\ 0 & 0 & 0 & 0 \\ 0 & 0 & 0 & 0 \end{bmatrix} \quad (3.51)$$

where  $\rho_{dc}$  and  $\rho_{dx}$  are diffuse albedos for co-polarized and cross-polarized scattering, which are scalars ranging between one and zero.

### 3.3.3 Comparison of PO and GO Models

The above derivations show that the PO and GO approaches, which start from different perspectives of rough surface scattering, end up with similar representations

for the “specular lobe”. Below we summarize the key assumptions made in the GO and PO models.

In general, the PO approach is more rigorous, since it is based on a coherent analysis of the fields. As a result, the PO method is applicable to very smooth and very rough surfaces [44]. In contrast, the GO approach is based on an incoherent sum of facet contributions from the outset, and is only valid for relatively rough surfaces that have a surface height standard deviation ( $\sigma$ ) that is large compared to the incident wavelength.

Beckmann decomposes scattered fields into “coherent” and “incoherent” terms. The coherent reflection comprises the specular ray reflected from a smooth surface. The incoherent reflection, referred to here as the specular lobe, accounts for scattering from relatively rough surfaces. These two terms dominate in different ranges of surface roughness. The geometrical optics limit is applied to the PO model in order to evaluate the integral arising in the Kirchhoff approximation [18]. As a result, there is no coherent term in our PO formulation, since no surface is perfectly smooth for an infinitesimal wavelength. Therefore, the BRDF formulation developed here is only valid for relatively rough surfaces ( $\sigma \gg \lambda$ ), which is the same condition imposed on the GO model.

Another key assumption about the surface geometry made in the PO approach is the tangent plane approximation, which requires the radius of surface curvature to be large compared to the incident wavelength. This assumption simplifies the evaluation of a required integral, but it also imposes a limit on the surface roughness. Specifically, the surface should have no edges. This criterion imposes a lower limit on the correlation distance ( $\ell$ ) for Gaussian-distributed surface heights.

Several assumptions are made for both the PO and GO models that lead to similar BRDF formulations. First, the sources are assumed to be in the far-field. Therefore, we can assume a planar incident wave in the PO model while an equivalent incident ray is used in the GO model. Second, Gaussian surface statistics are invoked (for the surface height distributions in PO and for surface slope in GO) are assumed to be Gaussian for both models. This assumption leads to a slope distribution that is a function of the local incident angle ( $\theta'_i$ ) and the surface roughness parameter ( $\sigma/\ell$ ).

In addition to the above differences, the GO approach involves two semi-empirical factors not used in the PO approach. The GO model introduces a “geometric attenuation function” to account for self-shadowing so that the model is applicable in near-grazing regimes. The diffuse term used in the GO model helps to account for internal scattering by the media.

### 3.3.4 A Proposed Polarimetric Mueller Matrix

A polarimetric Mueller matrix can be derived by combining features from the PO and GO approaches. It contains a broad specular lobe due to rough surface scattering and a Lambertian term that accounts for internal scattering. A self-shadowing correction term is adopted to extend the use of the proposed model into grazing regimes. Assumptions stated in the previous section define the limitations of the proposed model. It is valid for relatively rough surfaces without edges. Also the incident wavelength should be small compared to the variation in surface heights.

The proposed matrix combines three elements as follows:

$$\mathbf{M} = \mathbf{R}(\hat{\mathbf{k}}_s|\hat{\mathbf{k}}_i)G(\hat{\mathbf{k}}_s|\hat{\mathbf{k}}_i) + \mathbf{D} \quad (3.52)$$

The component  $\mathbf{R}$  was given in Equation (3.38). It includes scalar factors that depend on the surface roughness and source-target-viewer geometry, as well as a matrix factor that embodies the polarization dependence. Detailed descriptions of these components can be found in Equations (3.38) through (3.44).

As noted above,  $\mathbf{R}$  is derived by taking the geometrical optics limit in the PO formulation. As a result, the PO formulation becomes very similar to the GO form, which unfortunately includes a non-physical response at grazing angles. The factor  $G$  is the self-occlusion or geometric attenuation function described previously in Equation (2.41). This function provides a needed correction when either the source or viewing angle is near grazing.

The component  $\mathbf{D}$ , which can be found in Equation (3.51), accounts for diffuse scattering as a result of internal scattering beneath the reflecting surfaces. Polarimetric diffuse albedos can have a great influence on radiometric signatures. Due to a lack of measurement data, in this work those albedos are estimated empirically by comparing with measurements in the off-specular regimes, which is presented in Section 3.3.6.

### 3.3.5 Sample Rough-Surface BRDFs

We now use the model presented in Equation (3.52) to simulate the BRDFs of some rough surfaces and thereby illustrate some characteristics of the model. The results shown are the sum of the first two components ( $I_h$  and  $I_v$ ) of the scattering Stokes vector  $\mathbf{I}(\hat{\mathbf{k}}_s)$ , which is found by multiplying the Mueller matrix  $\mathbf{M}$  by an unpolarized incident Stokes vector  $\mathbf{I}(\hat{\mathbf{k}}_i) = [1/2 \ 1/2 \ 0 \ 0]^T$ .

Figure 3.23 uses facet color to illustrate the BRDF relative magnitude (in dB) over the upper hemisphere. The roughness parameter  $s^2 = 2(\sigma/\ell)^2$  was set to 0.01 in Figure 3.23, and the incident zenith angle was  $22^\circ$ . The refractive index ( $m$ ) was 1.5. A reflectance lobe is observed near the specular direction. A small, constant off-specular return is present elsewhere due to the diffuse scattering component. Based on the value of  $s^2$ , one can categorize this surface as moderately rough.

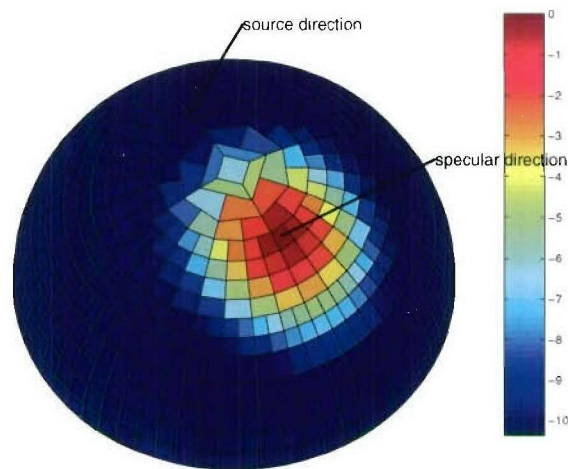


Figure 3.23: Moderately rough surface BRDF ( $\theta_i = 22^\circ$ ,  $s^2 = 0.01$ ,  $m = 1.5$ ,  $\rho_{dc}=0.01$ ,  $\rho_{dx} = 0.005$ ).

Altering the surface roughness parameter can produce dramatic changes in the BRDF. The value of  $s^2$  was reduced to 0.0025 in Figure 3.24(a), which makes the surface more smooth and the specular lobe much more compact than observed in Figure 3.23. The reflectance magnitude decreases significantly when the observer moves away from the specular direction. Conversely, if we increase  $s^2$  to 0.05 as shown

in Figure 3.24(b), the specular lobe becomes much broader and one even observes a substantial reflectance in the back-scattering direction.

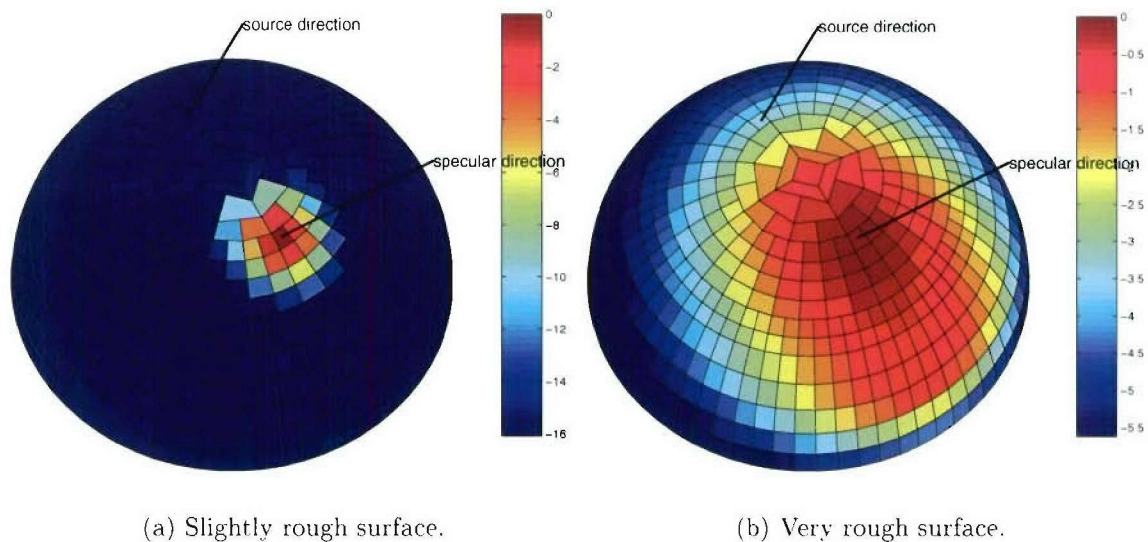


Figure 3.24: BRDFs of a slightly rough surface ( $s^2 = 0.0025$ ,  $m = 1.5$ ,  $\rho_{dc}=0.01$ ,  $\rho_{dx} = 0.005$ ) and a very rough surface ( $s^2 = 0.05$ ,  $m = 1.5$ ,  $\rho_{dc}=0.0075$ ,  $\rho_{dx} = 0.0037$ ) at  $\theta_i = 22^\circ$ .

Next, consider the model's dependence on the incident zenith angle  $\theta_i$ . In Figure 3.25(a), which was computed for  $s^2=0.0025$ , we observe that (as expected) the effect of moving the direction of incidence causes the scattered lobe to shift toward the (new) specular direction. However, for the rougher surface ( $s^2=0.05$ ) shown in Figure 3.25(b), the peak of the scattered signal significantly deviates from the specular direction. In this case, the BRDF maximum appears about  $20^\circ$  below the specular angle. The shift of the maximum scattering direction away from the specular direction for near grazing incidence has been observed in measurements [43]. Because the

effective surface height variance decreases in proportion to the cosine of the observer's zenith angle, a surface looks smoother near grazing so that the specular lobe of the BRDF becomes more compact and tends to shift toward grazing when a large incident angle is present. This phenomenon becomes more apparent for a rougher surface.

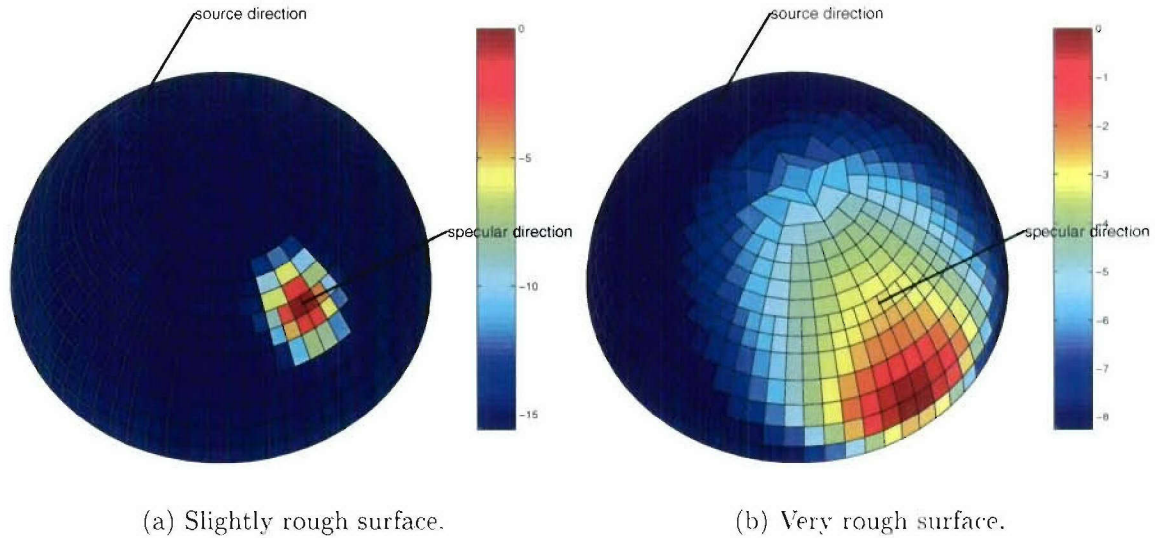


Figure 3.25: BRDFs of a slightly rough surface ( $s^2 = 0.0025$ ,  $m = 1.5$ ,  $\rho_{dc}=0.01$ ,  $\rho_{dx} = 0.005$ ) and a very rough surface ( $s^2 = 0.05$ ,  $m = 1.5$ ,  $\rho_{dc}=0.0075$ ,  $\rho_{dx} = 0.0037$ ) at  $\theta_i = 42^\circ$ .

The effect of the geometric attenuation function  $G$  described in Equation (2.41) is revealed by removing  $G$  from the model. Figure 3.26 shows the result of this change. Comparing Figure 3.26 with Figure 3.25(b) shows that  $G$  tends to shift the maximum away from grazing.

The foregoing simulations used a substantial diffuse component. Figure 3.27 shows the result of removing the diffuse component (a very small amount of diffuse albedo is still assigned to restrict the dynamic range of the plots). The result shows a sharp,

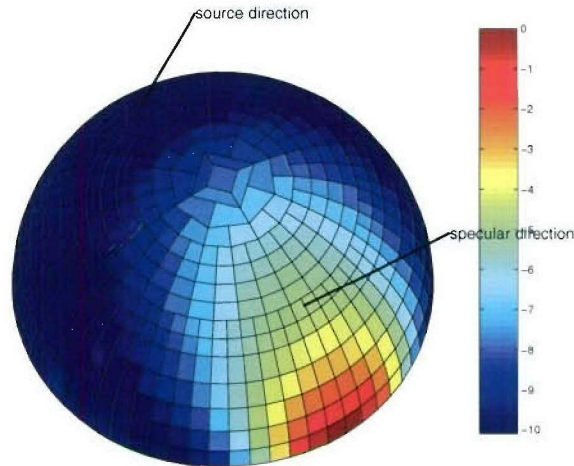


Figure 3.26: Very rough surface BRDF without the self-shadowing correction  $G$  ( $\theta_i = 42^\circ$ ,  $s^2 = 0.05$ ,  $m = 1.5$ ,  $\rho_{dc} = 0.0075$ ,  $\rho_{dx} = 0.0037$ ).

significant drop in scattering intensity as the observation angle moves away from the specular direction.

### 3.3.6 Comparison to Experimental BRDF Data

An extensive body of experimental measurements on rough surface BRDFs was collected by Willow Run Laboratories on a variety of materials, some of which are relevant to landmine detection [29, 34]. The materials examined included various types of painted metal, wood, sand, concrete and other natural clutter. In most experiments, four of the modified Mueller matrix entries were recorded, including the co-polarized reflectance for horizontal and vertical polarizations and the cross-polarized analogs (i.e.,  $\mathcal{F}_{hh}$ ,  $\mathcal{F}_{hv}$ ,  $\mathcal{F}_{vh}$ , and  $\mathcal{F}_{vv}$ ). Figures 3.28 (a) and (b) show the polarimetric reflectance of an aluminum surface with green paint and zinc chromate coatings. Results for the incidence angles  $20^\circ$  and  $60^\circ$  are shown. Using the BRDF

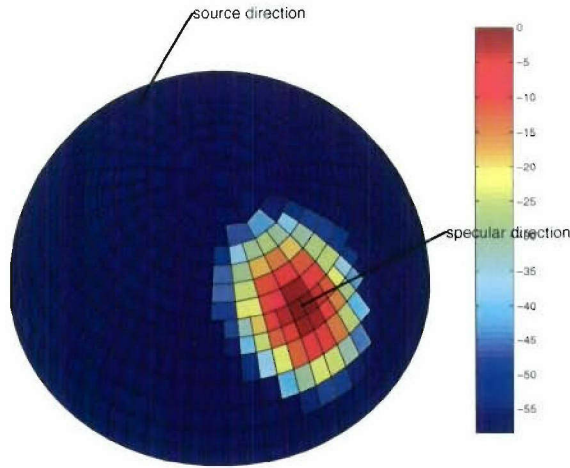


Figure 3.27: Slightly rough surface BRDF without the diffuse term ( $\theta_i = 42^\circ$ ,  $s^2 = 0.0025$ ,  $m = 1.5$ ,  $\rho_{dc} = 10^{-6}$ ,  $\rho_{dx} = 0.5 \times 10^{-6}$ ).

model described above, simulations were performed for user-defined surface parameters that included roughness  $s^2$ , refractive index  $m$ , and values for co- and cross-polarized albedos ( $\rho_{dc}$  and  $\rho_{dx}$ ). The simulated results in Figures 3.28 (c) and (d) show the computed reflectance curves. The results are generally in good agreement, although some discrepancies exist. Specific issues are as follows:

- The measured and modeled BRDFs are similar near the specular direction, but near backscattering the measurements show stronger reflectance, suggesting that possibly the diffuse component or multiple scattering components are under estimated.
- The ratios of reflectance for the co-polarized components are in good agreement around the specular lobe.

- The null in  $\mathcal{F}_{vv}$  due to total reflection around the Brewster angle is observed in both (b) and (d) of Figure 3.28<sup>10</sup>.
- For larger incident zenith angles, shifts in the angle of peak reflectance appear in both Figures 3.28 (b) and (d).

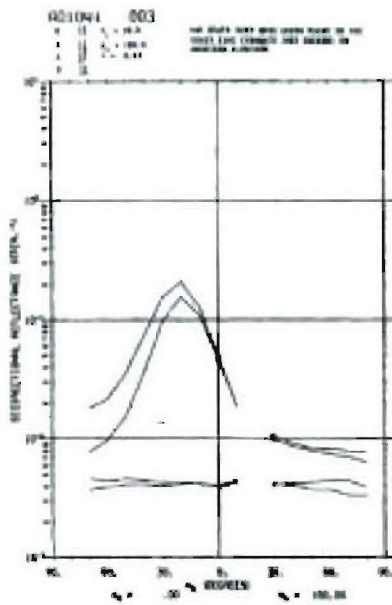
The incident wavelength can have a strong effect on the BRDF, since all of the surface features must be large compared to that wavelength. Figures 3.29 (a) and (b)<sup>11</sup> show the reflectance of a steel surface with green paint for visible ( $0.63 \mu\text{m}$ ) and LWIR ( $10.6 \mu\text{m}$ ) illumination. As expected, the BRDF shows a sharp lobe with its peak located around the specular direction for LWIR illumination, while the specular lobe width is somewhat wider for visible illumination.

Parameters were again selected for the BRDF model ( $s^2 = 0.015$ ,  $m = 1.5$ ) to reproduce the measured reflectance curves of painted steel at LWIR as shown in Figure 3.29 (d). Using the argument presented in Section 3.3.1 we rescaled the roughness parameter  $s^2$  according to the ratio of the LWIR and visible wavelengths. The derived simulated co-polarized reflectance values  $\mathcal{F}_{hh}$  and  $\mathcal{F}_{vv}$  agree with the experimental data both in peak magnitude and shape. Nonetheless, the BRDF model again fails to reproduce the measured behavior near backscattering.

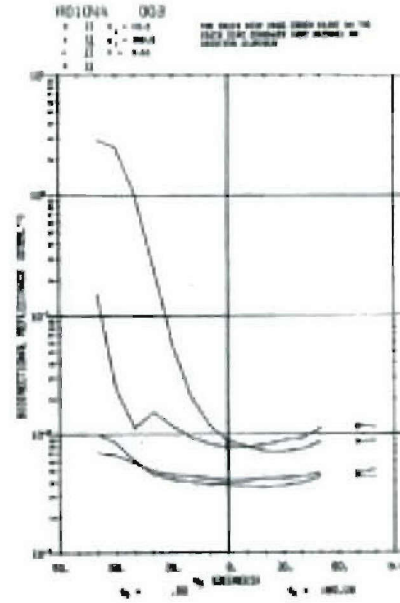
Finally, we consider the reflectance of material with a large roughness. Figure 3.30 shows the reflectance of a concrete surface for  $\theta_i = 20^\circ$  and  $\theta_i = 60^\circ$ . As the reflectance curves suggest, the concrete surface acts like a diffuse reflector. The measured BRDFs have small, near-constant values over a broad range of viewing angles. The surface

<sup>10</sup>The Brewster angle at  $53^\circ$  is clear in Figure 3.28 (d), while only a dip is observed in Figure 3.28 (b). The discrepancy may be due to low angular resolution in the measurements ( $10^\circ$  apart).

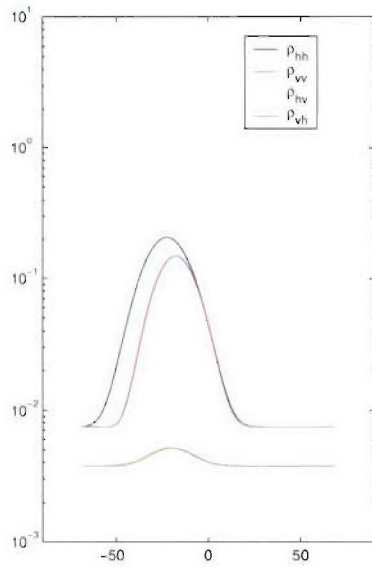
<sup>11</sup>Only  $\mathcal{F}_{vv}$  measurement are available in the LWIR case.



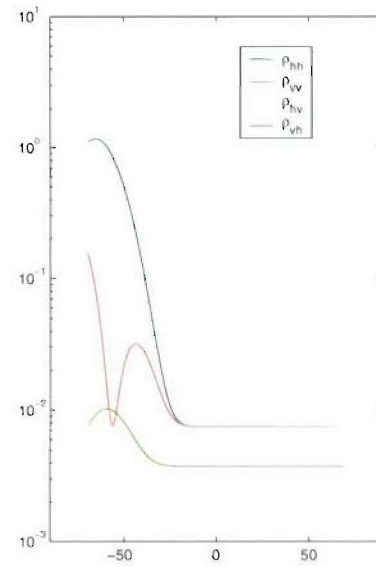
(a)  $\theta_i = 20^\circ$ .



(b)  $\theta_i = 60^\circ$ .

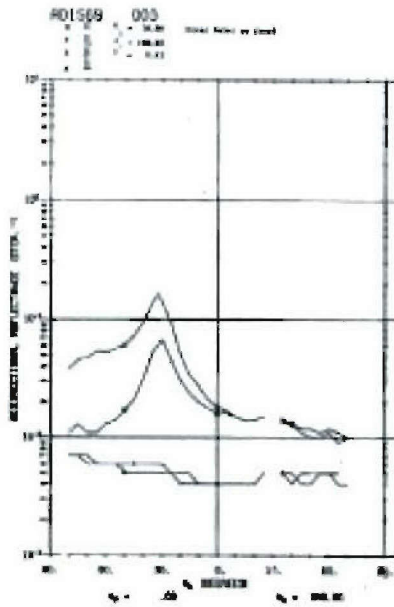


(c)  $\theta_i = 20^\circ$ .

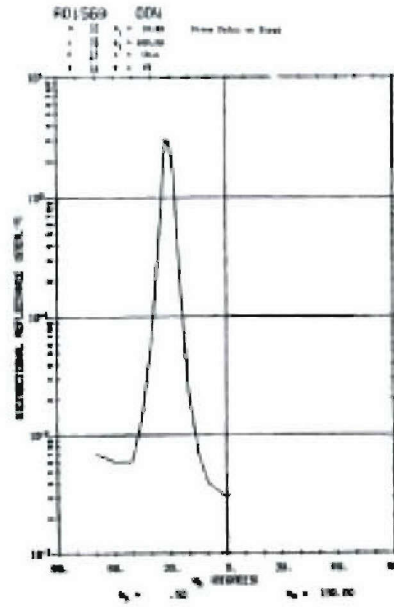


(d)  $\theta_i = 60^\circ$ .

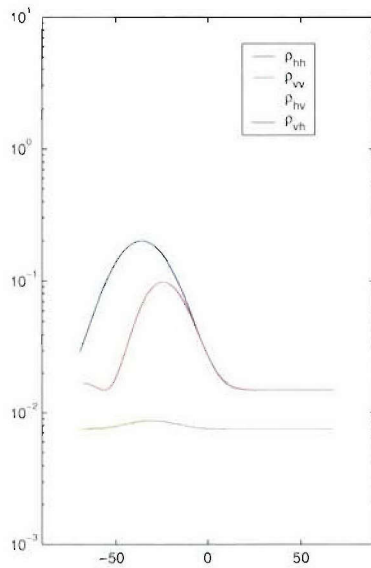
Figure 3.28: Comparison of measured and modeled BRDF results in the incident plane. The measured surface is aluminum with green paint and zinc chromate coatings. The illumination is  $0.63 \mu\text{m}$  wavelength. The simulated surface has the parameters  $s^2 = 0.01$ ,  $m = 1.5$ . Co- and cross-polarized diffuse albedos are 0.015 and 0.0075.



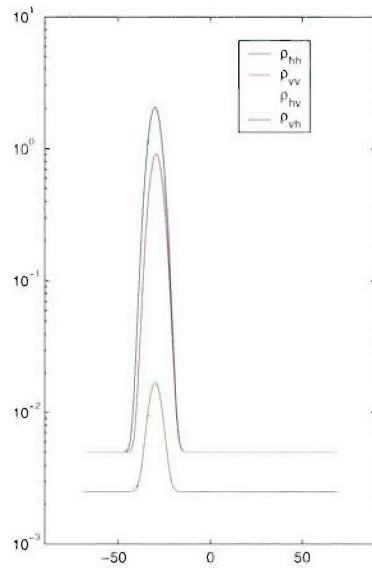
(a)  $\theta_i = 30^\circ$ ,  $\lambda = 0.63\mu m$ .



(b)  $\theta_i = 30^\circ$ ,  $\lambda = 10.6\mu m$ .



(c)  $\theta_i = 30^\circ$ ,  $s^2 = 0.0009$ .



(d)  $\theta_i = 30^\circ$ ,  $s^2 = 0.015$ .

Figure 3.29: Comparison of measured and modeled BRDF results in the incident plane. The measured surface is metal with green paint at  $0.63\mu m$  and  $10.6\mu m$ . The simulated surface has the parameters  $m = 1.5$ ,  $s^2=0.015$  and  $0.0009$ . Co- and cross-polarized diffuse albedos are 0.03 and 0.015 for  $0.63\mu m$  and 0.01 and 0.005 for  $10.6\mu m$ .

is strongly depolarizing, since the cross-polarization terms  $\mathcal{F}_{hv}$  and  $\mathcal{F}_{vh}$  are of the same order as  $\mathcal{F}_{hh}$  and  $\mathcal{F}_{vv}$ . The results suggest a good fit to the angle-independent Lambertian model assumed in the proposed BRDF model.

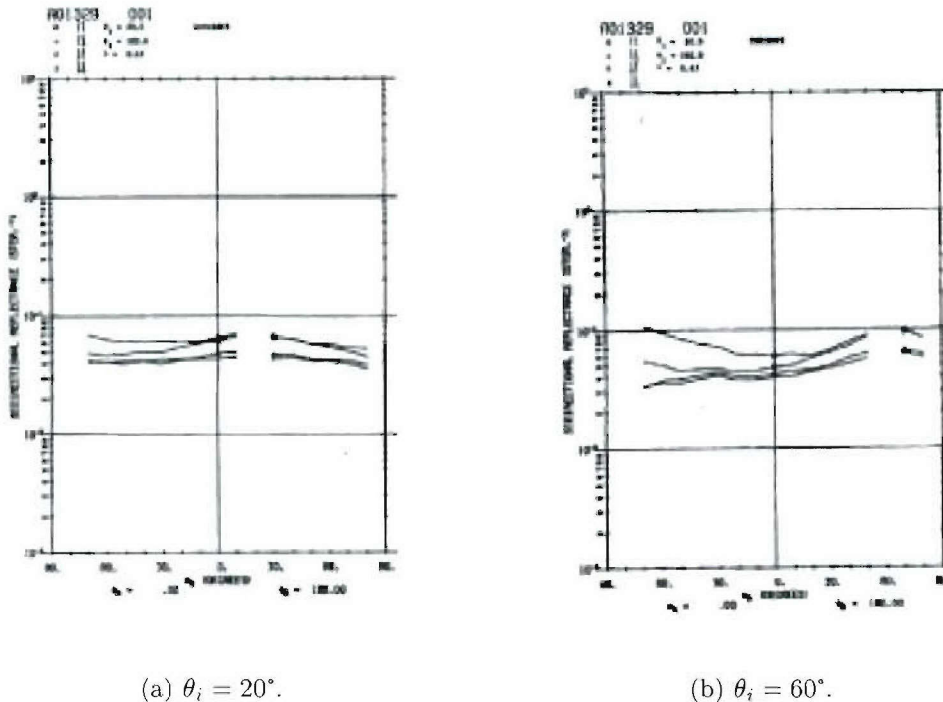


Figure 3.30: Measured BRDF results in the incident plane. The measured surface is concrete. The illumination is  $0.63 \mu\text{m}$  wavelength. The corresponding simulations (not shown) are simply constants.

### 3.3.7 Implementation of Emissivity Model

We stated in Section 2.6 that the directional emissivity of a surface can be found via spatial integration of its BRDF using the reciprocity principle and the law of energy conservation. For polarimetric sensors, the emissivities in the horizontal and

vertical directions are computed separately as

$$\mathcal{E}_h(\hat{\mathbf{k}}_i) = 1 - \int_0^{\pi/2} d\theta_s \sin \theta_s \int_0^{2\pi} d\phi_s [\mathcal{F}_{hh}(\hat{\mathbf{k}}_i, \hat{\mathbf{k}}_s) + \mathcal{F}_{vh}(\hat{\mathbf{k}}_i, \hat{\mathbf{k}}_s)] \quad (3.53)$$

$$\mathcal{E}_v(\hat{\mathbf{k}}_i) = 1 - \int_0^{\pi/2} d\theta_s \sin \theta_s \int_0^{2\pi} d\phi_s [\mathcal{F}_{vv}(\hat{\mathbf{k}}_i, \hat{\mathbf{k}}_s) + \mathcal{F}_{hv}(\hat{\mathbf{k}}_i, \hat{\mathbf{k}}_s)] \quad (3.54)$$

where  $\mathcal{F}_{hh}$ ,  $\mathcal{F}_{hv}$ ,  $\mathcal{F}_{vh}$ , and  $\mathcal{F}_{vv}$  are polarimetric BRDFs found as Mueller matrix entries ( $M_{11}$ ,  $M_{12}$ ,  $M_{21}$ , and  $M_{22}$ ) in the proposed model.

When the angular dependence of the BRDF is mild (certainly true for relatively rough surfaces), the spatial integral can be approximated via numerical integration, and Equations (3.53) and (3.54) become

$$\mathcal{E}_h(\hat{\mathbf{k}}_i) \approx 1 - \sum_m \Omega_m \cdot [\mathcal{F}_{hh}(\hat{\mathbf{k}}_i, \hat{\mathbf{k}}_s(m)) + \mathcal{F}_{vh}(\hat{\mathbf{k}}_i, \hat{\mathbf{k}}_s(m))] \quad (3.55)$$

$$\mathcal{E}_v(\hat{\mathbf{k}}_i) \approx 1 - \sum_m \Omega_m \cdot [\mathcal{F}_{vv}(\hat{\mathbf{k}}_i, \hat{\mathbf{k}}_s(m)) + \mathcal{F}_{hv}(\hat{\mathbf{k}}_i, \hat{\mathbf{k}}_s(m))] \quad (3.56)$$

in which  $\Omega_m$  is an element of solid angle and  $\hat{\mathbf{k}}_s(m)$  is a unit vector in its direction. A fine sampling of  $\Omega$  is used near the specular direction of the incident angle. Reflectances of nodes on the mesh are computed and summed to yield the emissivity used in Equations (3.55) and (3.56). A bigger mesh is needed for a rougher surface since its specular lobe is likely to be larger. A finer mesh is required for large incident angles because the lobe near grazing tends to be narrow with large gradients.

The emissivity vector is combined with the blackbody emittance of the surface to form the surface emission Stokes vector.

$$\mathbf{I}_{\mathcal{E}}(\theta_r) = \begin{bmatrix} I_h \\ I_v \\ U \\ V \end{bmatrix} = \begin{bmatrix} \mathcal{E}_h \\ \mathcal{E}_v \\ U_{\mathcal{E}} \\ V_{\mathcal{E}} \end{bmatrix} \cdot L_{BB} = \mathcal{E}(\theta_r) \cdot L_{BB} \quad (3.57)$$

The  $U$  and  $V$  components can be computed using Equations (2.51) and (2.52) and the numerical integration stated above, but for surfaces simulated in this work, their

values are nearly zero and are therefore neglected. Note that the dependence of emissivity on observation direction is represented by the elevation angle  $\theta_r$  only in Equation (3.57), because the surface roughness is assumed isotropic.

To better understand the emissivity implied by the BRDF model, emissivity profiles were computed for various surface properties. The diffuse component of the proposed BRDF model was ignored in these simulations, since its effect is trivial.

The refractive index affects the Fresnel reflection coefficients and, hence, the emissivity. Figure 3.31 plots the horizontal and vertical emissivity curves versus the observation (zenith) angle for a moderately rough surface ( $s^2=0.01$ ) and different refractive indices. The curves reveal that a lower refractive index results in less reflection and, hence, produces more emission. Also the effect of the Brewster angle is clearly visible for the vertical component, which is shown with a local maximum near  $50^\circ$ .

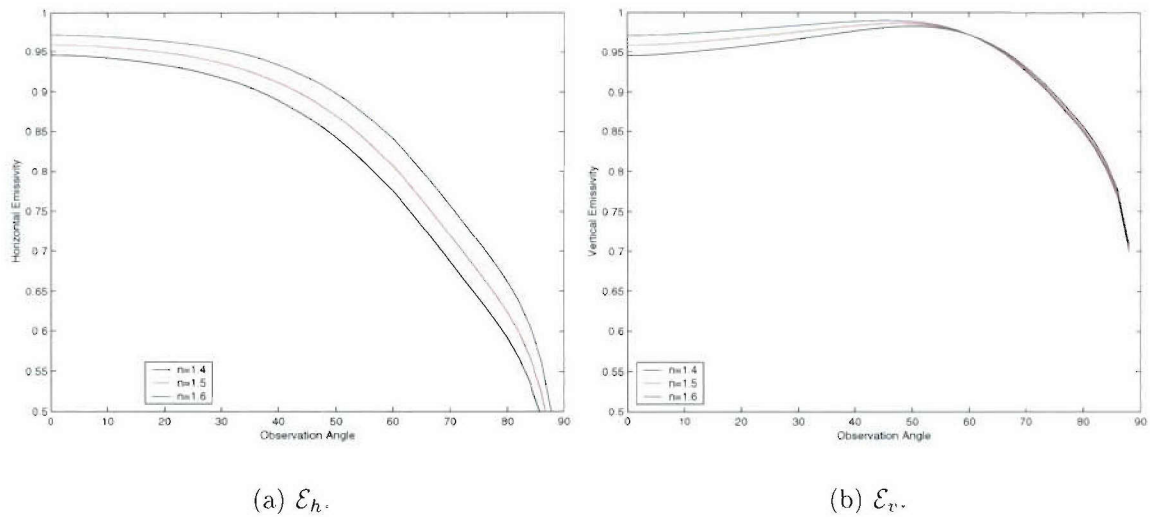


Figure 3.31: Horizontal and vertical emissivity for various refractive indices ( $s^2 = 0.01$ , no diffuse component).

Next, we examine in Figure 3.32 the effect of surface roughness on emissivity. The results show that as the roughness increases, the emissivity starts to drop at larger observation angles, and the effect of the Brewster angle becomes less apparent, which implies that emissions from rougher surfaces are less polarized.

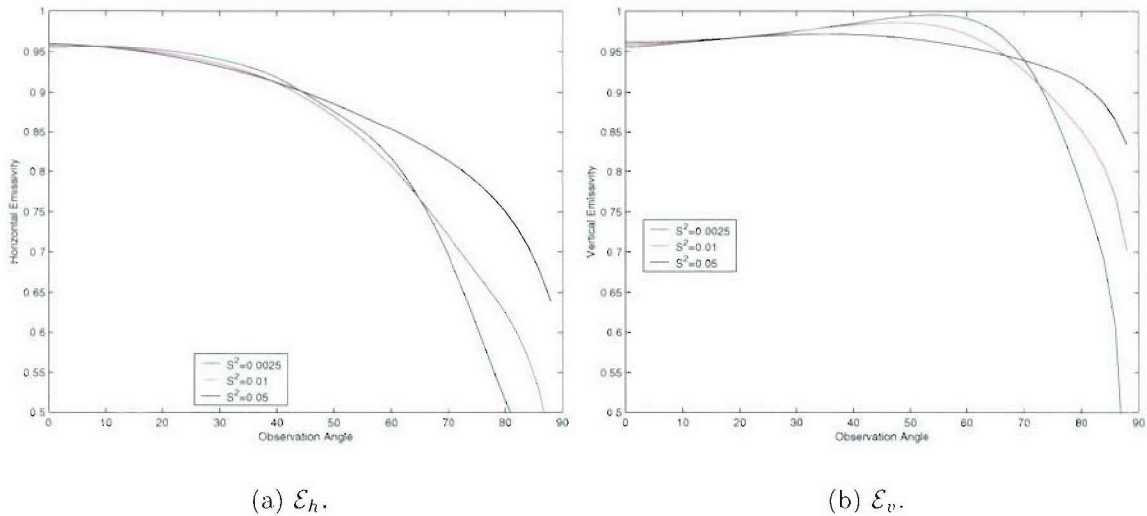


Figure 3.32: Horizontal and vertical emissivity for various surface roughnesses ( $m=1.5$ , no diffuse component).

The surface properties of the mine and soil were also simulated. The parameters used for these materials are within the ranges considered above. The contribution of the diffuse component is displayed in Figure 3.33. Little change is observed near nadir (less than 0.1), because the mine and soil are modeled as poor reflectors. The solid lines, which were computed with the diffuse component, are shifted downward because of Lambertian scattering. With incorporation of the diffuse component, the emissivities of the mine become comparable with those of the soil, because a slightly larger diffuse component was added to the mine's BRDF.

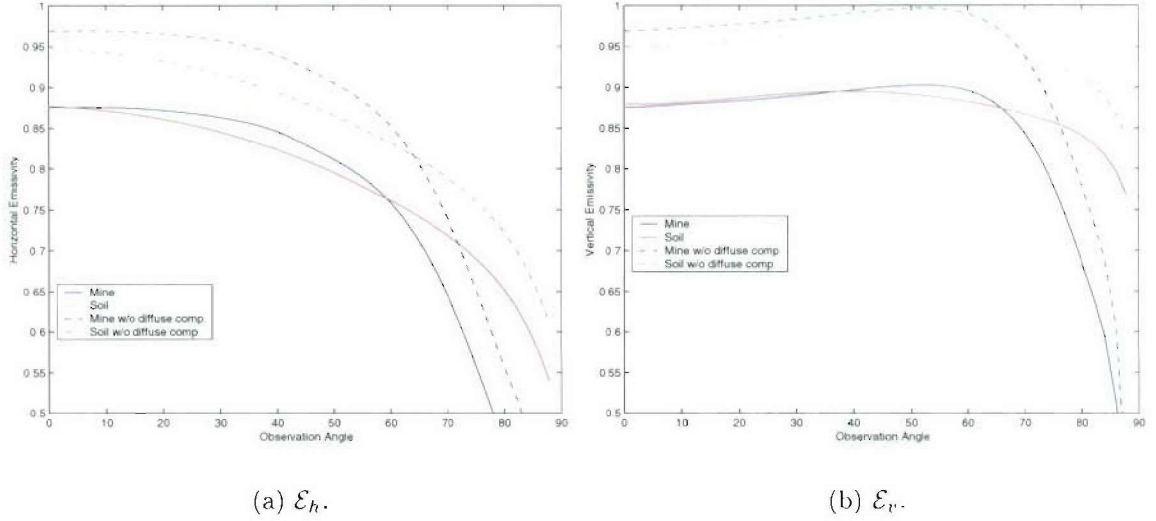


Figure 3.33: Horizontal and vertical emissivity of simulated mine and soil surfaces with and without the diffuse component (mine:  $s^2 = 0.0025$  and  $m=1.4$ ; soil:  $s^2 = 0.05$  and  $m=1.6$ ).

As indicated in Figure 3.33, the emissivity varies gradually as the observation angle changes. Therefore, in the radiometric model implementation the emissivity vector of desired observation angle is calculated on the fly by linearly interpolating a one-dimensional ( $\hat{\theta}_s$ ) emissivity profile<sup>12</sup>, which is computed off-line via the spatial integration of BRDF described in the beginning of this section. A spatial discretization like the sky mesh presented in Figure 3.17 is used to sample the BRDF. Solid angles  $\Omega_m$  associated with mesh facets are coupled with the BRDF and summed using Equation (3.55) and (3.56) to yield emissivities. This method saves computation time and is valid if the surface is isotropic and if the change in the BRDF is gradual.

<sup>12</sup>Profiles of horizontal and vertical emissivities of specified mine and soil surfaces are calculated every two degrees

## 3.4 Radiometric Model Construction

In this section we describe the integration of source models and surface scattering properties to produce a signature simulator. For reasons of computational efficiency, a ray tracing approach is used rather than a global illumination technique such as radiosity.

An overview of the radiometric model is presented in Section 3.4.1. Steps needed to initialize and execute the model are described. Key equations used to compute the radiance of individual components are given in Section 3.4.2.

### 3.4.1 Simulation Procedure

Figure 3.34 shows the processes and data streams important in simulation. The simulator performs three major functions: (1) setting up the model by defining the source-target-viewer geometry and target surface properties, (2) computing and summing the components of the radiometric signature, and (3) simulating the effect of the sensor. Implicit in this calculation is a loop over time and over all visible facets.

By far, the most computationally-intensive step is computing the received radiometric components. Five components are evaluated in the simulator as indicated in Figure 3.34 and their contributions are computed separately. The direct thermal emission and single-bounce solar reflection have been found to dominate the signatures of surface mines. These components are also easy to compute, since the transmission paths contain at most one scattering event. The remaining three components are far more difficult to compute, because they involve extended sources or multiple scattering events.

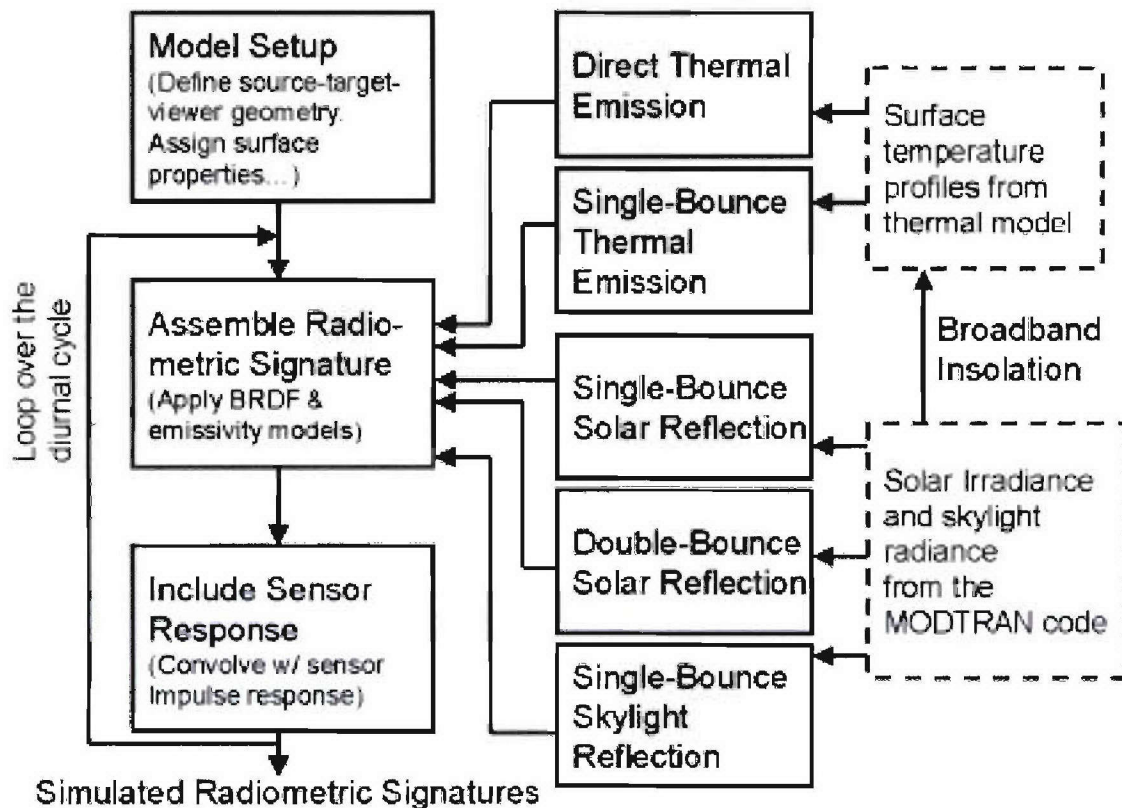


Figure 3.34: Block diagram of the activities and data sources used in generating radiometric mine signatures. The principle functions of the simulator appear in the left column. The radiometric components are given in the center column. The right column shows external data sources.

## Surface Temperature History

As indicated on the right of Figure 3.34, thermal model and the MODTRAN code provide radiometric source information. Those codes are run prior to the execution of the radiometric model.

Figure 3.35 illustrates the procedures used to compute the surface temperature history. The thermal model requires as input the thermal properties for all materials in the mine and soil, the date and the geolocation (latitude and longitude) of the mine, albedos for all visible surfaces in the solar band, and meteorological conditions such as the wind speed, humidity, and air temperature history. A mesh containing the mine and soil is created to define the computational space. Next, the mesh is refined near shadow boundaries and in other regions where high thermal gradients are expected (e.g., near the soil-air interface). Incident solar irradiances at each surface facet are computed for a 24 hour period with due consideration for surface shadowing. Using the above facet insolation and environmental conditions as inputs, the thermal model is run to convergence, and the surface temperature distribution for the final 24 hour segment is retained.

## Illumination Spatial Profiles and Thermal Histories

The incident radiance due to sunlight and skylight are computed using MODTRAN. Figure 3.36 shows the basic steps in this process. The time-varying illumination must be computed for a complete 24 hour period. The MODTRAN code requires an input file containing the solar zenith and azimuth angles and the atmosphere model (specified by the season, latitude, and environment parameters). To compute the skylight distribution, a hemispherical mesh that represents the sky is

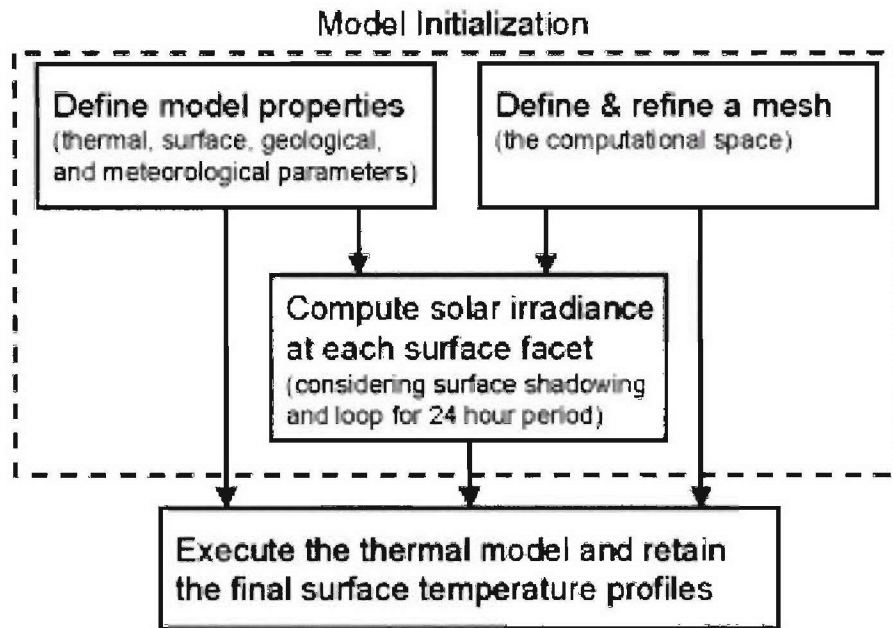


Figure 3.35: Block diagram of the procedures used in generating surface temperature profiles from the thermal model.

generated. The outputs of MODTRAN are the spectral insolation and the spectral skylight. We employ an integration over the sensor band to compute incident solar and skylight radiances for surface facets.

### Shadowing

In addition to the surface temperature history and illumination profiles, we also need to know which surface facets are visible to the sources and sensor to initialize the radiometric model. Visible surface determination is an important part of any radiometric simulation, and it is a critical component of this work. The basic procedure is well known and is documented in common textbooks [70]. In order to save computation time, the implementation used in this work is very basic, in that the

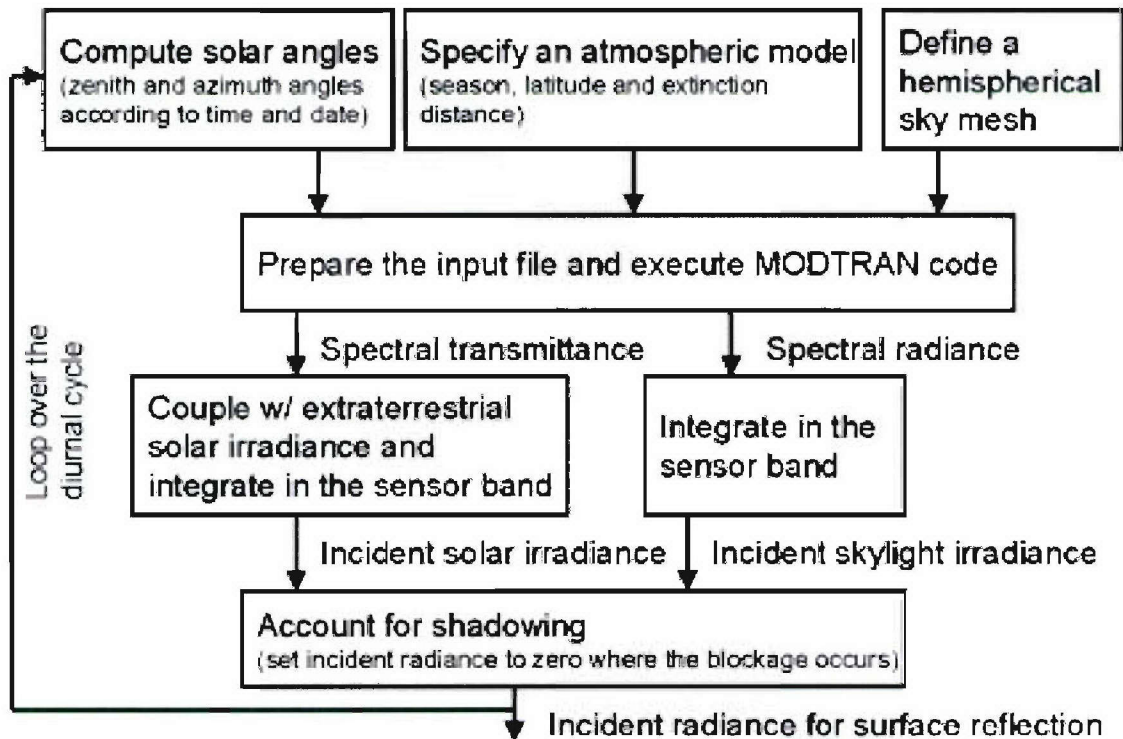


Figure 3.36: Block diagram of the procedures used in generating solar irradiance and skylight radiance from the MODTRAN code.

decision regarding facet visibility is made entirely on the basis of the facet centroid. That decision is applied to the entire facet. No allowance is made for partially visible facets.

A “visible facet” matrix and a corresponding “visible-facet projected solid angle” matrix (approximation of  $d\Omega_{i,m} \cos \theta_{i,m}$  in Equation (3.59)) are pre-computed using above approach to save computation time for higher-order components. For each observed point of the sensor, visibility tests are conducted by tracing rays emitted from the point to centroids of all facets (a total of 1686 facets for the LP\_B mine mesh simulated in this chapter). If the ray is not blocked by other facets, then the entry in the “visible facet” matrix is set to be “true” (1) and the projected solid angle is computed. The matrix is used when performing integration on extended sources, only radiances from visible facets are included. A similar “visible sky facet” matrix is computed to find visible sky mesh facets of observed points on the surface.

### Radiation Integral

A relation used throughout this work is the following integral, given previously as Equation (2.29)

$$\mathbf{I}_s(\hat{\mathbf{k}}_s, \mathbf{r}) = \int_{2\pi} d\Omega_i \cos \theta_i \mathbf{M}(\hat{\mathbf{k}}_s | \hat{\mathbf{k}}_i, \mathbf{r}) \cdot \mathbf{I}_i(\hat{\mathbf{k}}_i, \mathbf{r}) \quad (3.58)$$

in which  $\mathbf{I}_s(\hat{\mathbf{k}}_s, \mathbf{r})$  is the Stokes vector reflected from point  $\mathbf{r}$  in the direction  $\hat{\mathbf{k}}_s$ ,  $d\Omega_i \cos \theta_i$  is a differential projected solid angle in direction  $\hat{\mathbf{k}}_i$ , and  $\mathbf{I}_i(\hat{\mathbf{k}}_i, \mathbf{r})$  is the incident Stokes vector arriving at location  $\mathbf{r}$  along direction  $\hat{\mathbf{k}}_i$ . In general, this integral must be evaluated numerically. In this work, we make the assumption that  $\mathbf{M}(\hat{\mathbf{k}}_s | \hat{\mathbf{k}}_i, \mathbf{r})$  is constant over a facet. In addition, when  $\mathbf{I}_i(\hat{\mathbf{k}}_i, \mathbf{r})$  arrives from another

facet at position  $\mathbf{r}'$ , we assume that  $\mathbf{I}_i(\hat{\mathbf{k}}_i, \mathbf{r})$  is a constant over that facet. We have

$$\mathbf{I}_s(\hat{\mathbf{k}}_s, \mathbf{r}) \approx \sum_{\substack{\text{visible} \\ \text{facet } m}} \mathbf{M}(\hat{\mathbf{k}}_{s,m} | \hat{\mathbf{k}}_i, \mathbf{r}) \cdot \mathbf{I}_i(\hat{\mathbf{k}}_i, \mathbf{r}) \int_{\text{facet } m} d\Omega_{i,m} \cos \theta_{i,m} \quad (3.59)$$

The remaining integral over projected solid angle is closely related to the so-called “viewing factor” used in radiative heat transfer [71, Ch. 4]. A considerable amount of effort has been devoted to the evaluation of these quantities in closed form for special geometries. In the present work, however, quadrature has been used. The aforementioned facet-center based computation yields a fair approximation in projected solid angle for two well separated facets, but it fails for adjacent facets. A facet-refining algorithm is used to sub-divide nearby facets and recalculate projected solid angles. The refinement continues until the distance ( $|\mathbf{r}-\mathbf{r}'|$ ) is smaller than a preset threshold.

In performing this integration, it is often convenient to employ a facet-centered coordinate system for the integral. Ultimately, however, the local Stokes vector must be transformed to the sensor’s coordinate system. For a rotation of angle  $\psi$  about the viewing direction  $\hat{\mathbf{k}}_s$  the required transformation has been derived by Ishimaru [21, P. 36] and is given by

$$\mathbf{I}' = \mathbf{\Gamma} \mathbf{I} \quad (3.60)$$

$$\mathbf{\Gamma} = \begin{bmatrix} \cos^2 \psi & \sin^2 \psi & -1/2 \sin(2\psi) & 0 \\ \sin^2 \psi & \cos^2 \psi & 1/2 \sin(2\psi) & 0 \\ \sin(2\psi) & -\sin(2\psi) & \cos(2\psi) & 0 \\ 0 & 0 & 0 & 1 \end{bmatrix} \quad (3.61)$$

### 3.4.2 Derivation of Individual Components

In this section we derive the radiance received by the sensor from individual components. Each component is defined mathematically and its evaluation is discussed.

## Direct Thermal Emission

As noted above, the direct thermal emission is the easiest component to compute, because it involves no reflections. Furthermore, we make the assumption that there is no significant radiative exchange among facets. Hence, each “observed point” can be regarded as an isolated gray-body radiator.

The calculation of this component involves two steps which must be executed for each observed point  $\mathbf{r}$  (corresponding to pixel exploited by the sensor) is trivial given the previously computed surface temperature profile. For a facet at temperature  $T$ , we compute the blackbody emittance using Equation (A.14) and then weight by the surface emissivity Stokes vector. We have

$$\mathbf{I}_{emis}(\hat{\mathbf{k}}_s, \mathbf{r}) = \mathcal{E}(\theta_s)L_{BB}(T, \lambda) \quad (3.62)$$

The facet’s observation angle  $\theta_s$  is used to find  $\mathcal{E}$  by interpolating a previously computed emissivity profile.

## Single-Bounce Solar Radiance

The single-bounce solar reflection is slightly more troublesome to compute than the direct thermal emission, since the source position varies during the day and the Mueller matrices for mine and soil surfaces are needed. The calculation for the response at time  $t$  begins by using MODTRAN to compute the solar radiance  $L_{sun}$  in the sensor band. Then, for all facets that are both visible to the sensor and the sun, we evaluate

$$\mathbf{I}_{sun,ref}(\hat{\mathbf{k}}_s, \mathbf{r}) = \int_{2\pi} d\Omega_i \cos \theta_i \mathbf{M}(\hat{\mathbf{k}}_s | \hat{\mathbf{k}}_i, \mathbf{r}) \cdot \mathbf{I}_{sun}(\hat{\mathbf{k}}_i) \quad (3.63)$$

in which the solar Stokes vector is given by

$$\mathbf{I}_{sun}(\hat{\mathbf{k}}_i) = \begin{bmatrix} 1/2 \\ 1/2 \\ 0 \\ 0 \end{bmatrix} \cdot L_{sun}(\lambda)\delta(\theta_i - \theta_0)\delta(\phi_i - \phi_0)/\cos\theta_0 \quad (3.64)$$

where  $(\theta_0, \phi_0)$  are the sun angles and the vector  $[1/2 \ 1/2 \ 0 \ 0]^T$  indicates that solar radiance is unpolarized. The integral immediately evaluates to

$$\mathbf{I}_{sun,ref}(\hat{\mathbf{k}}_s, \mathbf{r}) = \mathbf{M}(\hat{\mathbf{k}}_s|\hat{\mathbf{k}}_0, \mathbf{r}) \cdot \mathbf{I}_{sun}(\hat{\mathbf{k}}_0) \quad (3.65)$$

### Single-Bounce Skylight Radiance

The calculation of reflected skylight follows the approach defined above for the reflected sunlight, but the implementation is significantly different, because of the extended nature of the source. We write

$$\mathbf{I}_{sky,ref}(\hat{\mathbf{k}}_s, \mathbf{r}) = \int_{2\pi} d\Omega_i \cos\theta_i \mathbf{M}(\hat{\mathbf{k}}_s|\hat{\mathbf{k}}_i, \mathbf{r}) \cdot \mathbf{I}_{sky}(\hat{\mathbf{k}}_i) \quad (3.66)$$

The intensity of  $\mathbf{I}_{sky}(\hat{\mathbf{k}}_i)$  is obtained from MODTRAN while its polarization is found via Equation (2.15). The integral over solid angle is done numerically using the hemispherical grid defined earlier. Using a rectangle rule for the quadrature produces

$$\begin{aligned} \mathbf{I}_{sky,ref}(\hat{\mathbf{k}}_s, \mathbf{r}) &\approx \sum_m \Delta\Omega_m \cos\theta_m \mathbf{M}(\hat{\mathbf{k}}_s|\hat{\mathbf{k}}_m, \mathbf{r}) \cdot \mathbf{I}_i(\hat{\mathbf{k}}_m) \\ &\approx \sum_{m'} \Delta\Omega_{m'} \cos\theta_{m'} \mathbf{M}(\hat{\mathbf{k}}_s|\hat{\mathbf{k}}_{m'}, \mathbf{r}) \cdot \mathbf{I}_i(\hat{\mathbf{k}}_{m'}) \end{aligned} \quad (3.67)$$

in which the subscript  $m$  ranges over all facets in the hemispherical grid and  $m'$  is a subset of sky facets viewable to  $\mathbf{r}$ . Pre-calculated matrices for “visible sky facets” and associated projected solid angles described in Section 3.4.1 is used to find  $m'$  and  $\Delta\Omega_{m'} \cos\theta_{m'}$ .

## Single-Bounce Thermal Emission

In addition to the direct path, thermal emission can reach the sensor via reflection from nearby facets. In this section we describe the procedure used to calculate single-bounce thermal emission. Like reflected skylight, single-bounce thermal emission involves extended sources. For each observed point  $\mathbf{r}$  in the scene we must evaluate

$$\begin{aligned} \mathbf{I}_{ther,ref}(\hat{\mathbf{k}}_s, \mathbf{r}) &= \int d\Omega_i \cos \theta_i \mathbf{M}(\hat{\mathbf{k}}_s | \hat{\mathbf{k}}_i, \mathbf{r}) \cdot \mathbf{I}_{thermal}(\hat{\mathbf{k}}_i, \mathbf{r}) \\ &= \sum_{n'} \int_{facet\ n'} d\Omega_{i,n'} \cos \theta_{i,n'} \mathbf{M}(\hat{\mathbf{k}}_s | \hat{\mathbf{k}}_{i,n'}, \mathbf{r}) \cdot \mathcal{E}(\hat{\mathbf{k}}_{i,n'}, \mathbf{r}'_{n'}) L_{BB}(\mathbf{r}'_{n'}) \end{aligned} \quad (3.68)$$

where  $n'$  loops over all facets that can be seen from the observed point  $\mathbf{r}$ , which is found in the “visible facet” matrix, and  $\mathbf{r}'$  is the intersection (if any) of surface facet  $n'$  with  $\hat{\mathbf{k}}_{i,n'}$  starting from  $\mathbf{r}$ . By assuming the emissivity Stokes vector is constant across the facet, approximating the integrated projected solid angle as  $\Delta\Omega'_n \cos \theta'_n$  and neglecting the effects of partially obscured facets, we write

$$\mathbf{I}_{ther,ref}(\hat{\mathbf{k}}_s, \mathbf{r}) \approx \sum_{n'} \Delta\Omega_{n'} \cos \theta_{n'} \mathbf{M}(\hat{\mathbf{k}}_s | \hat{\mathbf{k}}_{i,n'}, \mathbf{r}) \cdot \mathcal{E}(\hat{\mathbf{k}}_{i,n'}, \mathbf{r}'_{n'}) L_{BB}(\mathbf{r}'_{n'}) \quad (3.69)$$

An observed point in the scene reflects emission from visible nearby facets. Due to the short distance between facets, the projected solid angle of another facet varies dramatically as the observed point changes and, hence, the integral over the source distribution must be re-calculated for each point in the scene. The required calculations are very time consuming, since one must identify all facets visible from every visible point in the scene, and one must integrate over those facets. In general, however, this term does not have a significant contribution to the total radiance, since the surfaces involved are poor reflectors.

## Double-Bounce Solar Radiance

Higher-order scattering events contribute to radiometric mine signature, but in general the impact of those events is likely to be small, because the surfaces involved tend to be poor reflectors, and because the contribution of higher-order events decays geometrically with each scattering. Solar reflections are the strongest scattering events and, to investigate the contribution of higher-order scattering the double-bounce solar reflection has been evaluated.

The double-bounce solar contribution is given by

$$\mathbf{I}_{sol,ref2}(\hat{\mathbf{k}}_s, \mathbf{r}) = \int d\Omega_i \cos \theta_i \mathbf{M}(\hat{\mathbf{k}}_s | \hat{\mathbf{k}}_i, \mathbf{r}) \cdot \mathbf{I}_{sol,ref1}(\hat{\mathbf{k}}_i, \mathbf{r}) \quad (3.70)$$

where

$$\begin{aligned} \mathbf{I}_{sol,ref1}(\hat{\mathbf{k}}_i, \mathbf{r}) &= \int d\Omega'_i \cos \theta'_i \mathbf{M}(\hat{\mathbf{k}}_i | \hat{\mathbf{k}}'_i, \mathbf{r}') \cdot \mathbf{I}_{sun}(\hat{\mathbf{k}}_0) \\ &= \mathbf{M}(\hat{\mathbf{k}}_i | \hat{\mathbf{k}}_0, \mathbf{r}') \cdot \mathbf{I}_{sun}(\hat{\mathbf{k}}_0) \end{aligned} \quad (3.71)$$

was evaluated previously. In this expression  $\mathbf{r}'$  indicates the location of the facet producing the first reflection. Thus

$$\mathbf{I}_{sol,ref2}(\hat{\mathbf{k}}_s, \mathbf{r}) = \int d\Omega_i \cos \theta_i \mathbf{M}(\hat{\mathbf{k}}_s | \hat{\mathbf{k}}_i, \mathbf{r}) \cdot \mathbf{M}(\hat{\mathbf{k}}_i | \hat{\mathbf{k}}_0, \mathbf{r}') \mathbf{I}_{sun}(\hat{\mathbf{k}}_0) \quad (3.72)$$

The contributions of higher-order terms can be derived in an analogous fashion involving additional integrations. Using assumptions similar to those made for the single-bounce thermal emission, we write

$$\begin{aligned} \mathbf{I}_{sol,ref2}(\hat{\mathbf{k}}_s, \mathbf{r}) &= \sum_n \int_{facet\ n} d\Omega_{i,n} \cos \theta_{i,n} \mathbf{M}(\hat{\mathbf{k}}_s | \hat{\mathbf{k}}_{i,n}, \mathbf{r}) \cdot \mathbf{M}(\hat{\mathbf{k}}_{i,n} | \hat{\mathbf{k}}_0, \mathbf{r}'_n) \mathbf{I}_{sun}(\hat{\mathbf{k}}_0) \\ &\approx \sum_{n'} \Delta\Omega_{n'} \cos \theta_{n'} \mathbf{M}(\hat{\mathbf{k}}_s | \hat{\mathbf{k}}_{i,n'}, \mathbf{r}) \cdot \mathbf{M}(\hat{\mathbf{k}}_{i,n'} | \hat{\mathbf{k}}_0, \mathbf{r}'_{n'}) \mathbf{I}_{sun}(\hat{\mathbf{k}}_0) \end{aligned} \quad (3.73)$$

Like the single-bounce thermal emission, the double-bounce solar component is expensive to compute, since it requires that one identify all facets (points)  $\mathbf{r}'$  visible from  $\mathbf{r}$  and integrate their contributions.

### 3.5 Simulated Signatures For Ideal Sensors

In an effort to understand the behavior of the signature model, a number of idealized simulations were done in this section to assess the significance of different radiation components in nadir and oblique sensor orientations. Section 3.5.1 presents the individual radiometric components of a nadir-looking sensor and a discussion of their impact on the model. The case of an oblique-viewing sensor is studied in Section 3.5.2. The relation of surface reflection and the orientation of oblique-viewing sensor is presented in Section 3.5.3. Section 3.5.4 examines total and individual responses in different sensor bands. An analysis of temporal contrast of mine and background signatures is also presented.

The simulations have been performed using the environmental conditions from the “NT-S1” data set described in Section 2.7.1 and the target simulated is a LP\_B mine. The simulations in this section contain three images: The nadir-looking  $I$ ,  $Q$ , and  $U$  Stokes parameters. (In the absence of circularly polarized sources, no  $V$  component is produced for this geometry.) The sensor is assumed to be 10 meters above the mine. Each image chip contains  $128 \times 128$  pixels, which leads to a high resolution signature. However, for some higher-order components, the sampling rate was reduced in uninteresting image regions to save computation time.

### 3.5.1 Comparative Study of Radiometric Components

Figure 3.37 displays the direct thermal emission. The  $I$  component exhibits features similar to the surface temperature shown earlier in Figure 3.9, since the surface emissivities of mines and soil are similar at normal incidence. The  $Q$  and  $U$  images indicate that those Stokes parameters emphasize the horizontal/vertical and diagonal polarization, respectively. This is the result of the Stokes transformation described in Equations (3.60) and (3.61) that rotates local Stokes vectors to the fixed sensor's coordinate system. For points on a concentric circle under a nadir sensor,  $\mathcal{E}_h$  and  $\mathcal{E}_v$  are the same since the surfaces simulated are isotropic. However, the angle  $\phi$  relative to the sensor's coordinate system varies from 0 to  $2\pi$  and yields the pattern seen in  $Q$  and  $U$  components after transformation.

We see the energy in  $Q$  and  $U$  components is very small compared to the  $I$  image. (Recall that thermal emission at normal angles is nearly unpolarized for most materials.) Soil regions in the  $Q$  and  $U$  images show small values while those of the

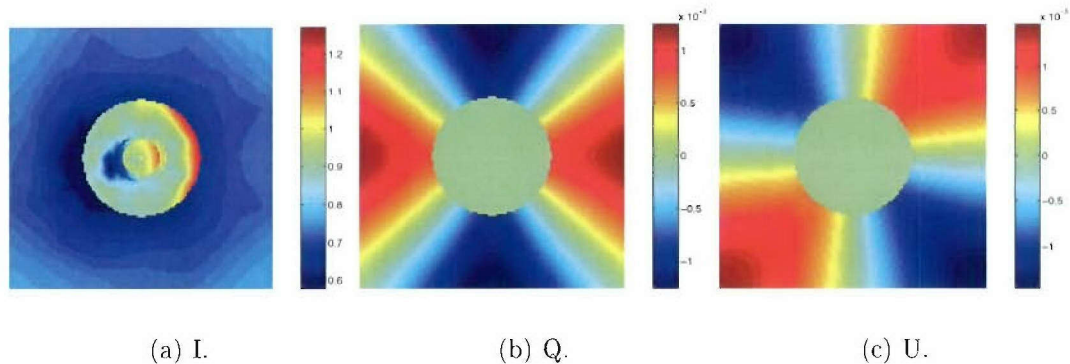


Figure 3.37: Simulated signatures in the  $I$ ,  $Q$ , and  $U$  components for direct thermal emission and nadir viewing.

mine are zero. These  $Q$  and  $U$  responses are produced by two causes: first, the mine surface is smoother than the soil and as a result, the mine has a smaller difference between horizontal and vertical emissivities near nadir. Figure 3.38 shows that the soil has a larger difference between vertical and horizontal emissivities. Second, for a finite sensor height, the mine's observation vector  $\hat{\mathbf{k}}_s$  has a smaller zenith angle than the soil's which accentuates the soil's apparent polarization. Since the sensor is assumed placed 10 meters above the target, there are small changes in observation vector across the scene. The distance between the center and the edge of the scene is approximately 35 cm, which produces a zenith angle around  $2^\circ$ . In contrast, the zenith angle at the mine's edge is approximately  $1^\circ$ . This example shows that small differences in surface properties and viewing geometry can produce variations in polarimetric signatures.

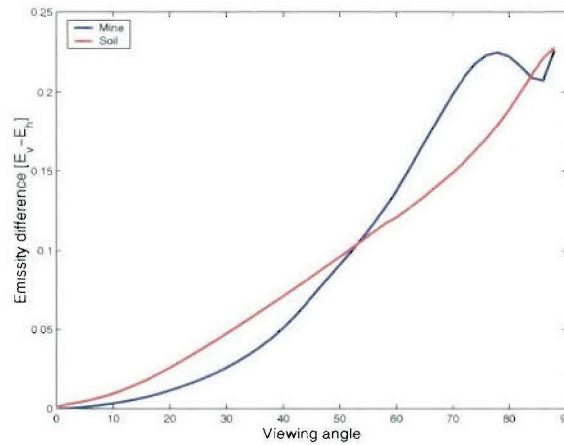


Figure 3.38: Emissivity difference ( $\mathcal{E}_v - \mathcal{E}_h$ ) for mine and soil surfaces.

Next, we examine the single-bounce solar reflection, which is shown in Figure 3.39. The sunlight comes from the right of the image with a  $40^\circ$  zenith angle. Because the sensor is directed away from the specular direction, the reflected-solar  $I$  component is

much smaller than the  $I$  component for direct thermal emission. The reflection from soil is stronger than that from the mine surface, since we assume that the soil surface is rougher and produces strong diffuse scattering. The shadow introduced by the 3-D mine structure is clear and oriented as required by the solar position. Because solar radiation is an unpolarized source, the  $Q$  and  $U$  images are weak. Note that the  $Q$  image is entirely negative, which occurs because the solar irradiance arrives from the right.

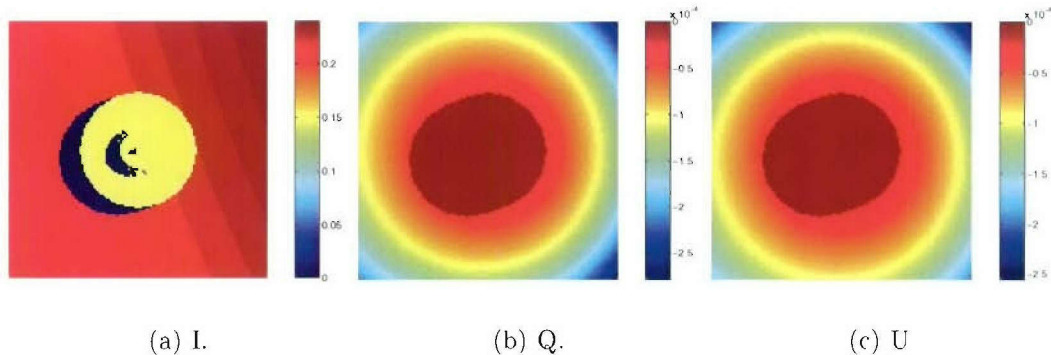


Figure 3.39: Simulated signatures in the  $I$ ,  $Q$ , and  $U$  components for single-bounce solar radiation and nadir viewing.

The Stokes components for skylight, an extended source, are shown in Figure 3.40. The  $I$  component is uniform across most of the computation surface, but the response is reduced near the mine's side wall, because the skylight is partially blocked. Immediately adjacent to the side wall, the reduction is 50%. The  $Q$  and  $U$  components exhibit similar patterns as seen in direct thermal emission signatures, which can be attributed to the Stokes rotation operation. Because skylight is partially polarized, the  $Q$  and  $U$  images contain more energy (relative to the  $I$  component) than thermal

emission or solar reflection. This finding is best quantified by the degree of linear polarization (DoLP), which is essentially the ratio  $Q/I$ .

$$\text{DoLP} = \frac{I_h - I_v}{I_h + I_v} \quad (3.74)$$

Figure 3.41 presents the DoLP for skylight, (direct) thermal emission, and (single-bounce) solar reflection, respectively. We note that the maximum of the skylight DoLP is about 0.15, which is much greater than the other two sources. However, the DoLP in the total Stokes vector is still small, since skylight is a relatively weak source.

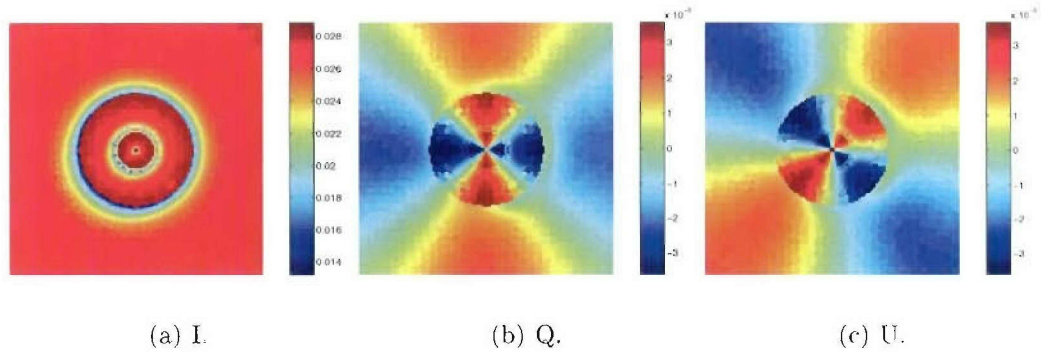


Figure 3.40: Simulated signatures in the  $I$ ,  $Q$ , and  $U$  components for single-bounce skylight radiation and nadir viewing.

### Higher-Order Components

As alluded to previously, higher-order radiometric components tend to be weak. Figure 3.42 shows the Stokes parameters for single-bounce thermal emission. The  $I$  component is largest near the mine walls, because the adjacent wall presents large projected solid angles to the adjacent soil, leading to a strong thermal interaction.

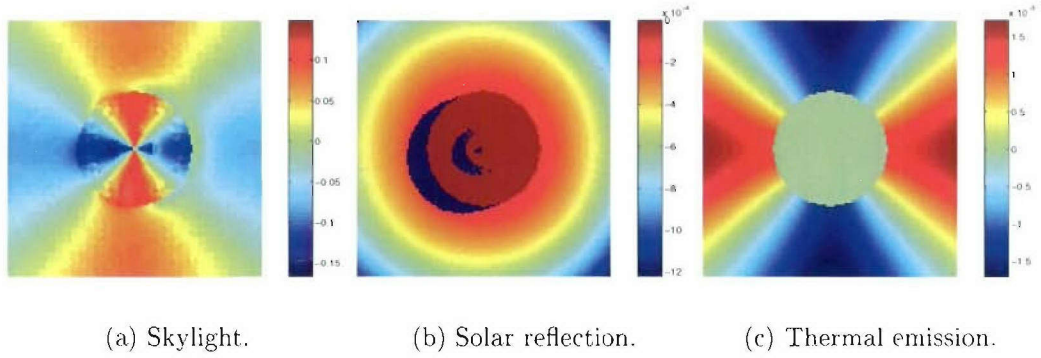


Figure 3.41: Degree of linear polarization (DoLP) for skylight, reflected sunlight, and thermal emission for nadir viewing.

Nonetheless, its magnitude is small compared to the direct thermal emission. Figure 3.43 shows the sum of direct and single-bounce thermal emission, which is essentially the same as the direct emission shown in Figure 3.37.

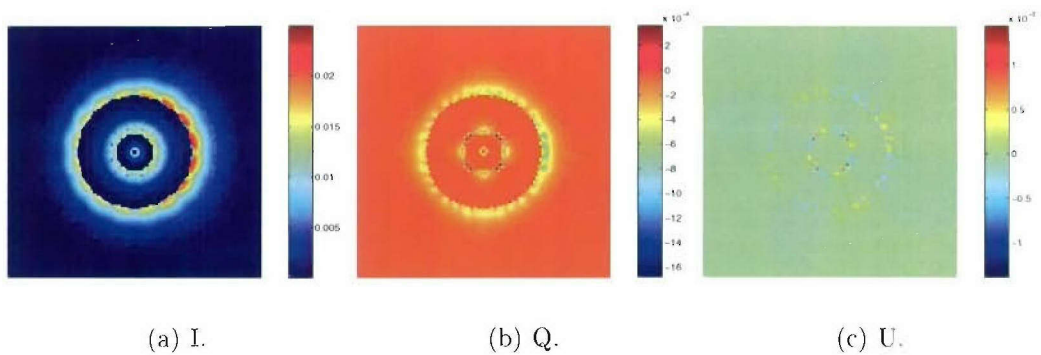


Figure 3.42: Simulated signature in the  $I$ ,  $Q$ , and  $U$  components for single-bounce thermal emission and nadir viewing.

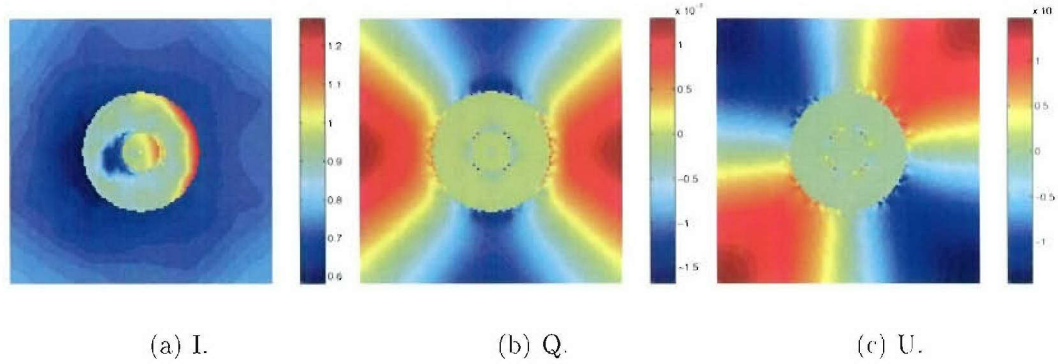


Figure 3.43: Simulated signature in the  $I$ ,  $Q$ , and  $U$  components for total thermal emission and nadir viewing.

The double-bounce solar reflection shown in Figure 3.44 is also small in magnitude, making a small correction to the total solar reflection in Figure 3.45<sup>13</sup>. The double-bounce solar reflection exhibits stronger depolarization than the single-bounce component, but its DoLP is still small. The  $Q$  and  $U$  components of the double-bounce solar reflection dominate the total solar reflection shown in Figures 3.45 (b) and (c).

Figure 3.46 shows the combined radiometric signature from all five components. The  $I$  signature is dominated by direct thermal emission, while the single-bounce solar reflection introduces a strong shadow. The remaining components have little effect on the total signature as shown in Figure 3.47 which presents the direct thermal and single-bounce solar signatures only. The  $I$  image from those two dominant components is virtually indistinguishable from the sum of all five components shown in Figure 3.46, but the skylight contribution has a strong effect on the  $Q$  and  $U$  images.

<sup>13</sup>The complex fractal-like pattern near the mine walls in the double-bounce solar reflection signature is the result of the mesh formulation. A polygon of 16 sides was used to approximate the mine's cylindrical shape.

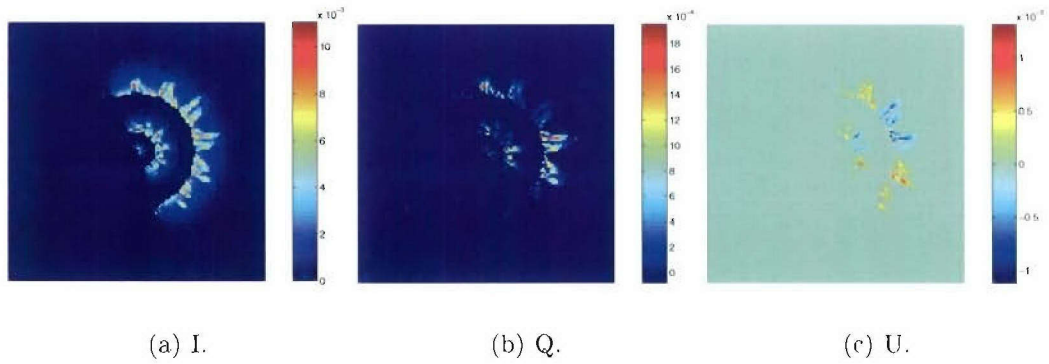


Figure 3.44: Simulated signature in the  $I$ ,  $Q$ , and  $U$  components for double-bounce solar radiation and nadir viewing.

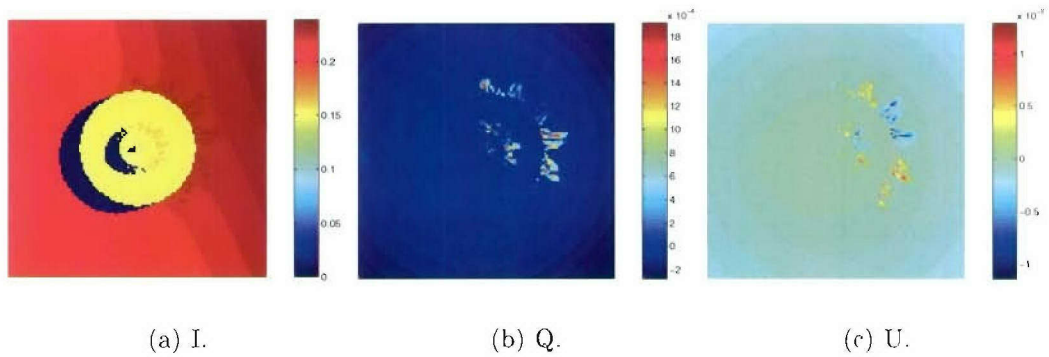


Figure 3.45: Simulated signature in the  $I$ ,  $Q$ , and  $U$  components for total solar radiation and nadir viewing.

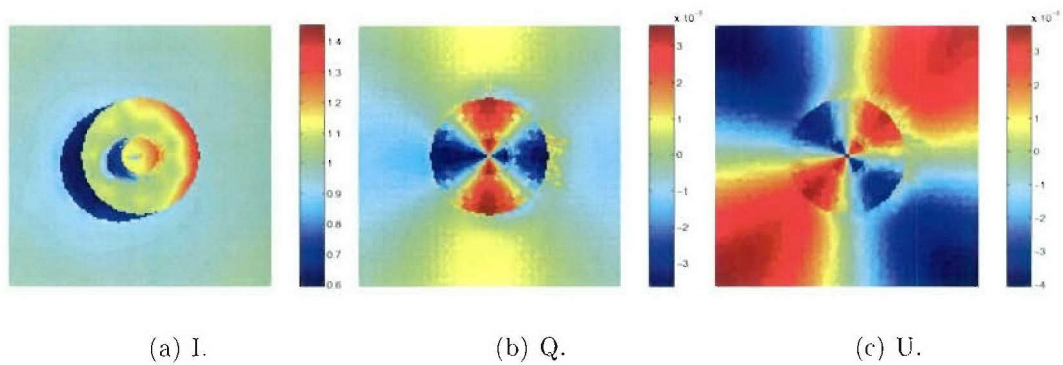


Figure 3.46: Simulated signature in the  $I$ ,  $Q$ , and  $U$  components for total radiation and nadir viewing.



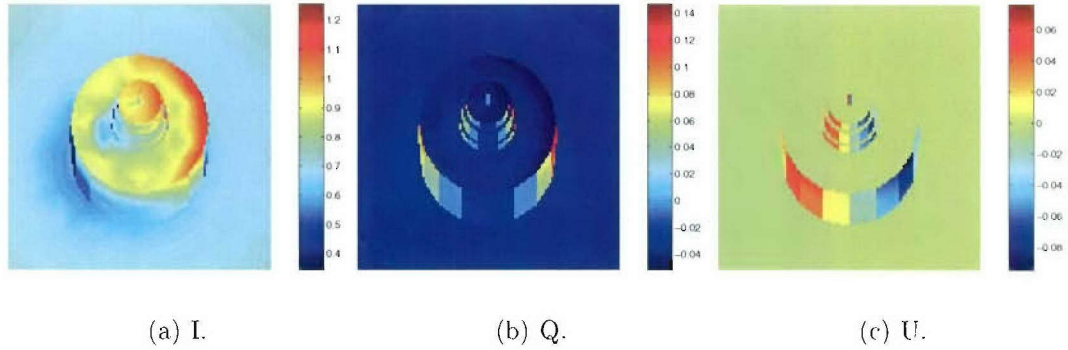


Figure 3.48: Simulated signatures in the  $I$ ,  $Q$ , and  $U$  components for direct thermal emission and oblique viewing ( $\theta_s = 45^\circ$ ).

The single-bounce solar reflection is shown in Figure 3.49. The Stokes vector components indicate that the return from the mine is unpolarized (only diffuse scattering is significant), since the mine’s BRDF is localized in the specular direction, but the sensor is viewing the mine in an off-specular direction. In contrast, the return from soil is slightly polarized due to its rougher surface, which results in a broader specular lobe. Note that the shadow region is also unpolarized, because it reflects no solar incidence.

The oblique-viewing skylight reflection signatures in Figure 3.50 are also significantly different from the nadir-looking component in Figure 3.40. The return from horizontal facets remains largely constant across the scene, while the return of vertical panels varies significantly due to the viewing geometry.

The DoLP for the above three radiometric components is shown in Figure 3.51. All three components have larger DoLP values in the oblique sensor case. The maxima in DoLP are increased approximately by the factors of 2, 10, and 100 for skylight, solar reflection, and thermal emission, respectively.

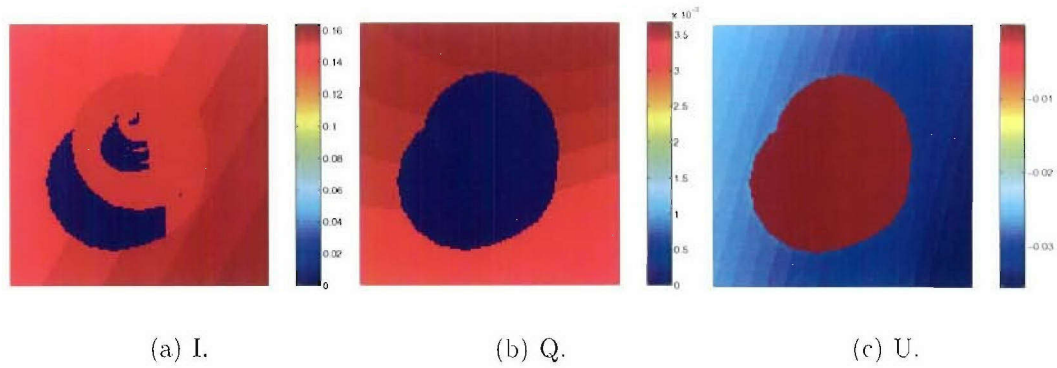


Figure 3.49: Simulated signatures in the  $I$ ,  $Q$ , and  $U$  components for single-bounce solar radiation and oblique viewing ( $\theta_s = 45^\circ$ ).

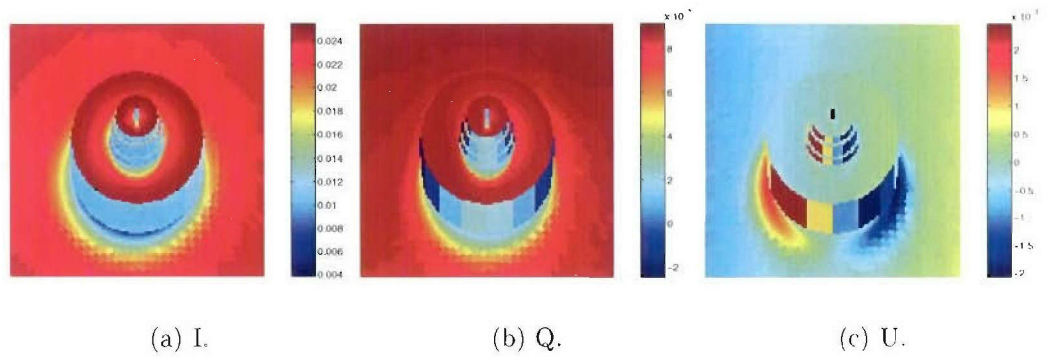


Figure 3.50: Simulated signatures in the  $I$ ,  $Q$ , and  $U$  components for single-bounce skylight radiation and oblique viewing ( $\theta_s = 45^\circ$ ).

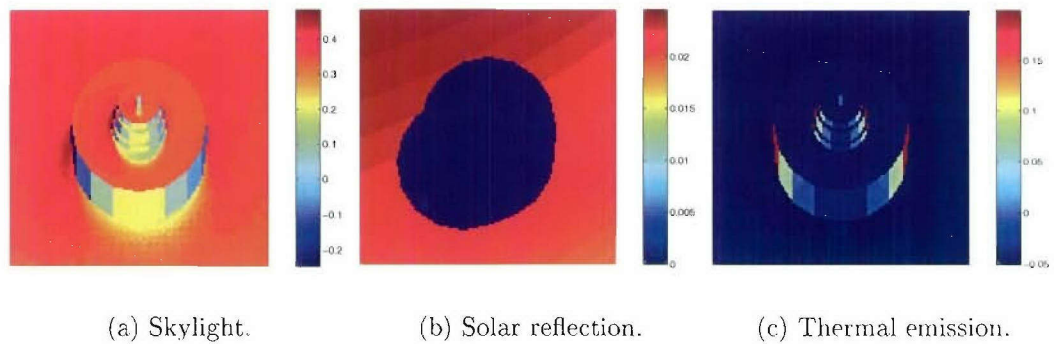


Figure 3.51: Degree of linear polarization (DoLP) for skylight, reflected sunlight, and thermal emission for oblique viewing ( $\theta_s = 45^\circ$ ).

Figures 3.52 and 3.53 show the higher-order components. Their intensities are weak, but some very localized “glints” appear. Some glints from the double-bounce solar reflection are visible in the total signature in Figure 3.54.

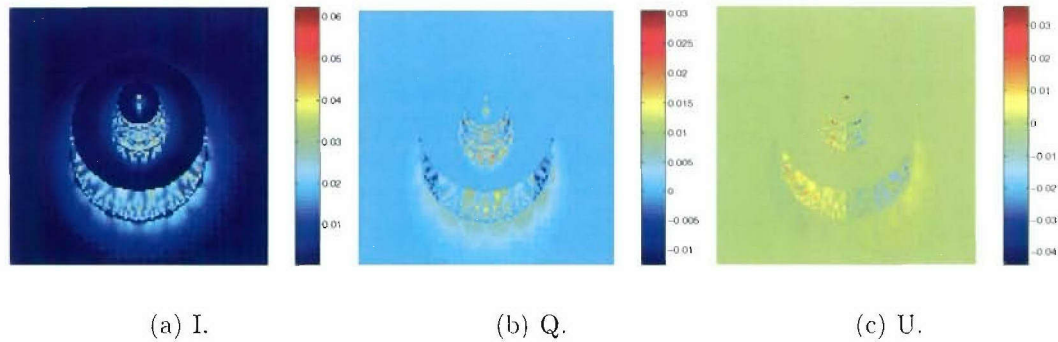


Figure 3.52: Simulated signature in the  $I$ ,  $Q$ , and  $U$  components for single-bounce thermal emission and oblique viewing ( $\theta_s = 45^\circ$ ).

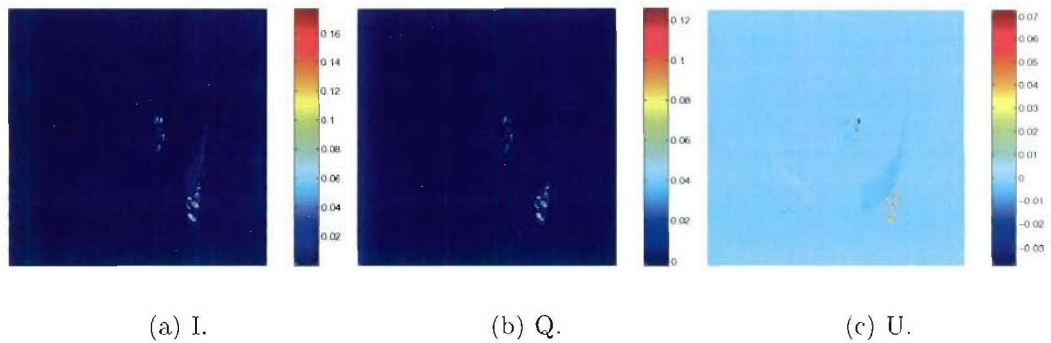


Figure 3.53: Simulated signature in the  $I$ ,  $Q$ , and  $U$  components for double-bounce solar radiation and oblique viewing ( $\theta_s = 45^\circ$ ).

By combining the above five components, we obtain the total signature shown in Figure 3.54. The intensity variation observed in the  $I$  image is very similar to that found in the nadir viewing case of Figure 3.46, but the shape is changed by the viewing angle. The polarimetric ( $Q$  and  $U$ ) components are again dominated by direct thermal emission, but the oblique viewing angle greatly increases the magnitudes of the  $Q$  and  $U$  components. The mine's shape becomes visible in the  $Q$  and  $U$  images, which implies that off-nadir viewing is valuable for passive polarimetric sensors.

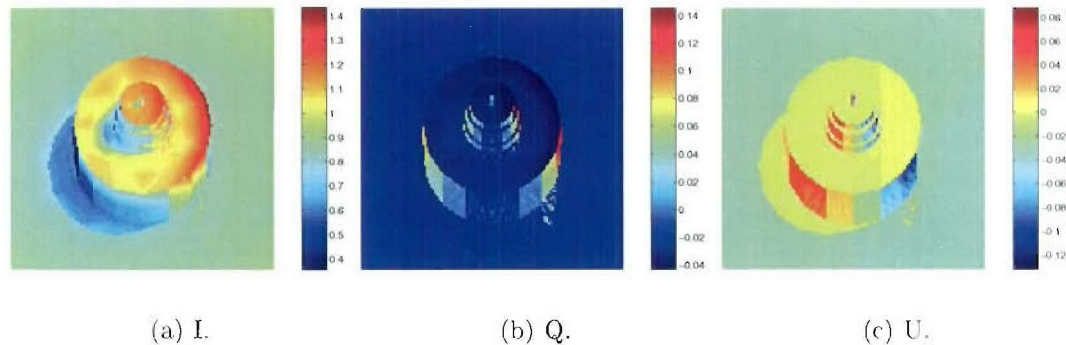


Figure 3.54: Simulated signature in the  $I$ ,  $Q$ , and  $U$  components for total radiation and oblique viewing ( $\theta_s = 45^\circ$ ).

### 3.5.3 Radiometric Signature and Sensor Orientation

In this section simulations of an oblique-viewing sensor, which was studied in Section 3.5.2, are performed with the sensor oriented toward east, south, west, and north directions to study the impact of sensor orientation. Only signatures of the single-bounce solar reflection are presented because its significant intensity in MWIR signatures. The direct thermal emission component has no  $\phi$  preference and is therefore invariant to the sensor orientation.

We first examine the intensity ( $I$ ) images in Figure 3.55. The orientations of the sensor were set in four directions and can be associated with the orientation of the shadow, which is imposed by a 11 AM sun (coming from south-east-south). The intensity of mine is constant over four images (about  $0.15 \text{ [W/m}^2\text{sr]}$ ) because the specular lobe of the mine's surface is narrow and above four sensors only receive returns from the diffuse component. On contrast, returns from soil surfaces is particularly strong (around  $0.45 \text{ [W/m}^2\text{sr}]$ ) in the south-looking sensor, which is closer to the specular region of the solar incidence.

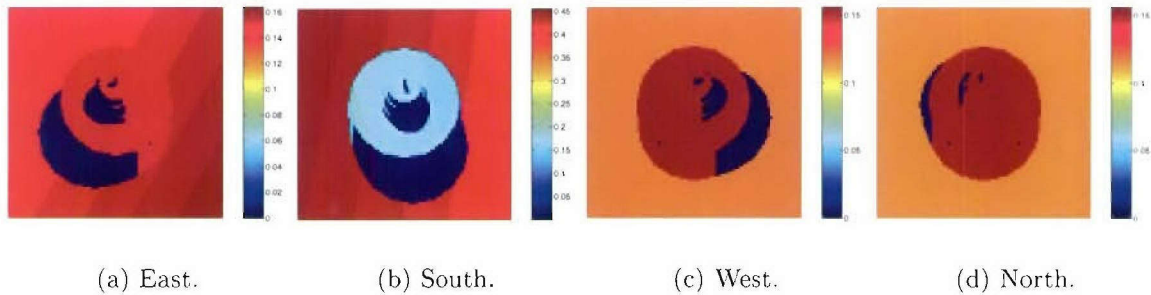


Figure 3.55: Simulated  $I$  images of an oblique sensor ( $\theta_s = 45$ ) oriented toward east, south, west and north.

The  $Q$  images in Figure 3.56 are proportional to the degree of linear polarization. We see the  $Q$  components from the mine's returns are essentially zero at all sensor directions. This result confirms that returns from the mine are diffuse in off-specular regions. The dynamic range of soil's returns experiences greater changes in different sensor orientations. The maximum  $Q$  in a south-looking sensor (near specular) is about ten times larger than those in east- and west-looking sensors and two orders larger than that in a north-looking sensor (near backscattering). Note that the sign

in  $Q$  is different to that in a sensor of opposite direction because the horizontal and vertical directions are defined differently as the sensor's orientation changes. Above result shows passive polarimetric sensors should be placed in (or near) the specular direction of its primary source of reflection to maximize the contrast in its polarimetric signatures.

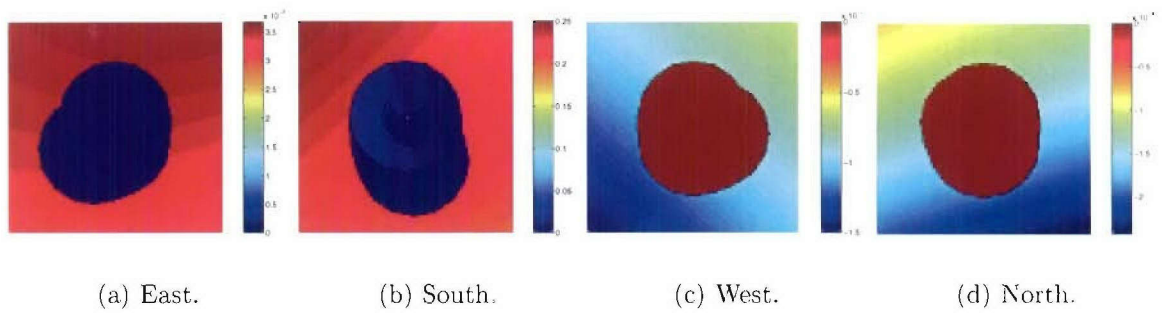


Figure 3.56: Simulated  $Q$  images of an oblique sensor ( $\theta_s = 45$ ) oriented toward east, south, west and north.

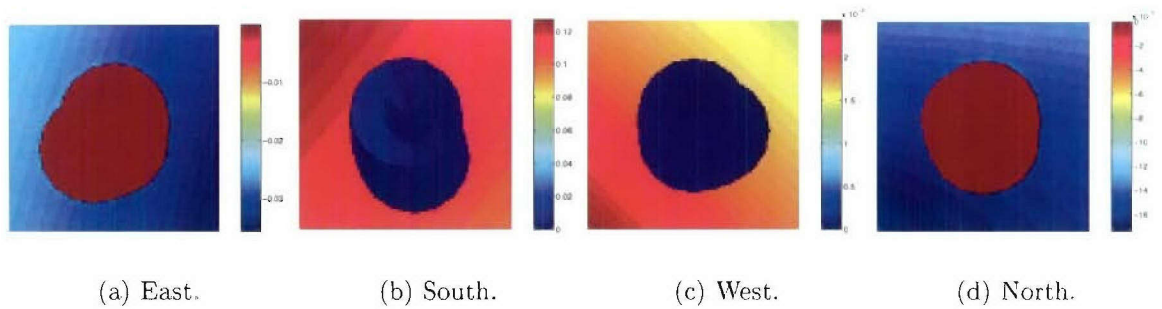


Figure 3.57: Simulated  $U$  images of an oblique sensor ( $\theta_s = 45$ ) oriented toward east, south, west and north.

The  $U$  images in Figure 3.57 exhibit similar features seen in Figure 3.56 except the sign changes in east- and west-looking sensors since the  $U$  component emphasizes the linear polarization  $45^\circ$  away from the  $Q$  component.

### 3.5.4 Comparative Study of Sensor Bands

The foregoing simulations were performed for an MWIR sensor (3-5  $\mu\text{m}$ ), and suggest that both thermal emissions and solar reflections contribute to a mine's radiometric signature. To understand the role of the sensor passband, a comparative study is presented in this section for MWIR, SWIR (1-3  $\mu\text{m}$ ), and LWIR (8-12  $\mu\text{m}$ ).

Changes in sensor passband require changes in source radiance and parameters used for surface roughness. A surface's degree of roughness varies with the wavelength of the incident radiation. Table 3.4 lists the values of key surface roughness parameters used in the three bands. Both the surface slope variance and the diffuse component of the BRDF model were adjusted in proportion to the mid-band wavelength.

Sensor band	SWIR (1-3 $\mu\text{m}$ )		MWIR (3-5 $\mu\text{m}$ )		LWIR (8-12 $\mu\text{m}$ )	
	Mine	Soil	Mine	Soil	Mine	Soil
Refractive index ( $m$ )	1.4	1.6	1.4	1.6	1.4	1.6
Slope variance ( $s^2$ )	0.005	0.1	0.0025	0.05	0.001	0.02
Diffuse component	0.04	0.03	0.02	0.015	0.01	0.0075
Depolarization ratio	0.5	0.5	0.5	0.5	0.5	0.5

Table 3.4: Surface scattering parameters for the mine and soil used in SWIR, MWIR, and LWIR sensor simulations.

The source radiance was re-calculated for each sensor band. For thermal emission, we simply changed the lower and upper limits in the integral in Equation (A.14). Sunlight and skylight spectral radiances were computed by modifying the MODTRAN input file. Figure 3.58 plots the solar irradiance versus the solar zenith angle for a mid-latitude winter atmosphere. We see that the attenuation of solar irradiance increases with wavelength. For an oblique sun ( $\theta_{sun}=45^\circ$ ) the amount of irradiance in the LWIR band is approximately one-tenth that in the MWIR band, and less than one percent that in the SWIR band. This agrees with the common observation that sunlight is significant in the SWIR band but negligible in the LWIR band.

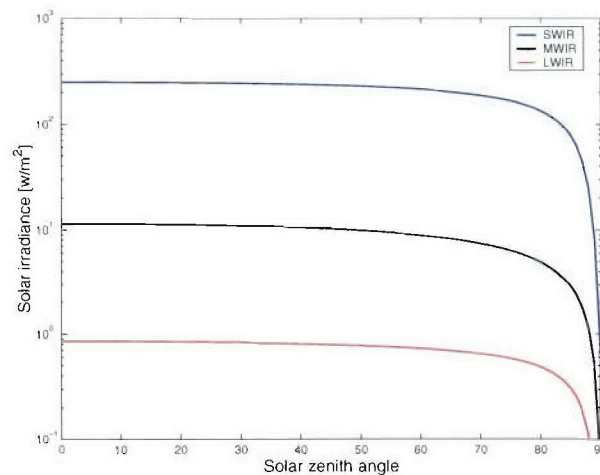


Figure 3.58: Solar irradiance versus solar zenith angle in various IR bands for a mid-latitude winter atmosphere.

Figure 3.59 illustrates the skylight intensity on the solar meridian. The spike in the SWIR (blue) curve indicates the location of the sun. The skylight radiance falls off away from that peak. The MWIR (black) curve shows a similar trend but is much weaker in magnitude. In the LWIR band, the skylight shows no spike at the solar

position, which means that skylight at LWIR is mainly thermal emission from air particles.

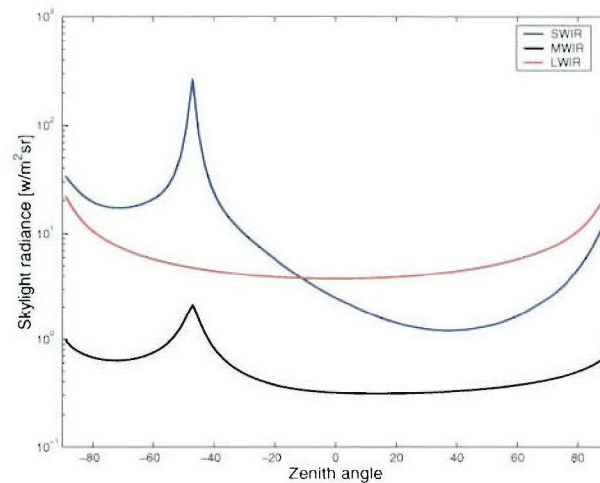


Figure 3.59: Skylight radiance at the solar meridian in various IR bands for a mid-latitude winter atmosphere.

Simulations were performed for SWIR and LWIR sensors to proceed comparisons with MWIR results. Figure 3.60 shows individual components and the total intensity ( $I$ ) signature of an SWIR sensor. The direct thermal emission signature is the same as that in Figure 3.37 (a), but the magnitude is much smaller. In contrast, the single-bounce solar reflection component dominates the total signature with minor corrections from double-bounce sunlight and skylight. With the surface parameters listed in Table 3.4, returns from mine and soil surfaces are comparable and make the shadow a high-contrast mine feature.

At LWIR wavelengths, thermal emission becomes the primary source for the received radiance. As seen in Figure 3.61, solar reflection is insignificant, and skylight

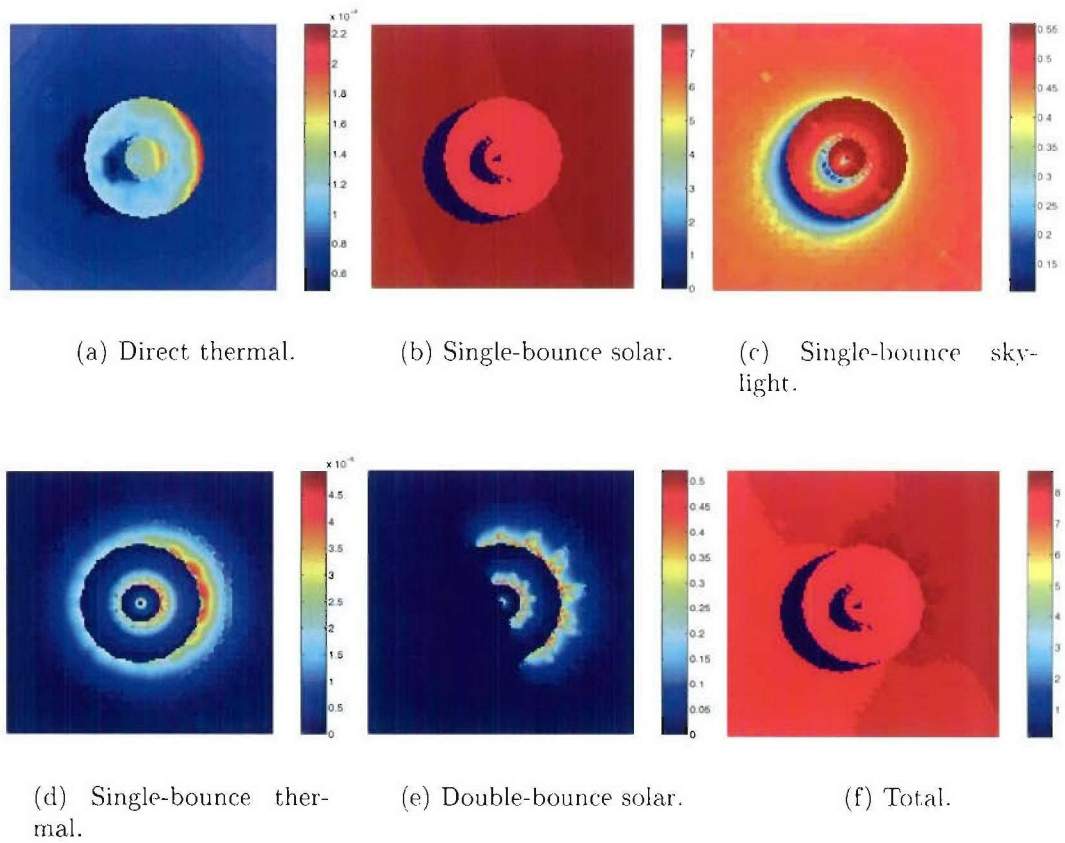


Figure 3.60: Simulated intensity images ( $I$ ) of individual components and the total signature in the SWIR band ( $1-3 \mu\text{m}$ ) for nadir viewing.

reflection is only a fraction of thermal emission. The shadow in the total LWIR signature is more diffuse and poorly defined because the nodal distribution of the thermal model mesh is coarse in this region.

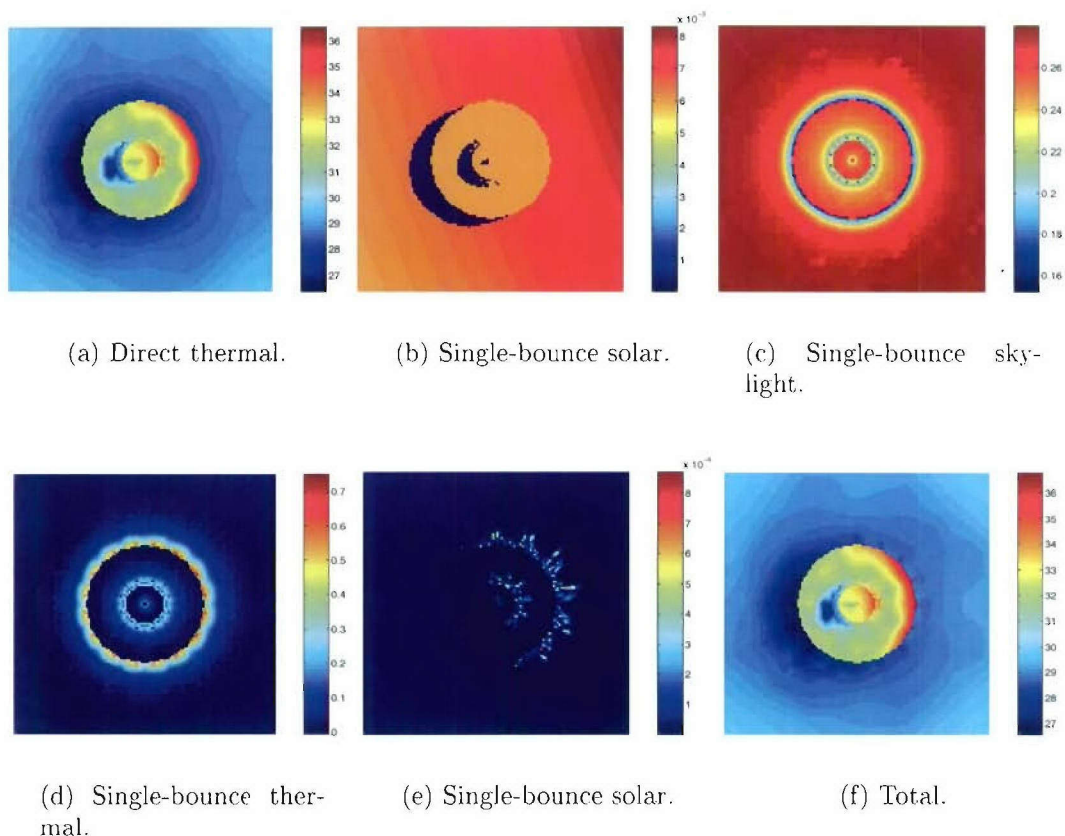


Figure 3.61: Simulated intensity images ( $I$ ) of individual components and the total signature in the LWIR band (8-12  $\mu\text{m}$ ) for nadir viewing.

### Temporal Dependence of Signature Contrast

To study the temporal dependence of the mine's signature, sequences of simulations in different sensor bands were conducted for a 24 hour period. To save computation time, only the direct thermal emission and single-bounce solar reflection were

considered because we have seen that other components have small contributions and they are expensive to compute. One practical objection of this study is an assessment of mine detection performance as a function of time and passband. As a surrogate for detector performance, we use contrast, the difference between signal intensities over the target and over the background. Target and background regions used in this calculation were defined previously in Figure 3.8.

First consider the MWIR band. Figure 3.62 (a) shows the received radiances from different regions of the simulated scene. For reference, the insolation is plotted as a green dashed line to indicate the daylight hours. The blue curve is the average radiance from the background region (soil) defined in Figure 3.8. The maximum radiance in the mine region and the minimum in the potential shadow region are plotted in red and black curves. The radiance from the mine exceeds the background during daytime and the contrast is reversed during the night. Also, if the shadow is present, its radiance tends to be smaller than that of other soil regions. Because the deviation of the mine's signature from the background is proportional to its detectability, we plot Figure 3.62 (a) the maximum difference (from either the mine surface or the shadow) over the diurnal cycle in . It is evident that the maximum contrast is achieved around mid day.

In the SWIR band, solar reflection is the dominant source. The zero contrast observed in darkness in Figure 3.63 (a) shows that the SWIR sensor cannot work without insolation. Because reflections from the surfaces of the mine and soil are similar in magnitude, the maximum deviation comes from the shadow as indicated in Figure 3.63 (b). The insolation (green dashed line) follows the maximum return from the mine (red line) but deviates slightly from the background (blue line). This result

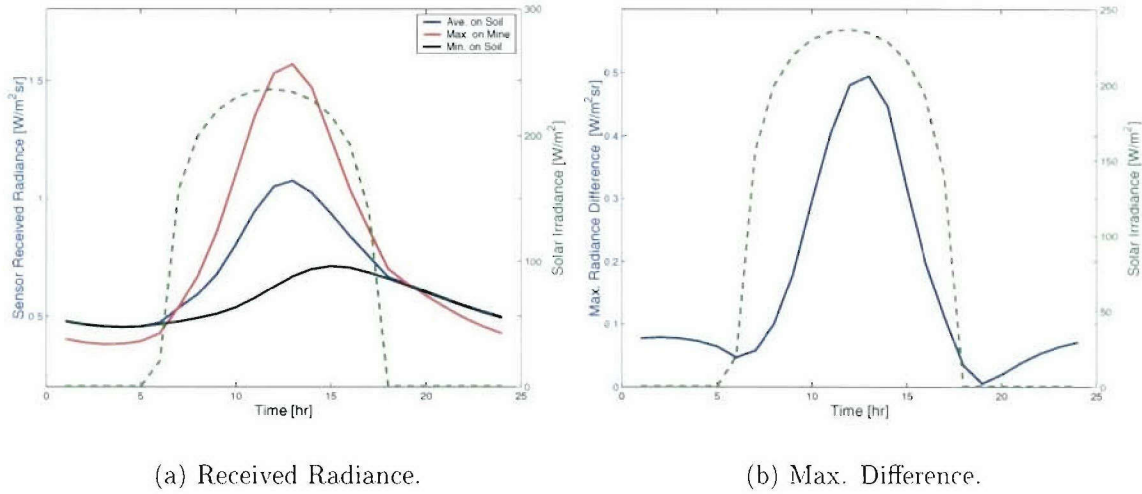


Figure 3.62: (a) Received radiance in the MWIR band ( $3-5 \mu m$ ) on soil (average), mine (maximum), and soil next to mine (minimum) where the shadow may be present. (b) Maximum deviation (from average soil radiance) for the mine or its shadow. The green dashed line indicates the incident solar irradiance.

was expected, mine reflection is mostly the diffuse component of the BRDF model, while the specular lobe of the rougher soil surface provides a different response.

The radiance and contrast curves for the LWIR sensor are shown in Figure 3.64, which is determined solely by the surface temperature history. Features of these curves are similar to the MWIR curves, except the difference between the shadow and the soil is smaller, and the interval between sunrise/sunset and the “cross over” events (equal intensities in mine and soil regions) is longer because very little solar reflection has little role in the LWIR band.

### 3.6 Sensor Point Spread Function

Sensor characteristics have a strong effect on mine signatures. The signature dependence on the spectral passband has already been discussed. The viewing angle

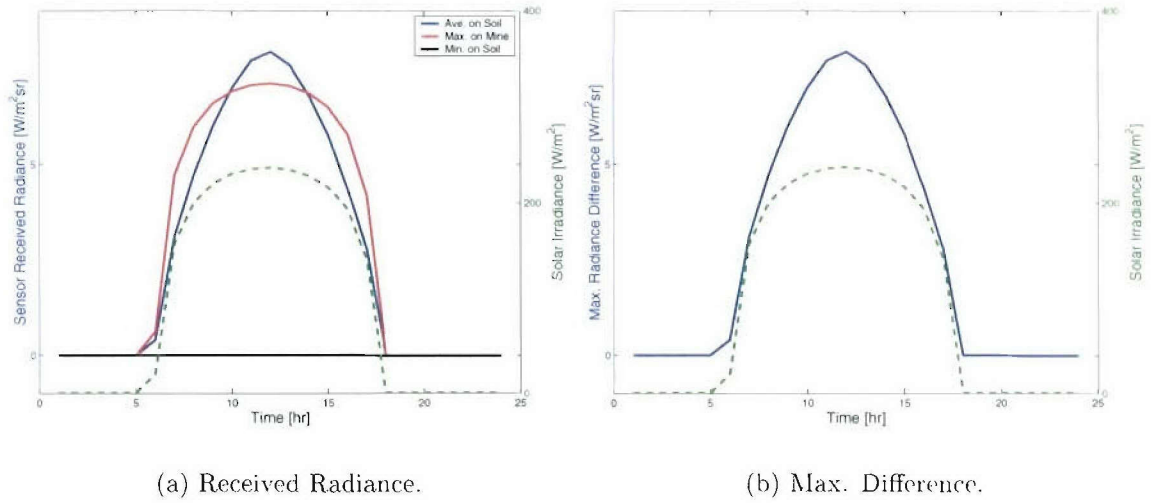


Figure 3.63: (a) Received radiance in the SWIR band ( $1-3 \mu\text{m}$ ) on soil (average), mine (maximum), and soil next to mine (minimum) where the shadow may be present. (b) Maximum deviation (from average soil radiance) for the mine or its shadow. The green dashed line indicates the incident solar irradiance.

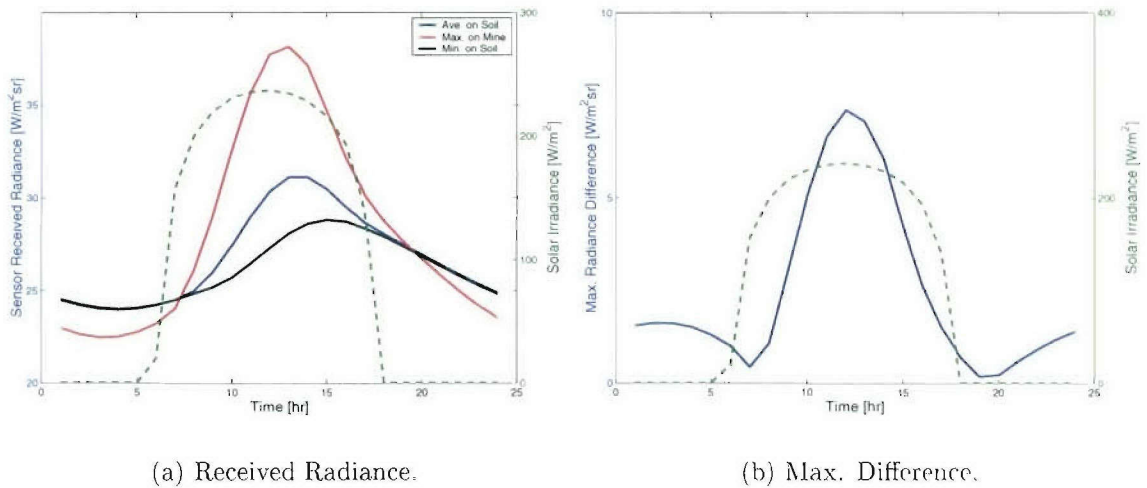


Figure 3.64: (a) Received radiance in the LWIR band ( $8-12 \mu\text{m}$ ) on soil (average), mine (maximum), and soil next to mine (minimum) where the shadow may be present. (b) Maximum deviation (from average soil radiance) for the mine or its shadow. The green dashed line indicates the incident solar irradiance.

also has a strong, obvious effect, with nadir viewing preferred for capturing the mine's circular shape.

The optical path of an imaging sensor will also affect image quality. At this time the optical response of the sensor is summarized by its point spread function. The principal characteristic addressed by this function is the sensor resolution. In this section, we describe a simple Gaussian filter model for the impulse response of the sensor. The filtered response can be down-sampled to yield images at the desired resolution.

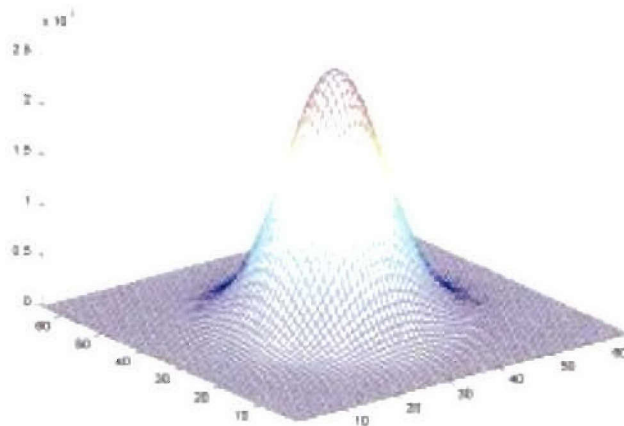


Figure 3.65: Gaussian impulse response of sensor.

The ground sample distance in the “NT-S1” data set is about 1.1 inches, but the resolution of the image is slightly worse at approximately 1.65 inches (approximately 1.5 pixels). In contrast, the resolution of simulated signatures is approximately 0.19 inches. A Gaussian filter of 1.65 inch half-width was applied to the simulated images

to mimic the impulse response of the sensor. Figure 3.65 illustrates the Gaussian filter, which has a half width of approximately 8.5 pixels in the simulation resolution.

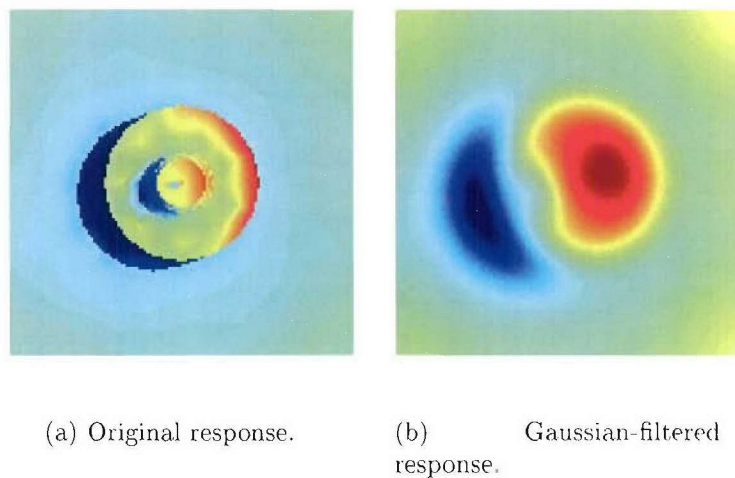


Figure 3.66: Radiometric mine signature before and after applying Gaussian filter that mimics the impulse response of the sensor

Figure 3.66 shows the effect of applying the Gaussian filter. High frequency information (e.g., edges) is suppressed, resulting in a blurred mine signature. The original detailed simulation has been replaced by a blob with a more uniform brightness distribution, and the shadow region is enlarged. The result was then down sampled to replicate sensor pixels. A rotation has also been introduced to facilitate later comparisons with measurements. Figure 3.67 shows the final product, which will be compared with measured images in Section 4.1.1.



Figure 3.67: Down-sampled and rotated simulated radiometric mine signature.

### 3.7 Summary

The implementation of the radiometric model was presented in this chapter. Source conditions, surface properties, and the viewing geometry are the major factors that define a mine's signature. It has been observed in prior studies that EO signatures are subject to changes in the operation time, weather, insolation conditions, thermal and roughness properties of mine and soil, sensor's impulse response, passband, orientation, and many other factors. A summary of key elements exploited in this radiometric model is presented below.

The thermal model provides the temperature histories required to calculate thermal emission. Computational meshes were built for mines that are bodies of revolution. Mesh refining techniques were applied to increase the nodal density in areas of large temperature gradients. Temperature histories were computed using the heat transfer equation and a time-stepping scheme. User supplied boundary conditions, which are time functions of the insolation and meteorological conditions, were defined.

A study of the temperature dependence on environmental conditions shows that the temperature contrast between the mine and background increases with increasing insolation. Convection, introduced mainly by the wind, tends to reduce the contrast. In general, the maximum contrast is achieved near mid day.

Solar radiation, either from direct (sunlight) or scattered (skylight), is the primary source for surface reflections. We employed the MODTRAN code to account for complex atmospheric scattering and absorption effects. The spectral transmittance and skylight radiance were integrated over the sensor passband to yield desired source radiances.

A polarimetric BRDF model was developed to address surface reflection and emission. This approach follows the classical PO model and adopts correction terms from the GO model. The proposed model contains three components: a term for rough surface scattering near the specular direction, a geometric attenuation function that accounts for self-shadowing and multiple scattering, and a diffuse term representing internal scattering. The surface was described by a Gaussian-distributed height and a Gaussian correlation function. A comparison with measured data shows that the model is valid for relatively rough mine-like surfaces. Directional emissivities for the surface were computed via a hemispherical integration of the surface's BRDF.

The radiometric model was assembled from the above source conditions and surface properties with consideration for the problem geometry. Thermal emission and solar reflection are basic components of the model and are computed in a straightforward manner. Calculation of the skylight reflection, which comes from an extended source, involves a spatial integration. Higher-order radiance components, which involve multiple scattering events, arise from the elevated surface-laid mine structure.

The ray tracing techniques was employed, but only the single-bounce thermal emission and double-bounce solar reflection were included because of the intensive computations involved and their limited influence on the signature.

Simulations of various sensor scenarios were conducted to study their effects. The sensor's zenith angle affects not only the mine's apparent shape, but also the polarimetric properties of the signature. An off-nadir sensor exploits differences in the horizontal and vertical polarimetric emissivities to yield significant polarization contrasts and, hence, oblique viewing is desirable for a passive polarimetric sensor. Furthermore, the study of sensor orientation shown that passive polarimetric sensors should be placed near the specular direction of insolation to receive a greater contrast in polarimetric signatures. Three IR sensor bands were explored using a common set of condition. A comparison of individual radiometric components shows that a SWIR signature is dominated by solar and skylight reflection, a MWIR signature is mainly comprised of thermal emission (and a solar reflection that highlights the shadow), and a LWIR signature is overwhelmingly dominated by thermal emission. We also examined the temporal dependence of the signature for the SWIR, MWIR and LWIR bands and found that maximum contrast is achieved during mid day for all bands. According to simulations, SWIR sensors have signatures of the greatest contrast because of the shadow, but their operation is limited to daylight hours. On the contrary, MWIR and LWIR sensors can be operated at all time, but the mine-to-clutter contrast is only a fraction of the received radiance (less than 33%). Finally, we modeled the sensor's point spread function with a Gaussian filter to replicate the blurring introduced by a low-resolution sensor.

## CHAPTER 4

### MODEL VALIDATION AND SIGNATURE ANALYSIS

In this chapter results are presented that validate the radiometric model. Simulations were conducted and successfully compared with images from several sites. Additional results are provided to explain the behavior of the signature.

Section 4.1 presents simulations of the NT-S1 data described in Section 2.7.1. A comparison of data at a specific time are presented first, followed by temporal signature variations for day time, night time, and the so-called “crossover”. Polarimetric signatures are investigated in Section 4.2. Simulations of obliquely viewed mines were performed and compared with polarimetric MWIR imagery collected by TNO. Finally, in Section 4.3 the performance of the model at visible wavelengths is explored using data collected at NT-S2 (see Section 2.7.2). Simulations designed to explore the relation of viewing angle and surface BRDF demonstrate good agreement with measurement and verify the BRDF model.

#### 4.1 Case 1: Temporal Response of Non-Polarimetric Sensor

For the NT-S1 data introduced in Section 2.7.1 one run was selected as the basis for the simulations, which was collected at 11 AM, Oct. 21st, 2002. In Section 4.1.1

the model is validated using data from that run. We also consider a second run collected under similar conditions except that the time was 3:30 PM.

In the remainder of this section, additional simulations are reported for similar conditions. A sequence of simulations was conducted with evenly spaced time steps to examine temporal features of the signatures. Three series of simulation were performed. First, simulations during daylight show that the size and orientation of the mine's shadow tracks the solar position. A second series of simulations studies thermal crossover, which occurs twice daily at dawn and dusk. Finally, simulations after dusk demonstrate different cooling rates for mine and soil.

#### 4.1.1 Radiometric Model Validation

Simulation results for LP\_B mines at NT-S1 at 11:00AM, October 21st were presented previously in Section 3.5.1 and are repeated in Figure 4.1 for convenience. Only the  $I$  component is shown, since only intensity data were measured. Figure 4.2 shows the total simulated intensity after reducing its resolution and rotating to match the sensor orientation.

Figure 4.3 illustrates seven chips containing LP\_B mines from the aforementioned sensor measurement run. Three plastic-cased LP\_B mines appear in three frames. In general, they agree well with the simulated result, including the mine size, shadow size, and general shape of the signatures. The shadow is observed in both simulated and measured images, but some measurements show a shadow that is extended or poorly defined, which we attribute to surface roughness or vegetation.

A quantitative comparison of the model and data is now presented. The measured images comprise pixel readout counts, which are not easily related to radiometric

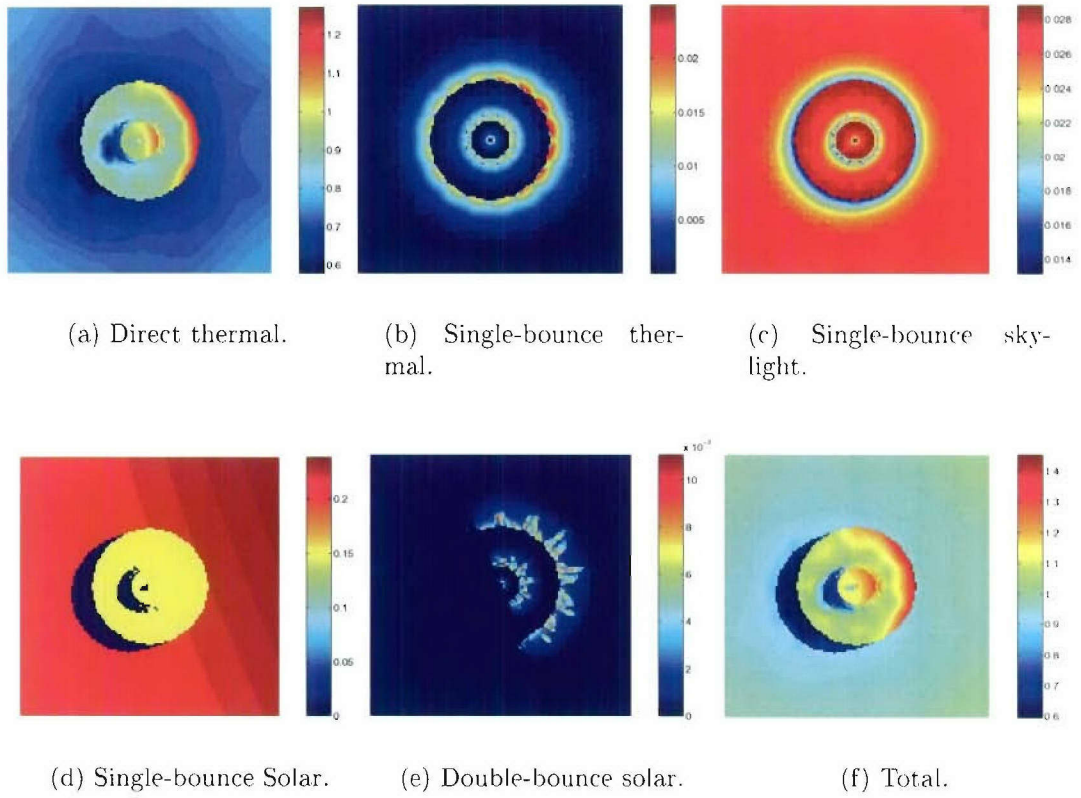


Figure 4.1:  $I$  component of individual and total signatures for “NT-S1” data set at 11:00, Oct. 21st.

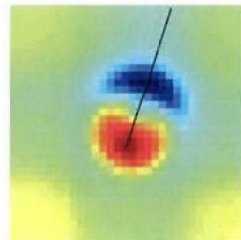


Figure 4.2: Simulated mine signature with cross-section line for radial profile analysis.

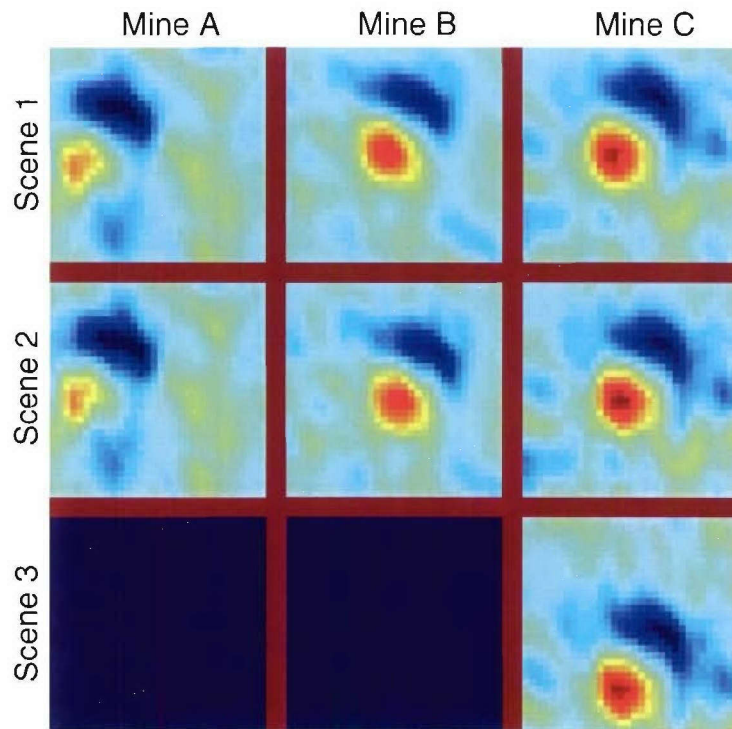


Figure 4.3: Sample mine chips collected at NT-S1, 11:30AM, October 21st, 2002.

units. For this reason, normalized values will be compared. Figure 4.4 compares pixel intensities in simulated and measured images along a cross-section that starts from the maximum (mine's center) and passes through the minimum (shadow's center) of the image (see Figure 4.2). The ensemble average of the measured chips shows that the measured shadow is larger than that seen in the simulation. This effect may be caused by an off-nadir sensor orientation<sup>14</sup> or by large-scale tilts on the soil surface. A thermal simulation of uneven soil by Sendur [12] reported a significant contrast in surface temperatures if large scale slopes were present on the simulated surface. Motion blur may also be present, but a meaningful analysis of platform motion has not been done to date. Overall, the simulator yields a fair approximation to measured data.

Next, simulations were done for 3:00 PM using same surface parameters and appropriate values for the time sensitive parameters (surface temperature profiles, solar angle and irradiance, and skylight distribution). The mine signature is shown in Figure 4.5. Comparing to Figure 4.1 (f), it is clear that the signature at 3:00 PM has a longer shadow and its orientation has rotated roughly 90 degrees. These changes are consistent with the shifts in solar elevation and hour angles.

It is also clear from the magnitude of the radiometric components that direct thermal emission is still the dominant contribution while single-bounce solar reflection provides a secondary correction, especially in the shadow. Therefore, as noted previously, it is sufficient to simulate those two components to obtain a reasonable signature.

<sup>14</sup>A nadir sensor was assumed in the simulation. The actual sensor angle in the measurement is unknown but is less than 10°

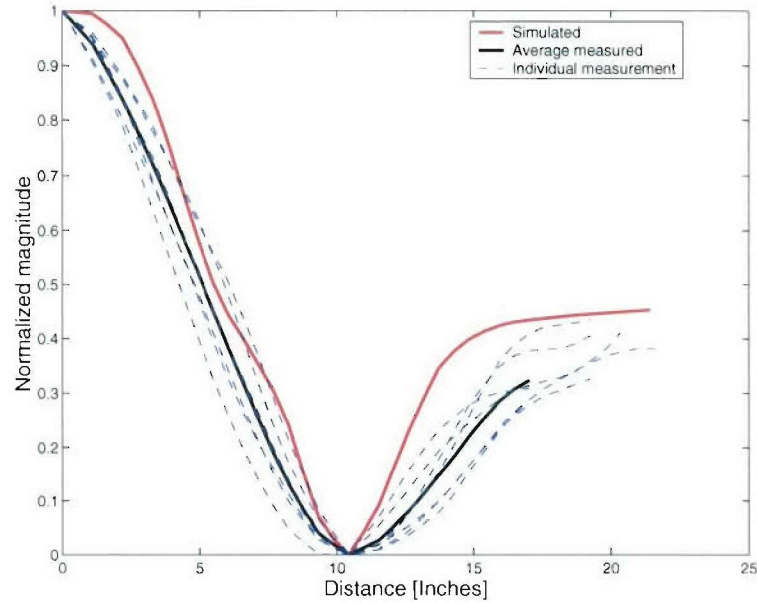


Figure 4.4: Intensity profiles of simulated and measured signatures along a cross-section.

Degrading the simulation’s resolution with the same point spread function in the 11:30 AM case and applying a rotation consistent with the camera heading produces the signature in Figure 4.6. This output compares favorably with the measured data in Figure 4.7, which shows three LP\_B mines in three scenes collected during the run at 3:30 PM. Individual mine signatures were consistent across different scenes, but the size of the shadow varied significantly. This phenomenon is better revealed in the cross-sections in Figure 4.8, which may be attributed to large scale soil roughness. Again, we conclude that the proposed radiometric model yields signatures having reasonable agreement with the measured data.

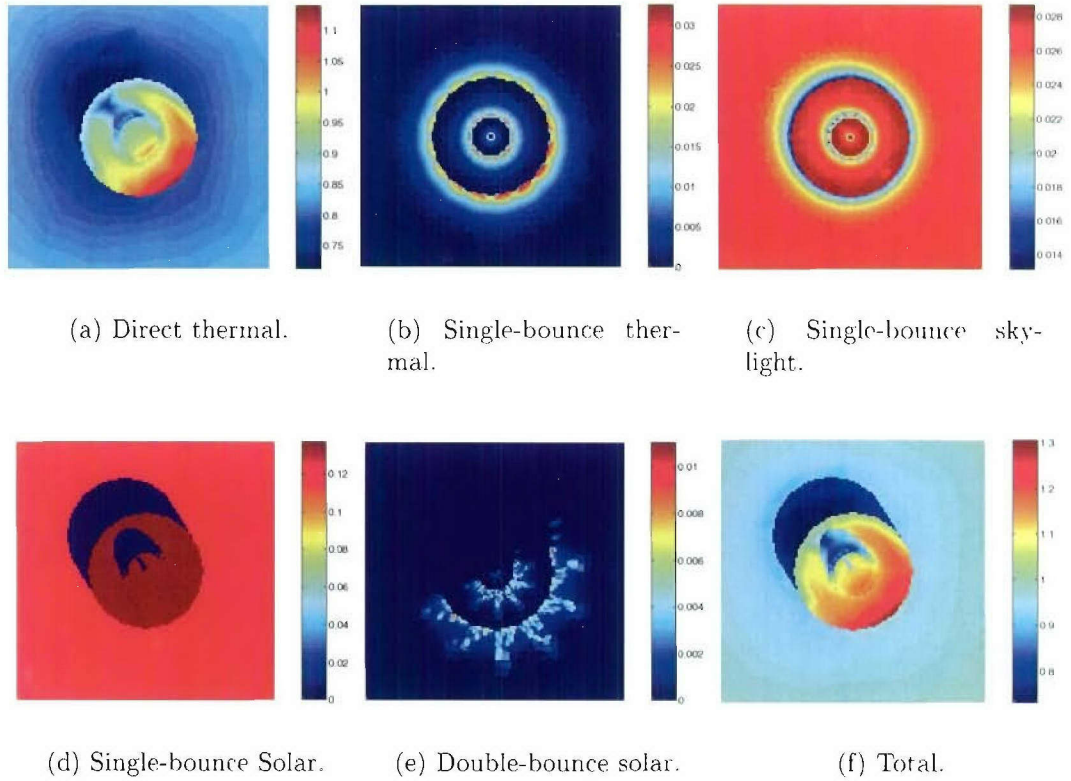


Figure 4.5:  $I$  component of individual and total signatures for “NT-S1” data set at 15:00, Oct. 21st.

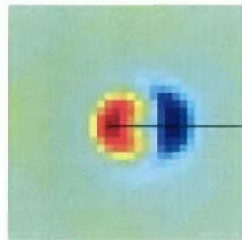


Figure 4.6: Simulated signature for the 3:30 PM run and the cross-section line used for radial profile analysis.

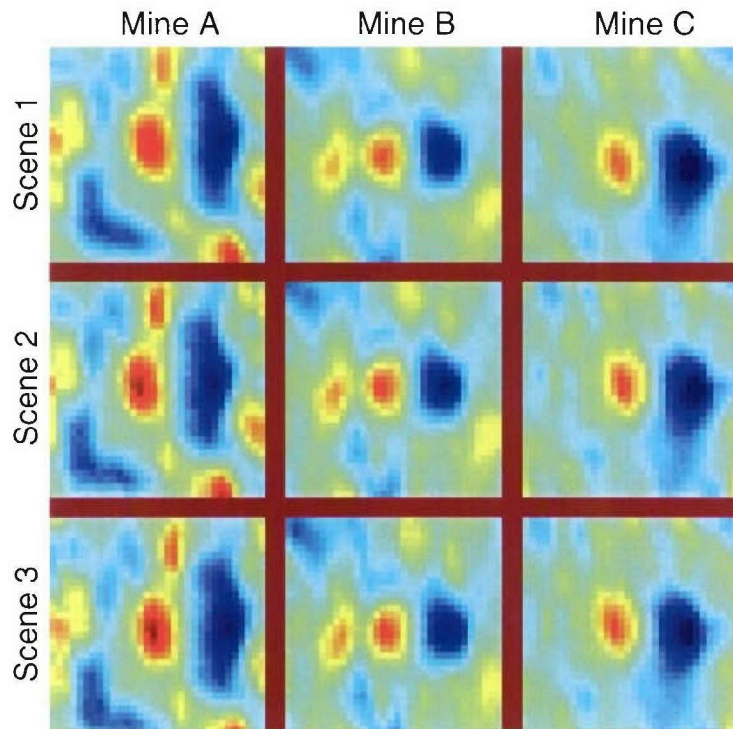


Figure 4.7: Sample mine chips collected at “NT-S1”, 15:29, Oct. 21, 2002.

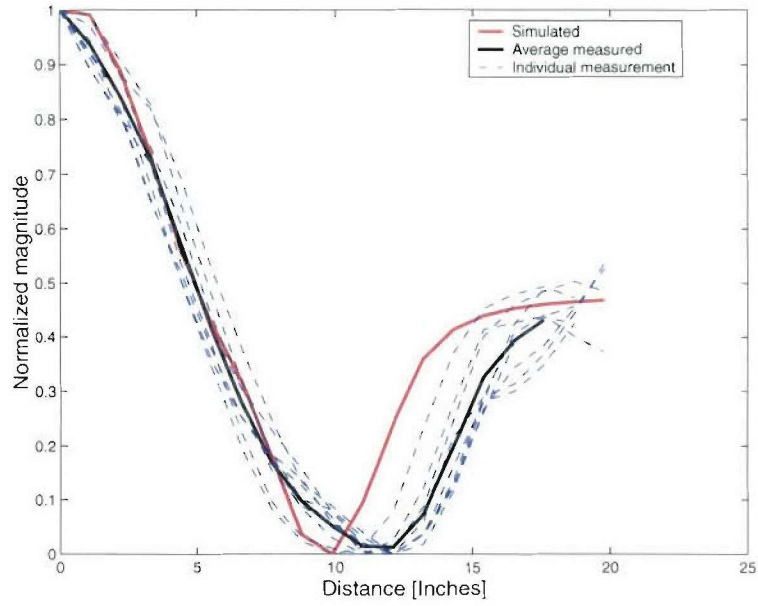
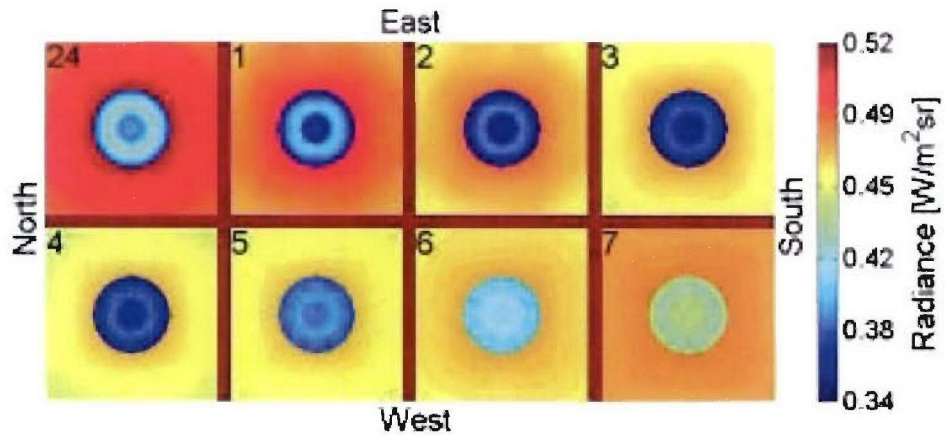


Figure 4.8: Intensity profiles of simulated and measured signatures along a cross-section.

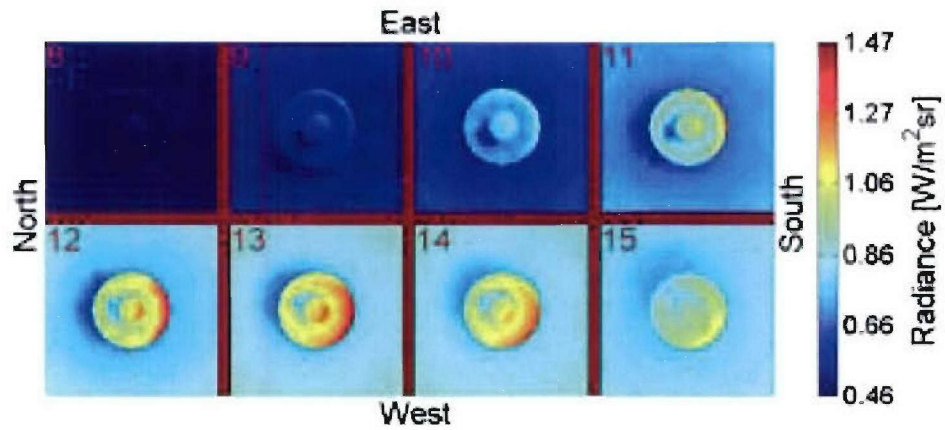
### 4.1.2 Signatures for Sunlit Conditions

Additional simulations were performed hourly for a 24 hour period to study the variation of signatures with time. In this section we present a study of signatures for sunlit conditions. Cases of darkness and crossover are presented subsequently. The signatures of direct thermal emission are shown in Figure 4.9, and the single-bounce solar reflections are added to form Figure 4.10. Comparison of these figures makes the solar contribution evident.

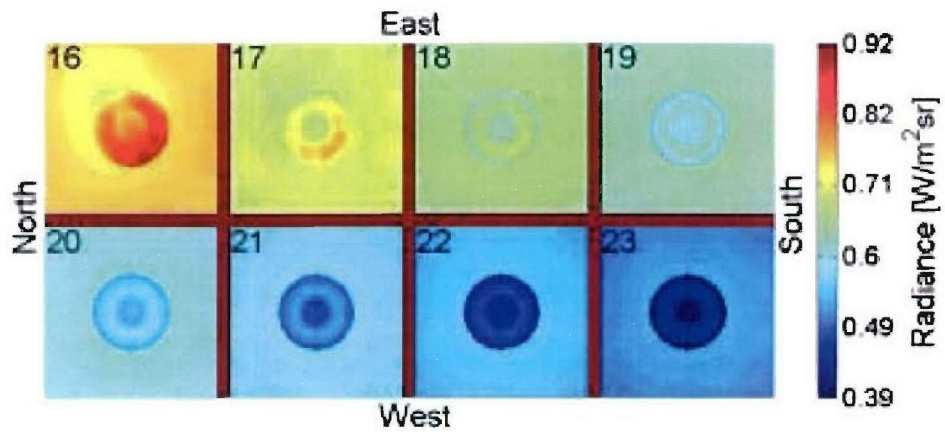
Figure 4.9 (b) shows a mosaic composed of thermal emission signatures simulated hourly from 8 AM through 3 PM. A common scale has been used for each block of 8 images to facilitate comparisons. Several signature features are evident. As expected, the soil is hotter during the afternoon (12 PM to 3 PM). The mine, which was cooler



(a) 24:00-7:00.

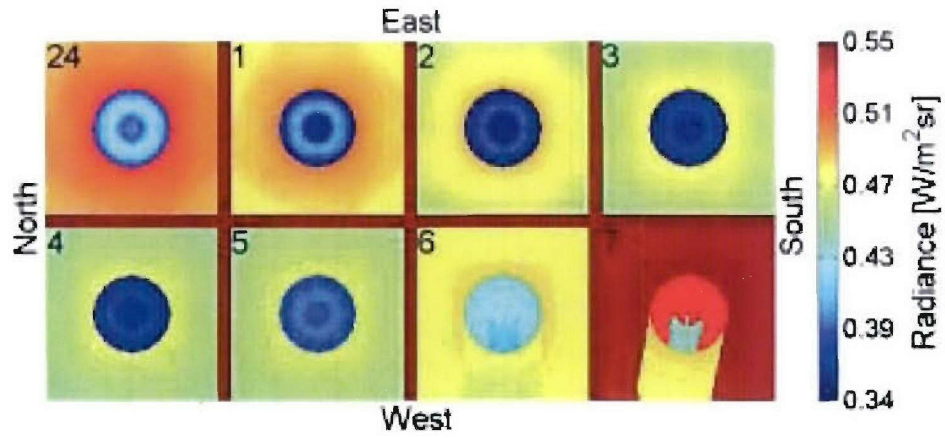


(b) 8:00-15:00.

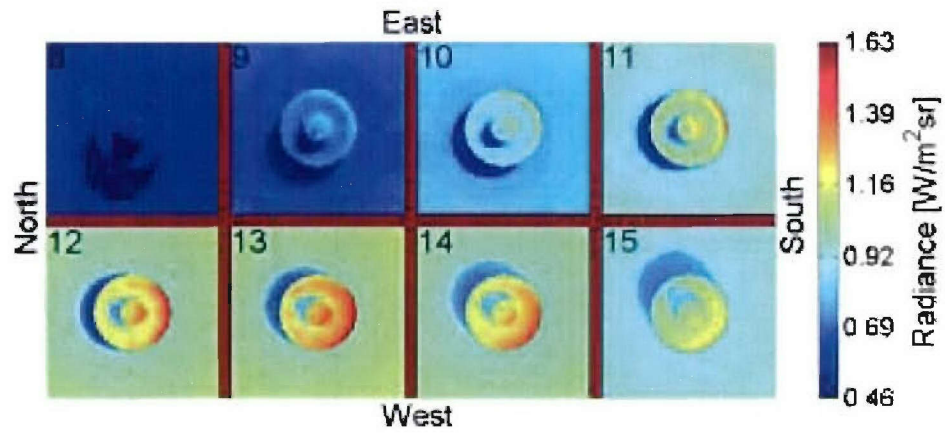


(c) 16:00-23:00.

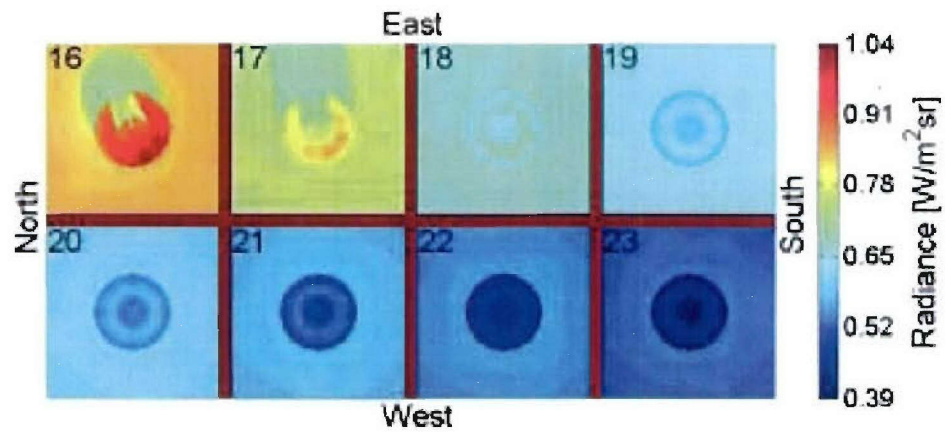
Figure 4.9: Mosaic of “direct thermal emission” during morning (24:00-7:00), noon (8:00-15:00) and evening (16:00-23:00).



(a) 24:00-7:00.



(b) 8:00-15:00.



(c) 16:00-23:00.

Figure 4.10: Mosaic of total radiometric signatures during morning (24:00-7:00), noon (8:00-15:00) and evening (16:00-23:00).

than the soil in the morning, was also heated by insolation, but the rate of change in the mine surface temperature was larger. This occurs because the mine contains an air space<sup>15</sup>, which isolates the top of the mine from the remainder below. Solar driven heating of the small thermal “mass” on top of the mine produces a larger temperature rise than the soil.

Because of computational limitations, the thermal model output does not accurately reproduce the shape of the shadow. The nodal density of the mesh decreases as the distance from the mine center increases and, hence, the spatial sampling density eventually becomes too low to accurately represent the shadow boundary. With sufficient memory and computation power, a more refined mesh should avoid this problem.

The mine’s shadow provides another potentially detectable thermal feature. Figure 4.11 plots the solar elevation angle and the amount of solar irradiance during a diurnal cycle, both of which are critical in determining the size and contrast of the shadow. The mine structure is clearly revealed by the reflected solar radiation (see Figure 4.12). When the soil near the mine is shadowed, its normal temperature evolution is stalled or reversed. The second deck of the mine also imposes a small shadow on the top of the first deck.

The contrast between the mine and soil is strongly influenced by their BRDFs and the solar elevation angle. For sensors that do not see a specular glint, solar reflections from the (relatively smooth) mine come mainly from the diffuse component, whose magnitude varies approximately as the cosine of the solar elevation angle. Conversely, the soil surface, which is assumed rougher, has a very broad scattering lobe that

<sup>15</sup>The air space is often the result of a construction process or the void required for a pressure activated trigger.

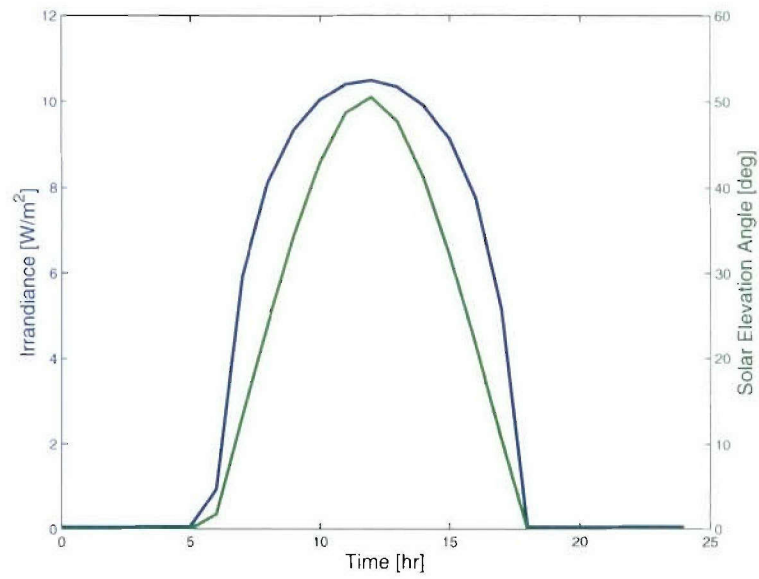


Figure 4.11: Solar elevation angle and irradiance on Oct. 21, at “NT-S1”.

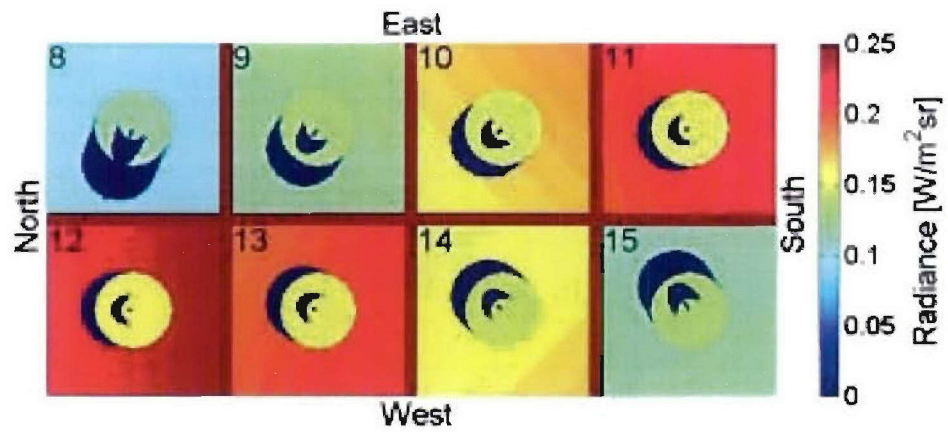


Figure 4.12: Mosaic of “single-bounce solar reflection” signatures during day time (8:00-15:00).

approximates a diffuse return. Figure 4.13 compares the radiance reflected from mines and soil surfaces at 8 AM and 12 PM at the solar meridian for nadir viewing. At 8 AM the nadir sensor only observes the diffuse components from both surfaces, and the mine provides a stronger reflection as required by its surface parameters (see Table 3.4). At 12 PM the main lobe of the soil BRDF encompasses the nadir direction and its intensity exceeds the mine's reflection. Hence, we see in Figure 4.12 that reflections from the soil are stronger around mid day (11:00-13:00).

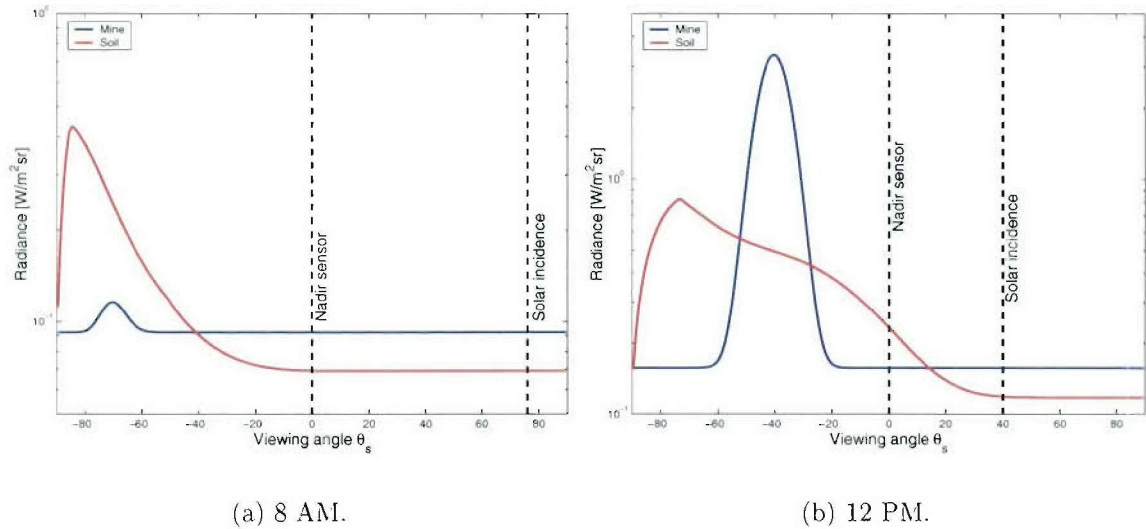


Figure 4.13: Reflected radiance on the solar meridian from mine and soil surfaces at 8 AM and 12 PM, Oct. 21st.

Figure 4.10 (b) illustrates the combined effect of direct thermal emission and single-bounce solar reflection. As noted in Chapter 3, the signatures are dominated by thermal emission, while the solar reflection provides a well-defined shadow. The simulations suggest that in the MWIR band surface landmines produce a stronger response in the early afternoon, because of higher surface temperatures.

### 4.1.3 Signatures During Darkness

Simulations were performed for the “NT-S1” conditions at 11 PM when no insolation is present. Of the five radiance components included in our model, only three components are present in this scenario: thermal emission (direct and single-bounce paths) and reflected skylight. Figure 4.14 shows the three components and indicates that direct thermal emission is the dominant factor. (Maxima of reflected skylight and single-bounce thermal emission are about 2% and 5% respectively of the maximum direct thermal emission.) Figure 4.15 compares the total signature and the surface temperature. Their features are essentially the same, and we conclude that during the night, only direct thermal emission is needed to simulate MWIR signatures.

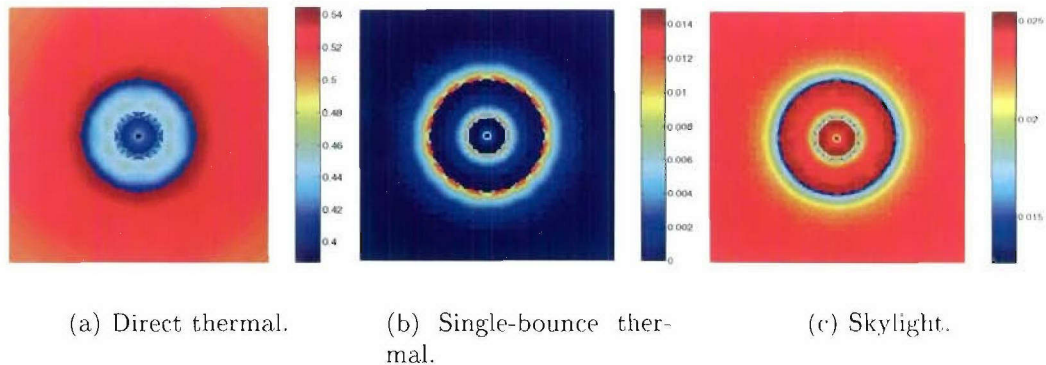


Figure 4.14: Simulated signatures of direct thermal, single-bounce thermal, and reflected skylight for “NT-S1” conditions at 23:00.

During darkness, stored energy is dissipated via emission and convection. A mine stores far less thermal energy than the surrounding soil, and it releases that energy more quickly. Note also that the upper deck of the mine, which has a larger surface-area/volume ratio because of the internal void, cools at an even faster rate. We

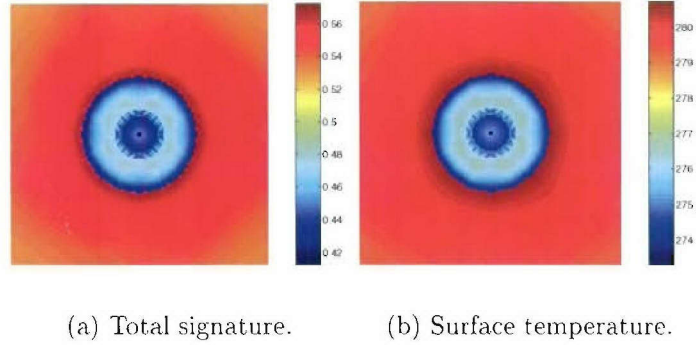


Figure 4.15: The total radiometric signature and surface temperature for “NT-S1” conditions at 23:00.

also find that the mine signature is symmetric in  $\hat{\phi}$  during darkness as shown in Figures 4.10 (a) and (c). This arises since the structure is symmetric, and there is no directional preference for thermal emission or convection in the model<sup>16</sup>.

#### 4.1.4 Signatures at Dawn and Dusk

An important phenomenon in IR surface mine detection is “thermal crossover”, which occurs when the surface temperatures of mine and soil are equal. During crossover, which occurs twice daily around dawn and dusk, EO sensors are less capable of differentiating mines from background, since thermal emission dominates the signature and the contrast vanishes. From previous simulations and discussions, however, we know that other components contribute to the radiometric signature. In this section we review simulations performed for dawn and dusk to better understand the underlying physics at these important times.

<sup>16</sup>Asymmetries in heating caused by the setting sun tend to be weak and rapidly decay in the absence of continued heating

Simulations around dawn can be found in Figures 4.10 (a) and (b). At 6 AM the sun has not risen, and the mine is cooler than the surrounding soil. At 7 AM the low angle sun casts a very long shadow while the radiance from the mine surface is still weaker than the soil. Thermal crossover occurs near 8 AM, when the intensity of mine and soil are largely equal except in the shadow. At 9 AM the mine surface is heating rapidly and shows a distinctive contrast.

The image at 8 AM has an interesting implication. Since the morning thermal crossover occurs after sunrise, the mine signature is still detectable because of the shadow. If mine detection is required around the morning crossover, it is appropriate to search for the shadow instead of the mine.

Next, we examined the afternoon thermal crossover. Simulation results around dusk are illustrated in Figure 4.10 (c). We found that thermal crossover occurs soon after sunset, since mines cool more rapidly than soil. Due to the lack of insolation, the night-time radiometric features are produced solely by thermal emission. Figure 4.10 (c) indicates that thermal crossover happens between 6 PM and 7 PM. Although the temperature is not homogeneous across the mine, detection is extremely difficult during the evening crossover, because no other helpful information (e.g., the shadow) is present.

## 4.2 Case 2: Polarimetric MWIR Signatures

Polarimetric imaging sensors are finding broader use in remote sensing, because they provide more information per pixel. Polarimetric sensors are also being explored for mine detection, and for this reason our radiometric model was built with polarimetric capabilities.

Various methods have been used to collect polarimetric imagery, including rotating polarizers or splitters that separate horizontally and vertically polarized light. A particularly convenient method of acquiring polarimetric data is to use a rotating linearly polarized filter at  $0^\circ$ ,  $45^\circ$ ,  $90^\circ$ , and  $135^\circ$ . The  $I$ ,  $Q$ , and  $U$  parameters can be derived using those four channels and appropriate transformations. Measurements made with two orthogonal filters ( $0^\circ$  and  $90^\circ$ ) will produce the  $I$  and  $Q$  parameters. Such measurement cannot be used to acquire the circularly polarized  $V$  component, since they comprise incoherent samples of linear polarization.

Polarimetric measurements of land mines were conducted by the TNO Physics and Electronics Laboratory [13] at the Netherlands during late November, 2001. The TNO data set was described briefly in Section 2.7.3. In this section, we present simulations performed to reproduce those measurements. The relative importance of individual radiometric components is discussed. Comparisons of simulated signatures and measured data appear at the end of this section.

### 4.2.1 Parameter Selection for TNO Data

Similar to what was done for the NT-S1 data set, model parameters had to be selected to describe the TNO environment. The viewing geometry requires a more precise description. Unlike the NT-S1 case, which involves long-range viewing at

near-nadir angles, the TNO sensor was positioned a shorter distance from the test site with a large nadir angle. This geometry can produce large variations in viewing angles across the scene, which must be taken into account during simulations.

The images used here are from the TNO surrogate LP mine indicated by the red box in Figure 2.7. The nominal viewing angle for this mine is  $70^\circ$  (with respect to nadir), but because of the aforementioned variation in viewing angles across the scene, as well as the potential for small site surface deviations from planarity, a  $68^\circ$  angle was found to better replicate the data.

Surface roughness depends on the degree of soil compaction. The BRDF model requires the surface roughness, the refractive index, the albedo ratio  $\rho_{dc}/\rho_{dx}$  for the diffuse term and the relative magnitudes of surface and diffuse scatterers. Because these properties of the site were not measured, they were estimated from the measurements.

The TNO surrogate mine has a case made with commercially available PVC pipe and flat sheets, and it was filled with RTV. Because of unavoidable construction differences between real and surrogate mines, it is reasonable to expect some differences in their signatures. To date, there have been few comparisons of real and surrogate mine signatures [6]. The scattering and thermal properties used for the surrogate mine were taken from the literature and adjusted to fit the measured data. Table 4.1 gives the mine and soil surface parameters used in this simulation. Note that slightly different surface parameters were used for the PVC plate (used for the mine's top surface) and pipes (side walls), corresponding to material with different finishes, or from different vendors.

Surface type	PVC pipe (mine sidewall)	PVC plate (mine top)	Soil
Refractive index ( $n$ )	1.4	1.4	1.6
Slope variance ( $s^2$ )	0.01	0.005	0.35
Diffuse component	0.01	0.005	0.005
Depolarization ratio	0.5	0.5	0.5

Table 4.1: Surface parameters used in simulations of TNO’s surrogate LP mines.

#### 4.2.2 Comparison to Measured Polarimetric Images

As observed in Section 3.6, it is important to consider the finite resolution of the sensor when comparing simulations to measurements. Because the TNO sensor is located close to the test site and the sensor resolution is relatively high, we a point spread function as described in Section 3.6 with a compact resolution (1.1 pixels) then down sample the simulations to yield the final product seen in the second row of Figure 4.16. The simulations are similar to the signatures in Figure 4.23, although some glints in the simulation do not appear in the measurements.

The measured TNO images are shown in the first row of Figure 4.16 with a color scale common to the simulated results, and they are in qualitative agreement with the simulations. High intensity regions, such as the side wall facing the sun, and cool regions, such as the shadow, appear in both sets of images. It is apparent, however, that the simulation predicts heated regions that are weaker than measured. Reasons

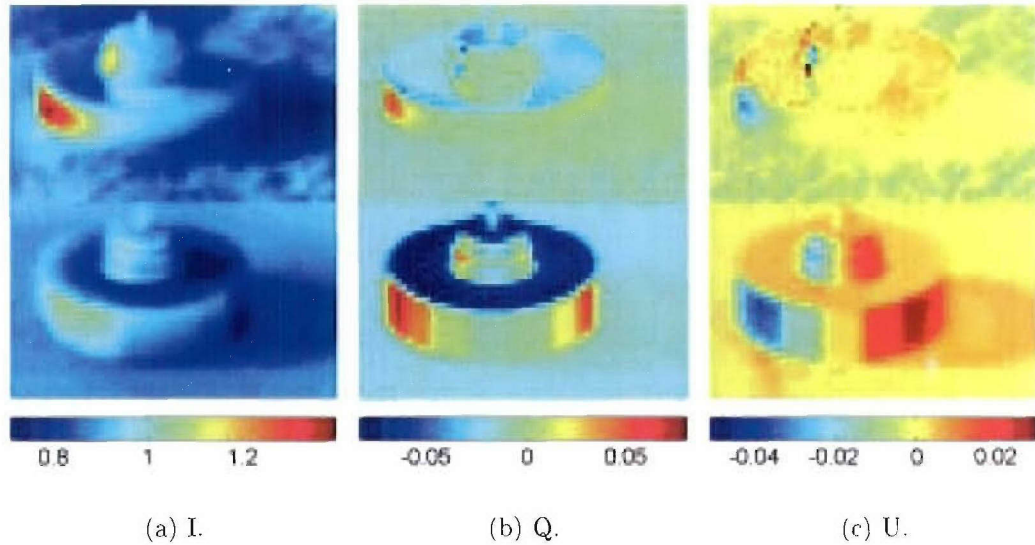


Figure 4.16: Simulated (first row) and measured (second row)  $I$ ,  $Q$ , and  $U$  parameters for the “TNO” data set with reduced sensor resolution.

for this difference may include incorrect thermal properties or solar-bands albedos for the mine’s PVC case.

Spot checks of the images suggest that good quantitative agreement in the background regions has been obtained, although the measured results show some variation that is probably related to large scale surface roughness in soil and soil inhomogeneities. A limitation of the simulation is that random large-scale variations in local surface tilt and thermal properties of soil have been ignored. In the measured data, the background area appears somewhat “blotchy” while the simulated signature captures only the average properties of the rough surface. Fine scale graininess in the measurement is the result of sensor noise.

### 4.2.3 Evaluation of Signature Components

In an effort to gain insight, the model was used to simulate the individual radiometric signature components. In this section the resulting Stokes parameters are shown.

Figure 4.17 illustrates the  $I$ ,  $Q$ , and  $U$  parameters for the direct thermal emission component. Because an MWIR sensor was used, thermal emission was expected to dominate the signature. The intensity ( $I$ ) parameter suggests that the south side of the mine's side wall is heated by the low-angle winter sun in The Netherlands. The soil (dry sand), which responds more quickly to insolation than the mine, produce a strong, well-defined shadow. For the  $Q$  and  $U$  parameters, the signatures were comparatively weak, since thermal emissions were only slightly polarized by the limited difference in horizontal and vertical emissivities. The signature reveals the local surface shape of the mine. High values in the  $Q$  parameter correspond to facets on the mine wall oriented to maximize depolarization. For a smooth surface, that orientation corresponds to the Brewster angle. For horizontal planar surfaces (i.e., the mine top and soil surface), differences in the  $Q$  parameter of mine and soil come from differences in the ratio of co- and cross-polarized emissivities near grazing. The  $U$  parameter, which indicates the degree of linear polarization in  $45^\circ$  planes, produces different signs across the axis of symmetry.

We next examined the single-bounce solar reflection, shown in Figure 4.18. The  $I$  parameter takes on only a few discrete values, because the camera was positioned and oriented far from the specular glints. As a result, the simulated results come mostly from the diffuse component. The  $Q$  parameter exhibits interesting features. The figure shows that  $Q$  values for the mine and its shadow are near zero, while

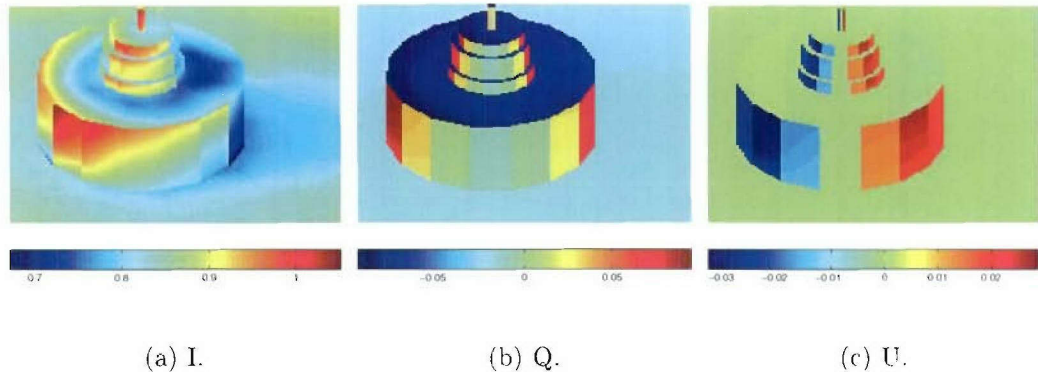
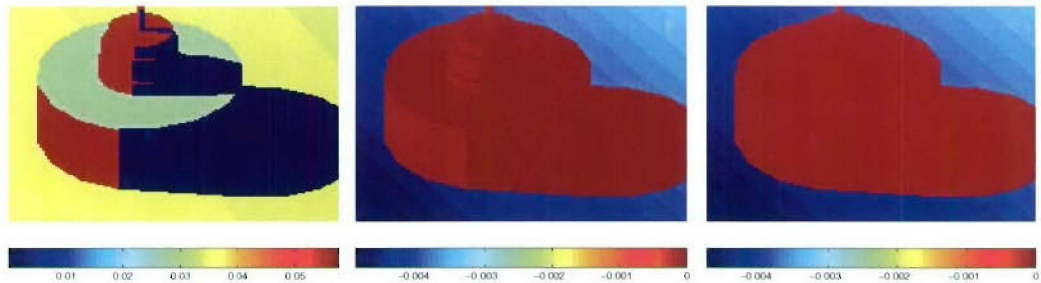


Figure 4.17: Simulated  $I$ ,  $Q$ , and  $U$  parameters for direct thermal emission for the “TNO” data set.

the rest of the soil shows a small negative value. Insight into this result is available from the DoLP plot shown in Figure 4.19, which can be explained by the BRDFs involved and their relation to the solar position. The illuminated surfaces of the mine in Figure 4.19 are relatively smooth. For those surfaces, the specular return is highly localized, producing very little radiance at the sensor. Therefore, the DoLP of the illuminated mine surface is dominated by the diffuse term, which produces zero DoLP. Conversely, surface scattering from the rough soil has a preferred polarization, resulting in a DoLP around -10%. The negative sign is a result of the solar position. The same logic can be used to explain the  $U$  image. Note that the DoLP in the shadow region in Figure 4.19 is not defined, since both  $I$  and  $Q$  are zero.

Figure 4.20 illustrates the single-bounce skylight reflection. This component has a weak intensity in the IR band, because air particles scatter weakly for longer waves. The single-bounce skylight signature at a point is approximately the product of the



(a)  $I$ .

(b)  $Q$ .

(c)  $U$ .

Figure 4.18: Simulated  $I$ ,  $Q$ , and  $U$  parameters for single-bounce solar radiation for the “TNO” data set.

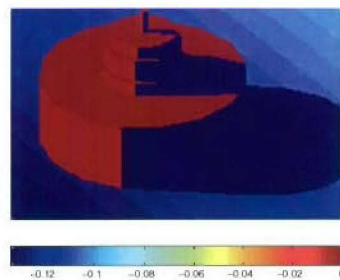


Figure 4.19: DoLP of single-bounce solar radiation for the “TNO” data set.

visible sky area and the incident diffuse skylight. Recall that skylight is partially linearly polarized, which leads to a nontrivial polarimetric response. The  $Q$  and  $U$  levels are comparable to those of the direct thermal and single-bounce solar components.

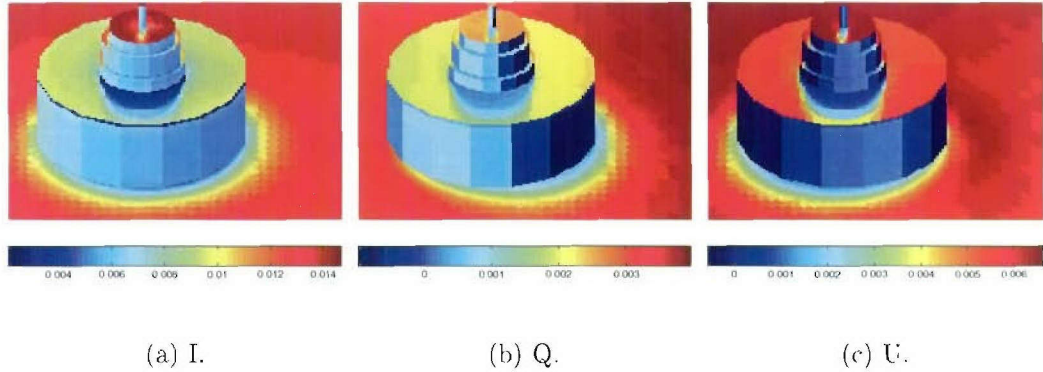


Figure 4.20: Simulated  $I$ ,  $Q$ , and  $U$  parameters for single-bounce skylight radiation for the “TNO” data set.

The single-bounce thermal emission is shown in Figure 4.21. In the  $I$  image, brighter pixels such as those on the side wall are the result of nearby facets that present larger projected solid angles and, hence, collect more reflected thermal emission. Nonetheless, even the strongest reflected thermal contribution is negligible compared to the direct thermal emission.

The  $Q$  image has many of the features described in Figure 4.17 (b). Because the mine’s side walls are orthogonal to horizontal soil surfaces, the polarizations of facets near where the mine contacts the soil switches as one moves from the the soil to the mine’s side walls Point pairs across the axis of symmetry have emissions with the same vertical field but horizontal fields of different signs, which leads to an inversion of the DoLP.

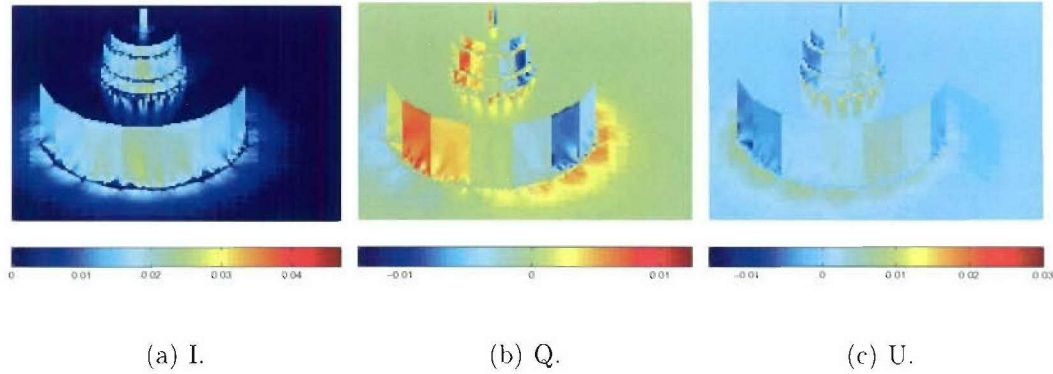


Figure 4.21: Simulated  $I$ ,  $Q$ , and  $U$  parameters for single-bounce thermal emission for the “TNO” data set.

Figure 4.22 shows the double-bounce solar reflection. The most intense pixels in these images are located on one panel of the mine’s polygonal side wall on both lower and upper decks and are caused by (imperfect) specular reflections of the sun by the soil and side wall in turn. Although the intensity  $I$  of this component is small compared to other components, its  $Q$  and  $U$  parameters are relatively strong.

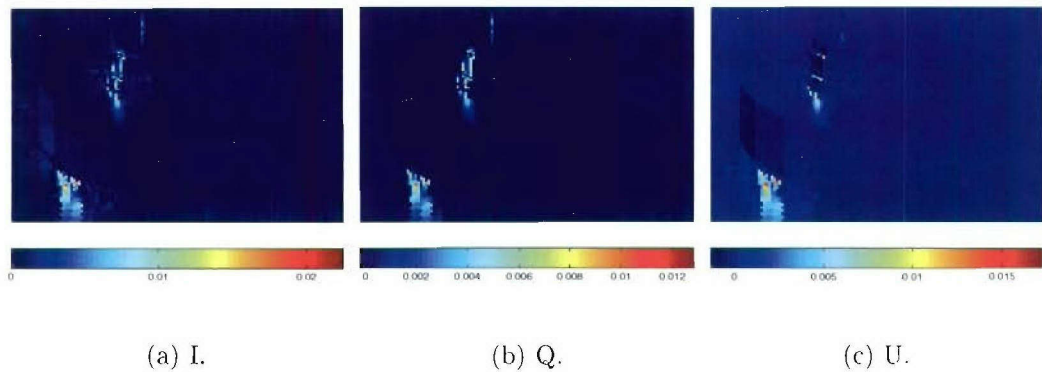


Figure 4.22: Simulated  $I$ ,  $Q$ , and  $U$  parameters for double-bounce solar radiation for the “TNO” data set.

Stokes parameters corresponding to the sum of all five components are displayed in Figure 4.23. As expected, the direct thermal emission dominates the  $I$  image, with corrections from the single-bounce solar reflection. For the  $Q$  and  $U$  images, every radiometric component makes a significant contribution, since they are all of the same order. The polygonal approximation of the mine is clearly evident, which suggests that a finer discretization is appropriate. Finally, the shadow of the mine is visible, because of strong scattering of the insolation by the rough soil surface.

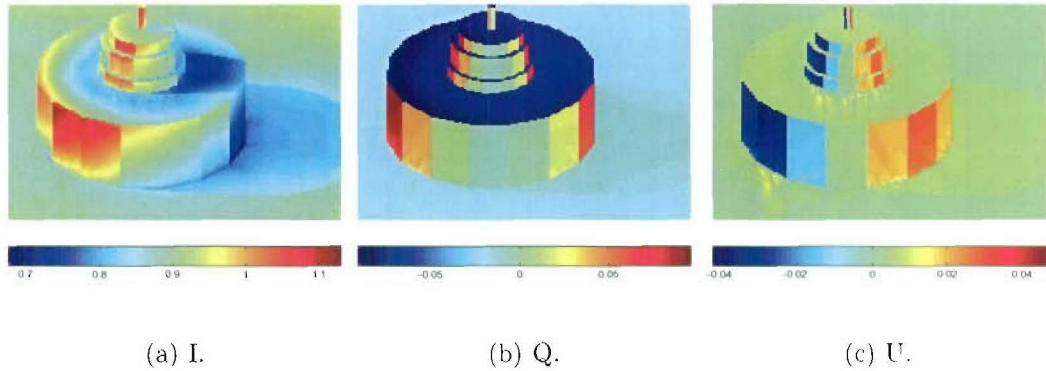


Figure 4.23: Simulated  $I$ ,  $Q$ , and  $U$  parameters for total radiation for the “TNO” data set.

Concluded from the comparison to measured signatures and the evaluation of individual components, we see that under an obliquely viewing sensor, polarimetric components are mostly the results of the viewing geometry and are less subjective to changes in temperature. Therefore, polarimetric signatures are prone to be more stationary features of mine and can be regarded as auxiliary channels to the intensity signature. Multispectral image processing techniques are applicable to enhance the signal-to-noise ration and improve the detection performance

### 4.3 Case 3: Non-polarimetric Visible Band Imagery

Sensors of visible band radiance are commonly used in mine detection, and in this section simulations of mine signature for visible cameras are presented. We noted that visible sensors are attractive for some applications, since they can be made compact with high resolution and low noise. (See Appendix B for further discussion.) Unfortunately, their effectiveness depends greatly on the environmental conditions. They cannot detect thermal emission. Passive visible sensors rely solely on reflected solar radiation, which is subject to greater absorption by hydrosols (clouds and fog). As a result, their use is restricted to daylight hours and clear weather.

As noted in Section 2.7.2, the US Army performed measurements on surface-laid mines using a visible camera during late May 2000 at site NT-S2. Multispectral imagery was collected by using a spinning wheel with five filters in front of the objective lens. Many measurements were performed including a series of images taken at the same site at different times. That image sequence forms the basis for the present study. Simulations were performed under similar conditions to further test the simulator.

#### 4.3.1 The NT-S2 May 2000 Data

Section 2.7.2 gives a detailed description of the test site. In this section we discuss some properties of the visible imagery.

The VNIR camera (visible and near IR) used at NT-S2 acquired imagery in five sub-bands. In this work images from three sub-bands, denoted red, green and blue, were combined to cover most of the visible band. Figure 4.24 illustrates the frequency

responses of the blue, green, and red sub-bands. The actual responses are shown as solid lines, while the dashed line shows the sum of all three channels.

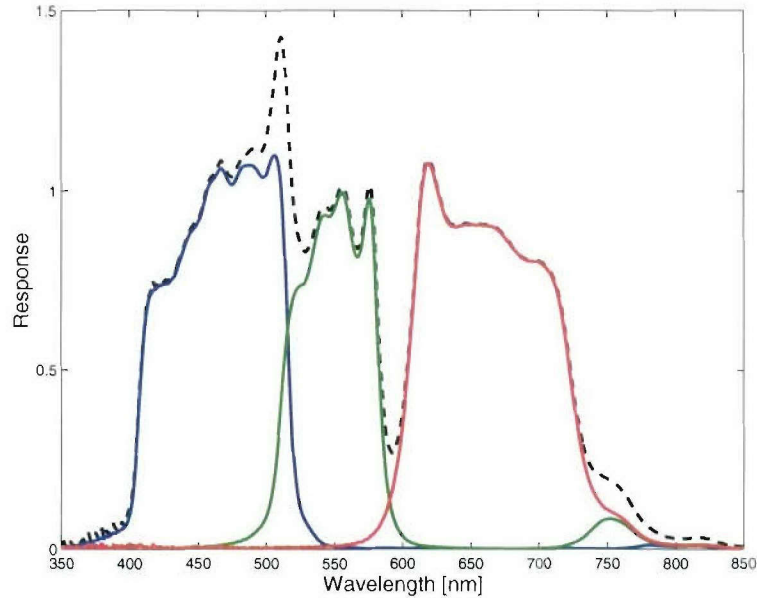


Figure 4.24: Frequency response of R, G, and B channels of the visible camera.

The raw imagery is pixel “counts” ( $C$ ), which are converted into radiance ( $L$ ) using an equation given by [72] as follows:

$$L = G \frac{C - O}{T_E + T_D} \quad (4.1)$$

where  $T_E$  and  $T_D$  are camera exposure time and shutter delay time respectively,  $O$  is the offset parameter, and  $G$  is the in-band radiance gain. Table 4.2 lists values of above parameters for the images in Figure 4.25.

Figure 4.25 shows blue, green and red sub-band images taken around 11 AM on May 24th, 2000. The responses in individual sub-bands are similar to one another. The synthesized broadband visible image, denoted “fused”, also shown in Figure 4.25,

Sensor channel	Red	Green	Blue
Radiance Gain $G$	0.299	0.207	0.096
Radiance Offset $O$	35.1	35.1	35.1
Exposure Time $T_E$	23	35	13
Shutter Delay $T_D$	12.88	12.88	12.88

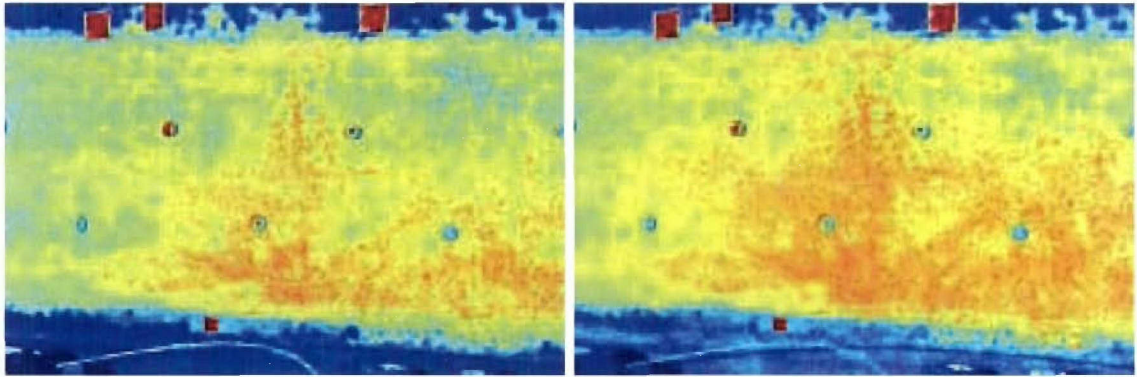
Table 4.2: Radiometric calibration parameters for visible band images at 11 AM, May 24th, NT-S2.

is, of course, similar to the sub band images. The broad horizontal region that fills most of the images is bare sand, which reflects the insolation. The top and bottom edges are covered with short grass, which absorbs strongly. Five surface-laid LM.B mines show high contrast with the sand background. Several square fiducial markers with strong responses appear near the lane boundaries. The lower right corner shows the tires of the scissors lift used to elevate the sensor.

In addition to the 11 AM images shown in Figure 4.25, three more fused images were composed to study the temporal variation of visible band mine signatures. Figure 4.26 shows the same scene at 12 PM, 3:30 PM, and 5 PM. The 5 PM image shows an unknown object in the lower-left corner, which will not affect the present study. During image collection the sensor’s FOV shifted slightly from one scene to another. The mine signatures were compared using image chips that were extracted manually from each scene.

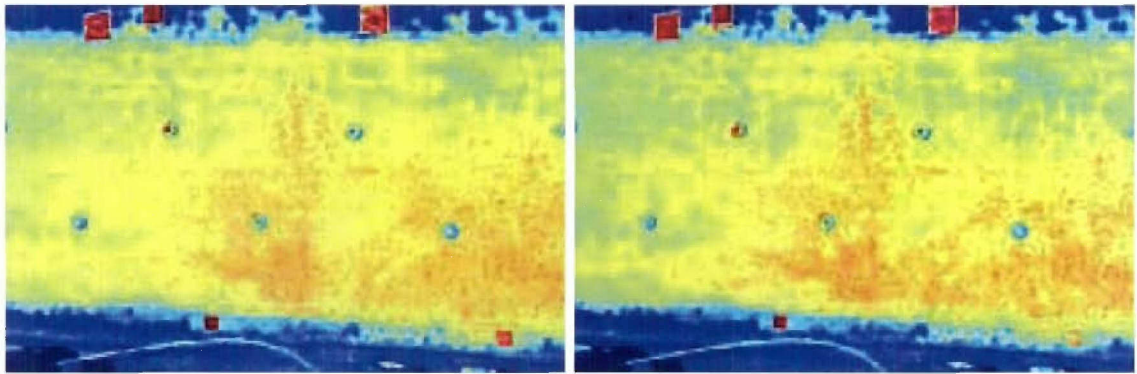
### 4.3.2 Illumination and Scattering Properties in the Visible Band

In addition to the sensor frequency response presented above, the simulation also requires a description of the incident radiance and the surface scattering properties of



(a) Blue.

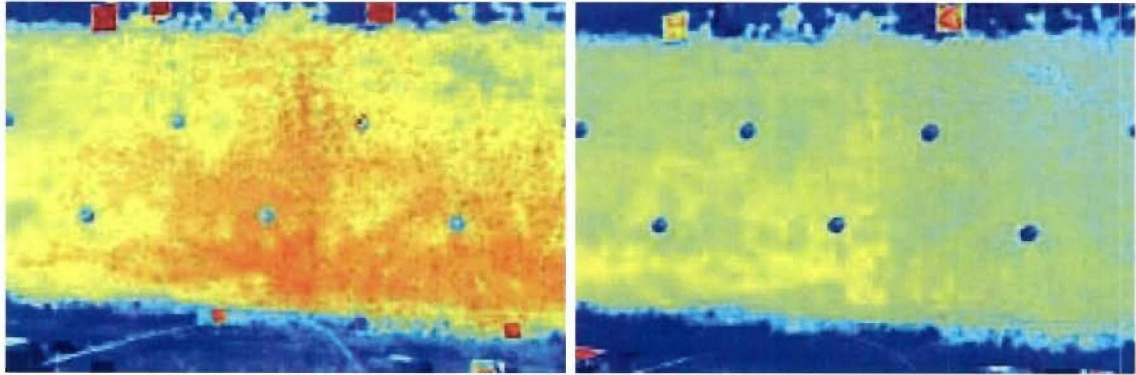
(b) Green.



(c) Red.

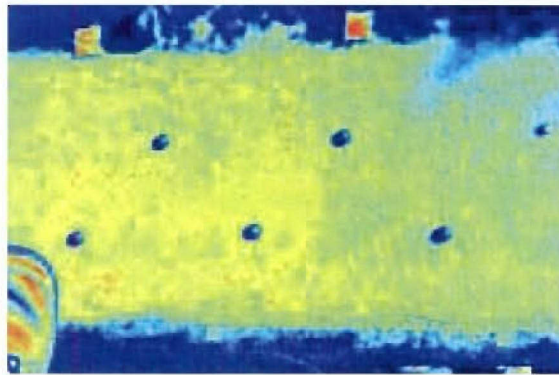
(d) Fused.

Figure 4.25: Measured response in R-, G-, and B-channels and fused image collected by the visible camera from the “NT-S2” data set at 11:00 AM, May 24th, 2000.



(a) 12:00 PM.

(b) 3:30 PM.



(c) 5:00 PM.

Figure 4.26: Fused measured images collected by the visible camera from the “NT-S2” data set at 12:00 PM, 3:30 PM, and 5:00 PM on May 24th, 2000.

the target and environment. In this section we first describe the visible band sources: sunlight and skylight. We next present surface roughness parameters in the visible band.

Procedures similar to those presented in Sections 3.2.3 and 3.2.4 were used to estimate the total (spectral) solar and skylight radiance. Planck's law predicts that thermal emission from objects near ambient temperatures ( $\sim 290^\circ\text{K}$ ) will be small at visible wavelengths. As an example consider the ratio

$$\frac{L_{BB}(\lambda = 0.5\mu\text{m}, T = 290\text{K})}{L_{BB}(\lambda = 5\mu\text{m}, T = 290\text{K})} = 10^{-5} \quad (4.2)$$

which shows that thermal emissions at visible wavelength are vastly weaker than those at MWIR. For this reason, thermal emissions are ignored in what follows. The solar irradiance calculation, which was performed for a mid-latitude summer atmosphere, is documented in Figure 4.27 for a sun at zenith. The blue curve is the extraterrestrial solar irradiance spectrum produced by MODTRAN. The spectral transmittance coefficients generated by MODTRAN are plotted in green, and the product of the two curves, shown in red, is the spectral solar irradiance on the ground. As done previously for broadband sensors, the spectral irradiance is integrated over the sensor pass-band to yield the total solar irradiance used in the radiometric model.

The solar irradiance varies with solar elevation angle as shown in Figure 4.28. In this result the spectral integration has already been done. Two atmospheric models are shown in the figure. The blue curve is the result of a rural extinction model, which contains fewer aerosols and allows more transmission of solar incident flux. The red curve, which represents an urban atmosphere is modeled by a greater aerosol density (from pollutants) and yields both a shorter extinction distance and a lower transmittance. In general, the total solar irradiance is much greater in the visible band

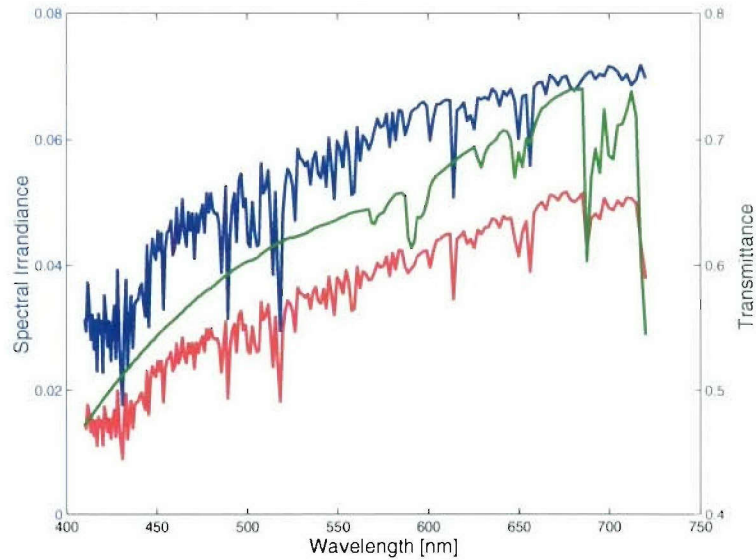


Figure 4.27: Sample visible band extraterrestrial and ground solar irradiance spectrum and atmosphere transmittance for a zenith sun.

than in the MWIR band (see Figure 3.15), primarily because of the sun's spectral signature (a  $5900^{\circ}$  K blackbody radiator).

Like the solar irradiance spectrum, the skylight spectral and angular distributions must be recalculated for each time. Figure 4.29 shows a sample skylight profile for 12 PM, May 24th, at NT-S2. The figure shows that the total skylight irradiance is about one third of the solar irradiance. Therefore, skylight, which can be neglected in the IR band, is an important source in the visible band.

The degree of linear polarization at visible wavelengths should be somewhat smaller than predicted by a simple Rayleigh model, because multiple scattering happens more frequently at shorter wavelengths and thus cancels the polarization. Nonetheless, we will continue to use the Rayleigh model [17] in Equation 2.15 to predict skylight polarization for two reasons. First, we use a clear-sky atmosphere model,

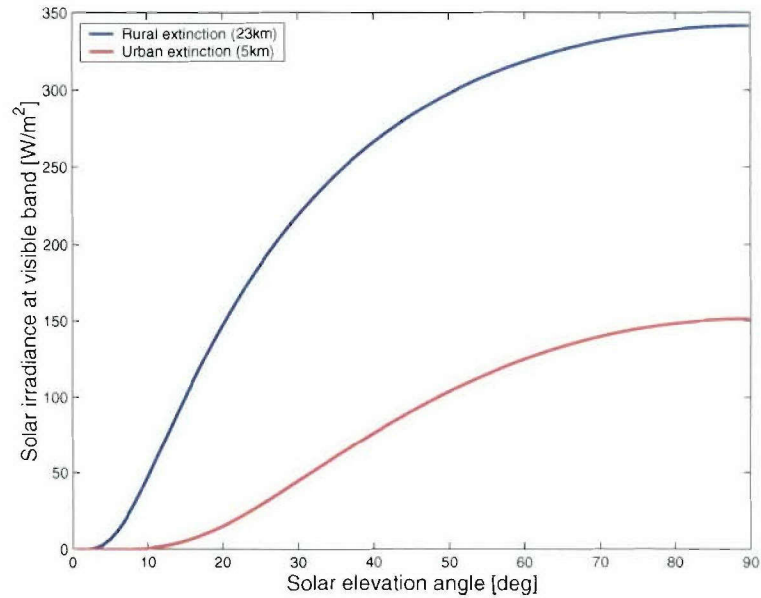


Figure 4.28: Sample visible band total solar irradiance versus solar elevation angle of rural and urban extinction at mid-latitude summer.

which contains fewer aerosols. Hence, multiple scattering is less common. Second, the received signature is the result of reflections from the entire sky. Polarimetric contributions from different parts of the sky tend to cancel, so that the residual is only slightly polarized in general. Thus, errors in skylight polarization tend to have a small effect on the overall solution.

As noted previously, for scattering purposes, surface roughness is quantified in terms of wavelength. A given surface appears rougher at shorter wavelengths because the effective surface slope variance includes more energy for a broader band in the spectral density function. Since visible wavelengths are much shorter than MWIR wavelengths, significant differences in scattering can arise, and new BRDF parameters will be required. Little information about mine surface properties is available. The parameters used in the visible band model, which are listed in Table 4.3, were derived

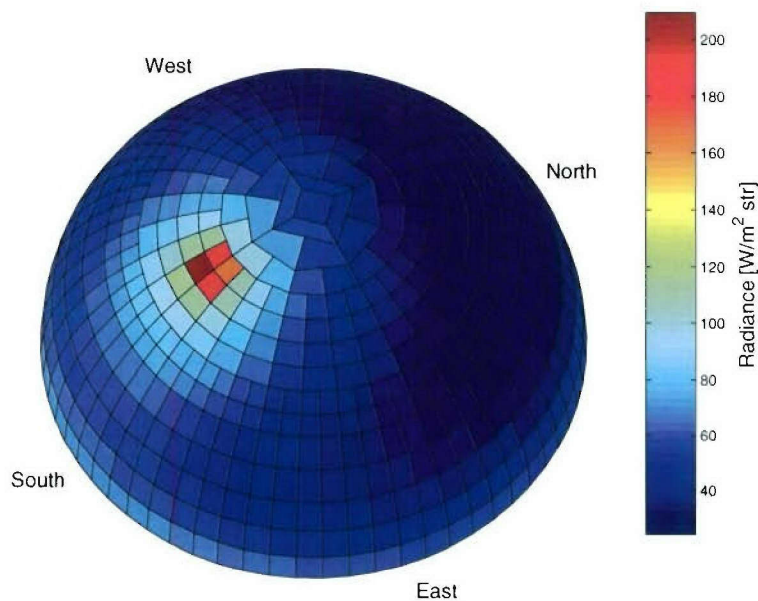


Figure 4.29: Sample visible band skylight radiance profile at 12 PM, May 24th, for NT-S2.

from the MWIR parameters and modified to improve agreement with measured data. The first two properties in the table (the refractive index and the slope variance) are critical in any description of surface scattering using the PO approach. The last two parameters define the magnitudes of co- and cross-polarized terms for the diffuse component. These parameters show that the mine's surface is smoother and has a stronger specular lobe, while most solar scattering comes from the diffuse component.

### 4.3.3 Comparison of Radiometric Components

Using the surface parameters and source components described above, we simulated visible band signatures. Figure 4.30 shows both the individual radiometric components (intensity  $I$  only) and the total signature. The polarimetric parameters

Surface type	Mine	Soil
Refractive index ( $n$ )	1.4	1.6
Slope variance ( $s^2$ )	0.015	0.3
Diffuse component	0.015	0.06
Depolarization ratio	0.5	0.5

Table 4.3: Surface parameters for LM\_B mine simulations at NT-S2 using a visible band camera.

$Q$ ,  $U$  and  $V$  have been omitted, since we do not have measured data for comparison. (Those parameters should be small, since the mines were viewed near normal incidence.) The simulation was performed for the environmental conditions of 12 PM, May 24th, at NT-S2.

A comparison of the individual radiometric components and the total signature in Figure 4.30 (f) shows that only the single-bounce solar and skylight reflections have significant roles in the visible band signature. Therefore, in what follows simulations were conducted using those components only. The results show that reflections from soil are stronger than those from the mine for both skylight and solar components, since the soil is assumed rough with a larger diffuse reflectance. The simulated images show two darker concentric rings on the mine caused by sloping surfaces that separate planar decks at three elevations.

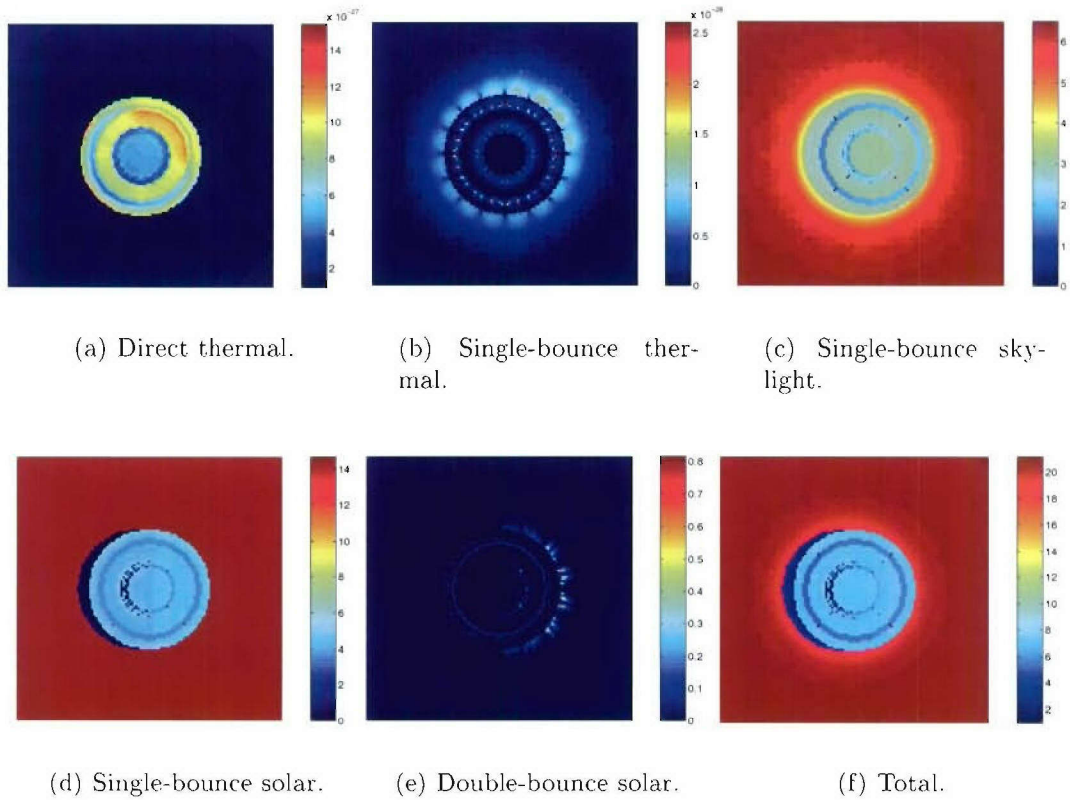


Figure 4.30:  $I$  component of individual and total signatures for “NT-S2” data set at 12 PM, May 24th.

### 4.3.4 Model Validation for the Visible Band

In this section we compare measured and simulated mine signatures in the visible band. A careful study of the measurements in Figure 4.25 and 4.26 reveals that the reflected intensity is not the same for different mines in the same scene. Furthermore, mine signatures are not consistent from scene to scene. For example, in Figure 4.25 (d), the upper-left mine is the brightest while the upper-right mine in Figure 4.26 (a) is the brightest in that image. It was observed in the discussion of the TNO data that a large sensor FOV will produce different viewing geometries in different parts of the scene. Therefore, before comparing measured and simulated images, we investigate the effects of viewing geometry on the measured mine signatures.

Figure 4.31 presents a measured image (taken at 11 AM) with information on sensor and sun positions. The square boxes indicate three mine locations. Simulations were performed with viewing geometries corresponding to those locations. The apparent motion of the sun is also indicated. At 11 AM, the sun, the sensor, and mine “A” approximate a specular geometry. At 12 PM, it is mine “B” that forms a possible specular geometry.

The sensor FOVs in the horizontal and vertical directions are reported to be  $30^\circ$  and  $20^\circ$ , respectively. Using the known sensor height and the mine positions in the images, we manually estimated the approximate sensor nadir angles in proportion to the sensor FOVs for the mines denoted “A”, “B”, and “C”. Those approximate angles were modified slightly (less than two degrees to original estimates) to improve agreement with the measured data. The zenith and hour angles of mine locations “A”, “B”, and “C” determined using the above method are given in Table 4.4.

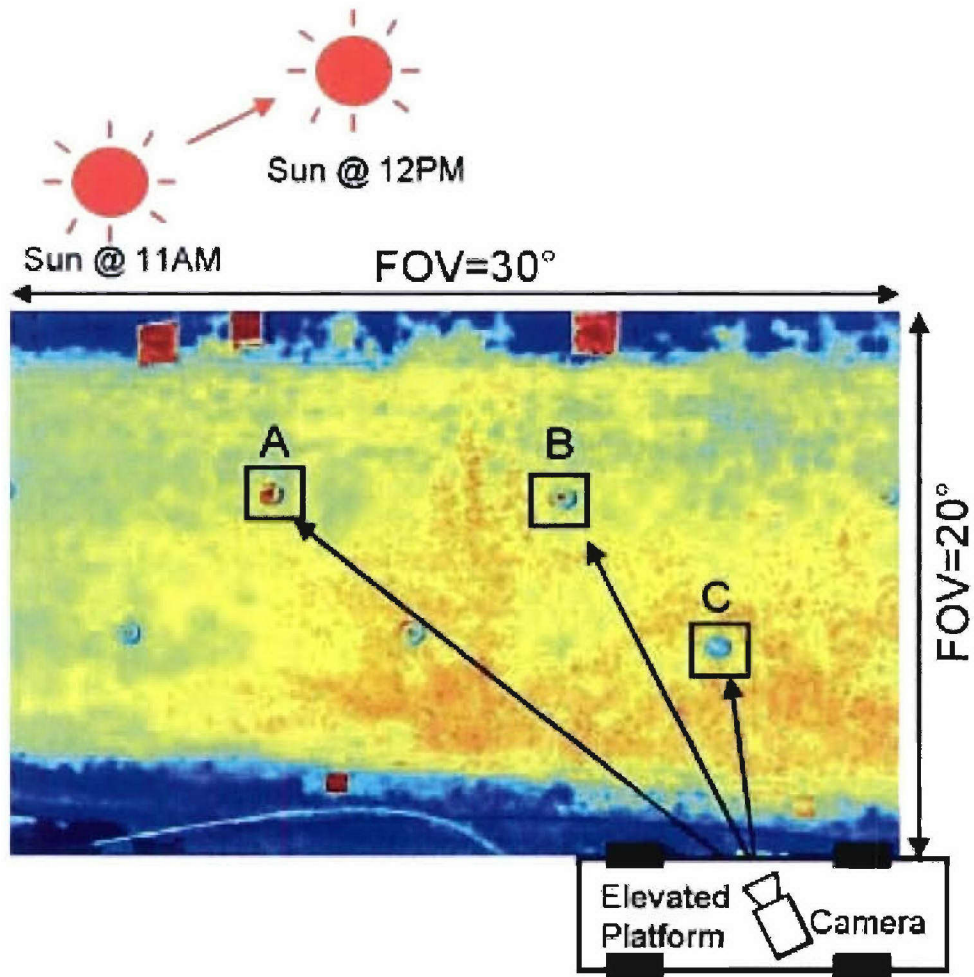


Figure 4.31: Geometric relations of the sensor, the sun and mine positions in the measured image.

Site	A	B	C
Zenith angle	19°	16.5°	13°
Hour angle	45°	20°	10°

Table 4.4: Sensor zenith and hour angles for simulation sites “A”, “B”, and “C”.

Using the angles in Table 4.4 and the surface parameters reported in Table 4.3, we performed simulations for the three mine locations at 11 AM, 12 PM, 3 PM, and 5 PM. Figure 4.32 exhibits the results. We found that at 11 AM, mine “A”, which forms a specular relation with the sun, produces the highest intensity. Mine “B”, which is farther from the specular angle yields a weaker response, but still shows high contrast. Scattering from mine “C” is dominated by the diffuse component and shows a negative contrast with respect to background. The second row, which shows results at 12 PM, indicates that the shift in solar position changes the strongest “target” from mine “A” to “B”. Mine “C”, which is closer to mine “B”, also shows a stronger reflection compared to the 11 AM results.

In the afternoon, the sun appears at a small elevation angle, and none of the mines form a specular geometry. Therefore, all three mines show low contrast. The mine’s shadow also grows compared to the images acquired earlier in the day. Bright spots appear on the tapered rim of the mine structure, where the surface form a specular geometry. At 5 PM the shadow is extended further, and the mine intensity is suppressed due to the reduction in solar irradiance.

Figure 4.33 shows measured mine chips for locations A, B, and C. It is evident that the simulations are in good agreement with the measurements. The most significant features in the measurement are largely replicated in the simulations. The maximum radiance observed in Figure 4.33 is 55 [W/m<sup>2</sup>sr], while the background radiances (the average around the chip’s boundaries) for the four times are 30, 36, 26, and 12. For the simulated results in Figure 4.32, the maximum is 37.4 and the background averages are 20, 21, 17, and 8, respectively. The measured values are roughly 50% more than the simulated ones, but ratios among measured data and simulated results

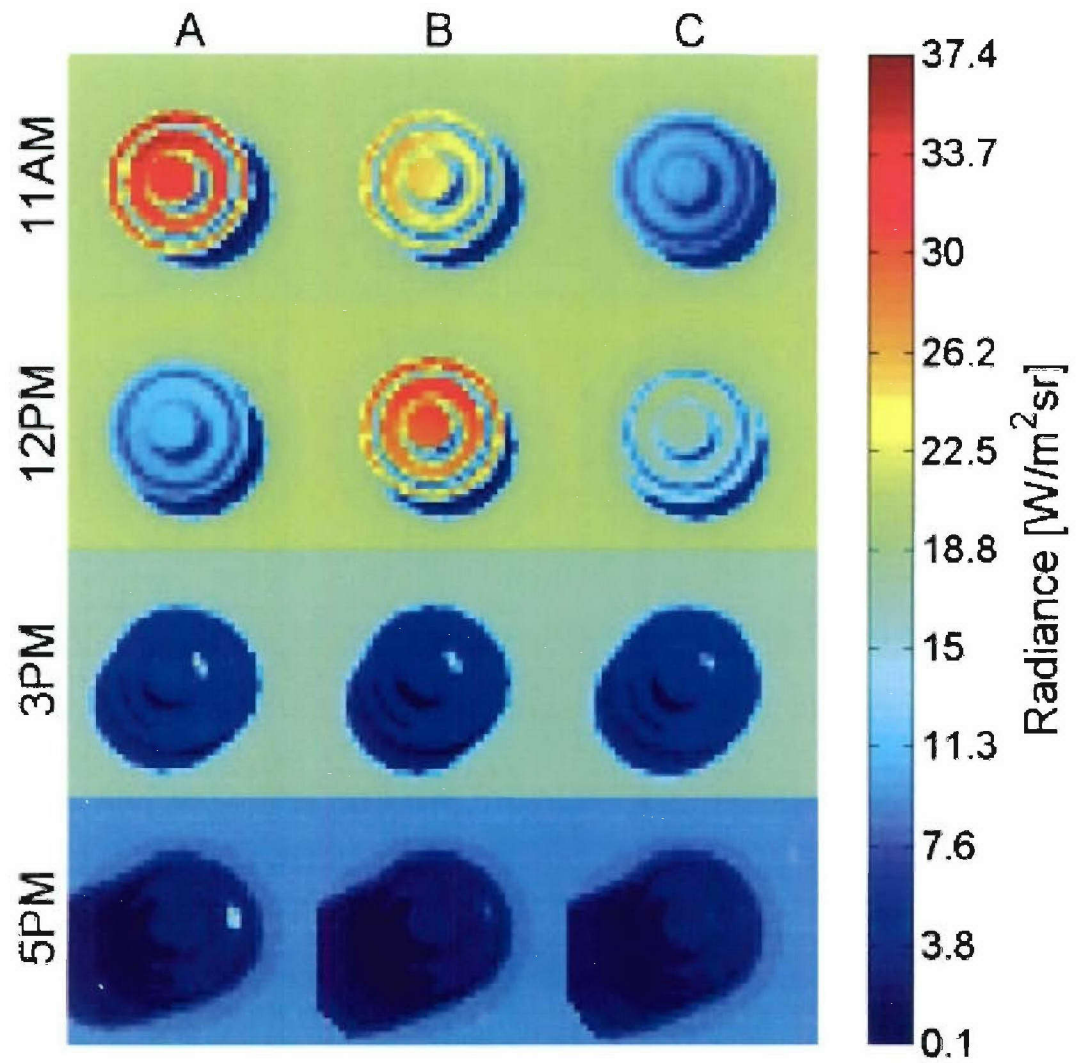


Figure 4.32: Simulated signatures for LMB mines at location “A”, “B”, and “C” at four times (11 AM, 12 PM, 3 PM, and 5 PM) on May 24th, at NT-S2.

are consistent. The difference in reflected radiance may be the result of errors in estimating the incident solar irradiance. As indicated in Figure 4.28, changes in the atmosphere model result in great variations in incident solar and skylight radiances. Other disagreements observed include (1) the brighter central disk (the mine's trigger assembly) for mines A and B at 11 AM and 12 PM, (2) a pronounced asymmetry in reflections from mine B's sloping sections at 11 AM and 12 PM, and (3) multiple glints from those sections at 3 PM and 5 PM.

The comparison presented in this section showed that visible band signatures are dominated by surface scattering of sunlight and skylight. Unlike IR (MWIR and beyond) signatures, which are determined by surface temperature and gradual varying emissivity profiles (except the grazing region), visible signatures are very sensitive to source and viewing directions. A larger variation in scattered radiance from mine surfaces is observed due to a greater importance in mine's specular lobe return.

#### **4.4 Summary**

In this chapter we exercised the simulator on three sets of measured data in different scenarios. The goals of this effort were both model validation and further insight into the nature of mine signatures. The dominant features of mine signatures seen in the NT-S1 data (collected with a nadir-looking airborne MWIR sensor) are replicated by the model. A study of the mine's temporal dependence was conducted for the environmental conditions of NT-S1. It was found that the maximum mine-background contrast appears around mid-day, which is the optimal time to operate the sensor. The solar reflection contributes a strong shadow and makes it possible to

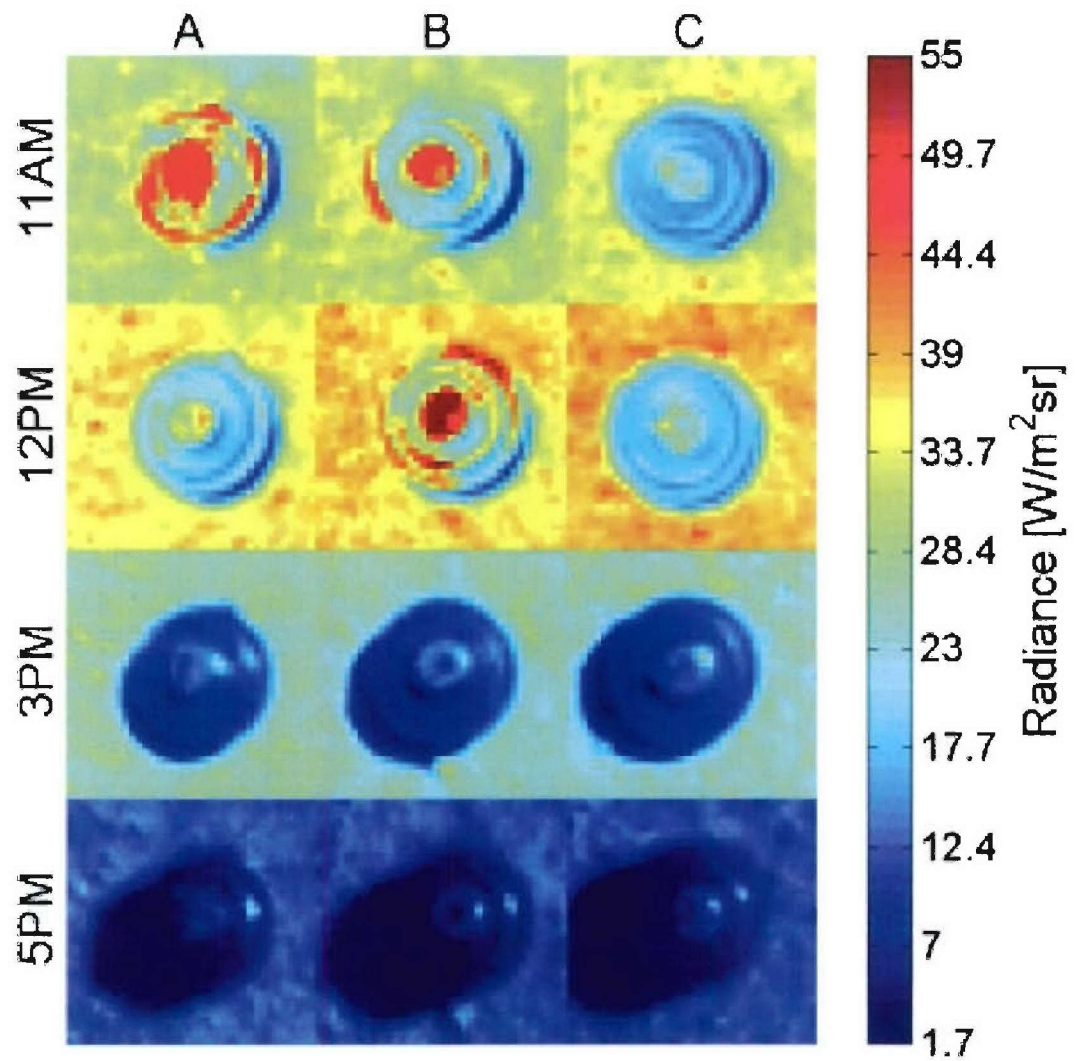


Figure 4.33: Measured signatures for LM\_B mines at location “A”, “B”, and “C” at four times (11 AM, 12 PM, 3 PM, and 5 PM) on May 24th, at NT-S2.

detect mines during the crossover in the morning. The absence of a shadow during the evening crossover makes detection particularly difficult at that time.

The polarimetric properties of mine signatures were explored through simulations of the TNO data. The off-nadir viewing geometry introduced stronger depolarization for thermal emissions, leading to higher contrast for the polarimetric signatures, which could enhance mine detection rates.

A study of measured signatures in the visible band revealed that the characteristics of a mine vary greatly as the sensor and solar positions change. Simulations were conducted, and good agreement was found with measured images. This outcome increases confidence in the BRDF model, since essentially all visible band radiance is a result of rough surface scattering of insolation.

Although the simulator showed good agreement with the three data sets in general, several areas for improvement were identified. For the NT-S1 data set we observed discrepancies in the size of the shadow which may be related to limitations in computational resources. For the TNO data, the predicted thermal solution was larger than measured, which may stem from errors in the assumed properties of the mine's case. For the visible-band NT-S2 data, the mine's trigger assembly appears brighter than the simulation, which may also be an error in the mine's assumed properties. The difference in received radiance indicates error in the estimation of atmospheric attenuation. In addition, disagreement was seen in simulated and measured backgrounds. Most natural objects are multi-scale rough surfaces, and measured images often exhibit a blotchy background due to decimeter scale surface tilts. The existing rough surface model describes single-scale surfaces only, which can only replicate the average behavior of a true surface.

Through comparisons with measurements we confirmed that IR sensors are greatly influenced by surface temperatures and less subjective to current illumination conditions, which can be dramatically changed by the sensor position and the presence of clouds. Above characteristics make IR signatures a more reliable feature for mine detection that can be seen at all time except at crossovers, although we have shown that mid day is a more favorable operational time. On contrast, since visible signatures are more sensitive to illumination conditions and the viewing geometry, their features are more volatile and the operation is limited to daylight hours. However, the contrast between scattering from mine and soil surfaces can be large if the sensor is setup carefully. The choice of knowledge about potential mines and deployment conditions. Therefore, a multi-sensor suite might be an attractive choice for detection systems.

## CHAPTER 5

### MINE DETECTION ALGORITHMS FOR EO IMAGERY

In this chapter we present studies of algorithms for mine detection in EO imagery. An effective detection algorithm is a key element of a successful mine detection system. In order to cope with changing environmental conditions, background and target estimation techniques are used to make the algorithms adaptive.

This chapter is organized as follows: Section 5.1 reviews the literature on mine detection using EO sensors. The RX algorithm [14, 15] served as the mine detector for the US Marines Coastal Battlefield Reconnaissance and Analysis (COBRA-ATD) program. That well-known algorithm, which is reviewed in Section 5.2 and derived in a slightly more general form in Appendix C, is an anomaly detector that cannot exploit the modeling information described in Chapters 2 through 4. Alternative implementations of the RX algorithm are presented in Section 5.3, including a computationally efficient approach. Two performance improving techniques are described in Section 5.4. The first is a modified RX algorithm that uses a multi-component reference to better estimate the target amplitude. The second is a whitening filter that decorrelates the clutter, as required by the RX algorithm.

An estimator-correlator (EC) algorithm is introduced in Section 5.5 as an alternative to RX. Several features make the EC algorithm attractive. It uses a random

signal model to account for mine signature variations caused by clutter and environmental conditions. Simulated signatures can be exploited directly. Implementation issues are discussed in Section 5.6. A locally adaptive version of the EC algorithm is described in Section 5.7 for nonstationary clutter such as abrupt transitions in background textures.

Performance evaluations of the RX and EC algorithms are presented in Section 5.8 using a multispectral IR data set described in Section 2.7.2. Through a comparison of RX and EC ROC curves, we demonstrate that the locally adaptive EC detector provides a significant performance gain.

## 5.1 Prior Works

Many researchers have explored target detection in multi- and hyper-spectral imagery. A widely referenced approach to this problem is the RX algorithm presumably, named for its authors Reed and (Xiaoli) Yu [14]. This algorithm has been extended to include spectrally correlated (but spatially uncorrelated) clutter [15]. The spectral covariance matrix is estimated with an adaptive algorithm and used to design a spectral pre-whitening filter. It was found that a priori knowledge of the target spectral distribution often makes little difference in performance [15]. Those authors and their co-workers have proposed several forms of the algorithm [73, 74, 75], and, as noted above, RX is used in the COBRA-ATD system [76]. An application of RX to hyper-spectral detection of military and cultural features was described by Stellman et al. [77].

Other detection approaches using EO sensor imagery have been examined. Schweizer and Moura [78] developed a CFAR algorithm based on a first-order Gauss-Markov

random field (GMRF) model for the clutter. In that algorithm a maximum likelihood (ML) technique was used to estimate the clutter parameters, which were then used in a GLRT detector. Solberg et al. [79, 80, 81], who used the Markov random field model to develop a land-use classifier for satellite imagery, noticed that temporal variations of target signatures could be utilized to enhance detector performance. Chen et al. [82] designed detectors that exploit the difference in temperature histories of mine and soil.

Several authors have attempted to exploit target spectral characteristics. Ashton [83] used clustering algorithms to find sub-pixel anomalies in multi-spectral IR terrain imagery. Ashton and Schaum [84] used RX to search for anomalies in background-suppressed spectral signatures.

In addition to algorithms developed from classical statistical detection theory (GLRT, etc.), many unconventional detectors have been explored for mine detection. A unique approach was explored by Banerji and Goutsias [85], who used mathematical morphology to detect mines in individual bands followed by fusion of the band information. Correlation among the bands was addressed by using a maximum noise fraction transform to generate independent bands. Agarwal et al. [86] proposed a false alarm mitigation scheme using gray-scale moments, which preserved the shape and intensity profiles of mine signatures. Support vector machines [87, 88], which differentiate patterns formed by feature vectors in a multi-dimensional space, have also been applied [89].

Another popular choice for EO mine detectors is the neural network. Daud et al. [90] developed a feed-forward neural network to recognize mines in EO imagery. Investigations of the position, rotation, and scaling invariance (PRSI) properties of

a higher-order neural network (HONN) [91, 92, 93] have shown that a third-order HONN will exhibit PRSI. A wavelet-based HONN detector [94] was recently trained to discriminate mines and clutter. The input of the neural network is not limited to spatial patterns. A mine detection scheme proposed by Ramaswary et al. [95] used a feed-forward neural network to fuse confidence parameters extracted from multiple sensors.

## 5.2 RX Algorithm (GLRT Approach)

The RX algorithm has become the standard algorithm for mine detection, because of its simple implementation and its robust (albeit not entirely satisfactory) performance. In this section the basics of the RX algorithm are described. Implementation issues and performance improving techniques are presented in later sections.

The RX algorithm, which is based on a generalized likelihood ratio test (GLRT), comprises a locally adaptive constant false alarm rate (CFAR) detector. It uses maximum likelihood estimation (MLE) to find both the unknown target amplitude and clutter covariance in multispectral imagery.

The algorithm processes multispectral imagery by converting it into an equivalent vector representation. Signals in an interesting region of size  $N_1 \times N_2$  pixels are scanned column-wise into vectors of size  $N \times 1$ , where  $N = N_1 \cdot N_2$ . In a similar manner, multi-channel imagery of  $J$  channels is reformed into a matrix  $\mathbf{y}$  of dimensions  $N \times J$ .

The RX algorithm is based on several assumptions about the properties of targets and clutter in EO imagery. It assumes that the shape of the target is given by a known  $N \times 1$  matrix  $\mathbf{S}$  with an unknown  $1 \times J$  spectral amplitude  $\mathbf{B}$ . Many

mines have a circular or square shape with a uniform signature amplitude. However, when the image resolution is sufficiently high, some mines are better described by multiple regions of uniform intensity. In particular, the central trigger mechanism may have a different signature. A modified RX algorithm with a multi-component signature is devised in Section 5.4.1. Like the original RX algorithm it also requires that the clutter  $\mathbf{N}$  be Gaussian-distributed, zero-mean and spatially uncorrelated with an unknown correlation between spectral channels. The Gaussian distribution requirement is not met for most EO imagery. Indeed, in real images, pixels have spatial correlation and are non-Gaussian distributed [74, 14]. Nonetheless, Reed and Yu [14] showed that by removing the image's local mean, the residual intensity does approximate a Gaussian distribution. The requirement of spatially uncorrelated clutter is only fulfilled when the image resolution is low. In high resolution images, which are used in most mine detection applications, the correlation between adjacent pixels is not negligible. In order to eliminate clutter correlation, a whitening filter, which is presented in Section 5.4.2, was developed as a preprocessor for the RX algorithm.

For reference, a derivation of the likelihood ratio test used in the RX detector is provided in Appendix C.

### 5.3 Implementations of the RX Algorithm

In this section, we describe several RX implementations, each of which has advantages in specific circumstances.

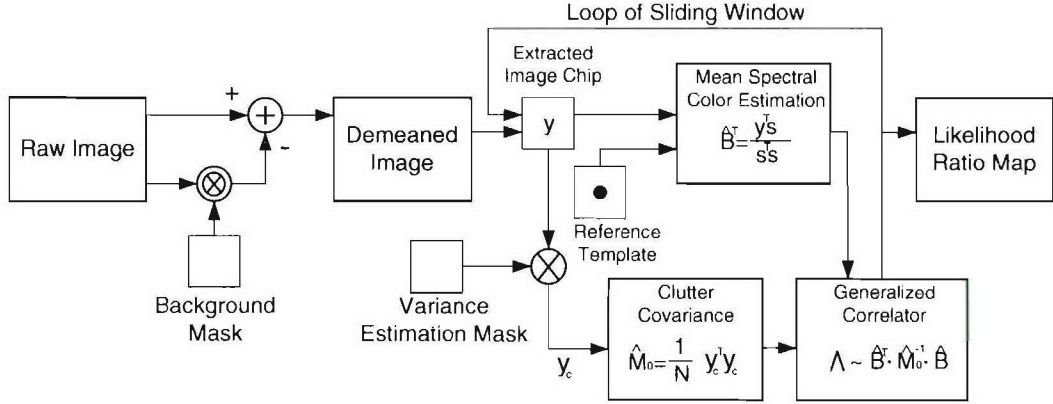


Figure 5.1: Block diagram of standard RX algorithm implementation.

### 5.3.1 Standard RX Algorithm

Figure 5.1 shows the block diagram of the standard RX algorithm. As mentioned before, it is necessary to remove the local mean to obtain Gaussian distributed clutter. The local mean is estimated by convolving the raw image with a uniform kernel. The estimated local mean is then subtracted pixel-wise from the raw image. For a multi-channel image, this process is performed on each channel.

Next, the likelihood ratio estimates are computed via Equation (5.3) using a sliding window process. At each position in an image of  $J$  channels, a  $N_1 \times N_2$  subimage is extracted and scanned column-wise into a vector  $\mathbf{y}$  of  $N$  rows and  $J$  columns. We have

$$\mathbf{y} = [y(1), \dots, y(N)]^T \quad (5.1)$$

$$y(n) = [y_1(n) \ y_2(n) \ \dots \ y_J(n)] \quad (5.2)$$

The likelihood ratio is given by [14]

$$\Lambda'''(\mathbf{y}) = \hat{\mathbf{B}} \cdot (\mathbf{y}^T \mathbf{y})^{-1} \cdot \hat{\mathbf{B}}^T \begin{cases} \geq \tau''', & \text{then } H_1 \\ < \tau''', & \text{then } H_0 \end{cases} \quad (5.3)$$

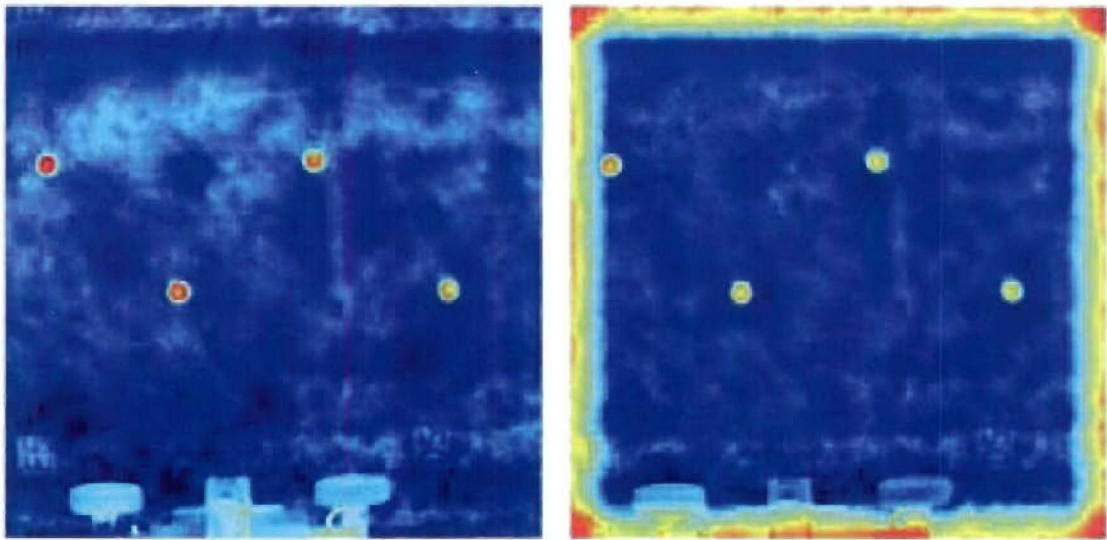
where  $\hat{\mathbf{B}}$  is the aforementioned target magnitude estimate. Given the normalized target signature  $\mathbf{S}$ , it is straightforward to evaluate the likelihood ratio within the window. The covariance estimate is formed using pixels that appear in the window. In the standard RX implementation, all pixels in the window are used, but some variants of that scheme are described below. In many cases, the calculation of  $\hat{\mathbf{B}}$  can be made more efficient. The target  $\mathbf{S}$  is typically nonzero only within a small portion of the window, referred to hereafter as the “target region”. The calculation of  $\mathbf{y}^T \mathbf{S}$  can be restricted to those pixels. By shifting the window across the scene, we construct a likelihood ratio estimate at each position (a “map”) for scoring. Figure 5.2 (a) shows a sample IR raw image. The demeaned image shown in Figure 5.2 (b) has a somewhat more uniform background although the edges are not correctly estimated by the convolution. The resulting likelihood ratio map<sup>17</sup> in Figure 5.2 (c) reveals the target locations as local maxima.

### 5.3.2 Modified RX Algorithm

A modified RX algorithm was devised by Holmes et al. [76] for use in the US Marines COBRA-ATD program. The major feature introduced by Holmes et al. was the use of a “guard-band” mask in covariance estimation. In this context, a guard band kernel is a uniform annular kernel, for which the size of the interior void is strictly larger than the target region. The annular region is used to estimate the background covariance around the target.

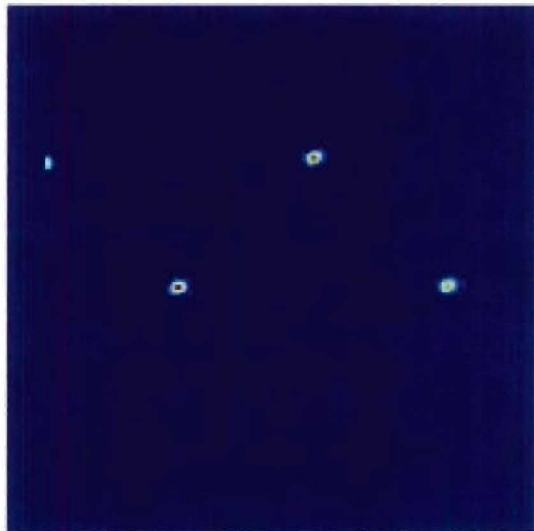
The guard-band region is defined as the pixels between the target region and the background pixels. Pixels within the guard-band are ignored and have no effect on

<sup>17</sup>The likelihood ratio map shown was generated with the modified RX algorithm presented below.



(a) Sample raw image.

(b) Sample demeaned image.



(c) Sample likelihood ratio map.

Figure 5.2: Sample RX processing results.

the resulting estimates. Figure 5.3 shows the target and covariance masks used to generate Figure 5.2.

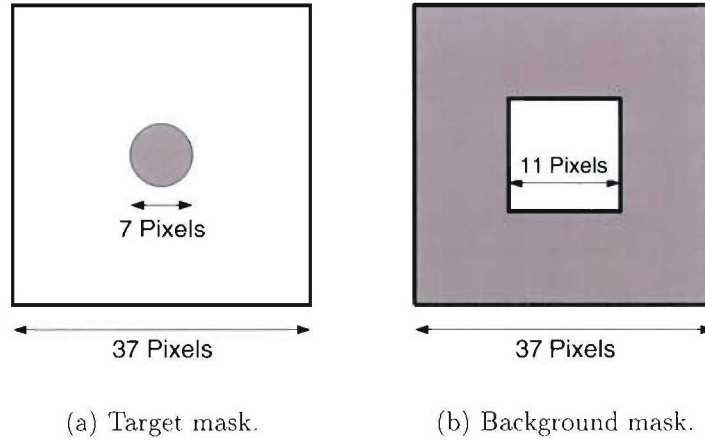


Figure 5.3: Target and background covariance estimation masks.

A mine detection mission may encounter a variety of mines, and a practical mine detector should respond to all such mines. As noted above, the RX algorithm can be regarded as an anomaly detector, which tolerates some variation in mine size and shape. Examining Equation (5.3), we see that for single-channel data, the likelihood ratio can be rewritten as<sup>18</sup>

$$\Lambda'''(\mathbf{y}) = \frac{\hat{\mathbf{B}}^T \hat{\mathbf{B}}}{\mathbf{y}^T \mathbf{y}} \begin{cases} \geq \tau''', & \text{then } H_1 \\ < \tau''', & \text{then } H_0 \end{cases} \quad (5.4)$$

We noted previously that the above expression is the ratio of signal energy to signal plus noise energy. If the target is larger than anticipated the target will contaminate the covariance estimate. The concept of a guard band avoids this problem by excluding a region slightly larger than the nominal target. By masking the window

<sup>18</sup>For multi-channel data,  $\mathbf{y}^T \mathbf{y}$  is not a scalar.

pixels we eliminate the additional variance due to the target, thereby increasing the likelihood ratio. The price of this change is that our estimate of the covariance  $\mathbf{M}$  will be based on fewer pixels, and it will therefore have higher variance.

The performance of the standard and modified RX algorithms was evaluated by processing the NT-S2 sensor described in Section 2.7.2. Recall that six types of anti-vehicle mines were placed in those test lanes, the largest of which was around twelve pixels in diameter while the smallest was approximately five pixels.

Because of the mine size variation described above, a circular target of 5 pixels in diameter was used. The background window was chosen to be a square of 36 pixels in length. For the modified RX algorithm, a guard band of 14 pixels was chosen so that even the largest mine was excluded from the covariance estimation. Figure 5.4 shows the ROC curves<sup>19</sup> for the standard and modified RX algorithms. Apparently, the modified RX detector provides better performance in the low FARs region. Hence, the modified detector will be used as the baseline in performance comparisons with other algorithms developed herein.

### 5.3.3 Frequency-Domain RX Implementation

Although the RX algorithm has been described with processing done in a sliding window, a moment's consideration reveals that virtually all of the operations are equivalent to convolution. Pointwise evaluation on  $\mathbf{S}^T\mathbf{B}$  is obviously so. The covariance estimation is also equivalent to a convolution of the relevant mask with the pixel-wise squared image. A significant increase in speed is obtained by performing these convolutions in the Fourier domain using FFTs. In tests it was found that

<sup>19</sup>By definition, a ROC curve plots the probability of detection versus the probability of false alarm. Because the size of a false alarm event is difficult to define in images, false alarm rate (number of false alarms/scanned area size) is used instead.

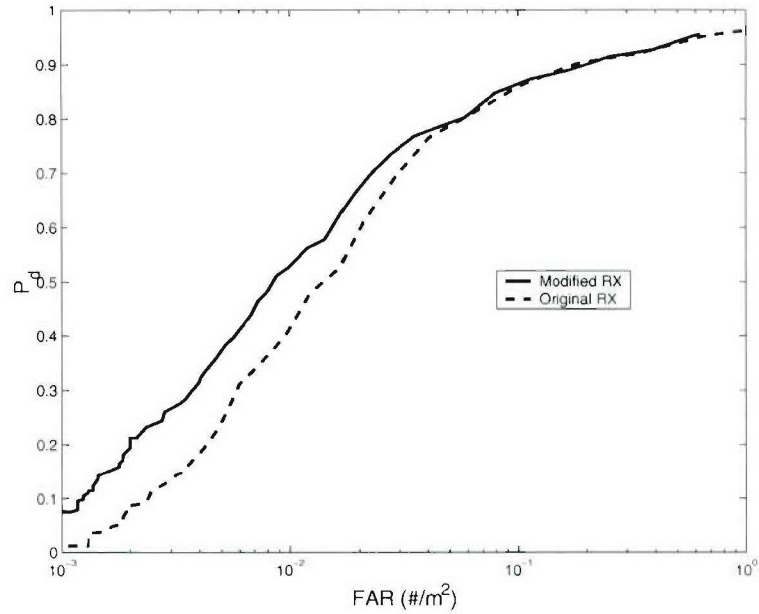


Figure 5.4: Performance comparison of standard and modified RX algorithms.

the frequency-domain RX implementation was significantly faster than the original implementation, but the improvement is strongly dependent on the kernel sizes.

## 5.4 Performance Enhancements

The performance of RX is ultimately limited by the assumptions on which it is based. In this section modifications to the algorithm are described that remove the restrictions imposed by more complex targets and spatially-correlated clutter.

### 5.4.1 Multiple Target Components

In the original RX formulation,  $\mathbf{S}$  was taken to be a region (a circle or a square) of constant pixel intensities. As noted previously, many types of mines do not possess such a homogeneous signature, and it is natural to explore whether a more complex signature  $\mathbf{S}$  would improve performance.

The problem can be overcome by using a target model with multiple components. The derivation of a multi-component RX algorithm begins by re-defining the target reference  $\mathbf{S}$ . For single-component RX algorithm,  $\mathbf{S}$  is a binary column vector defining the target region. For the multi-component case,  $\mathbf{S}$  contains several columns describing different sections of the target. Expressions appearing in Equations (C.2) through (C.14) are still valid for the multiple component case. The likelihood ratio in Equation (C.14) can be formed by taking the determinants of covariance estimates  $\hat{\mathbf{M}}_0$  and  $\hat{\mathbf{M}}_1$ , which appear in Equations (C.9) and (C.10).

Compared to the single-component RX detector, the multi-component RX algorithm provides better detection performance on non-uniform targets and equal performance on uniform targets. Applying a single-component reference to a multi-component target introduces estimation errors and yields a lower likelihood ratio. In the worst case scenario, a multi-component target may go unseen by the single-component RX detector even though its signal-to-noise ratio is high<sup>20</sup>.

Although the concept has a number of theoretical advantages, several factors limit the benefit of using a multi-component RX detector. Although many types of landmines show uniform regions of different intensities, the contrast among regions is smaller than the contrast between the average amplitude of the mine and the background. Hence, a single-component  $\mathbf{S}$  may be adequate to detect mines, since the whole target average does not deviate significantly from averages in individual sections. Unless the extreme example mentioned earlier is possible, the single-component  $\mathbf{S}$  may be preferred for an unknown minefield because of its simpler implementation.

<sup>20</sup>This extreme case would require the average mine signature to be similar to the background average, a situation never encountered by the author in practice.

Furthermore, the multi-component RX works best only when the section boundaries in  $\mathbf{S}$  are good approximations to those of actual mines. In general, the multi-component RX algorithm will demonstrate an advantage only when the minefield is dominated by a known mine type having multiple sections.

## 5.4.2 Clutter Whitening

As mentioned in Section 5.2, the RX algorithm assumes spatially uncorrelated clutter, which may not be satisfied by high-resolution EO imagery. Figures 5.5 (a) and 5.5 (c) show sample image chips and power spectra for a surface mine (MP\_A) and clutter. It is apparent that the clutter is not white, and that its power spectrum overlaps the mine spectrum.

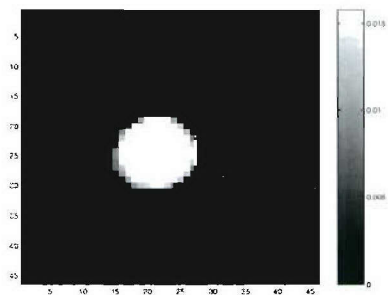
A classical whitening filter was investigated to reduce the clutter spatial correlation. The filter was constructed from the local covariance matrix in a manner similar to the concept used in the generalized matched filter. If the local clutter covariance estimate  $\Sigma$  is available, one can use a Cholesky factorization or an eigenvector decomposition of its inverse to construct the whitening filter  $\mathbf{V}$ .

$$\Sigma^{-1} = \mathbf{V}^T \mathbf{V} \quad (5.5)$$

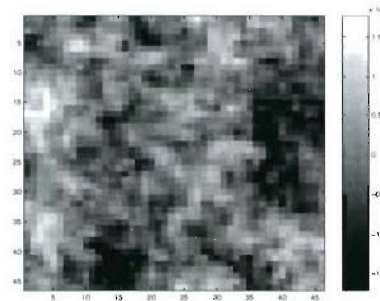
Before applying the RX algorithm, the whitening filter  $\mathbf{V}$  is applied to both the input imagery  $\mathbf{y}$  and the reference  $\mathbf{S}$  as follows

$$\begin{aligned} \mathbf{y} &\rightarrow \mathbf{V}\mathbf{y} \\ \mathbf{S} &\rightarrow \mathbf{V}\mathbf{S} \\ \mathbf{y}^T \mathbf{S} &\rightarrow (\mathbf{V} \cdot \mathbf{y})^T (\mathbf{V} \cdot \mathbf{S}) \end{aligned} \quad (5.6)$$

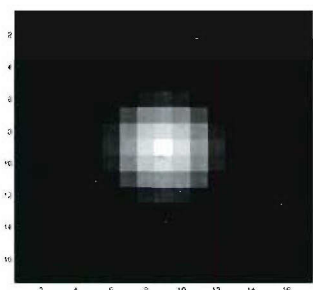
The approach described above is theoretically sound but impractical, because of the difficulty in estimating the local clutter covariance matrix  $\Sigma$ . An image chip of  $N$  pixels and  $J$  channels requires at least  $JN$  chips to make a valid estimate. Since



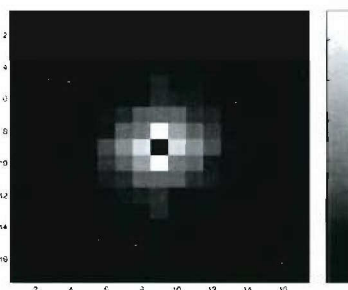
(a) MP\_A mine.



(b) Clutter.



(c) MP\_A spectra.



(d) Clutter spectra.

Figure 5.5: Sample mine and clutter chips and their power spectra.

the local clutter is nonstationary (due to changes in terrain, vegetation or weather conditions), it is virtually impossible to find enough samples to form  $\Sigma$ . Furthermore, the matrix inversion and decomposition are time consuming.

In this work, an alternative approach was used, which is based on an assumption about the clutter. If the clutter is first-order Markov, then a pixel's intensity is only correlated with its adjacent pixels. In this case the clutter correlation is described by an exponential function that can be described analytically in terms of a correlation coefficient  $\rho$ . Arcess et al. [96] show that the whitening filter can be expressed as a  $3 \times 3$  matrix

$$\begin{bmatrix} \rho^2 & -\rho(1 + \rho^2) & \rho^2 \\ -\rho(1 + \rho^2) & (1 + \rho^2)^2 & -\rho(1 + \rho^2) \\ \rho^2 & -\rho(1 + \rho^2) & \rho^2 \end{bmatrix} \quad (5.7)$$

To find the correlation coefficient  $\rho$ , we first computed the auto-correlation matrix of a zero mean clutter chip and then estimated the coefficient  $\rho$  of an exponential function that approximated the computed correlation. By using the coefficient value in Equation (5.7), we formed the whitening filter. This filter was then convolved with the input image and the reference. Note that the correlation coefficient estimation and whitening preprocessing were done separately for each channel. Although estimation error (as well as errors in the Gauss-Markov assumption) can prevent this whitening approach from eliminating all colored noise, it still manages to reduce clutter spatial correlation and to improve RX performance with a modest computation cost.

## 5.5 Random Signal Approach (Estimator Correlator)

In this section we introduce an alternative to the RX algorithm based on a random signal model. We assume the signature of a given mine is largely known, but is distorted by the viewing geometry, illumination conditions and environmental factors.

The image data  $x$  (at a single pixel) is modeled by the target signature  $h$  convolved with a random distortion term  $t$  plus noise  $n$ .

$$x = \begin{cases} h \otimes t + n; & H_1 \\ n; & H_0 \end{cases} \quad (5.8)$$

Consider next an image of size  $N_1 \times N_2$  and let  $N = N_1 N_2$ . By reshaping the image data and model components into column vectors, we can rewrite the above equation as

$$\mathbf{x} = \mathbf{h}\mathbf{t} + \mathbf{n} \quad (5.9)$$

where  $\mathbf{x}$ ,  $\mathbf{t}$  and  $\mathbf{n}$  are  $N \times 1$  column vectors and  $\mathbf{h}$  is a  $N \times N$  matrix. Using  $N_2$  sub-matrices  $\mathbf{h}_0 \mathbf{h}_1 \cdots \mathbf{h}_{N_2-1}$ ,  $\mathbf{h}$  can be expressed as

$$\mathbf{h} = \begin{bmatrix} \mathbf{h}_0 & \mathbf{h}_{N_2-1} & \mathbf{h}_{N_2-2} & \cdots & \mathbf{h}_1 \\ \mathbf{h}_1 & \mathbf{h}_0 & \mathbf{h}_{N_2-1} & \cdots & \mathbf{h}_2 \\ \mathbf{h}_2 & \mathbf{h}_1 & \mathbf{h}_0 & \cdots & \mathbf{h}_3 \\ \vdots & & & & \\ \mathbf{h}_{N_2-1} & \mathbf{h}_{N_2-2} & \mathbf{h}_{N_2-3} & \cdots & \mathbf{h}_0 \end{bmatrix} \quad (5.10)$$

and the sub matrices are

$$\mathbf{h}_k = \begin{bmatrix} h(k, 0) & h(k, N_1 - 1) & h(k, N_1 - 2) & \cdots & h(k, 1) \\ h(k, 1) & h(k, 0) & h(k, N_1 - 1) & \cdots & h(k, 2) \\ h(k, 2) & h(k, 1) & h(k, 0) & \cdots & h(k, 3) \\ \vdots & & & & \\ h(k, N_1 - 1) & h(k, N_1 - 2) & h(k, N_1 - 3) & \cdots & h(k, 0) \end{bmatrix} \quad (5.11)$$

The real matrix  $\mathbf{h}$  has a block circulant form. A real block circulant matrix is symmetric and can be represented via the eigen-decomposition

$$\mathbf{h} = \mathbf{V}\mathbf{H}\mathbf{V}^H \quad (5.12)$$

where  $\mathbf{V}$  is the matrix of column eigenvectors and  $\mathbf{H}$  is a diagonal matrix containing eigenvalues of  $\mathbf{h}$ . Gray [97] has shown that the eigenvalues of a large  $N \times N$  symmetric Toeplitz matrix uniformly sample values of the power spectral density  $P$  as

$$\lambda_k = P\left(\frac{\pi k}{N}\right) \quad (5.13)$$

At the same time, its eigenvectors approximate the discrete Fourier basis, so that the eigenvector matrix  $\mathbf{V}$  becomes an  $N \times N$  unitary DFT matrix. The entries of  $\mathbf{V}$  are

$$[\mathbf{V}]_{k,p} = \frac{1}{\sqrt{N}} e^{-j \frac{2\pi}{N} kp} \quad (5.14)$$

Therefore  $\mathbf{V}$  in Equation (5.12) can be a unitary DFT matrix and  $\mathbf{H}$  is the discrete Fourier transform of  $\mathbf{h}$  in the form of a diagonal matrix.

For the above-described problem involving a random signal in additive noise, one can employ an estimator-correlator (EC) detector [98]. This approach involves first filtering the input data to estimate the unknown random signal, and then correlating the estimated signal with the input data. The clutter is assumed to be zero-mean Gaussian distributed noise  $\mathbf{n} \sim \mathcal{N}(0, \mathbf{C}_n)$  where  $\mathbf{C}_n$  is the clutter covariance. We noted in Section 5.4.2 that EO imagery is not zero-mean Gaussian in general, but when the local clutter mean is removed the residual intensities are approximately Gaussian.

We now review the derivation of the EC detector. We first consider the simple case  $\mathbf{h} \rightarrow I$  for a Gaussian distributed signal  $\mathbf{s} \sim \mathcal{N}(\mu_s, \mathbf{C}_s)$ .

The likelihood ratio of the two hypotheses can be expressed as

$$\Lambda(\mathbf{x}) = \frac{\Pr(\mathbf{x}|H_1)}{\Pr(\mathbf{x}|H_0)} = \frac{[\det(\mathbf{C}_n)]^{1/2}}{[\det(\mathbf{C}_n + \mathbf{C}_s)]^{1/2}} \frac{e^{-(\mathbf{x}-\mu_s)^T(\mathbf{C}_n+\mathbf{C}_s)^{-1}(\mathbf{x}-\mu_s)/2}}{e^{-\mathbf{x}^T\mathbf{C}_n^{-1}\mathbf{x}/2}} \quad (5.15)$$

in which  $\mu_s$  and  $\mu_n$  are the respective (vector) means of the signal and clutter, and similarly for the covariance matrix  $\mathbf{C}_s + \mathbf{C}_n$ . The log of Equation (5.15) yields

$$\begin{aligned} 2 \ln \Lambda(\mathbf{x}) &= \ln[\det(\mathbf{C}_n)] - \ln[\det(\mathbf{C}_n + \mathbf{C}_s)] \\ &\quad + \mathbf{x}^T \mathbf{C}_n^{-1} \mathbf{x} - (\mathbf{x} - \mu_s)^T (\mathbf{C}_n + \mathbf{C}_s)^{-1} (\mathbf{x} - \mu_s) \end{aligned} \quad (5.16)$$

Using the matrix identity

$$\mathbf{C}_n^{-1} - (\mathbf{C}_n + \mathbf{C}_s)^{-1} = \mathbf{C}_n^{-1} \mathbf{C}_s (\mathbf{C}_n + \mathbf{C}_s)^{-1} \quad (5.17)$$

we find

$$\begin{aligned}
2 \ln \Lambda(\mathbf{x}) &= \ln[\det(\mathbf{C}_n)] - \ln[\det(\mathbf{C}_n + \mathbf{C}_s)] \\
&\quad + 2\mathbf{x}^T (\mathbf{C}_n + \mathbf{C}_s)^{-1} \mu_s - \mu_s^T (\mathbf{C}_n + \mathbf{C}_s)^{-1} \mu_s \\
&\quad + \mathbf{x}^T \mathbf{C}_n^{-1} \mathbf{C}_s (\mathbf{C}_n + \mathbf{C}_s)^{-1} \mu_s
\end{aligned} \tag{5.13}$$

By omitting the data invariant terms, the likelihood ratio reduces to the equivalent quantity

$$\Gamma(\mathbf{x}) = \mathbf{x}^T (\mathbf{C}_n + \mathbf{C}_s)^{-1} \mu_s + \frac{1}{2} \mathbf{x}^T \mathbf{C}_n^{-1} \mathbf{C}_s \mu_s^T (\mathbf{C}_s + \mathbf{C}_n)^{-1} \mathbf{x} \tag{5.19}$$

Covariance matrices for stationary processes have a block circulant form [99], which is symmetric and positive definite, so that the existence of a symmetric eigenvector decomposition is guaranteed. As the number of samples approaches infinity, the covariance matrix  $\mathbf{C}$  becomes real and Toeplitz. Thus a covariance matrix  $\mathbf{C}$  is asymptotically determined by its power spectral density  $P$ .

Generalizing the above results to an arbitrary signature  $\mathbf{h}$  simply requires the substitutions

$$\begin{aligned}
\mathbf{C}_s &= \mathbf{h} \mathbf{C}_t \mathbf{h}^T \\
\mu_s &= \mathbf{h} \mu_t
\end{aligned}$$

and yields

$$\begin{aligned}
\Gamma(\mathbf{x}) &= \mathbf{x}^T (\mathbf{C}_n + \mathbf{h} \mathbf{C}_t \mathbf{h}^T)^{-1} \mathbf{h} \mu_t \\
&\quad + \frac{1}{2} \mathbf{x}^T \mathbf{C}_n^{-1} \mathbf{h} \mathbf{C}_t \mathbf{h}^T (\mathbf{h} \mathbf{C}_t \mathbf{h}^T + \mathbf{C}_n)^{-1} \mathbf{x}
\end{aligned} \tag{5.20}$$

which is the likelihood ratio of the estimator-correlator expressed in the spatial domain. Using the eigen-decompositions of  $\mathbf{C}_t$ ,  $\mathbf{C}_n$  and  $\mathbf{h}$ , the estimator-correlator in

Equation (5.20) becomes

$$\begin{aligned}\Gamma(\mathbf{x}) &= (\mathbf{x}^T \mathbf{V})(P_n + \mathbf{H}^* P_t \mathbf{H})^{-1} \mathbf{H}^* (\mathbf{V}^H \boldsymbol{\mu}_t) \\ &\quad + \frac{1}{2} (\mathbf{x}^T \mathbf{V})(P_n)^{-1} \mathbf{H}^* P_t \mathbf{H} (\mathbf{H}^* P_t \mathbf{H} + P_n)^{-1} (\mathbf{V}^H \mathbf{x})\end{aligned}\quad (5.21)$$

where we used the following properties of the DFT matrix  $\mathbf{V}$

$$\begin{aligned}\mathbf{V} \mathbf{V}^H &= \mathbf{V}^H \mathbf{V} = \mathbf{I} \\ \mathbf{V}^{-1} &= \mathbf{V}^H \\ (\mathbf{V} \mathbf{A} \mathbf{V}^H)^{-1} &= \mathbf{V} \mathbf{A}^{-1} \mathbf{V}^H\end{aligned}$$

After recognizing the Fourier transform of  $\mathbf{x}$  and  $\boldsymbol{\mu}_t$ ,

$$\begin{aligned}\mathbf{X} &= \mathbf{V}^H \mathbf{x} \\ \mathbf{M}_t &= \mathbf{V}^H \boldsymbol{\mu}_t\end{aligned}$$

and recognizing that only scalar operations remain, Equation (5.21) can be expressed as:

$$\Gamma(\mathbf{x}) = \frac{\mathbf{X} \mathbf{H}^* \mathbf{M}_t^*}{P_n + |\mathbf{H}|^2 P_t} + \frac{|\mathbf{X}|^2 |\mathbf{H}|^2 P_t}{2P_n (|\mathbf{H}|^2 P_t + P_n)} \quad (5.22)$$

Hunt [100] has shown that the above 1-D transforms of the column vectors in  $\mathbf{X}$  are equivalent to the standard 2-D transforms of the original image. Hence, we can formulate the likelihood ratio test using 2-D Fourier transforms analogous to Equation (5.22). The random signal model in the spatial-spectral domain is

$$X(k_x, k_y) = H(k_x, k_y) T(k_x, k_y) + N(k_x, k_y) \quad (5.23)$$

and the transform of the likelihood ratio test  $\Gamma(\mathbf{x})$  at frequencies  $(k_x, k_y)$  becomes

$$\begin{aligned}\mathcal{R}_{\mathbf{x}}(k_x, k_y) &= \frac{X(k_x, k_y) H^*(k_x, k_y) \mathcal{E}[T^*(k_x, k_y)]}{S_N(k_x, k_y) + |H(k_x, k_y)|^2 S_T(k_x, k_y)} \\ &\quad + \frac{|X(k_x, k_y)|^2 |H(k_x, k_y)|^2 S_T(k_x, k_y)}{2S_N(k_x, k_y) (|H(k_x, k_y)|^2 S_T(k_x, k_y) + S_N(k_x, k_y))}\end{aligned}\quad (5.24)$$

where  $\mathcal{E}$  is the expectation operator, and  $S_T(k_x, k_y)$  and  $S_N(k_x, k_y)$  are the power spectral densities. For mine detection the signal variance is small compared to the signal mean, and the above equation is dominated by its first term. In this scenario, Equation (5.24) can be approximated as

$$\begin{aligned}\mathcal{R}_x(k_x, k_y) &\approx \frac{X(k_x, k_y)H^*(k_x, k_y)\mathcal{E}[T^*(k_x, k_y)]}{S_N(k_x, k_y) + |H(k_x, k_y)|^2 S_T(k_x, k_y)} \\ &= X(k_x, k_y)W(k_x, k_y)\end{aligned}\quad (5.25)$$

which is the product of the input signal Fourier transform  $X$  and a Wiener filter  $W$  similar to that derived by Pratt [101]

$$W(k_x, k_y) = \frac{H^*(k_x, k_y)\mathcal{E}[T^*(k_x, k_y)]}{S_N(k_x, k_y) + |H(k_x, k_y)|^2 S_T(k_x, k_y)}\quad (5.26)$$

In the case of high signal-to-noise ratio, the Wiener filter  $W$  performs deconvolution of  $X$ . It whitens the signal and results in an impulse in the spatial domain, which can be used in target detection. For a low signal-to-noise environment, the Wiener filter degenerates to a generalized matched filter, which whitens the clutter. These two features combine to enhance the contrast between target and clutter, which makes the estimator-correlator an attractive approach for mine detection.

## 5.6 Implementation of EC Algorithm

The implementation of the EC algorithm for mine detection is primarily the construction of the Wiener filter shown in Equation (5.26). The filter requires that we estimate power spectra for targets and clutter, as described in Section 5.6.1. Sample Wiener filters are presented in Section 5.6.2. A filter-bank configuration, which allows the EC algorithm to function in minefields containing diverse mines, is detailed in Section 5.6.3.

### 5.6.1 Construction of EC Detector Elements

Figure 5.6 depicts the block diagram of an estimator-correlator implementation. Four quantities are needed to construct the Wiener filter: the target signature  $H$ , the target distortion  $T$ , the target PSD  $S_T$  and the clutter PSD  $S_N$ . Models and estimation methods for the above quantities are described in what follows.

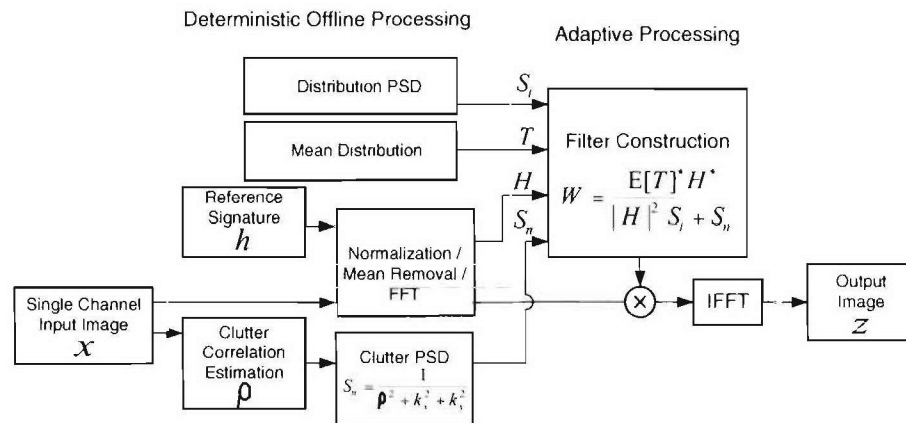


Figure 5.6: Block diagram of EC algorithm.

### Construction of Target Signature

The performance of the EC algorithm improves when the reference  $H$  matches the input signal. An ideal reference template not only matches the mine's overall size and shape but also mimics the spatial variation of pixel intensity.

Real minefields, however, may contain multiple mine types with different sizes and shapes. In addition, differences in paints and construction materials can produce different thermal and scattering properties. As a result, it is impossible to match all types of mines with one reference  $H$ , and multiple reference signatures are of interest.

In this section we discuss the task of creating a reference. In Section 5.6.3 we discuss a technique for processing multiple references in parallel.

The Wiener filter attempts to decorrelate the clutter, which has the byproduct of enhancing the target edges. From prior experience, edges are known to play a dominant role in detector performance. Mines of similar sizes and shapes (and, hence, similar edges) can often share a common reference. This fact reduces the number of references and makes EC a more practical algorithm.

In our implementation, two reference templates were created for detection of large and small mines. We first extracted sample mine image chips and removed the background clutter. Centering the chips and averaging the pixel intensities along concentric circles allowed us to estimate the signature's radial profile. A circularly symmetric reference was constructed with this profile.

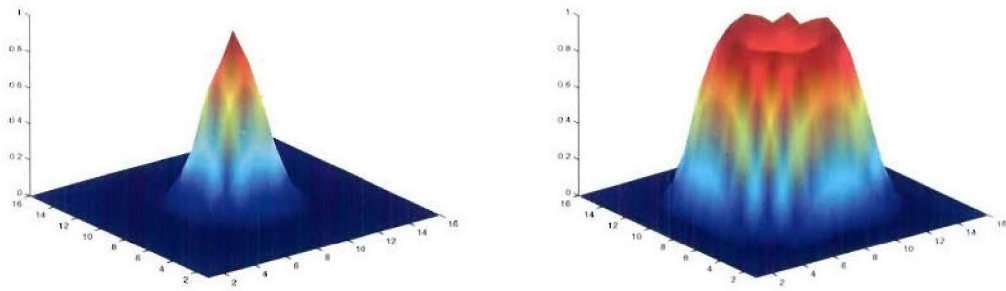
Figure 5.7 shows the spatial variation of the two reference templates. The template diameters are roughly 11 and 7 pixels respectively. Note that pixel intensities in the templates have been normalized to a unit peak. The actual target signature  $h$  can be modeled by a normalized signature  $\hat{h}$  times an unknown mine amplitude  $\alpha$

$$h(x, y) = \alpha \cdot \hat{h}(x, y) \quad (5.27)$$

Substituting Equation (5.27) into Equation (5.26), we have

$$W_j(k_x, k_y) = \frac{\alpha_j \hat{H}_j^*(k_x, k_y) \mathcal{E}[T^*(k_x, k_y)]}{S_N(k_x, k_y) + \alpha_j^2 |\hat{H}_j(k_x, k_y)|^2 S_T(k_x, k_y)} \quad (5.28)$$

in which the subscript  $j$  represents the reference type, which is either a small or large reference in our implementation.



(a) Amplitude-normalized template  $\hat{h}_1(x, y)$  for the small mines.      (b) Amplitude-normalized template  $\hat{h}_2(x, y)$  for the larger mines.

Figure 5.7: EC algorithm templates.

### Imagery Normalization

Variations in environmental conditions change the amplitudes of both targets and clutter. Image intensities are mainly affected by incident (solar and sky) light and surface temperature (thermal emission). The latter is also determined by recent solar insolation. Because the images were taken at different times and under different meteorological conditions, the image dynamic range might vary significantly from one scene to another. To address this problem, a two step procedure is used in processing the imagery. We first removed the mean of the image, and then normalized the residual intensities (mostly clutter) to unit variance. Therefore, the PSD estimated from the normalized image  $\hat{S}_N$  must be multiplied by the clutter variance  $\beta^2$  to yield the clutter PSD,  $S_N = \beta^2 \hat{S}_N$ .

Figure 5.8 shows the signature amplitudes after image mean removal and normalization of the clutter to unit variance. This result indicates that the resulting mine

signatures have consistent amplitudes. Reading from the plots, the ratios  $\alpha_j/\beta$  of large mines are around 3, while the ratios of small mines are about 4. This finding permits off-line estimation of  $\alpha_j/\beta$  for reference  $j$ . A detailed study reveals that optimum detection performance is achieved when  $\alpha_{small}/\beta = 0.39$  and  $\alpha_{large}/\beta = 0.81$ , for small and large mine, respectively. These values are roughly consistent with the ratios of the reference areas ( $7^2/11^2=0.40$  and  $\alpha_{small}/\alpha_{large} = 0.48$ ). Multiplying the normalized signatures  $\hat{H}_j$  by the  $\alpha_j/\beta$  values identified above yields the desired results.

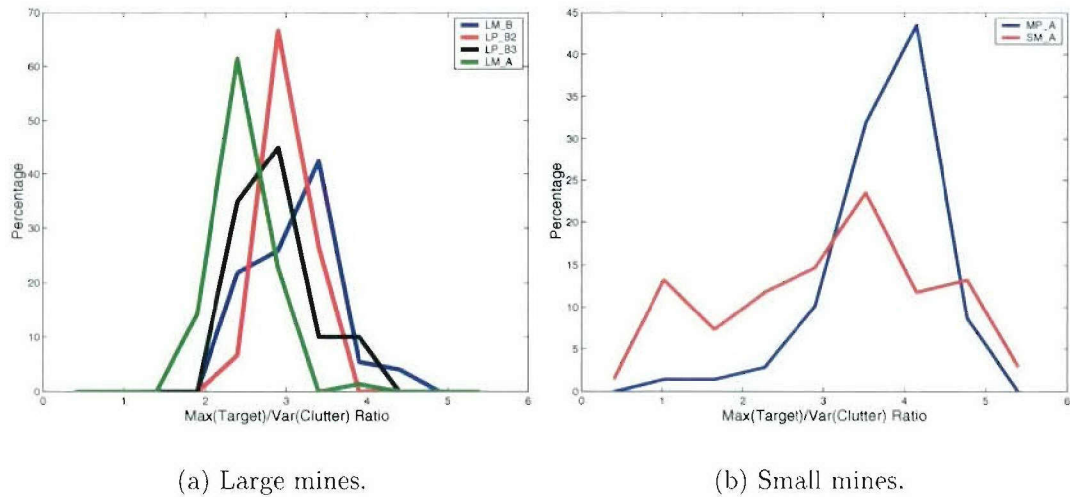


Figure 5.8: Histograms of the ratios of mine amplitudes to clutter standard deviations.

### Estimation of Target Distortion

The reference template  $h$  represents the target signature in an ideal environment, while the distortion term  $T$  accounts for the effects of random factors such as mine tilt, shadowing by ground vegetation, dirty mine surfaces, illumination conditions,

viewing angles, etc. In our implementation, the random distortion is assumed to have a Gaussian power spectral density of the form

$$S_T(k_x, k_y) = e^{-(k_x^2 + k_y^2)\sigma^2} \quad (5.29)$$

and a mean given by

$$\mu_T = e^{-(x^2 + y^2)/2\sigma^2} \quad (5.30)$$

When the variance  $\sigma^2$  approaches zero, the distortion  $t$  becomes a  $\delta$ -function implying that no distortion is present. We empirically determined  $\sigma$  to have the value 1.4 pixels, and we apply this value for every mine type in all scenes.

### Estimation of Clutter Spectrum

The construction of reference templates and the distortion PSD are deterministic processes that can be done off-line as illustrated in Figure 5.6. On the other hand, the clutter spectrum needs to be estimated on the fly, because it is nonstationary. In the discussion of the RX pre-whitening filter (presented in Section 5.4.2), we estimated the clutter correlation using a first-order Markov model. The same assumption can be employed here. The PSD of a two-dimensional first-order Markov process is given by [101]

$$\hat{S}_N(k_x, k_y) = \frac{2}{\rho^2 + k_x^2 + k_y^2} \quad (5.31)$$

where  $\rho$  is the correlation coefficient estimated by approximating the radial profile of the image autocorrelation matrix with an exponential distribution.

### 5.6.2 Sample Wiener Filter

Using the parameter estimates described above, a Wiener filter can be constructed as in Equation (5.28). Figure 5.9 shows the four filter components, and Figure 5.10

gives the resulting Wiener filter. The ring structure indicates that the Wiener filter has a band-pass response.

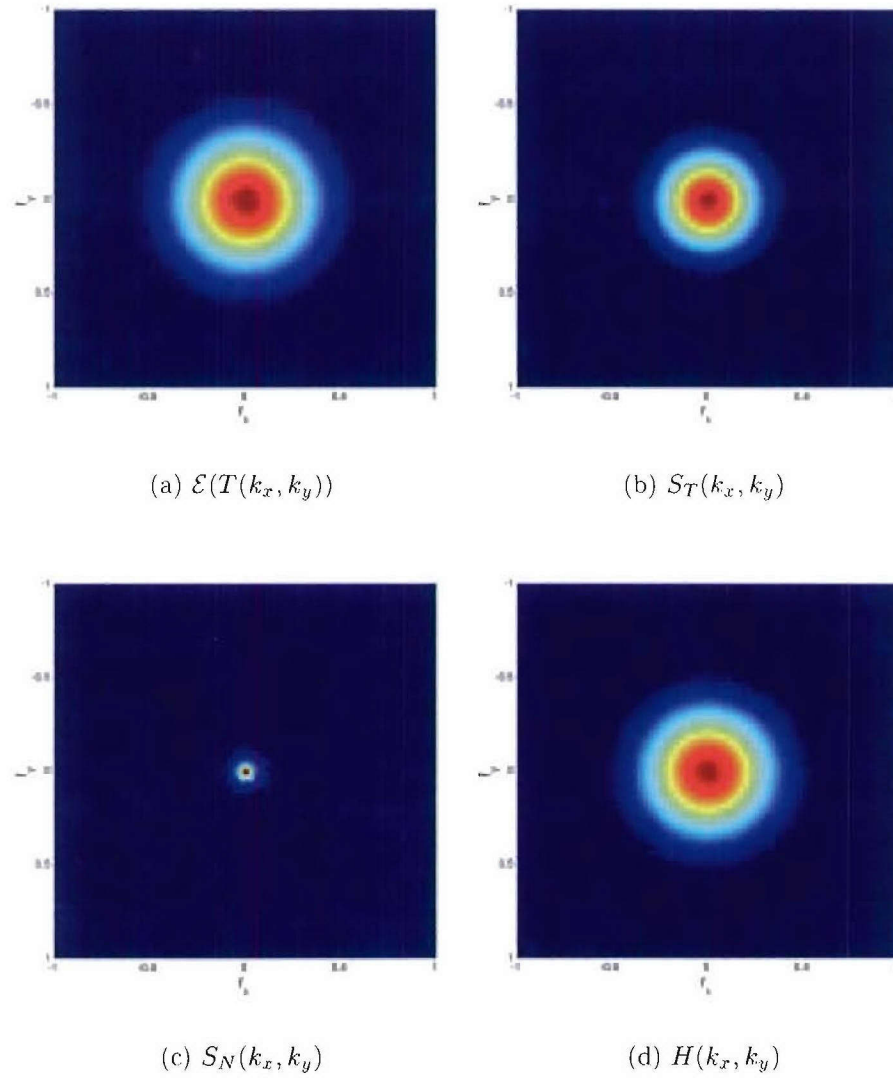


Figure 5.9: Essential components of the Wiener filter.

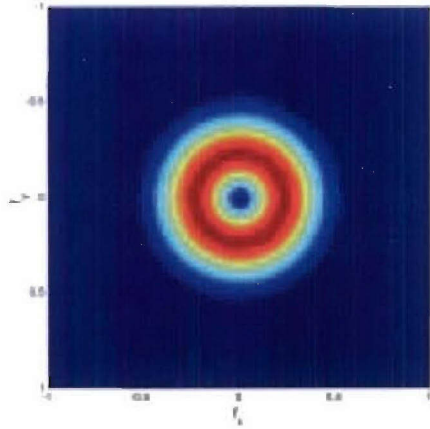


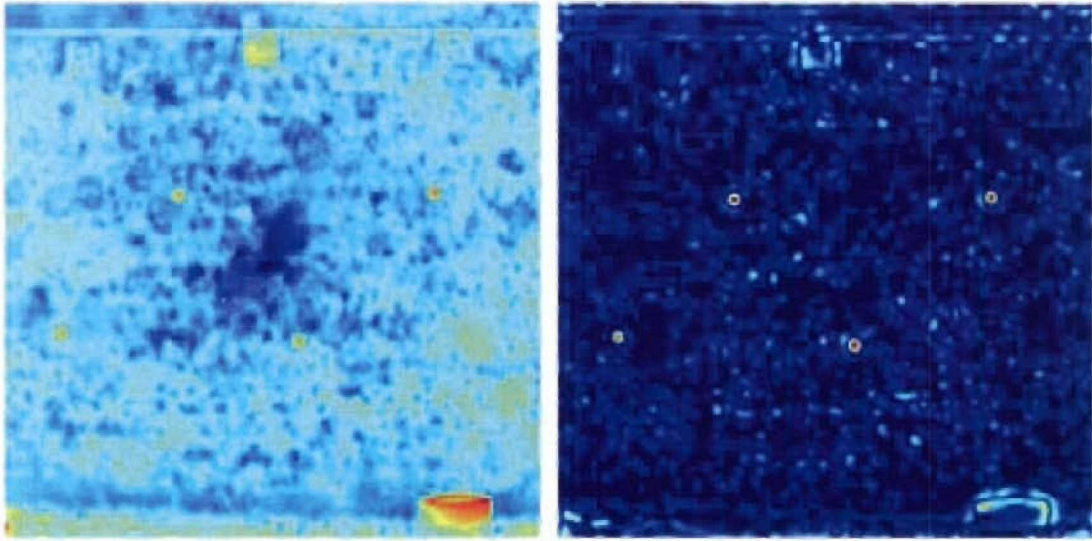
Figure 5.10: The Wiener filter for LMLB mine.

Figure 5.11 shows sample input and output images. The filtered output shows that the Wiener filter deconvolves the target signature and yields impulse-like responses at the target locations.

Figure 5.12 provides a closer look to the response around the mine position before and after Wiener filtering. The two images are normalized to unit energy for comparison. It is evident that most energy is concentrated in the mine region by the filtering process.

### 5.6.3 Filter-Bank Configuration

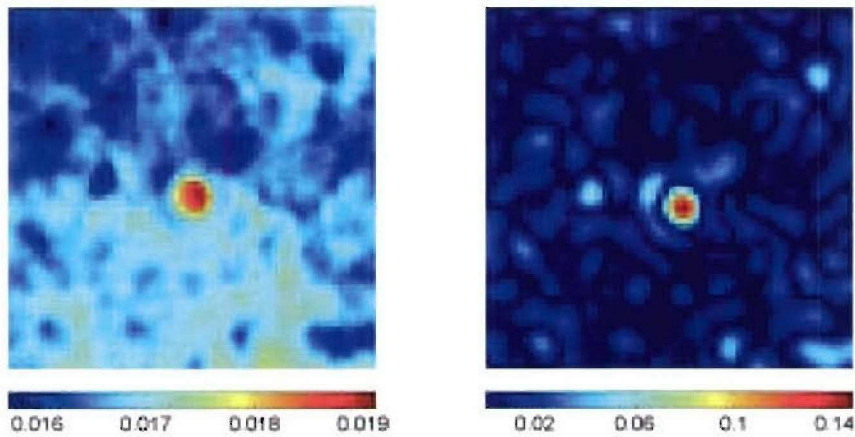
The use of a filter bank boosts the performance of the EC algorithm when diverse mines are present, because the Wiener filter is sensitive to the reference templates, and each template can only be used to detect anomalies of similar shape and size. Since the computational cost of forming and applying additional filters is relatively low, it is practical to simultaneously process the input data with multiple references. Furthermore, since the filter tends to respond to only one type of mine, the results



(a) Raw image.

(b) Filtered image.

Figure 5.11: Sample raw and filtered images.



(a) Raw image.

(b) Filtered image.

Figure 5.12: Normalized images around the mine position before and after Wiener filtering.

of different templates are likely to be disjoint. In addition, because we construct each Wiener filter using normalized signature  $\hat{h}$  and clutter  $\hat{S}_N$ , the mine amplitude parameter  $\alpha_j$  and clutter variance  $\beta$  described in Section 5.6.1 are required to estimate the likelihood ratio. Thus, the likelihood ratio of a mine using multiple references can be approximated by fusing the inverse transform of the filtered result  $\mathcal{R}_{\mathbf{x},j}(k_r, k_y)$  of each reference with a maximum operator.

The number of mine references should be minimized in the interest of efficiency. Prior knowledge of the mine types in a given locale can help determine what references should be included. Figure 5.13 illustrates the EC detector in a filter-bank configuration.

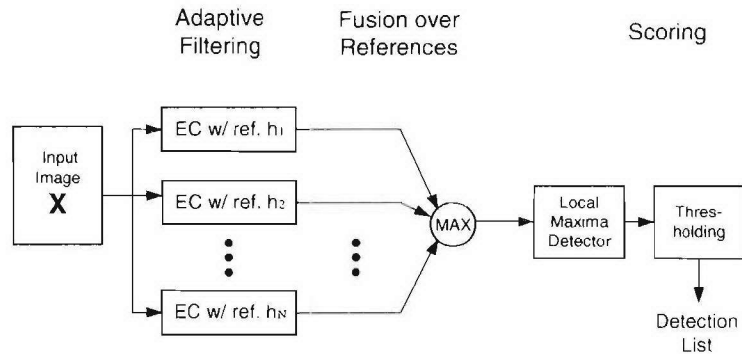


Figure 5.13: Block diagram of the filter-bank configuration.

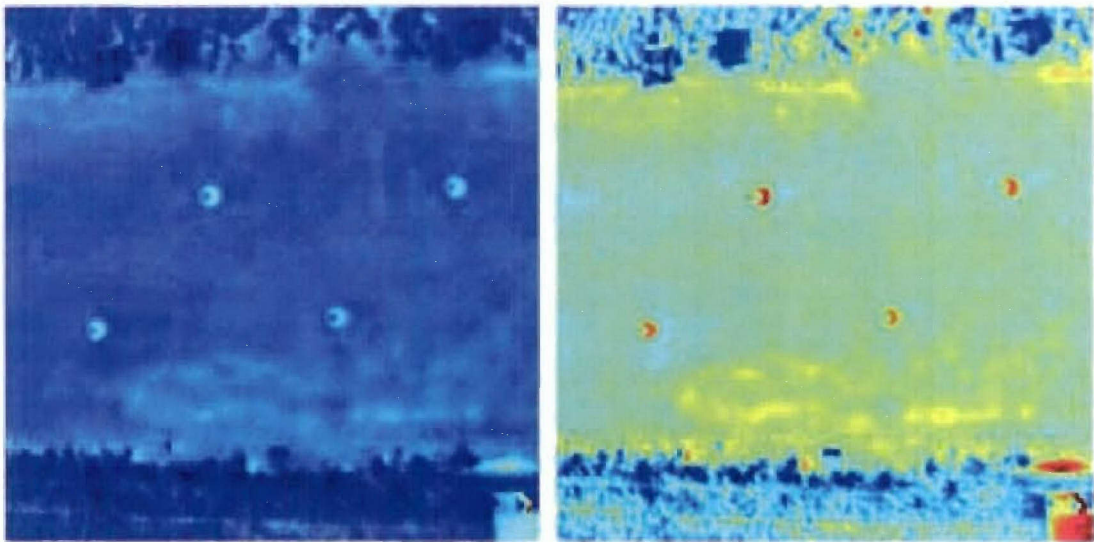
## 5.7 Locally Adaptive EC Detector

In this section, we describe a locally adaptive version of the EC detector to reduce clutter estimation errors due to inhomogeneous background. When the background clutter is homogeneous, the clutter PSD  $\hat{S}_N$  can be estimated for the whole input

image. If an abrupt transition of background type occurs within the image, this estimate is not valid. Figure 5.14 (b) shows an image that has bare soil at the center and rough grass at the top and bottom of the image. Figure 5.14 (c) shows the filtered result with a global  $\hat{S}_N$  estimate. The soil area is relatively smooth, while the grass area contains inhomogeneities that may trigger false alarms. Another scenario that benefits from local clutter estimation is the presence of a large clutter object that occupies a significant portion of the image.

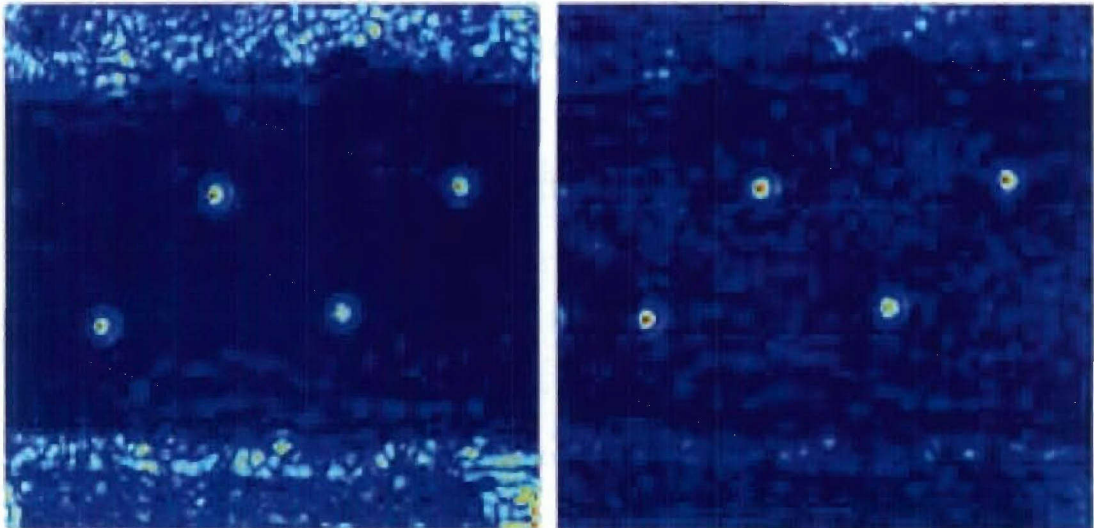
To deal with nonstationary clutter, we employed a sliding window to locally perform clutter estimation and Wiener filtering. In our implementation, the sliding window size was  $48 \times 48$  pixels. This window was further divided into 9 sub-windows and a pixel correlation  $\rho_i$  was estimated in each  $16 \times 16$  pixel sub-window except the center sub-window (to avoid the potential target signature). The effective  $\rho$  was the average of the eight values  $\rho_i$  estimated from the sub-windows. After filtering at one window position, the window was shifted by 16 pixels, and the above process repeated. This 16 pixels step size was chosen to correspond to the scale of local clutter variations and to improve efficiency. Figure 5.14 (d) demonstrates that this locally adaptive EC algorithm can reduce the false alarm rate.

The most significant drawback of the locally adaptive approach is the increase in computational time. Hence, this approach is only recommended when the background texture is changing abruptly. Otherwise, a global EC detector is sufficient for detection in homogeneous backgrounds.



(a) Raw image.

(b) Saturated input image.



(c) Global estimation filtering.

(d) Locally adaptive filtering.

Figure 5.14: Sample EC processing results with global and local clutter estimation.

## 5.8 Performance Evaluation

In this section, receiver operating characteristic (ROC) curves were computed showing probability of target detection ( $P_d$ ) and clutter false alarm rate (FAR [#/ $m^2$ ]) plotted as the ordinate and abscissa respectively. Because very low FARs are of interest, the  $x$ -axis is plotted with a logarithmic scale. The data set used here was the NT-S2 collection described in Section 2.7.2.

After several necessary but uninteresting preprocessing steps<sup>21</sup>, the NT-S2 MWIR data set was processed by the RX, EC and locally adaptive EC algorithms to produce the results shown in Figure 5.15. The EC result with global clutter estimation is inferior to the results for the RX algorithm and the EC algorithm with local clutter estimation. This is a result of clutter PSD errors introduced by inhomogeneous backgrounds, which produce false alarms in the offending areas. Figure 5.15 also indicates that by using local clutter estimation, the EC algorithm can outperform the RX algorithm. One noticeable feature of the locally adaptive EC is its maximum  $P_d$ . Because the (modified) RX algorithm uses a large annular region to estimate the clutter variance, it cannot detect targets near the image edges. The width of the blind region is related to the radius of the annulus. The EC algorithm, however, uses Fourier transforms for applying the filter. As a result, mines near the edges are more likely to be detected, although the periodic extension properties inherent in Fourier approach can introduce other errors.

It was noted above that the locally adaptive EC detector performs better in challenging clutter, but it is more expensive to compute than the EC algorithm with a

<sup>21</sup>Figure 5.14 (b) shows a processed example with correction of corrupted pixels and saturation of highly reflective clutter.

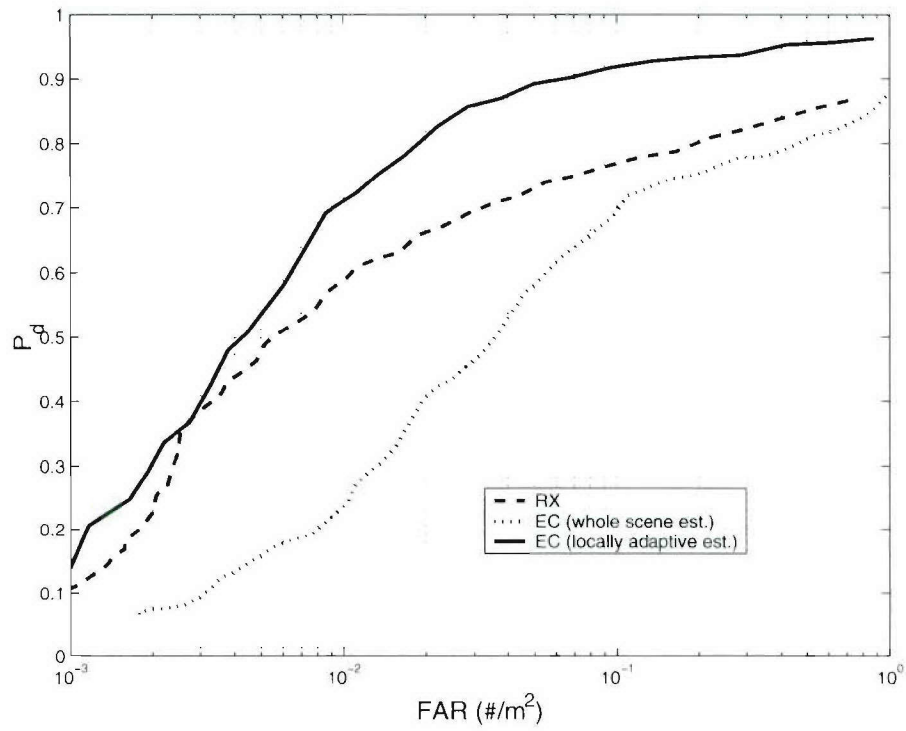


Figure 5.15: Performance of RX and EC algorithms.

global clutter estimation and unnecessary in homogeneous environments. To demonstrate this fact, Figure 5.16 shows ROC curves obtained by processing images that have had the top and bottom edges cropped to avoid the lane boundary and other unintended clutter. For those cropped images the EC algorithm is seen to produce a higher detection rate at low FARs.

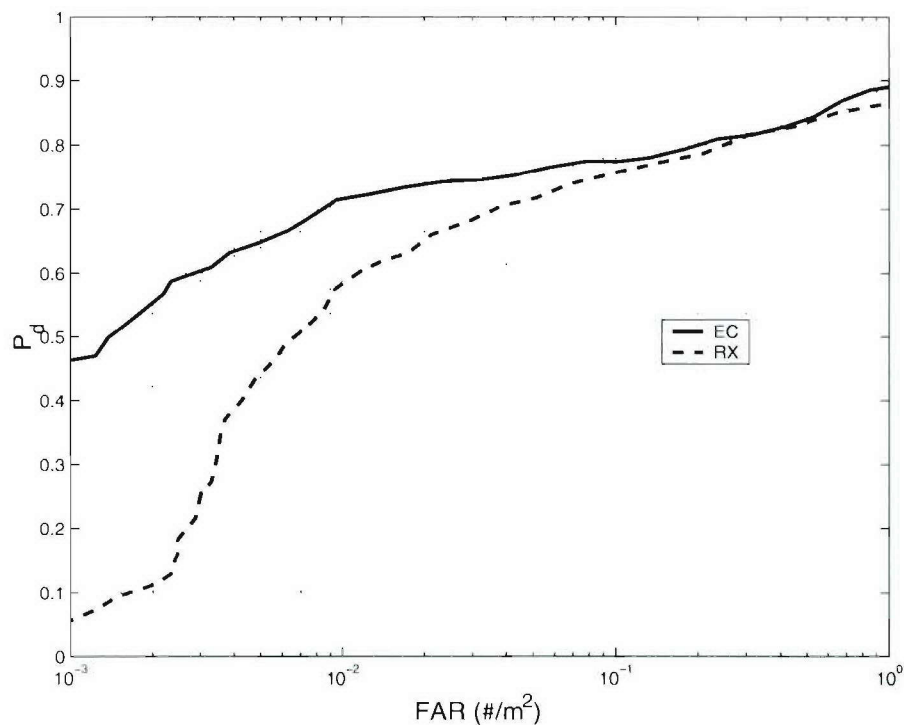


Figure 5.16: Performance of RX and EC algorithms with global clutter estimation in homogeneous background.

Finally, we examine the benefit of using a filter-bank with the EC implementation. Figure 5.17 illustrates the difference between using a single reference and the fused results of large and small references. Apparently, the EC algorithm performance is

improved by using multiple references. Note that the false alarm rate of the fused detector is increased at low FARs due to the strong clutter present in large and small reference results. Nonetheless, fusion helps detect both small and large mines efficiently.

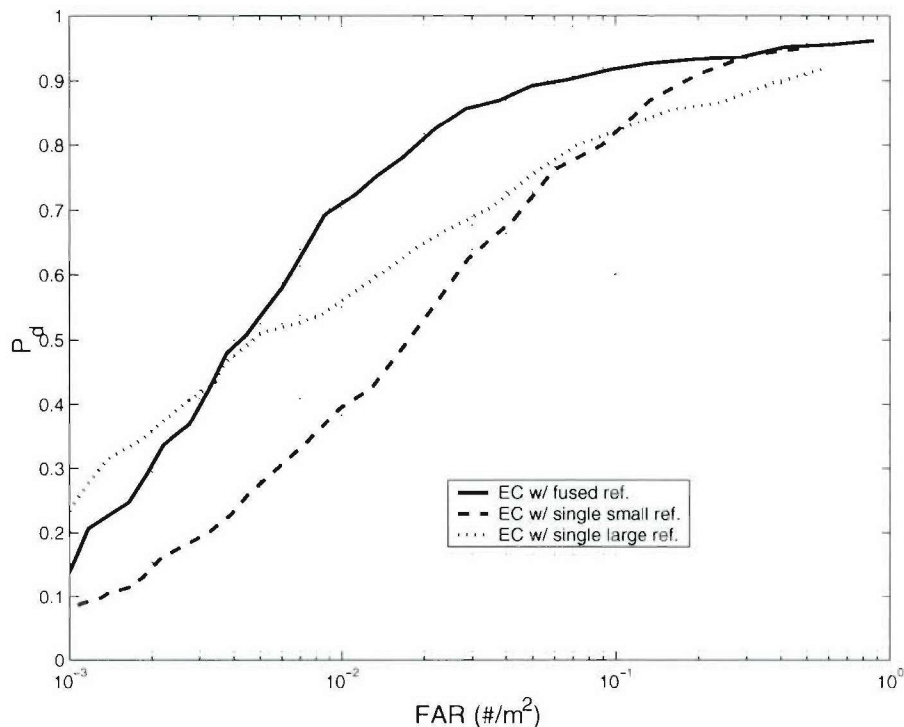


Figure 5.17: Performance of EC algorithm with fused and single references.

Above results demonstrated that the EC algorithm achieve a significant improvement compared to the existing RX algorithm. However, it still not meet the specified detection criteria<sup>22</sup> for scanning sensors, which is 0.95  $P_d$  at 0.02 false alarm per square meter<sup>23</sup>, because only two references are used to detect six types of mine at

<sup>22</sup><http://www.uxocoe.brtrc.com/Archived/1999/A53.htm>

<sup>23</sup>The locally adaptive EC and RX achieved 0.81 and 0.66  $P_d$  at 0.02 FAR for the NT-S2 collection.

various times. The EC algorithm performance is expected to be improved by using more specialized references that matches the mine response under different environmental conditions. The radiometric model explored in this work may be useful for above application. The integration of the EC algorithm and the radiometric model can be an interesting future work topic.

## 5.9 Summary

In this chapter we examined two mine detection algorithms of different strategies. The RX algorithm detects anomalies introduced by surface-laid mines with a general reference that includes only size and shape information. The EC algorithm uses specialized references, which can be generated by the radiometric model presented in previous chapters, to capture specific types of mine. Although slightly more complex (two components) mine models were considered here, the use of results from this radiometric model is left as future work.

The RX algorithm requires minimal knowledge about potential mines. The detector can be easily implemented and tolerates variations in mine signatures. The performance of the RX detector is limited by the similarities among mine and clutter signatures. Since RX is an anomaly detector, it may suffer a high false alarm rate if the clutter is similar in size and shape to the mine. Performance improving techniques for the RX algorithm were investigated. The clutter whitening scheme helps to reduce the clutter correlation to improve RX performance. The multi-component RX is theoretically sound but may have limited improvement in practice.

The EC algorithm can make use of information about the mine including its type, time of operation, date of the year, and environmental conditions. That knowledge

can be utilized to produce well-matched references (and better performance) using the radiometric model developed in this work. However, highly detailed, very specific references are not always favorable for general mine detection, since variation in mine shape and surface properties are commonly observed. A filter bank configuration is recommended to make the EC detector adaptive across different mine types. An adaptive EC detector was developed using a localized clutter estimation scheme to maintain reliable detection performance.

The EC detector with a filter-bank implementation was shown to provide a substantial performance gain compared to the RX detector. A locally adaptive EC detector is needed for the imagery used here, because it contains inhomogeneous backgrounds that trigger false alarms.

In practice, the EC detector requires more tune-up to adapt a new set of mine imagery. For RX detectors, the operator only needs to adjust the reference and window sizes for potential mine types. For EC detectors, the spatial profile of the mine, which is subject to changes in sensor passband and environmental conditions, is desired to construct a matched reference. Furthermore, if a multi-reference EC detector is implemented, the selection of the amplitude weights  $\alpha$  described in Section 5.6.1 need to be tuned to achieve optimal performance. However, the pay back for the extra efforts of EC implementation is the superior detection performance.

## CHAPTER 6

### CONCLUSION

In this work the problem of mine detection using EO imagery was explored. This work presents several contributions: (1) A polarimetric radiometric model was constructed and used to produce detailed mine signatures. The predicted signatures were validated with multiple sets of measured data. (2) General guidelines for sensor deployment were defined to improve mine target-to-clutter ratios. (3) An attractive detection algorithm based on an estimator-correlator formulation was devised and tested with measured imagery. Comparisons to the baseline algorithm (the “RX” algorithm of Reed and Yu) show significant performance gains.

The findings of this dissertation are useful to both sensor system designers and algorithm developers. By simulating mine signatures under different environmental conditions, system designers can identify deployment conditions that will ensure high image quality. For algorithm developers, the estimator-correlator algorithm can provide immediate performance improvements. The algorithm’s ability to use more detailed signature information can provide additional gains, but has not been explored here in any detail.

In the remainder of this section we elaborate on the above remarks. In Sections 6.1 and 6.2 we highlight major findings of the work. Potential topics for future work are presented in Section 6.3.

## 6.1 Summary of and Findings for the Radiometric Model

A simulator was developed to predict polarimetric properties of passive EO mine signatures. Source radiances considered by the simulator are surface temperatures predicted by a thermal model and solar radiation computed by MODTRAN. It addresses the source-target-sensor geometry, atmospheric effects, and statistical descriptions of rough surfaces. In this model environmental conditions and sensor parameters such as passband, orientation, viewing angle, and impulse response are adjustable. A polarimetric BRDF model was developed for scattering of mine-like (moderately rough) surfaces and validated with published data. Primary radiation sources such as thermal emission, direct and scattered solar radiation were modeled with realistic temporal dependences so that designers can simulate signatures at any time of the day to develop guidelines for sensor deployment. An extensive body of simulation was conducted to study the significance of radiometric components under different sensor passbands, the temporal variation in mine signatures, effects of environmental conditions on thermal signatures, and effects of sensor geometry. The resulting signatures show good agreement with measurements of several data sets.

Specific findings drawn from the the work are listed below.

- **Polarimetric properties of passive signatures:** Simulations show that the source-target-sensor geometry is the primary factor in signature polarization. An obliquely viewing sensor is advantageous for passive polarimetric sensing.

Effects of higher-order scattering components have little contribution to the total image.

- **Component significance and sensor passbands:** The significance of each radiometric component was examined to understand the spectral properties of mine signatures. Thermal emission becomes important as the wavelength increases, and we see it dominate in the MWIR band and beyond. Mine detection at longer wavelengths (MWIR and LWIR) is based on temperature contrast and differences in thermal properties and emissivity. Direct and scattered solar radiation are the dominant sources in the visible and SWIR bands, but they become negligible at longer wavelengths. Visible and SWIR sensors only work during daylight hours and the shadow is often an important feature in detection.
- **Temporal variation in mine signatures:** EO mine signatures vary strongly with time. Solar reflections only appear during day time and are proportional to the insolation. The surface temperature of a mine (a thermal insulator) is greater than that of the background during the day, and the temperature contrast is inverted after sunset. Around dawn and dusk, thermal “crossovers” occur, which correspond to equal temperatures on mine and soil surfaces. (Since mines and clutter do not show a uniform temperature, this concept must be interpreted loosely.) The shadow produced by sunlight is an important feature of daytime signatures. In particular, the shadow is the only detectable signature component during the morning crossover.
- **Mueller Matrices for Mine and Soil Scattering:** By combining a polarimetric version of Beckmann’s model with concepts described by Torrance and

Sparrow, a Mueller matrix was developed that is capable of predicting scattering from rough surfaces encountered by demining sensors. The proposed model produced BRDFs in good agreement with measured data. An extensive comparison made for visible wavelengths suggests that the model is valid for moderately rough (mine) surfaces. For natural surfaces (background), which tend to have a multi-scale roughness, a composite rough surface model (not implemented in this work) could be used by employing tilted FEM mesh facets to reproduce decimeter-scale blotches seen in the background.

- **Effects of environmental conditions on thermal signatures:** The effect of environmental conditions on surface temperatures was studied via simulations of different time-of-day, day-of-year and wind speeds. The greatest target contrast was found near mid-day. Wind was shown to reduce the range of temperature difference as a result of greater convection.
- **Effects of sensor geometry:** Several sensor parameters are examined to see their impacts on signatures. DoLPs of solar reflection are sensitive to the sensor's orientation toward the source. DoLPs near specular regions are two orders greater than those in backscattering regions.
- **Guidelines for sensor deployment:** Operational guidelines can be derived from this work. The insolation is at its peak and the temperature contrast is greatest around mid-day. Shadows can be a useful cue for operations near sunrise. Operation at sunset is particularly challenging and should be avoided. Low wind speeds are preferred, since convection reduces the contrast. Passive polarimetric sensors should use an oblique viewing angle. Also, a polarimetric

sensor should be oriented very close to the solar specular direction to take advantage of the mine's large DoLP.

- **Use of a multi-sensor suite:** Simulations conducted in this work show that sensors of different passbands exhibit distinctive features in signatures. Some easily detectable features only show at certain time or environmental and operational conditions. A detection system with a multi-sensor suite (of visible, SWIR, MWIR, and LWIR) may take advantage of those features to enhance the detection rate with multispectral image processing techniques.

## 6.2 Summary of and Findings for Mine Detection Algorithms

In the second part of this dissertation, algorithms were studied for mine detection in EO imagery. An estimator-correlator approach was used to develop an alternative to the current baseline (RX algorithm). The estimator-correlator exploits the spatial structure of clutter and mines. It degenerates to a Wiener filter when the clutter is Gaussian distributed. Unlike the RX detector, which is an anomaly detector useful when knowledge about the mines is limited, the EC detector can be adapted to find specific mines in certain circumstances. The development of the radiometric model make it possible (in principle) to use carefully tuned references to achieve a superior detection rate. Some specific findings are as follows:

- **RX performance enhancements:** Several techniques were described (and tested) for improving the performance of the RX algorithm. A clutter whitening filter was used to reduce correlation in adjacent pixels. Another modification for multicomponent targets will improve detection if reliable information about

potential mine types is available. Finally, a frequency domain RX implementation was found to greatly improve computational efficiency.

- **Performance studies of the EC detector:** The EC detector described above was implemented and tested on measured imagery. Two major modifications to the basic concept were found to improve performance. First, by applying the algorithm in a sliding window, the algorithm can be adapted to local clutter statistics. Second, multiple reference targets can be processed in parallel, making the algorithm effective against diverse target sets. Comparisons of the RX and EC algorithm showed a significant advantage to EC when these modifications were used.

### 6.3 Future Work

In the course of preparing this dissertation, it became apparent that several topics require further investigation.

- **Modeling of vegetation:** Simulations conducted in this work assume background a flat, homogeneous soil, which simplifies the modeling. In reality, however, most sites contain some vegetation, which has distinctive thermal and surface roughness properties. For example, grass may have non uniform densities and preferred scattering directions. Spatial, spectral and polarimetric models for vegetation background are needed to simulate real EO signatures.
- **Mesh Generation:** Solar shadows can produce strong surface temperature differences over distances on the order of one centimeter. Creating a FEM mesh with a sufficient node density strains one's computational resources, especially

when it is noted that the shadow boundary moves with time. The meshes used in the work were derived from a body of revolution model and subsequently refined off-line to include more nodes at large radial distances. The improvement derived from that refinement process was limited. An iterative mesh refining scheme should be explored that will sub-divide facets with larger temperature gradients on the fly.

- **Modeling of localized source conditions:** The current implementation of the thermal model only includes a few localized source conditions introduced by the geometric structure of a surface-laid mine. Variations in thermal emission and convection on a surface point due to nearby landmine structure should be considered to improve the accuracy of the thermal model results.
- **Active sensors:** The simulations presented in this work all involve natural radiation sources and passive sensors. Active sensors, involving laser illuminations, are also being considered for mine detection. Since lasers are easily polarized, the polarimetric properties of surface scattering are better revealed by such sensors. The proposed radiometric model can be readily modified to simulate active sensor signatures. Most active sensors view back-scattered radiation, which simplifies the BRDF modeling task considerably.
- **Integration of the radiometric model and mine detection algorithms:** The proposed EC detector can utilize the detailed signatures simulated by the radiometric model. An adaptive scheme that updates the reference target on the fly according to changes in sensor geometry and environmental conditions could further improve the mine detection rate.

## 6.4 Concluding Remarks on EO Mine Detection

Mine detection with airborne EO sensors is meant to be a fast and safe approach. However, a great variation in EO mine signatures due to the changes in environmental conditions prevents a reliable detection performance that is essential to achieve the goal of a real-time minefield detection system. Accuracy and computational efficiency of the current mine detection algorithm needs to be improved. Furthermore, deployment guidelines are necessary to ensure image quality. Throughout this work, we demonstrated that the radiometric signature model is capable of predicting realistic mine signatures and providing physical insights to the EO mine detection process so that system designers can optimize the detector under different operation conditions. The benefits of the signature model can be forwarded to the estimator-correlator detection algorithm to improve and ensure mine detection and clutter rejection performance. The achievements made in this work provides one step forward to construct a real-time airborne EO minefield detector.

## APPENDIX A

### RADIOMETRY

EO mine detection is based in radiometry, which is the measurement of quantities associated with radiant energy and process of radiative transfer. Definitions of basic radiometric quantities and properties are given here, as well as the fundamental equation of radiative transfer. A brief description of the elements of an EO sensor system is also presented in this section. The blackbody radiation law, which forms the fundamental thermal emission model, is briefly reviewed in the end of this section.

#### A.1 Radiometry Terms

Radiometric terms are essential to describe an optical system. They includes definitions of energy, power, and geometric characteristics that arise during radiative transfer. Listed below are some critical radiometric quantities.

##### A.1.1 Solid Angle and Projected Solid Angle

Solid angle is a critical concept in radiative transfer. Similar to the definition of angle, which is the ratio of an arc length to its radius, a solid angle is the ratio of a spherical area to the square of its radius.

$$\Omega = \frac{A \cos \theta}{r^2} \quad (\text{A.1})$$

Solid angle has the dimensionless units of steradians.

Most surfaces are not spherical, and solid angle is commonly expressed in differential form. The differential solid angle of surface 1 viewed from surface 2 is given by

$$d\Omega_{12} = \frac{dA_1 \cos \theta_1}{r^2} \quad (\text{A.2})$$

The surface area visible to an observer is reduced as the surface normal tilts away from the line of sight. The effective area is termed the “projected” area. The same concept is used to define a “projected” solid angle. If  $\theta_1$  is the angle of the surface normal with respect to the direction of radiation, and  $\theta_2$  is the angle of the surface normal with respect to the observer, the projected solid angle  $\Omega_{p12}$  is given by

$$d\Omega_{p12} = d\Omega_{12} \cos \theta_2 = \frac{dA_1 \cos \theta_1}{r^2} \cos \theta_2 \quad (\text{A.3})$$

This quantity is helpful in simplifying the expression of radiative transfer.

### A.1.2 Flux, Radiance, and Irradiance

The rate of change of radiant energy (i.e., the power) is referred to as flux  $\Phi$  in radiometry.

$$\Phi = \frac{\partial Q}{\partial t} [\text{W}] \quad (\text{A.4})$$

The flux density, which is the area density of power, is referred to as irradiance. In some cases, the irradiance is further specified as “radiant exitance” or “radiant incidence” if the energy is emitted from or incident on the surface, respectively.

$$E = \frac{\partial \Phi}{\partial A} [\text{W}/\text{m}^2] \quad (\text{A.5})$$

The fundamental radiometric quantity is radiance, which is the quantity of flux per unit solid angle leaving or arriving at a surface. Its propagation direction is confined

to an elementary cone containing a specific direction. Radiance is defined as the flux per unit projected area and per unit solid angle.

$$L = \frac{\partial\Phi}{\partial A \cos\theta \partial\Omega} \quad (\text{A.6})$$

### A.1.3 Spectral Dependency

Spectral variables are often used in radiometric analysis, since the surface properties of most materials and the transmittance of the atmosphere vary across the spectrum. To stress the spectral dependency, radiometric quantities are often expressed as functions of wavelength or frequency. The spectral radiance below is an example.

$$L_\lambda = \frac{\partial L}{\partial\lambda} \quad (\text{A.7})$$

## A.2 Radiative Transfer

The fundamental equation of radiative transfer, which appears in Equation (A.8), provides a means to calculate the energy propagating from one surface to another.

$$d\Phi_{21} = L_1 \frac{dA_1 \cos\theta_1 dA_2 \cos\theta_2}{r^2} \quad (\text{A.8})$$

The relation defines the time rate of change of radiant flux leaving surface 1 to surface 2 in a vacuum space.

Using definitions stated in Section A.1.1, we can show the radiance exchanged between two surfaces in a vacuum is invariant. Define the quantities

$$L_2 = \frac{d\Phi_{21}}{dA_2 \cos\theta_2 d\Omega_{12}} \quad (\text{A.9})$$

$$d\Omega_{12} = \frac{dA_1 \cos\theta_1}{r^2} \quad (\text{A.10})$$

$$d\Omega_{21} = \frac{dA_2 \cos\theta_2}{r^2} \quad (\text{A.11})$$

Substituting Equations (A.8) and (A.10) into (A.9), we have

$$L_1 d\Omega_{12} = L_2 d\Omega_{21} \quad (\text{A.12})$$

which shows that the radiance emitted from surface 1 toward surface 2 ( $L_1$ ) equals the radiance surface 2 receives from surface 1 ( $L_2$ ).

The fundamental equation of radiative transfer can be applied to more complicated scenarios. Say we want to know the radiance arriving on surface 2, which includes not only a direct emission ( $L_1$ ) from some surface 1, but also reflections from other sources by surface 1. Then  $L_2$  can be expressed as the sum of the direct emission and the integral of radiance ( $L_{EXT}$ ) over the hemisphere viewable from surface 1. With the help of the geometric parameters ( $\theta$ ,  $\phi$ , and  $\mathbf{r}$ ) and the bidirectional reflectance distribution function  $\mathcal{F}$ , which is defined in Section 2.4, we can specify  $L_2$  as

$$L_2(\theta, \phi, \mathbf{r}) = L_1(\theta, \phi, \mathbf{r}) + \int_0^{\pi/2} d\theta' \sin \theta' \int_0^{2\pi} d\phi' \mathcal{F}(\theta, \phi, \theta', \phi') L_{EXT}(\theta', \phi', \mathbf{r}) \quad (\text{A.13})$$

In this result it is assumed that radiant sources other than surface 1 are placed far away, so that mutual coupling between sources and surfaces can be neglected. Also, other sources are assumed to not be viewable from surface 2, and surface 1 is presumed infinitesimally small to simplify the expression.

### A.3 Radiometric Framework of EO Sensors

Figure A.1 illustrates basic elements of radiometric measurement for EO sensors [102, 27, 103], and it is applicable to landmine detection.

The EO sensor, which is usually a CCD camera, receives reflected and emitted radiances as shown by the blue and red lines in Figure A.1. The radiation sources include illuminators, targets, and background. The illuminator can be the sun in a

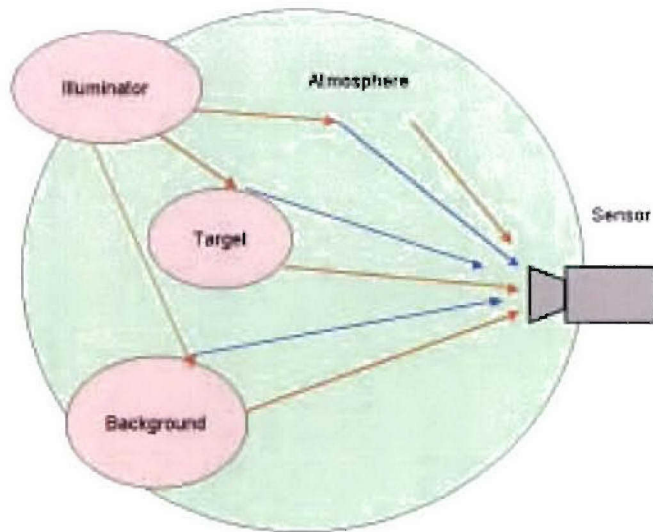


Figure A.1: Radiometric framework of EO Sensors.

passive sensor system or a laser beam in an active sensor system. Thermal emission from targets and background located within the detector's field of view (FOV) reaches the sensor directly. The radiance emitted from illuminators may reach the detector directly or via reflection. Note that the figure doesn't show multiple scattering, which is important in some environments. The atmosphere can also be an important factor, since it contains particles and molecules that emit, scatter, and absorb radiance.

#### A.4 Blackbody Radiation

Because passive radiation sources encountered in remote sensing generate radiance via thermal emission, it is appropriate to discuss the basic mechanism for thermal emission: blackbody radiation. Also described as Planck's radiation law, it predicts the spectral radiance of a perfect emitter. A convenient expression of Planck's radiation law is given by Rybicki [104] who writes the spectral radiance as a function of

wavelength and surface temperature,

$$L_{BB}(\lambda, T) = \frac{2c^2h}{\lambda^5} \frac{1}{e^{h\nu/kT} - 1} [\text{W m}^{-2} \text{sr}^{-1} \mu\text{m}^{-1}] \quad (\text{A.14})$$

where  $c$  is the speed of light in a vacuum,  $h$  is Planck's constant,  $\nu$  is the frequency, and  $k$  is Boltzmann's constant. This function serves as the basic model for thermal emitters. The spectrum of a real surface is less than that predicted by Planck's law. Such surfaces are referred to as graybodies, and the ratio of the true and blackbody emission is denoted the emissivity  $\mathcal{E}$ , which is a number between zero and one. Thus, the thermal emission from a surface is known if one has knowledge of both the surface temperature and surface emissivity.

## APPENDIX B

### ELECTRO-OPTIC SENSORS

Optical sensors are devices that can convert radiant electromagnetic energy into other forms. For example, a conventional camera, an imaging optical sensor, stores photometric information via chemical reactions. In this work, we are interested in electro-optic (EO) sensors that convert optical energy into electric energy.

#### B.1 Physics of EO sensors

A typical EO sensor is a semiconductor device that changes its conductivity according to the number of photons impinging on it. Its spectral sensitivity is determined by the type and amount of impurity dopings. Sensors that reacts to a narrow bandwidth are good for observing laser backscattering while broadband sensors are suitable for passive terrestrial observations.

Three types of semiconductor components are found in EO sensors: photoconductive (PC), photovoltaic (PV), and charge coupled devices (CCD). A PC detector, whose resistance is inversely proportional to the radiation exposure, is connected in series with a load resistor. The signal is read out as the voltage across the detector or the load resistor. The advantages of a PC detector are its fast response time and its ability to work at longer wavelengths. Its primary disadvantage is that the change in

detector resistance is a function of the substrate temperature, which leads to frequent calibration. The PV detector is a diode that produce a current proportional to the number of incoming photons. It is usually used in an operational amplifier feedback circuit. Many devices that work in the visible or near IR ranges are made of PV detectors.

Unlike the single element devices described above, array devices have become popular due to their imaging efficiency and higher resolution. The CCD detector is the most popular of the array sensors, and airborne mine detection systems are likely to use CCD detectors. A CCD detector comprises an array of MOS capacitors aligned in rows. Each capacitor represents a pixel and it creates electro-hole pairs during exposure, then the charges are shifted sequentially to the output register and read out via an output amplifier. The simple structure of a CCD detector makes it possible to produce high-resolution imaging sensors. Silicon-based CCD detectors are suitable for making visible and near IR sensors, but, it is more challenging and expensive to manufacture infrared sensors responding to longer wavelengths.

## **B.2 Types of EO sensors**

EO sensor systems can be categorized according to their spectral bandwidth, spatial resolution, radiation source, and polarimetric dependence. In this section we summarize the types of EO sensors commonly used in mine detection.

### **Visible, IR, and UV Sensors**

Wide-band EO sensors can be roughly divided into UV (10-400 nm), visible (400-750 nm), near IR (750-1000 nm), short wavelength IR (1-3  $\mu\text{m}$ ), mid wavelength IR (3-5  $\mu\text{m}$ ), long wavelength IR (8-14  $\mu\text{m}$ ), and very long wavelength IR (14-20

$\mu\text{m}$ ). The choice of sensor bandwidth should be made according to the properties of the radiation source and reflection/emission characteristics of the intended targets. As an example, solar radiation, which is well approximated by a  $5800^\circ\text{K}$  blackbody, is strongest in the visible band, while thermal emission from terrestrial objects at  $285\pm 30^\circ\text{K}$  dominates near  $10\ \mu\text{m}$  wavelengths. Therefore visible cameras work best with daylight or artificial light sources, while night-vision goggles employ IR sensors.

Other differences between visible and IR sensors include their resolutions and optical components [102]. Because IR sensors respond to longer waves, the resolving power of IR optics is much coarser than visible optics. Although similar optical components (i.e., prisms, lenses and mirrors) are employed in both visible and IR sensors, the materials used are different. Ordinary glass is transparent in the visible band but is opaque in IR. On the other hand, germanium is opaque to visible light but is transparent to IR waves.

Ultraviolet (UV) or even x-ray sensors are also used in remote sensing, and are popular choices for sensors mounted on space platforms. Several advantages come with their short wavelengths [105], which permits optical lenses to be made smaller and detector arrays to be constructed with higher densities. Furthermore, internal noise is not as severe at UV as IR, and no active cooling equipment is needed. However, the atmosphere has a greater impact on the scattering and absorption of UV radiation than visible or IR radiation. Limited studies and experiments have been done in the UV band, which prevents UV sensors from seeing more extensive use.

## B.2.1 Passive and Active Sensors

EO sensor systems can be grouped into passive and active types based on the illumination source. Passive systems employ natural radiation sources such as sunlight and thermal emission, leading to a simple sensor configuration. A CCD camera with a shutter control is essentially a passive sensing system. The disadvantages of passive sensors are a lack of control over the source radiance and complicated radiation paths. As an example, when a visible camera is used to scan the reflected solar radiation from a minefield during the day, the magnitude and direction of sunlight varies with time and weather conditions (i.e. the presence of clouds and other aerosols) during the measurement. As a result, calibration is needed to process images collected at different times and locales. Furthermore, it is challenging to construct a signature model for passive sensors, because the sensor output is a summation of irradiance from various sources and different transmission mechanisms. A detailed discussion of the radiation sources observed by passive sensors is given in Section 2.2

Active sensors typically rely on target backscattering, which involves the reflection characteristic of the target surfaces. In mine detection, an active sensor could employ a laser source that generates a beam of narrow-band radiation. Although this type of sensor requires a separate source, it has some desirable properties not available to passive sensors. Specifically, the scattering geometry is simplified because the source and the receiver are co-located. Hence, only backscattering from the target needs to be considered, while the complete BRDF must be known to model passive sensors. In addition, smooth (man-made) and rough (natural) objects can be differentiated via the de-polarization that occurs preferentially for rough objects illuminated by

polarized sources. Also, the dependence on environmental conditions is reduced since the sensor carries its own source.

### **B.2.2 Single- and Multi-Spectral Sensors**

A single-channel sensor reports the integrated spectral irradiance received within the passband of the sensor, while a multi-channel sensor records data in parallel in several sub-bands. Multi-spectral sensors are desirable when the reflection and emission properties of the target and clutter are strongly wavelength dependent. More target features such as the sub-band correlation can be extracted by using multi-spectral sensors. This extra information is often helpful in detection and classification, since one can develop processing algorithms to exploit multiple channels. Sensors used in space exploration usually contain several channels to utilize every bit of information.

Multispectral sensors are made either by combining individual spectral sensors from different bands or by placing several filters in front of the same EO sensor. The first approach involves integrating different systems and may require registration of images from different sensors while the latter approach needs only a few extra components. The benefit of the first method, however, is the parallel acquisition of data.

### **B.2.3 Polarimetric Sensors**

Polarimetric sensors are another method of maximizing the amount of information in each pixel. Polarimetric sensors preserve the polarization information in the received signal for later processing.

In surface-laid mine detection, polarimetric sensors provide a means to improve target discrimination, since man-made objects (i.e. smoother surfaces) depolarize

less than natural clutter (i.e. rougher surfaces). A model for the polarimetric signatures of potential targets and clutter can help identify the polarimetric parameters that are critical to target classification, thereby reducing the number of necessary measurements.

## APPENDIX C

### DERIVATION OF THE RX ALGORITHM

Here we review the derivation of the RX algorithm, which is a GLRT approach. The hypotheses of the mine and clutter are modeled by

$$\begin{aligned} H_0 &: \mathbf{y} = \mathbf{N} \\ H_1 &: \mathbf{y} = \mathbf{N} + \mathbf{S}\mathbf{B} \end{aligned} \quad (\text{C.1})$$

in which  $\mathbf{B}$  and the covariance of  $\mathbf{N}$  are unknown.

The detection problem defined by Equation C.1 can be treated with the generalized likelihood ratio test. An application of this well known techniques yields the following likelihood ratio

$$L_G(\mathbf{y}) = \frac{p(\mathbf{y}|\hat{\mathbf{B}}_1, \hat{\mathbf{M}}_1, H_1)}{p(\mathbf{y}|\hat{\mathbf{B}}_0, \hat{\mathbf{M}}_0, H_0)} \quad (\text{C.2})$$

where  $\hat{\mathbf{B}}$  and  $\hat{\mathbf{M}}$  are the ML estimates for the target amplitude and covariance respectively.

The clutter probability density function (PDF) conditioned on  $\mathbf{B}$  and  $\mathbf{M}$  is given by

$$\begin{aligned} p(\mathbf{y}|\mathbf{B}_i, \mathbf{M}_i) &= \frac{1}{2\pi^{NJ/2}|\mathbf{M}_i|^{N/2}} \\ &\cdot \exp\left\{\frac{-1}{2}\text{Tr}[\mathbf{M}_i^{-1}(\mathbf{y} - \mathbf{E}[\mathbf{y}])^T(\mathbf{y} - \mathbf{E}[\mathbf{y}])]\right\} \end{aligned} \quad (\text{C.3})$$

Using the values for  $E[\mathbf{y}]$  defined above yields:

$$p_0(\mathbf{y}|\mathbf{M}_0) = \frac{1}{2\pi^{NJ/2}|\mathbf{M}_0|^{N/2}} \cdot \exp\left\{\frac{-1}{2}\text{Tr}[\mathbf{M}_0^{-1}\mathbf{y}^T\mathbf{y}]\right\} \quad (\text{C.4})$$

$$p_1(\mathbf{y}|\mathbf{B}, \mathbf{M}_1) = \frac{1}{2\pi^{NJ/2}|\mathbf{M}_1|^{N/2}} \cdot \exp\left\{\frac{-1}{2}\text{Tr}[\mathbf{M}_1^{-1}(\mathbf{y} - \mathbf{S}\mathbf{B})^T(\mathbf{y} - \mathbf{S}\mathbf{B})]\right\} \quad (\text{C.5})$$

The maximum likelihood estimate  $\hat{\mathbf{B}}$  is readily derived. Because the conditional pdf in Equation (C.5) is continuous and nonsingular, it is sufficient to consider

$$\frac{\partial \log(p_1(\mathbf{y}|\mathbf{B}, \mathbf{M}_1))}{\partial \mathbf{B}} = -\frac{1}{2}\mathbf{M}_1^{-1}(\mathbf{y} - \mathbf{S}\mathbf{B})^T \cdot (-\mathbf{S}) \quad (\text{C.6})$$

The maximum value is found by setting the right hand side to zero. Since  $\mathbf{M}_1$  is positive definite, the only solution occurs when

$$\mathbf{y}^T\mathbf{S} - \hat{\mathbf{B}}^T\mathbf{S}^T\mathbf{S} = 0 \quad (\text{C.7})$$

Hence, the maximum likelihood estimate of  $\mathbf{B}$  for  $H_1$  is

$$\hat{\mathbf{B}}^T = \mathbf{y}^T\mathbf{S}(\mathbf{S}^T\mathbf{S})^{-1} \quad (\text{C.8})$$

The corresponding estimate for covariance matrix  $\hat{\mathbf{M}}_1$  is found by using Lemma 3.2.2 of [106]. We find

$$\hat{\mathbf{M}}_1 = \frac{1}{N}(\mathbf{y} - \mathbf{S}\hat{\mathbf{B}}^T)^T(\mathbf{y} - \mathbf{S}\hat{\mathbf{B}}^T) \quad (\text{C.9})$$

Similarly, the estimate for covariance matrix  $\hat{\mathbf{M}}_0$  is

$$\hat{\mathbf{M}}_0 = \frac{1}{N}\mathbf{y}^T\mathbf{y} \quad (\text{C.10})$$

Substituting Equations (C.8), (C.9), and (C.10) into Equations (C.4) and (C.5) yields

$$\max_{\mathbf{B}, \mathbf{M} \in \Lambda_1} p_1(\mathbf{y}|\mathbf{B}, \mathbf{M}) = \frac{1}{2\pi^{NJ/2}|\hat{\mathbf{M}}_1|^{N/2}} \exp\left(\frac{-NJ}{2}\right) \quad (\text{C.11})$$

$$\max_{\mathbf{M} \in \Lambda_0} p_0(\mathbf{y}|\mathbf{M}) = \frac{1}{2\pi^{NJ/2}|\hat{\mathbf{M}}_0|^{N/2}} \exp\left(\frac{-NJ}{2}\right) \quad (\text{C.12})$$

and the likelihood ratio test becomes

$$\Lambda(\mathbf{y}) = \frac{|\hat{\mathbf{M}}_0|^{N/2}}{|\hat{\mathbf{M}}_1|^{N/2}} \begin{cases} \geq \tau, & \text{then } H_1 \\ < \tau, & \text{then } H_0 \end{cases} \quad (\text{C.13})$$

Taking the log of  $\Lambda(\mathbf{y})$  produces an equivalent LRT  $\Lambda'$

$$\Lambda'(\mathbf{y}) = \frac{|\hat{\mathbf{M}}_0|}{|\hat{\mathbf{M}}_1|} \begin{cases} \geq \tau', & \text{then } H_1 \\ < \tau', & \text{then } H_0 \end{cases} \quad (\text{C.14})$$

For a target with uniform amplitude, which has  $\mathbf{S}$  as a vector, the estimate  $\hat{\mathbf{B}}^T$  can be written as

$$\hat{\mathbf{B}} = \frac{\mathbf{y}^T \mathbf{S}}{\mathbf{S}^T \mathbf{S}} \quad (\text{C.15})$$

since  $\mathbf{S}^T \mathbf{S}$  is a scalar. Reed and Yu [14] went on by substituting  $\hat{\mathbf{B}}$  in Equation (C.8) to the expression for  $\hat{\mathbf{M}}_1$  in Equation (C.9).

$$\begin{aligned} \hat{\mathbf{M}}_1 &= \frac{1}{N} (\mathbf{y} - \mathbf{S} \frac{\mathbf{y}^T \mathbf{S}}{\mathbf{S}^T \mathbf{S}})^T (\mathbf{y} - \mathbf{S} \frac{\mathbf{y}^T \mathbf{S}}{\mathbf{S}^T \mathbf{S}}) \\ &= \frac{1}{N} \left( \mathbf{y}^T \mathbf{y} - \frac{(\mathbf{y}^T \mathbf{S})^T (\mathbf{y}^T \mathbf{S})}{\mathbf{S}^T \mathbf{S}} \right) \end{aligned} \quad (\text{C.16})$$

which leads to

$$\Lambda'(\mathbf{y}) = \frac{|\mathbf{y}^T \mathbf{y}|}{|\mathbf{y}^T \mathbf{y} - \frac{(\mathbf{y}^T \mathbf{S})^T (\mathbf{y}^T \mathbf{S})}{\mathbf{S}^T \mathbf{S}}|} \begin{cases} \geq \tau', & \text{then } H_1 \\ < \tau', & \text{then } H_0 \end{cases} \quad (\text{C.17})$$

Factoring the scalar  $|\mathbf{y}^T \mathbf{y}|$  from both the nominator and denominator leads to

$$\begin{aligned} \Lambda'(\mathbf{y}) &= \frac{|\mathbf{y}^T \mathbf{y}|}{|\mathbf{y}^T \mathbf{y}| \left| 1 - \frac{(\mathbf{y}^T \mathbf{S})^T (\mathbf{y}^T \mathbf{y})^{-1} (\mathbf{y}^T \mathbf{S})}{\mathbf{S}^T \mathbf{S}} \right|} \\ &= \frac{1}{1 - \frac{(\mathbf{y}^T \mathbf{S})^T (\mathbf{y}^T \mathbf{y})^{-1} (\mathbf{y}^T \mathbf{S})}{\mathbf{S}^T \mathbf{S}}} \end{aligned} \quad (\text{C.18})$$

where the last expression is done with a determinant identity given in [74].

Finally, an equivalent test can be derived by recognizing that  $1/(1-x)$  is a non-linear but one-to-one transform. Hence, a simpler likelihood ratio test is

$$\Lambda''(\mathbf{y}) = \frac{(\mathbf{y}^T \mathbf{S})^T (\mathbf{y}^T \mathbf{y})^{-1} (\mathbf{y}^T \mathbf{S})}{\mathbf{S}^T \mathbf{S}} \begin{cases} \geq \tau'', & \text{then } H_1 \\ < \tau'', & \text{then } H_0 \end{cases} \quad (\text{C.19})$$

Multiplying Equation (C.19) by the constant  $(1/\mathbf{S}^T\mathbf{S})$  and using the estimated amplitude  $\hat{\mathbf{B}}$  in Equation (C.8), the likelihood ratio test can be written in the equivalent form

$$\Lambda'''(\mathbf{y}) = \hat{\mathbf{B}} \cdot (\mathbf{y}^T\mathbf{y})^{-1} \cdot \hat{\mathbf{B}}^T \begin{cases} \geq \tau''', & \text{then } H_1 \\ < \tau''', & \text{then } H_0 \end{cases} \quad (\text{C.20})$$

For a multi-channel image, the dimensions of target amplitude estimate  $\hat{\mathbf{B}}$  are  $J \times 1$ , and those of the reference  $\mathbf{S}$  are  $N \times J$ . This results in a scalar value for  $\Lambda'''$ . The above likelihood ratio test can be interpreted as the ratio of the integrated target energy and the integrated input energy. The latter may include clutter and targets. Since  $\mathbf{S}^T\mathbf{S}$  is a constant, Equation (C.19) shows that the performance of RX is largely determined by the simple projection  $(\mathbf{y}^T\mathbf{S})$ . As a result, RX tends to be relatively insensitive to fine structure in the shape  $\mathbf{S}$ , and it is sometimes referred to as a “blob” or “anomaly” detector.

## BIBLIOGRAPHY

- [1] C. Stewart, "Summary of mine detection research (U)," Tech. Rep. 1636-TR, Vol. 1, DTIC AD320124, U.S. Army Engineer Research and Development Laboratories, Corps of Engineers, Fort Belvoir, VA. May 1960.
- [2] N. H. Witherspoon and J. J. H. Holloway, "Video based multispectral detection of land mines, a technology applicable for use in law enforcement," in *Surveillance Technologies II*, Proceedings of SPIE, vol. 1693, pp. 185-194, 1992.
- [3] N. H. Witherspoon, J. J. H. Holloway, K. S. Davis, R. W. Miller, and A. C. Dubey, "The coastal battlefield reconnaissance and analysis (COBRA) program for minefield detection," in *Detection Technologies for Mines and Minelike Targets II*, Proceedings of SPIE, vol. 2496, pp. 500-508, 1995.
- [4] R. R. Muise, J. A. Wright, and Q. A. Holmes, "Coastal mine detection using COBRA multispectral sensor," in *Detection and Remediation Technologies for Mines and Minelike Targets*, Proceedings of SPIE, vol. 2765, pp. 15-24, 1996.
- [5] J. H. Ballard, R. M. Castellane, B. H. Miles, and K. G. Wesolowicz, "The Remote Minefield Detection System (REMIDS) II, Major Components and Operation," Tech. Rep. EL-92-30, NTIS AD-B175 759, US Army Waterways Experimental Station, Corps of Engineers, 1992.
- [6] G. Maksymonko and K. Breiter, "ASTAMIDS minefield detection performance at Aberdeen Proving Ground test site," in *Detection and Remediation Technologies for Mines and Minelike Targets II*, Proceedings of SPIE, vol. 3079, pp. 726-737, 1997.
- [7] S. B. Achal, J. E. McFee, and C. D. Anger, "Identification of surface-laid mines by classification of compact airborne spectrographic imager (CASI) reflectance spectra," in *Detection Technologies for Mines and Minelike Targets II*, Proceedings of SPIE, vol. 2496, pp. 324-335, 1995.
- [8] J. E. McFee, H. T. Ripley, R. Buxton, and A. M. Thruscutt, "Preliminary study of detection of buried landmines using a programmable hyperspectral imager," in *Detection and Remediation Technologies for Mines and Minelike Targets*, Proceedings of SPIE, vol. 2765, pp. 476-488, 1996.

- [9] J. E. McFee and H. T. Ripley, "Detection of buried landmines using a CASI hyperspectral imager," in *Detection and Remediation Technologies for Mines and Minelike Targets II*, Proceedings of SPIE, vol. 3079, pp. 738–749, 1997.
- [10] S. B. Achal, C. D. Anger, J. E. McFee, and R. W. Herring, "Detection of surface-laid mine fields in VNIR hyperspectral high spatial resolution data," in *Detection Technologies for Mines and Minelike Targets IV*, Proceedings of SPIE, vol. 3710, pp. 808–818, 1999.
- [11] A. M. Smith, A. C. Kenton, R. Horvath, L. S. Nooden, J. Michael, J. A. Wright, J. Mars, J. K. Crowley, M. Sullivan, S. Causey, D. Lee, M. Williams, and K. Montavon, "Hyperspectral mine detection phenomenology program," in *Detection Technologies for Mines and Minelike Targets IV*, Proceedings of SPIE, vol. 3710, pp. 819–829, 1999.
- [12] I. K. Sendur, *Three-Dimensional Thermal and Radiometric Modeling of Land Mine Signatures*. PhD thesis, The Ohio State University, Columbus, OH, 2001.
- [13] F. Cremer, W. de Jong, K. Schutte, J. T. Johnson, and B. A. Baertlein, "Surface mine signature modeling for passive polarimetric IR," in *Detection and Remediation Technology for Mine and Minelike Targets VI*, Proceedings of SPIE, vol. 4742, pp. 51–62, 2002.
- [14] I. S. Reed and X. Yu, "Adaptive multiple-band CFAR detection of an optical pattern with unknown spectral distribution," *IEEE Trans. Acoustics, Speech and Signal Proc.*, vol. 38, no. 10, pp. 1760–1770, October 1990.
- [15] X. Yu and I. S. Reed, "Comparative performance analysis of adaptive multispectral detectors," *IEEE Trans. Acoustics, Speech and Signal Proc.*, vol. 41, no. 8, pp. 2639–2654, August 1993.
- [16] G. G. Stokes, "On the composition and resolution of streams of polarized light from different sources," *Trans. Cambridge Phil. Soc.*, vol. 9, pp. 399–416, 1852.
- [17] S. Chandrasekhar, *Radiative Transfer*. Oxford, UK: Oxford University Press, 1950.
- [18] L. Tsang, J. A. Kong, and R. T. Shin, *Theory of Microwave Remote Sensing*. New York, NY: Wiley, 1985.
- [19] B. K. P. Horn and R. W. Sjoberg, "Calculating the reflectance map," *Applied Optics*, vol. 18, pp. 1770–1779, 1979.
- [20] W. G. Egan, *Photometry and Polarization in Remote Sensing*. Amsterdam, Netherlands: Elsevier Science, 1985.

- [21] A. Ishimaru, *Wave Propagation and Scattering in Random Media*. New York, NY: Academic Press, 1978.
- [22] M. Q. Brewster, *Thermal Radiative Transfer and Properties*. New York, NY: Wiley-Interscience, 1992.
- [23] W. D. Wood, H. W. Deem, and C. F. Lucks, *Thermal Radiative Properties*. New York, NY: Plenum Press, 1964.
- [24] K. L. Coulson, *Polarization and Intensity of Light in the Atmosphere*. Hampton VA: A. Deepak, 1988.
- [25] L. Elterman, "UV, Visible and IR Attenuation for Altitudes to 50 km," Tech. Rep. AFCRL-68-0153, Env. Res. Pap. No. 285, U.S. Air Force, 1968.
- [26] J. R. Schott, *Remote Sensing*. Oxford University Press: Oxford, UK, 1997.
- [27] F. E. Nicodemus, *Radiometry*. New York, NY: Academic, 1967.
- [28] J. Radatz, *The IEEE Standard Dictionary of Electrical and Electronics Terms*. Institute of Electrical and Electronics Engineers, Inc., Sixth ed., 1997.
- [29] Willow Run Laboratories, *Target Signature Analysis Center: Data Compilation Eleventh Supplement Volume I. Bidirectional Reflectance: Definition, Discussion, and Utilization*. Springfield, VA: U.S. Department of Commerce, 1972.
- [30] H. Mueller, "The foundation of optics," *J. Opt. Soc. Amer.*, vol. 38, p. 661, July 1948.
- [31] H. C. Van de Hulst, *Light Scattering by Small Particles*. New York, NY: Wiley, 1957.
- [32] D. Deirmendjian, *Electromagnetic Scattering on Spherical Polydispersions*. New York, NY: Elsevier, 1969.
- [33] A. K. Fung, *Microwave Scattering and Emission Models and Their Applications*. Norwood, MA: Artech House, 1994.
- [34] W. R. Laboratories, *Target Signature Analysis Center: Data Compilation Eleventh Supplement Volume II. Bidirectional Reflectance: Graphic Data*. Springfield, VA: U.S. Department of Commerce, 1972.
- [35] C. Goral, K. E. Torrance, D. P. Greenberg, and B. Battaile, "Modeling the interaction of light between diffuse surfaces," *Computer Graphics*, vol. 18, no. 3, pp. 212-222, 1984.

- [36] W. A. Shurcliff, *Polarization Light: Production and Use*. Cambridge, MA: Harvard University Press, 1962.
- [37] P. Hanrahan and W. Krueger, "Reflection from layered surfaces due to subsurface scattering," in *ACM Computer Graphics Proceedings*, vol. SIGGRAPH 93, pp. 65–174, 1993.
- [38] L. B. Wolff, "Diffuse-reflectance model for smooth dielectric surfaces," *J. Opt. Soc. Am. A*, vol. 11, pp. 2956–2968, November 1994.
- [39] M. Oren and S. K. Nayar, "Generalization of Lambert's reflection model," in *ACM Computer Graphics Proceedings*, vol. SIGGRAPH 94, pp. 65–174, 1994.
- [40] L. B. Wolff, S. K. Nayar, and M. Oren, "Improved diffuse reflectance models for computer vision," *International Journal of Computer Vision*, vol. 30, no. 1, pp. 55–71, 1998.
- [41] B. Phong, "Illumination for computer-generated pictures." *Comm. ACM*, vol. 18, no. 6, pp. 311–317, 1975.
- [42] P. Beckmann and A. Spizzochino, *The Scattering of Electromagnetic Waves from Rough Surfaces*. New York, NY: Pergamon, 1963.
- [43] K. E. Torrance and E. M. Sparrow, "Theory for off specular reflection from roughened surfaces," *J. Opt. Soc. Am.*, vol. 57, no. 9, pp. 1105–1114, Sept. 1967.
- [44] S. K. Nayar, K. Ikeuchi, and T. Kanade, "Surface reflection: physical and geometrical perspectives," *IEEE Trans. on Pattern Anal. and Machine Intell.*, vol. 13, no. 7, pp. 611–634, 1991.
- [45] R. L. Cook and K. E. Torrance, "A reflectance model for computer graphics," *Computer Graphics*, vol. 15, no. 3, pp. 307–316, 1982.
- [46] J. R. Maxwell, J. Beard, S. Weiner, and D. Ladd, "Bidirectional Reflectance Model Validation and Utilization," Tech. Rep. AFAL-TR-73-303, Environmental Research Institute of Michigan (ERIM), Ann Arbor, MI, 1973.
- [47] L. B. Wolff, "Shape from polarization images," *Proc. IEEE Workshop on Computer Vision*, pp. 79–85, 1987.
- [48] H. Westlund and G. W. Meyer, "A BRDF database employing the Beard-Maxwell reflection model," in *Proc. Graphics Interface*, (Calgary, Alberta), pp. 189–201, May 2002.

- [49] S. O. Rice, "Reflection of EM waves by slightly rough surfaces," *Comm. Pure Appl. Math.*, no. 4, pp. 351-378, 1951.
- [50] D. Holliday, "Resolution of a controversy surrounding the Kirchoff approximation and the small perturbation method in rough surface scattering theory," *IEEE Trans. Antennas Propagat.*, vol. 35, pp. 120-122, 1987.
- [51] A. G. Voronovich, *Wave Scattering from Rough Surfaces*. Berlin, Germany: Springer-Verlag, 1994.
- [52] D. R. Jackson, D. P. Winebrenner, and A. Ishimaru, "Application of the composite roughness model to high-frequency bottom backscattering," *J. Acoust. Soc. Am.*, vol. 79, pp. 1410-1422, 1986.
- [53] E. L. Dereniak and G. D. Boreman, *Infrared Detectors and Systems*. Boston, MA: Addison-Wesley, 1996.
- [54] G. Macelloni, G. Nesti, P. Pampaloni, S. Sigismondi, D. Tarchi, and S. Lolli, "Experimental validation of surface scattering and emission models.," *IEEE Trans. Geosci. Remote Sensing*, vol. 38, no. 1, pp. 459-469, 2000.
- [55] S. H. Yueh, R. Kwok, F. K. Li, S. V. Nghiem, and W. J. Wilson, "Polarimetric passive remote sensing of ocean wind vectors.," *Radio Sci.*, vol. 29, pp. 799-814, 1994.
- [56] J. T. Johnson and M. Zhang, "Theoretical study of the small slope approximation for ocean polarimetric thermal emission," *IEEE Trans. Geosci. Remote Sensing*, vol. 37, pp. 2305-2316, 1999.
- [57] I. K. Sendur, J. T. Johnson, and B. A. Baertlein, "Analysis of polarimetric IR phenomena for detection of surface mines," in *Detection Technologies for Mines and Minelike Targets VI*, Proceedings of SPIE, vol. 4394, pp. 153-163, 2001.
- [58] R. A. Millikan, "A study of the polarization of the light emitted by incandescent solid and liquid surfaces," *Phys. Rev.*, no. 3, pp. 81-99, 1895.
- [59] L. B. Wolff, A. Lundberg, and R. Tang, "Image understanding from thermal emission polarization," in *IEEE Proc. on Computer Vision and Pattern Recognition*, (Santa Barbara, CA), pp. 625-631, June 1998.
- [60] J. D. Howe, M. A. Miller, R. V. Blumer, T. E. Petty, M. A. Stevens, D. M. Teale, and M. H. Smith, "Polarization sensing for target acquisition and mine detection," in *Detection and Remediation Technologies for Mine and Minelike Targets V*, Proceedings of SPIE, vol. 4133, pp. 202-213, 2000.

- [61] G. J. Zissis, *Sources of Radiation; The Infrared and Electro-Optical Systems Handbook*, vol. 1. Bellingham, WA: SPIE Press, 1996.
- [62] A. B. Kahle, "A simple thermal model of the earth's surface for geologic mapping by remote sensing.," *Journal of Geophysical Research.*, vol. 82, pp. 1673-1680, 1977.
- [63] A. W. England, "Radiometric of diurnally heated, freezing soil.," *IEEE Trans. Geosci. Remote Sensing*, vol. 28, no. 4, pp. 464-476, 1990.
- [64] K. Y. Kondratyev, *Radiation in the Atmosphere*. New York, NY: Academic Press, 1969.
- [65] K. Watson, "Geologic application of thermal infrared images," in *Guided Optical Communications*, Proceedings of SPIE, vol. 63, pp. 128-137, 1975.
- [66] S. Mohan and J.-F. Lee, "Three-dimensional finite element mesh generation using delaunay triangulation," in *Antennas and Propagation Society International Symposium, 1993. AP-S*, vol. 1, pp. 312-315, 1993.
- [67] Hukseflux Thermal Sensors, *Thermal Conductivity Science*. Delft, Netherlands: Hukseflux Thermal Sensors, 2002. Webpage: [www.hukseflux.com/thermalconductivity/thermal.htm](http://www.hukseflux.com/thermalconductivity/thermal.htm).
- [68] The Nautical Almanac Office United States Naval Observatory and Her Majesty's Nautical Almanac Office United Kingdom, *Astronomical Phenomena for the Year 2003*. Washington, DC: U.S. Printing Office, 2000.
- [69] R. Siegel and J. R. Howell, *Thermal Radiation Heat Transfer*. London, UK: Taylor and Francis, 2002.
- [70] J. D. Foley, A. V. Damm, S. K. Feiner, and J. F. Hughes, *Computer Graphics: Principle and Practice*. Boston, MA: Addison-Wesley, 1996.
- [71] M. F. Modest, *Radiative Heat Transfer*. New York, NY: McGraw-Hill, 1993.
- [72] MTL Systems, Inc, "Multispectral Surface Mine Utility Program (MuSuMUP) VNIR Imagery Data Distribution Report," Tech. Rep. DAAB07-96-D-H754 (D.O. 0232), MTL Systems, Inc, Beavercreek, OH, July 2000.
- [73] J. Y. Chen and I. S. Reed, "A detection algorithm for optical targets in clutter," *IEEE Trans. Aerospace and Electronic Systems.*, vol. AES-23, pp. 46-58, 1987.
- [74] A. Margalit, I. S. Reed, and R. M. Gagliardi, "Adaptive target detection using correlated images," *IEEE Trans. Aerospace and Electronic Systems.*, vol. AES-21, pp. 394-405, June 1985.

- [75] X. Yu, L. E. Hoff, I. S. Reed, A. M. Chen, and L. B. Stotts, "Automatic target detection and recognition in multiband imagery: A unified ML detection and estimation approach," *IEEE Trans. on Image Processing*, vol. 6, pp. 143-156, 1997.
- [76] Q. A. Holmes, C. R. Schwartz, J. H. Seldin, J. A. Wright, and L. W. Witter, "Adaptive multispectral CFAR detection of land mines," in *Detection Technologies for Mines and Minelike Targets II*, Proceedings of SPIE, vol. 2496, pp. 421-432, 1995.
- [77] C. M. Stellman, G. G. Hazel, F. Bucholtz, J. V. Michalowsicz, A. Stocker, and W. Schaaf, "Real-time hyperspectral detection and cuing," *Opt. Eng.*, vol. 39, pp. 1928-1935, 2000.
- [78] S. M. Schweizer and J. M. F. Moura, "Hyperspectral imagery: clutter adaptation in anomaly detection," *IEEE Trans. on Information Theory.*, vol. 46, no. 5, pp. 1855-1871, 2000.
- [79] A. H. S. Solberg, T. Taxt, and A. K. Jain, "A Markov random field model for classification of multispectral satellite imagery," *IEEE Trans. Geosci. Remote Sensing*, vol. 34, no. 1, pp. 100-113, 1996.
- [80] A. H. S. Solberg, A. K. Jain, and T. Taxt, "Multisource classification of remotely sensed data: fusion of Landsat TM and SAR images," *IEEE Trans. Geosci. Remote Sensing*, vol. 32, no. 4, pp. 768-778, 1994.
- [81] A. H. S. Solberg, "Contextual data fusion applied to forest map revision," *IEEE Trans. Geosci. Remote Sensing*, vol. 37, no. 3, pp. 1234-1243, 1999.
- [82] D.-H. Chen, I. K. Sendur, W.-J. Liao, and B. A. Baertlein, "Using physical models to improve thermal IR detection of buried mines," in *Detection Technologies for Mines and Minelike Targets VI*, Proceedings of SPIE, vol. 4394, pp. 207-218, 2001.
- [83] E. A. Ashton, "Detection of subpixel anomalies in multispectral infrared imagery using an adaptive Bayesian classifier," *IEEE Trans. Geosci. Remote Sensing*, vol. 36, no. 2, pp. 506-517, 1998.
- [84] E. A. Ashton and A. Schaum, "Algorithms for the detection of sub-pixel targets in multispectral imagery," *Photogrammetric Engineering and Remote Sensing*, vol. 64, no. 7, pp. 723-731, 1998.
- [85] A. Banerji and J. Goutsias, "A morphological approach to automatic mine detection problems," *IEEE Trans. Aerospace and Electronic Systems.*, vol. 34, no. 7, pp. 1085-1096, 1998.

- [86] S. Agarwal, H. Ramachandran, S. Kummamuru, and O. R. Mitchell, "Algorithms and architecture for airborne minefield detection," in *Detection Technologies for Mines and Minelike Targets VI*, Proceedings of SPIE, vol. 4394, pp. 96–107, 2001.
- [87] V. Vapnik, *The Nature of the Statistical Learning Theory*. New York, NY: Springer Verlag, Second ed., 2000.
- [88] B. Scholkopf, C. J. C. Burges, and A. J. Smola, *Advances in Kernel Methods: Support Vector Learning*. Cambridge, MA: MIT Press, 1999.
- [89] L.-Q. Zhang, Z.-X. Sun, B.-B. Peng, and H.-F. Wang, "Image retrieval using object template," in *Proceedings of the First International Conference on Machine Learning and Cybernetics*, (Beijing, China), vol. 4, pp. 2090–2096, 2002.
- [90] T. Daud, T. Duong, H. Langenbacher, H. Tsu, and A. Thakoor, "Mine discrimination using multispectral imagery with feedforward neural networks," in *Detection Technologies for Mines and Minelike Targets II*, Proceedings of SPIE, vol. 2496, pp. 614–625, 1995.
- [91] M. Minsky and S. Papert, *Perceptrons: An Introduction to Computational Geometry*. Cambridge, MA: MIT Press, 1972.
- [92] Y. C. Lee, G. Doolen, H. H. Chen, G. Z. Sun, T. Maxwell, and H. Y. Lee, "Maching learning using a higher order neural network," *Physica*, vol. 22D, pp. 276–306, 1986.
- [93] C. L. Giles and T. Maxwell, "Learning, invariance, and generalization in higher-order neural networks," *Applied Optics*, vol. 26, no. 23, pp. 4972–4978, 1987.
- [94] B. A. Baertlein and W.-J. Liao, "Wavlet-based higher order neural networks for mine detection in thermal IR imagery," in *Detection and Remediation Technologies for Mine and Minelike Targets V*, Proceedings of SPIE, vol. 4038, pp. 168–178, 2000.
- [95] K. Ramaswary, S. Agarwal, and V. Rao, "Data fusion and evidence accumulation for landmine detection using Dempster-Shafer algorithm," in *Detection Technologies for Mines and Minelike Targets V*, Proceedings of SPIE, vol. 4038, pp. 865–875, 2000.
- [96] A. Arcess, P. H. Mengaert, and E. W. Trombini, "Image detection through bipolar correlation," *IEEE Trans. on Information Theory*, vol. 16, no. 5, pp. 534–541, 1970.
- [97] R. M. Gray, "On the asymptotic eigenvalue distribution of Toeplitz matrices," *IEEE Trans. on Information Theory*, vol. 18, pp. 725–730, 1972.

- [98] S. M. Kay, *Fundamentals of Statistical Signal Processing*. Saddle River, NJ: Prentice - Hall, 1998.
- [99] R. C. Gonzalez and R. E. Woods, *Digital Image Processing*. Boston, MA: Addison-Wesley, 1992.
- [100] B. R. Hunt, "The application of constrained least squares estimation to image restoration by digital computer," *IEEE Trans. Comput.*, vol. C-22, no. 9, pp. 805-812, 1973.
- [101] W. K. Pratt, *Digital Image Processing*. New York, NY: Wiley-Interscience, 1978.
- [102] M. Schlessinger, *Infrared technology fundamentals*. New York, NY: Marcel Dekker, 1995.
- [103] G. J. Zissis, "Fundamentals of infrared - a review," in *Modern Utilization of Infrared Technology I*, Proceedings of SPIE, vol. 62, pp. 67-94, 1975.
- [104] G. B. Rybicki and A. P. Lightman, *Radiative process in astrophysics*. New York, NY: Wiley-Interscience, 1979.
- [105] R. E. Huffman, *Atmospheric Ultraviolet Remote Sensing*. San Diego, CA: Academic Press, 1992.
- [106] T. W. Anderson, *An introduction to Multivariate Statistical Analysis*. New York, NY: Wiley, 1958.